

https://dspace.org/

An investigation into increasing the carbon monoxide tolerance of proton exchange membrane fuel cell systems using gold-based catalysts

Steyn, Johann

2008-12-08T12:53:10Z
http://hdl.handle.net/10539/5875

Downloaded from a DSpace repository. https://dspace.org/

An Investigation into Increasing the Carbon Monoxide Tolerance of Proton Exchange Membrane Fuel Cell Systems Using Gold-based Catalysts

Johann Steyn

PhD

2006

AN INVESTIGATION INTO INCREASING THE CARBON MONOXIDE TOLERANCE OF PROTON EXCHANGE MEMBRANE FUEL CELL SYSTEMS USING GOLD-BASED CATALYSTS

Johann Steyn

A thesis submitted to the Faculty of Engineering and the Built Environment, University of the Witwatersrand, Johannesburg, in fulfillment of the requirements for the degree of Doctor of Philosophy.

Johannesburg, 2006

DECLARATION

I declare that this thesis is my own, unaided work. It is being submitted for the Degree of Doctor of Philosophy in the University of the Witwatersrand, Johannesburg. It has not been submitted before for any degree or examination in any other University.

_____

Johann Steyn

_____ day of _____ year _____

ABSTRACT

Trace amounts of carbon monoxide, typically as low as 10 ppm CO, have a deleterious effect on the activation overpotential losses in proton exchange membrane (PEM) fuel cells. This is because CO preferentially adsorbs on the Pt electrocatalyst at the anode at typical PEM fuel cell operating temperatures, thereby preventing the absorption and ionisation of hydrogen. The inability of current preferential oxidation steps to completely remove CO from hydrogen-rich gas streams has stimulated research into CO tolerant anodes. As opposed to other CO oxidation catalysts, metal oxide supported gold catalysts have been shown to be active for the afore mentioned reaction at low temperatures, making it ideal for the 80°C operating temperatures of PEM fuel cells.

The objective of this study was to investigate the viability of incorporating titanium dioxide supported gold (Au/TiO_2) catalysts inside a PEM fuel cell system to remove CO to levels low enough to prevent poisoning of the Pt-containing anode. Two distinct methods were investigated.

In the first method, the incorporation of the said Au/TiO_2 catalyst inside the membrane electrode assembly (MEA) of a PEM fuel cell for the selective/preferential oxidation of carbon monoxide to carbon dioxide in hydrogen-rich gas fuels, facilitated by the injection of an air bleed stream, was investigated. It was important for this study to simulate typical fuel cell operating conditions in an external CO oxidation test rig. Factors such as gold loading, oxygen concentration, temperature, pressure, membrane electrode assembly constituents, water formation, and selectivity in hydrogen-rich gas streams, were investigated. The Au/TiO_2 catalysts were prepared via deposition-precipitation, a preparation procedure proven to yield nano-sized gold particles, suggested in literature as being crucial for activity on the metal oxide support. The most active catalysts were incorporated into the MEA and its performance tested in a single cell PEM fuel cell.

The catalysts proved to yield exceptional activity for all test conditions inside the CO oxidation test rig. However, no significant improvement in CO tolerance was observed

when these catalysts were incorporated into the MEA. It was concluded that the thin bi-layer configuration resulted in mass transfer and contact time limitations between the catalysts and the simulated reformate gas mixture. Other factors highlighted as possible causes of deactivation included the deleterious effect of the acidic environment in the fuel cell, the formation of liquid water on the catalyst's surface, and the adverse effect of the organic MEA constituents during the MEA production procedure.

The second method investigated was the incorporation of the Au/TiO_2 catalyst in an isolated catalyst chamber in the hydrogen feed line to the fuel cell, between the CO contaminated hydrogen gas cylinder and the anode humidifier. Test work in a CO oxidation test rig indicated that with this configuration, the Au/TiO_2 catalysts were able to remove CO from concentrations of 2000 ppm to less that 1.3 ppm at a space velocity (SV) of 850 000 $ml.g_{cat}^{-1}.h^{-1}$ while introducing a 2 per cent air bleed stream. Incorporation of this Au/TiO_2 preferential oxidation system into a Johnson Matthey single cell PEM fuel cell test station prevented any measurable CO poisoning when 100 and/or 1000 ppm CO, 2 per cent air in hydrogen was introduced to a 0.39 mg $Pt.cm^{-2}$ Pt/C anode. These results were superior compared to other state of the art CO tolerance technologies. An economic viability study indicated that the former can be achieved at a cost of gold equal to 0.8 per cent of the USDoE target cost of $45/kW. This concept might allow fuel cells to operate on less pure hydrogen-rich gas, e.g. from H_2 that would be stored in a fuel tank/cylinder but that would have some CO contamination and would essentially be dry. The use of less pure H_2 should allow a cost incentive to the end user in that less pure H_2 can be produced at a significantly lower cost.

ACKNOWLEDGEMENTS

It gives me great pleasure to thank AngloGold Ashanti, Mintek, and the University of the Witwatersrand Johannesburg who have made this achievement possible through their financial and technical contributions to this study.

Thanks must also be extended to my supervisors, Prof Mike Scurrell, Prof Diane Hildebrandt, and Prof David Glasser for their technical inputs and guidance.

A special word of thanks goes to the Project AuTEK team, especially Dr. Gary Pattrick for his mentorship, and Mr. Stephen Roberts for his technical inputs. I would also like to thank Dr. Elma van der Lingen for her dynamic involvement in Project AuTEK; in particular the work presented in this document.

I wish to thank Dr. Barry Murrer, Dr. Dave Thompsett, and Dr. Sarah Ball, all from Johnson Matthey, for the opportunity to conduct a part of this work at the Johnson Matthey Technology Center, Sonning Common, Reading, UK.

I was fortunate enough to have had Dr. David Thompson from the World Gold Council and consultant to Project AuTEK as a colleague and friend, and I would like to thank him for his interest and enthusiastic involvement in finding new industrial applications for gold, especially related to the work in this document.

Finally, I wish to thank my parents, Thinus and Marietjie, for being the role models that they are and for bringing me this far in life. Truly, this achievement serves as authentication of their inspiration and belief in my abilities, and for that I will always be grateful to them.

CONTENTS

DECLARATION ..... **i**
ABSTRACT ..... **ii**
ACKNOWLEDGEMENTS ..... **iv**
CONTENTS ..... **v**
LIST OF FIGURES ..... **ix**
LIST OF TABLES ..... **xviii**
LIST OF SYMBOLS ..... **xxi**
NOMENCLATURE ..... **xxiv**

1 INTRODUCTION AND SCOPE OF WORK **1**
1.1 Industrial background on fuel cells 1
1.2 Basic fuel cell operation 2
1.3 Types of fuel cells 3
1.4 Proton exchange membrane (PEM) fuel cells 4
1.5 Sources of hydrogen 5
1.5.1 Production of hydrogen via reforming 6
1.6 Tolerance of CO in fuel cell systems 7
1.7 Removal of CO from H_2-rich gas streams 8

2 LITERATURE REVIEW: CATALYTIC ACTIVITY OF GOLD **11**
2.1 Gold based catalysts for CO oxidation 11
2.1.1 Preparation methods 12
2.1.2 Synthesis conditions 13
2.1.3 Catalyst performance measurement 14
2.1.4 Catalyst stability 16
2.1.5 Catalyst reactor design - monoliths 17
2.1.6 Alternative supports – Au/CeO_2 18

3 LITERATURE REVIEW: ELECTROCHEMISTRY OF FUEL CELLS **20**
3.1 Electrochemical energy conversion of H_2/O_2 fuel cells 20

3.2 Cell potential-current relation 21
3.3 Efficiency of fuel cells 26
3.4 Power as a function of current 28

4 OBJECTIVES OF THIS STUDY 31

5 EXPERIMENTAL 33
5.1 Introduction 33
5.2 Gold catalysts 33
5.2.1 Catalyst preparation 33
5.2.2 Catalyst characterisation 34
5.2.3 Activity measurements and catalyst screening for application in MEA 35
5.2.4 Au/TiO_2 catalysts in simulated fuel cell conditions for application in PROX system 36
5.3 Incorporation of the Au/TiO_2 catalysts into the MEA of a PEM fuel cell 38
5.3.1 MEA fabrication 38
5.3.2 Bi-layer formation 39
5.3.3 Polarisation experiments 40
5.3.4 CO poisoning tests 41
5.4 Incorporation of Au/TiO_2 PROX reactor in actual fuel cell system 42

6 RESULTS AND DISCUSSIONS: Au/TiO_2 BI-LAYER CONFIGURATION 43
6.1 Catalyst characterisation 43
6.2 Au/TiO_2 catalytic activity 46
6.2.1Influence of gold loading 46
6.2.2 Influence of hydrogen as background gas 50
6.2.3 Influence of calcination 54
6.2.4 Influence of pressure 57
6.2.5 Influence of temperature 58
6.2.6 Influence of MEA constituents 59
6.2.7 Influence of water formation on catalytic activity 63
6.3 Fuel cell results – bi-layer configuration 65

6.3.1 MEA fabrication and bi-layer formation 65
6.3.2 Polarisation results 66
6.3.3 Influence of Au/TiO_2 on CO tolerance 67
6.4 Fuel cell results – catalyst chamber configuration 70

7 RESULTS AND DISCUSSIONS: Au/TiO_2 PREFERENTIAL OXIDATION (PROX) SYSTEM 72
7.1 Introduction 72
7.1.1 Selection of CO oxidation system 72
7.2 Comparison of Au/TiO_2 powder, granulate, and monolith systems 73
7.3 Influence of Au concentration on CO conversion over Au/TiO_2 coated monoliths 76
7.4 Influence of CO_2 on activity of Au/TiO_2 79
7.5 Online deactivation of Au/TiO_2 granulates and Au/TiO_2 coated monoliths 81
7.5.1 Influence of Carbonate species on deactivation 81
7.5.2 Deactivation due to gold particle size growth during online operation 94
7.5.3 Influence of catalyst bed temperature on activation 95
7.6 Electrochemical investigation 97
7.6.1 Pt/C 98
7.6.2 PtRu/C 99
7.6.3 PtMo/C 101
7.6.4 Influence of Au/TiO_2 PROX system on fuel efficiency 104
7.7 Alternative support – Au/CeO_2 107

8 ECONOMICS AND COMMERCIAL VIABILITY OF SYSTEM 108
8.1 Economic feasibility analysis of Au/TiO_2 PROX system 108
8.2 Projected gold usage 112
8.3 Other practical aspects 115
8.4 Fuel cells: Technical targets 117

9 CONCLUSIONS 118
9.1 Bi-layer system 118
9.2 Isolated catalyst chamber / PROX system 120

10 REFERENCES 122

APPENDIX I 132
APPENDIX II 133
APPENDIX III 134
APPENDIX IV 135
APPENDIX V 136
APPENDIX VI 137
APPENDIX VII 138
APPENDIX VIII 139
APPENDIX IX 140
APPENDIX X 143
APPENDIX XI 144
APPENDIX XII 148
APPENDIX XIII 149
APPENDIX XIV 150

LIST OF FIGURES

Figure 1: Schematic illustration of basis operation of fuel cells. 2

Figure 2: Schematic illustration of the construction of a single cell Proton Exchange Membrane fuel cell. 4

Figure 3: Determination of the cell potential from the anodic and cathodic electrode potentials. 22

Figure 4: Illustration of the decrease in terminal cell potential with increasing current densities due to: Region A – activation overpotential losses; Region B – ohmic overpotential losses; Region C – mass transfer overpotential losses. 22

Figure 5: Influence of i_o on the cell potential at different current densities and constant R_i and i_L values. This also serves as an illustration of the effect of CO poisoning. 24

Figure 6: Influence of R_i on the cell potential at different current densities and constant i_o and i_L values. 25

Figure 7: Influence of i_L on the cell potential at different current densities and constant R_i and i_o values. 25

Figure 8: Power vs. current relation, indicating the reasons for power losses at various currents, after Bockris and Srinivasan [65]. 28

Figure 9: Influence of the internal resistance on the power drawn at specific current values. 29

Figure 10: Influence of the exchange current density on the power drawn at specific current values. 29

Figure 11: Influence of the limiting current on the power drawn at specific current values. 29

Figure 12: Schematic illustration of the incorporation of a titanium dioxide gold catalyst layer in the MEA of a PEM fuel cell. 31

Figure 13: Schematic illustration of the Au-based catalyst chamber in the H_2 feed line between the H_2 containing cylinder and the PEM fuel cell. 32

Figure 14: TEM images of 3wt% Au dispersed on P25 TiO_2 at different magnifications: a,b,c. 44

Figure 15: Size distribution of the Au particles on the P25 TiO_2 support (3wt% Au/TiO_2, number of particles considered (N) = 46) 45

Figure 16: HAADF image of 3wt% Au/TiO_2 catalyst 45

Figure 17: EDX analysis of 3wt% Au/TiO_2 catalyst. 46

Figure 18: Influence of gold loading on CO conversion (0.2% CO in air at 1000 $l.g_{cat}^{-1}.h^{-1}$, 25°C) 47

Figure 19: TEM image showing the gold particle size and dispersion of a 1.3 wt% gold catalyst prepared via deposition precipitation onto P25 titania. 48

Figure 20: TEM image showing the gold particle size and dispersion of a 3.5 wt% gold catalyst prepared via deposition precipitation onto P25 titania. 48

Figure 21: TEM image showing the gold particle size and dispersion of a 4.67 wt% gold catalyst prepared via deposition precipitation onto P25 titania. 49

Figure 22: TEM image showing the gold particle size and dispersion of an 11 wt% gold catalyst prepared via deposition precipitation onto P25 titania. 49

Figure 23: Influence of background gas on CO conversion (0.2% CO, 1000 $l.g_{cat}^{-1}.h^{-1}$, 25°C) 51

Figure 24: Effect of a 10-fold decrease in space velocity on CO conversion in hydrogen as background gas, 0.2% CO and a 2% air bleed at 25°C 52

Figure 25: Influence of air concentration on CO conversion and an indication of selectivity over a 5 wt% Au catalyst (0.2% CO, 1000 $l.g_{cat}^{-1}.h^{-1}$, 25°C). 53

Figure 26: Influence of calcination on the catalytic activity of an extruded titania granule supported gold catalyst (0.5 wt% Au, 1% CO, 600 $l.g_{cat}^{-1}.h^{-1}$, 25°C) [68]. 54

Figure 27: Influence of calcination on the catalytic activity of a P25 titania supported gold catalyst (4.5 wt% Au, 0.2% CO, 1000 $l.g_{cat}^{-1}.h^{-1}$, 25°C) 55

Figure 28: Influence of calcination on the catalytic activity of a P25 titania supported gold catalyst (10 wt% Au, 0.2% CO, 1000 $l.g_{cat}^{-1}.h^{-1}$, 25°C) 56

Figure 29: Influence of calcination on the catalytic activity of a P25 titania supported gold catalyst (20 wt% Au, 0.2% CO, 1000 $l.g_{cat}^{-1}.h^{-1}$, 25°C) 56

Figure 30: Schematic illustration of the comparison between gold loading on extruded titania granules and P25 titania nano-particles. 57

Figure 31: Calculation of the pressure factor, n, for the rate of CO conversion..... 58

Figure 32: Calculation of the activation energy for the CO oxidation reaction over a 1 wt% Au on P25 titania catalyst from an Arrhenius plot. 59

Figure 33: Influence of catalyst ink additives on the catalytic activity of a 4.5 wt% Au/TiO_2 catalyst (1000 $l.g_{cat}^{-1}.h^{-1}$, 0.2% CO, 25°C, JS5_3C)..... 60

Figure 34: Influence of calcining at 300°C for 2.5 hours on catalytic activity of a 4.5 wt% Au catalyst containing 30 wt% Teflon or Nafion (1000 $l.g_{cat}^{-1}.h^{-1}$, 0.2% CO, 25°C, JS5_3C)..... 61

Figure 35: Influence of 25 wt% C-black and 30 wt% Teflon on catalytic activity of a 10 wt% Au/TiO_2 catalyst (1000 $l.g_{cat}^{-1}.h^{-1}$, 0.2% CO, 25°C)..... 62

Figure 36: Influence of water formation on the catalyst surface on CO conversion (1000 $l.g_{cat}^{-1}.h^{-1}$, 0.2% CO, 25°C, 5 wt% Au/TiO_2, dried at 120°C for 14 hours) 63

Figure 37: Influence of water formation on the catalyst surface on CO conversion (10 wt% Au, 75:25 Au:C-black, 30 wt% Teflon, dried at 120°C for 14 hours, calcined at 300°C for 2.5 hours, 1000 $l.g_{cat}^{-1}.h^{-1}$, 0.2% CO, 25°C)..... 64

Figure 38: Comparison between the polarisation performance of a standard Electrochem Inc. MEA and an in-house produced Mintek MEAs. (Fuel flow rate: 42 $ml.min^{-1}$ + 15.35 $ml.min^{-1}.A^{-1}$; Oxidiser flow rate: 34.86 $ml.min^{-1}$ + 12.82 $ml.min^{-1}.A^{-1}$; 80°C, 25 psi)..... 67

Figure 39: Poisoning effect of 350 ppm CO on the Mintek SM3 and SM4 MEAs (217 $mA.cm^{-2}$, fuel flow rate: 42 $ml.min^{-1}$ + 15.35 $ml.min^{-1}.A^{-1}$; oxidiser flow rate: 34.86 $ml.min^{-1}$ + 12.82 $ml.min^{-1}.A^{-1}$; 80°C, 25 psi). Air was introduced into the H_2 fuel as a 2% bleed stream. 68

Figure 40: Poisoning effect of 350 ppm CO on the in-house produced Mintek MEAs (217 $mA.cm^{-2}$, fuel flow rate: 42 $ml.min^{-1}$ + 15.35 $ml.min^{-1}.A^{-1}$; oxidiser flow rate: 34.86 $ml.min^{-1}$ + 12.82 $ml.min^{-1}.A^{-1}$; 80°C, 25 psi). Air was introduced into the H_2 fuel as a 2% bleed stream. 70

Figure 41: Influence of a 20 wt% Au on TiO_2 catalyst on the CO tolerance of a 1 mg $Pt.cm^{-2}$ MEA. (Fuel flow rate: 42 $ml.min^{-1}$ + 15.35 $ml.min^{-1}.A^{-1}$; Oxidiser flow rate: 34.86 $ml.min^{-1}$ + 12.82 $ml.min^{-1}.A^{-1}$; 80°C, 25 psi). Air was introduced into the H_2 fuel as a 2% bleed stream..... 71

Figure 42: Comparison between CO conversion over a 5wt% Au on TiO_2 coated monolith, 5wt% Au on TiO_2 granules, and 5wt% Au on TiO_2 nano-powder (0.2% CO, 2% air, balance H_2, SV 850 000 $ml.g_{cat}^{-1}.h^{-1}$, dry, 25°C) 73

Figure 43: Comparison between CO conversion over a 3 wt% Au on TiO_2 coated monolith, 3wt% Au on TiO_2 granules, and 3wt% Au on TiO_2 powder (50 ppm CO, 2% air, balance H_2, SV 850 000 $ml.g_{cat}^{-1}.h^{-1}$, dry, 25°C)..... 74

Figure 44: CO removal from dry hydrogen gas containing 50 ppm CO over Au/TiO_2 catalysts on cordierite monoliths at 850 000 $ml.g_{cat}^{-1}.h^{-1}$, and 25°C..... 77

Figure 45: Effect of calcination on catalytic activity of Au/TiO_2 catalysts on cordierite monoliths (850 000 $ml.g_{cat}^{-1}.h^{-1}$, 50 ppm CO, 2% air, balance H_2)77

Figure 46: Influence of space velocity on CO conversion over a 5 wt% Au/TiO_2 catalyst on cordierite monolith (50 ppm CO, 2% air, balance H_2) 78

Figure 47: Influence of CO_2 on CO conversion (5 wt% Au/TiO_2 granulate catalyst, 25°C, 80 ppm CO in H_2, 2% air bleed stream, SV = 2 000 000 $ml.g_{cat}^{-1}.h^{-1}$) 79

Figure 48: Influence of CO concentration on deactivation of a 3 wt% Au/TiO_2 granulate (+500 μm -710 μm) catalyst (2% air, balance H_2, SV = 1 700 000 $ml.cat^{-1}.h^{-1}$) .. 82

Figure 49: Influence of CO concentration in the H_2 feed gas on the deactivation of a 3 wt% Au/TiO_2 granulate catalyst (granule size +500 μm -710 μm, gas composition: 2% air, balance H_2, SV = 1 700 000 $ml.g_{cat}^{-1}.h^{-1}$) 82

Figure 50: Influence of CO concentration on the initial and final rate of deactivation of a 3 wt% Au/TiO_2 granulate catalyst (granule size +500 μm -710 μm, gas composition: 2% air, balance H_2, SV = 1 700 000 $ml.g_{cat}^{-1}.h^{-1}$) 83

Figure 51: Correlation between catalyst online deactivation and unaccounted CO_2 (80 ppm CO, 2% air, balance H_2, 4 500 000 $ml.g_{cat}^{-1}.h^{-1}$, 3 wt% Au/TiO_2)..... 86

Figure 52: Influence of 2000 ppm CO_2 on deactivation of a 5wt% Au/TiO_2 granulate catalyst (80 ppm CO, balance H_2, 2% air bleed, SV = 2 000 000 $ml.g_{cat}^{-1}.h^{-1}$, 25°C). 87

Figure 53: FTIR spectra recorded before and after CO oxidation over Au/TiO_2 (5 wt% Au/TiO_2, CO oxidation tests: 80 ppm CO in H_2, 2% air, with or without 0.2% CO_2, SV = 2 000 000 $ml.g_{cat}^{-1}.h^{-1}$, 25°C, 23 hours online operation). Figure a) spaced view, b) aligned view. 88

Figure 54: FTIR spectra recorded (1525 – 800 cm^{-1}) before and after CO oxidation over Au/TiO_2 (5 wt% Au/TiO_2, CO oxidation tests: 80 ppm CO in H_2, 2% air, with or without 0.2% CO_2, SV = 2 000 000 $ml.g_{cat}^{-1}.h^{-1}$, 25°C, 23 hours online operation). 89

Figure 55: Influence of catalyst bed temperature and drying on the deactivation of a 5wt% Au/TiO_2 granulate catalyst (50 ppm CO in H_2, 2% air, 2000 ppm CO_2, SV = 2 000 000 $ml.g_{cat}^{-1}.h^{-1}$). 90

Figure 56: Influence of 12 hour 5N H_2 treatment on catalytic activity of a 5 wt% Au/TiO_2 granulate catalyst (CO conversion from gas mixture containing 50 ppm CO in H_2, 2% air, 2000 ppm CO_2, SV = 2 000 000 $ml.g_{cat}^{-1}.h^{-1}$, 25°C). 92

Figure 57: Difference in the rate of deactivation of a 5 wt% Au/TiO_2 catalyst in the presence and absence of oxygen (50 ppm CO, 2000 ppm CO_2, balance H_2, 2% air bleed, SV=2 000 000 $ml.g_{cat}^{-1}.h^{-1}$, 25°C). 92

Figure 58: Influence of reducing/oxidizing atmosphere on the catalytic activity of a 5 wt% Au/TiO_2 granulate catalyst (50 ppm CO, 2000 ppm CO_2, balance H_2, 2% air bleed, SV = 2 000 000 ml.g_{cat}^{-1}.h^{-1}, 25°C). 93

Figure 59: TEM images of: A) fresh 5 wt% Au/TiO_2 granulate catalyst, and B) the same 5 wt% Au/TiO_2 catalyst exposed to 1000 ml.min^{-1} 5N pure H_2 for 12 hours at 25°C. 94

Figure 60: Influence of online operation on catalytic activity of a 3wt% Au/TiO_2 coated monolith (1.66% air bleed, 2000 ppm CO, balance H_2, SV = 850 000 ml.g_{cat}^{-1}.h^{-1}, 25°C) 95

Figure 61: Online activation of a 3 wt% Au/TiO_2 nano-powder catalyst (2% air bleed, 2000 ppm CO, balance H_2, SV = 2 500 000 ml.g_{cat}^{-1}.h^{-1}, analysis via infra-red (IR) analyser). 96

Figure 62: Temperature effect during online activation of a 3 wt% Au/TiO_2 nano-powder catalyst (2% air bleed, 2000 ppm CO, balance H_2, SV = 2 500 000 ml.g_{cat}^{-1}.h^{-1}, analysis via infrared analyser). 97

Figure 63: CO tolerance of a 0.39g Pt.cm^{-2} Pt/C anode with and without a 3wt% Au/TiO_2 coated monolith PROX reactor (1000 ppm CO, 0.5 A.cm^{-2}, 1.5x stoichiometric H_2 flow rate, SV over Au/TiO_2 catalyst 250 000 ml.g_{cat}^{-1}.h^{-1}, catalyst chamber at 25°C, cell temperature at 80°C, 0.84 mgPt.cm^{-2} Pt/C cathode). 98

Figure 64: CO tolerance of a 0.39 mg Pt.cm^{-2} Pt/C anode with and without a 3wt% Au/TiO_2 coated monolith PROX reactor (100 ppm CO, 0.5 A.cm^{-2}, 1.5x stoichiometric H_2 flow rate, SV over Au/TiO_2 catalyst 330 000 ml.g_{cat}^{-1}.h^{-1}, catalyst chamber at 25°C, cell temperature 80°C, 0.84 mg Pt.cm^{-2} Pt/C cathode). 99

Figure 65: CO tolerance of a 0.5 mg $Pt.cm^{-2}$ PtRu/C anode with and without a 3wt% Au/TiO_2 coated monolith PROX reactor (1000 ppm CO, 0.5 $A.cm^{-2}$, 1.5x stoichiometric H_2 flow rate, SV over Au/TiO_2 catalyst 250 000 $ml.g_{cat}^{-1}.h^{-1}$, catalyst chamber at 25°C, cell temperature 80°C, 0.84 mg $Pt.cm^{-2}$ Pt/C cathode). 100

Figure 66: CO tolerance of a 0.5 mg $Pt.cm^{-2}$ PtRu/C anode with and without a 3wt% Au/TiO_2 coated monolith PROX reactor (100 ppm CO, 0.5 $A.cm^{-2}$, 1.5x stoichiometric H_2 flow rate, SV over Au/TiO_2 catalyst 330 000 $ml.g_{cat}^{-1}.h^{-1}$, catalyst chamber at 25°C, cell temperature 80°C, 0.84 mg $Pt.cm^{-2}$ Pt/C cathode). 101

Figure 67: CO tolerance of a 0.52 mg $Pt.cm^{-2}$ PtMo/C anode with and without a 3wt% Au/TiO_2 coated monolith PROX reactor (1000 ppm CO, 0.5 $A.cm^{-2}$, 1.5x stoichiometric H_2 flow rate, SV over Au/TiO_2 catalyst 250 000 $ml.g_{cat}^{-1}.h^{-1}$, catalyst chamber at 25°C, cell temperature 80°C, 0.84 mg $Pt.cm^{-2}$ cathode). 102

Figure 68: CO tolerance of a 0.52 mg $Pt.cm^{-2}$ PtMo/C anode with and without a 3wt% Au/TiO_2 coated monolith PROX reactor (100 ppm CO, 0.5 $A.cm^{-2}$, 1.5x stoichiometric H_2 flow rate, SV over Au/TiO_2 catalyst 330 000 $ml.g_{cat}^{-1}.h^{-1}$, catalyst chamber at 25°C, cell temperature 80°C, 0.84 mg $Pt.cm^{-2}$ cathode). 102

Figure 69: Summary of CO tolerance results (1000 ppm CO, 0.5 $A.cm^{-2}$, 1.5x stoichiometric H_2 flow rate, SV over 3 wt% Au/TiO_2 catalyst = 250 000 $ml.g_{cat}^{-1}.h^{-1}$, catalyst chamber 25°C, fuel cell 80°C)..... 103

Figure 70: Summary of CO tolerance results (100 ppm CO, 0.5 $A.cm^{-2}$, 1.5x stoichiometric H_2 flow rate, SV over 3 wt% Au/TiO_2 catalyst = 330 000 $ml.g_{cat}^{-1}.h^{-1}$, catalyst chamber 25°C, fuel cell 80°C)..... 103

Figure 71: The comparative performance of a fuel cell operating at 0.7 $A.cm^{-2}$ and H_2 stoichiometry of 1.02 (290 000 $ml.g_{cat}^{-1}.h^{-1}$) and a 2% air bleed stream in the absence and presence of the 3 wt% Au/TiO_2 PROX system (anode: 0.39 mg $Pt.cm^{-2}$, cathode: 0.84 mg $Pt.cm^{-2}$, fuel cell at 80°C, Au/TiO_2 PROX system at room temperature, 25 psi.) 106

Figure 72: Comparison between the catalytic activity of Au/TiO_2 and Au/CeO_2 powders (0.2% CO, 2% air, balance H_2, 850 000 $ml.g_{cat}^{-1}.h^{-1}$, dry) 107

Figure 73: Sensitivity analysis of the influence of the gold price and the wt% gold on the cost of gold in a 60 kW fuel cell system operating at peak power and at a potential of 0.65 V (drawing 92 308 A). Calculations based on a SV of 850 000 $ml.g_{cat}^{-1}.h^{-1}$ over the Au/TiO_2 PROX system. 111

Figure 74: Sensitivity analysis of the influence of the gold price and the wt% gold on percentage cost of gold relative to the USDoE target cost of $45/kW. Calculations based on a 60 kW fuel cell system operating at peak power and at a potential of 0.65 V (drawing 92 308 A). Gas flow calculations based on a SV of 850 000 $ml.g_{cat}^{-1}.h^{-1}$ over the Au/TiO_2 PROX system. 112

Figure 75: Estimated annual gold usage based on different levels of market penetration (by 2020) and different gold loadings for a Au-based catalyst PROX system operating at 850 000 $ml.g_{cat}^{-1}.h^{-1}$ (Assume 60 kW fuel cell systems, and annual vehicle production in 2020 = 78.1 million). 114

Figure 76: Estimated annual gold revenue based on projected market penetration by 2020 and different gold prices for a 3 wt% Au-based PROX system operating at 850 000 $ml.g_{cat}^{-1}.h^{-1}$ (Assume 60 kW fuel cell systems, and annual vehicle production in 2020 = 78.1 million). 114

LIST OF TABLES

Table 1: List of the different types of fuel cells. Differences include the electrolyte material, operating parameters and the possible applications. List includes acidic fuel cells (AFC), direct methanol fuel cells (DMFC), molten carbonate fuel cells (MCFC), phosphoric acid fuel cells (PAFC), proton exchange membrane fuel cells (PEMFC), and solid oxide fuel cells (SOFC). 3

Table 2: Progressive poisoning from 10, 40 and 100 ppm CO on pure Pt and $Pt_{0.5}Ru_{0.5}$ alloy anodes. Data obtained from [16]. 8

Table 3: Standard current and gas flow rate settings for obtaining polarisation data. H_2 flow rates are based on 2.2x stoichiometry and O_2 on 3.67x stoichiometry. 41

Table 4: Calculations highlighting the effect of gold loading on the estimated space velocity over the gold based catalysts in the MEA of a 25 cm^2 single cell PEM fuel cell. Calculations are based on a fuel cell system operating at 500 $mA.cm^{-2}$ and H_2 stoichiometry of 2.2 (as used in standardised single cell testing procedure [66]). ... 65

Table 5: Calculated pressure drop, in kPa, over the different catalyst packed-bed systems using the Ergun Equation (1500 $ml.min^{-1}$, SV = 850 000 $ml.g_{cat}^{-1}.h^{-1}$). Detailed calculations are presented in Appendix VIII. *(* L = d = 0.4 cm)*..... 75

Table 6: The effect of CO_2 on CO conversion obtained over a 5 wt% Au/TiO_2 granulate catalyst (25°C, 80 ppm CO in H_2, 2% air bleed stream, SV = 2 000 000 $ml.g_{cat}^{-1}.h^{-1}$) 80

Table 7: Influence of PROX system on the electrochemical performance of the fuel cell. 106

Table 8: A presentation of the mass of gold needed at different amounts of catalysts with different gold loadings, yielding different space velocities. Calculations are based on the following conditions and assumptions: Assume 60 kW system operating at peak output at 0.65 V (drawing 92 308 A). Hydrogen flow to fuel cell at 1.02 stoichiometry, thus 656 $\ell.min^{-1}$ (calculation of this flow rate is shown in Appendix X). 109

Table 9: A presentation of the cost associated with different amounts of catalysts with different gold loadings, yielding different space velocities. Calculations are based on the following conditions and assumptions: Assume 60 kW system operating at peak output at 0.65 V (drawing 92 308 A). Hydrogen flow to fuel cell at 1.02 stoichiometry, thus 656 $\ell.min^{-1}$ (calculation of this flow rate is shown in Appendix X). Assume gold price of $500/oz. 109

Table 10: A presentation of the percentage cost of Au relative to the USDoE cost target of $45/kW for different amounts of catalysts with different gold loadings, yielding different space velocities. Calculations are based on assuming a 60 kW system operating at peak output at 0.65 V (drawing 92 308 A). Hydrogen flow to fuel cell at 1.02 stoichiometry, thus 656 $\ell.min^{-1}$ (calculation of this flow rate is shown in Appendix X). Assume gold price of $500/oz. 110

Table 11: Indication of new vehicle production in 1990 and 2000. 112

Table 12: An estimation of the volume required by the catalyst reactor for three different systems and different amounts of catalysts. Calculations are based on the following conditions and assumptions: Assume 60 kW system operating at peak output at 0.65 V (drawing 92 308 A). Hydrogen flow to fuel cell at 1.02 stoichiometric, thus 656 $\ell.min^{-1}$ (calculation of this flow rate is shown in Appendix X)..... 116

Table 13: Calculation of the pressure drop over the 3 different catalyst systems for a 60 kW fuel cell system operating at peak output at 0.65 V (drawing 92 308 A). Hydrogen flow to fuel cell at 1.02 stoichiometric, thus 656 $\ell.min^{-1}$ (calculation of this flow rate is shown in Appendix X). Particle sizes used for the calculations were 500 um for the granules and 75 um for the powder catalyst. The simulated reactor had a length : diameter ratio of 2:1. 116

LIST OF SYMBOLS

Symbol	Description	Units
A	Cross sectional area of catalyst bed	m^2
A_p	Surface area of particle	m^2
D_p	Equivalent spherical diameter of particle	m
d	Width of catalyst bed	m
dCO_f/dt	Change in final CO conversion with time	%
dCO_i/dt	Change in initial CO conversion with time	%
CO_{in}	Inlet carbon monoxide concentration	$mol.dm^{-3}$
CO_{out}	Outlet carbon monoxide concentration	$mol.dm^{-3}$
E	Potential	V
$E_{corrected}$	Resistance compensated potential	V
E_A	Activation energy	$J.mol^{-1}$
E_i	Initial potential	V
E_f	Final potential	V
E_r	Thermodynamic reversible potential	V
E^o	Thermodynamic half cell potential	V
e^-	Electron	-
ε	Void fraction	-
ϵ_i	Intrinsic maximum efficiency	-
ϵ_e	Voltage efficiency	-
ϵ_f	Faradaic efficiency	-
F	Faraday's constant	$96485\ C/mol^{e-}$
f_p	Friction factor	-
ΔG	Gibbs free energy of reaction	$J.mol^{-1}$
ΔH	Enthalpy change of reaction	$J.mol^{-1}$
I	Current	A
I_m	Theoretically expected current	A
i_L	Limiting current density	$A.cm^{-2}$

i_o	Exchange current density	$A.cm^{-2}$
k'	Chemical rate constant	-
L	Length of catalyst bed	m
m	Stoichiometric factor	-
m_{Au}	Mass of gold	g
m_c	Mass of catalyst	g
M_{pen}	Market penetration	%
n	Number of moles	-
$\eta_{a,act}$	Anodic activation overpotential loss	V
$\eta_{a,conc}$	Anodic mass transfer overpotential loss	V
$\eta_{c,act}$	Cathodic activation overpotential loss	V
$\eta_{c,conc}$	Cathodic mass transfer overpotential loss	V
η_{ohm}	Ohmic loss inside fuel cell	V
n^{e-}	Number of moles of electrons	-
N_{nv}	Number of new vehicles produced annually	-
$(O_2)_{in}$	Inlet oxygen concentration	$mol.dm^{-3}$
$(O_2)_{out}$	Outlet oxygen concentration	$mol.dm^{-3}$
P	Power	W
P_{total}	Total pressure	Pa
Δp	Pressure drop	Pa
ρ	Density	$g.cm^{-3}$
ρ_b	Bulk density	$g.cm^{-3}$
ρ_p	Particle/material density	$g.cm^{-3}$
Q	Volumetric flow rate	ℓ/min
r	Rate of conversion of carbon monoxide	$\mu mol\ CO.g_{cat}^{-1}.s^{-1}$
R	Universal gas constant	$8.314\ J.mol^{-1}.K^{-1}$
R_e	Resistance of external load	ohm
Re_p	Reynolds number	-
R_i	Internal resistance of cell	ohm
ΔS	Change in entropy	$J.mol^{-1}.K^{-1}$
S_{CO}	Selectivity for CO oxidation	%

T	Absolute temperature	K
μ	Dynamic viscosity	Pa.s
V_a	Anodic half cell potential	V
V_c	Cathodic half cell potential	V
V_p	Volume of particle	m^3
$V_{r,a}$	Reversible potential of anode	V
$V_{r,c}$	Reversible potential of cathode	V
V_s	Superficial velocity	$m.s^{-1}$
X_{CO}	Mole fraction of carbon monoxide	-
X_{O2}	Mole fraction of oxygen	-

NOMENCLATURE

ACF	Acidic fuel cell
Au/Al_2O_3	Gold supported on alumina
$Au/\alpha\text{-}Fe_2O_3$	Gold supported on alpha-iron oxide
Au/CeO_2	Gold supported on cerium dioxide
Au/MOx	Gold supported on a metal oxide
Au/TiO_2	Gold supported on titanium dioxide
CCU	Computer controlled unit
CI	Current interrupt
DMFC	Direct methanol fuel cell
FC	Fuel cell
FCT	Fuel cell test station
FID	Flame ionisation detector
FTIR	Fourier transform infrared spectroscopy
GC	Gas chromatograph
GDL	Gas diffusion layer
$HAuCl_4$	Aurochloric acid
ICE	Internal combustion engine
ICPES	Inductively coupled plasma emission spectroscopy
ID	Internal diameter
IR	Infra-red
JMTC	Johnson Matthey Technology Center
LabMax	Automatic lab reactor

MEA	Membrane electrode assembly
MCFC	Molten carbonate fuel cell
MFC	Mass flow controller
MHSV	Mass hourly space velocity
Mintek	Government / private laboratories for mineral technology – South Africa
Nafion	Perfluorosulfonate ionomer
NASA	National aeronautics and space administration
PAFC	Phosphoric acid fuel cell
PDHID	Pulse discharge helium ionisation detector
PEM	Proton exchange membrane
PEMFC	Proton exchange membrane fuel cell
PNGV	Partnership for a new generation of vehicles
POX	Partial oxidation
PROX	Preferential oxidation
PSA	Pressure swing adsorption
PTFE	Polytetrafluoroethylene
Pt/C	Platinum supported on carbon
PtMo	Platinum-molybdenum bi-metal alloy
PtMo/C	Platinum-molybdenum bi-metal alloy supported on carbon
PtRu	Platinum-ruthenium bi-metal alloy
PtRu/C	Platinum-ruthenium bi-metal alloy supported on carbon
P25 TiO_2	Nano-sized titanium dioxide powder (21 nm particles)
RH	Relative humidity

SELOX	Selective oxidation
SHE	Standard hydrogen electrode
SOFC	Solid oxide fuel cell
SV	Space velocity
TCD	Thermal conductivity detector
Teflon	Polytetrafluoroethylene
TEM	Transmission electron microscope
USDoE	United States Department of Energy
V_{SHE}	Potential relative to standard hydrogen electrode
WGS	Water-gas shift

Chapter 1

INTRODUCTION AND SCOPE OF WORK

1.1 Industrial background on fuel cells

The principle of the fuel cell has been understood for more than one hundred and fifty years. Although the first fuel cell was made by Sir William Robert Grove in 1839, the first kilowatt-scale fuel cell was only developed about four decades ago. Over the past few years, the direct conversion of chemical into electrical energy via fuel cells has been at the center of electrochemical research and development. This drive for fuel cell research and development is a result of society's strive towards developing environmentally-friendly power generation systems. In the reaction between hydrogen and oxygen, for example, the only chemical product is water. Since its initial application as an on-board power supply unit for spacecraft in the sixties, the fuel cell has found various new applications in powering submarines, in decentralized power supply systems, in portable products, and in sensor technology. In the quest for highly efficient, emission-free drive systems, the development of automotive fuel cell units is also proving to be promising.

The European Union and the United States of America have designated their commitment to developing ultra-low and zero emission vehicles by initiating and funding various fuel cell research and development programs. The announcement of the California Environmental legislation in the late 1980's, the Partnership for a New Generation of Vehicles (PNGV) program in 1993, and the *freedom*CAR initiative by the United States Department of Energy (USDoE) in January 2002 are prime examples of such commitment. However, fuel cell technology constitutes a highly varied, challenging interdisciplinary field. It extends from the available fuels and their processing, through the fundamentals of electrochemical processes, especially electrocatalysis, to the numerous new concepts in system technology for complete fuel cell aggregates including

the control of gas, water and heat management. Although significant advances have been made over the past three decades, large scale fuel cell commercialisation has still not been achieved. The main challenges that remain include the cost of the fuel cell system, durability of the fuel cell components and catalysts, hydrogen purity, the cost of supplying ultra-pure hydrogen, and establishing a hydrogen infrastructure.

1.2 Basic fuel cell operation

Fuel cells generate electricity from an electrochemical reaction in which oxygen and hydrogen combine to form water, as depicted in Figure 1.

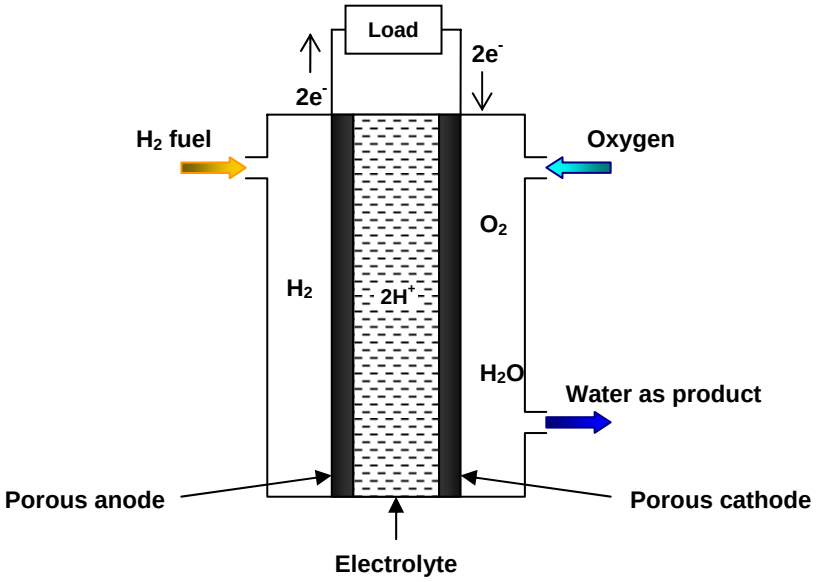

Figure 1: Schematic illustration of basis operation of fuel cells.

Platinum catalysts are generally used to accelerate the electrochemical reactions at the electrodes. A fuel cell typically consists of a fuel electrode, or the anode, and an oxidant electrode, namely the cathode. The electrodes are connected electrically through a load by means of a metallic external circuit. In the metallic part of the circuit electric current is transported by the flow of electrons, whereas in the electrolyte it is transported by the flow of ions, such as the hydrogen ion. Electrons that flow to the cathode are then used in the reduction reaction, where oxygen and hydrogen ions combine to form water as

exhaust gas. Fuel cells are similar to batteries in that both produce electricity. However, whereas batteries have a finite energy supply, fuel cells can continue to produce electricity as long as fuel and air (oxygen) is supplied to the cell. The end result is the elimination of long recharging times, sudden power loss, and the disposal problem associated with batteries.

1.3 Types of fuel cells

There are various types of fuel cells, but they are all based on a central design; this being a two electrode system separated by a solid or liquid electrolyte. Fuel cells are generally classified according to the nature of the electrolyte. Each type requires particular materials and fuels and is suitable for different applications. Table 1 lists the various types of fuel cells, the required fuel and electrolyte, as well as the maximum deliverable power.

PEM fuel cells have distinct advantages over other fuel cells. One of these advantages is that PEM fuel cells can deliver a specific power and power density higher than any other kind of fuel cell. PEM fuel cells also operate at low temperatures, typically 80°C. In addition, its rapid response to varying loads makes it ideal for automobile applications.

Table 1: List of the different types of fuel cells. Differences include the electrolyte material, operating parameters and the possible applications. List includes acidic fuel cells (AFC), direct methanol fuel cells (DMFC), molten carbonate fuel cells (MCFC), phosphoric acid fuel cells (PAFC), proton exchange membrane fuel cells (PEMFC), and solid oxide fuel cells (SOFC).

Fuel cell type	AFC	DMFC	MCFC	PAFC	PEMFC	SOFC
Electrolyte	Potassium Hydroxide	Polymer membrane	Immobilised molten carbon	Immobilised Phosphoric acid	Ion exchange membrane	Ceramic
Operating Temperature	60 – 90°C	60 – 130°C	650°C	200°C	80°C	1000°C
Efficiency	45 – 60%	40%	45 – 60%	35 – 40%	40 – 60%	50 – 65%
Electrical Power	Up to 20 kW	< 10 kW	> 1 MW	> 50 kW	Up to 250 kW	> 200 kW
Possible Applications	Spacecraft	Portable applications	Power stations	Power stations	Vehicles; residential	Power stations

1.4 Proton exchange membrane (PEM) fuel cells

PEM fuel cells were the first kind of fuel cells to find application in NASA's Gemini space flights in the 1960s. Although this technology remained undeveloped for about twenty years thereafter, the California Environmental Legislation and the USA Partnership for a New Generation of Vehicles revitalised research in this field. This regeneration resulted in new research and development programs for portable power and power generation applications. A schematic representation of a single cell PEM fuel cell is shown in Figure 2. Carbon bipolar plates separate individual single cells and also contain gas flow field channels for the fuel and oxidizer gases respectively. Even gas distribution to the electrodes is ensured by means of porous carbon gas diffusion layers (GDLs), located between the bipolar plates and the electrodes. The GDLs are generally rendered hydrophobic by impregnation with polytetrafluoroethylene (PTFE) solution to assist with water management inside the cell. The membrane electrode assembly (MEA) is located in the center of the cell and consists of the platinum containing anode and cathode, as well as the proton exchange membrane. The proton exchange membrane (PEM) is typically constructed from a perfluorosulfonic acid material such as Nafion^{TM}, but the expensive nature of this material has stimulated research in the field of less expensive membranes.

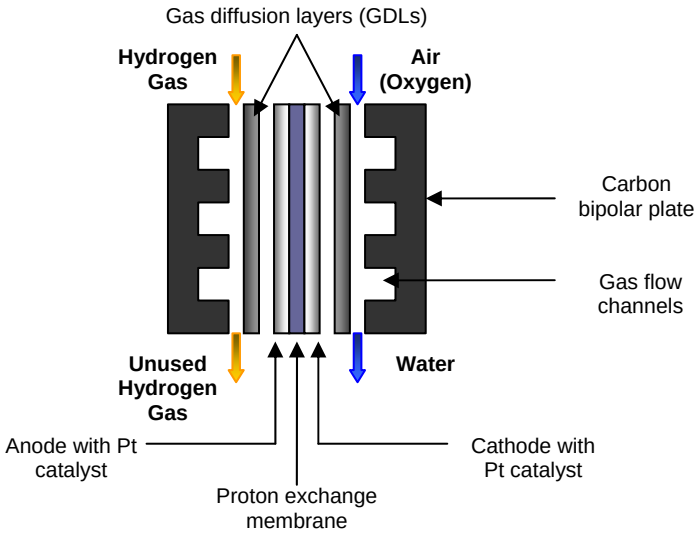

Figure 2: Schematic illustration of the construction of a single cell Proton Exchange Membrane fuel cell.

Hydrogen electro-oxidation on platinum group metals (PGMs) show a key advantage compared to other metals in that they have the required stability to operate in the acidic environment inside the MEA. Platinum, for example, is very active for the electro-oxidation of hydrogen; evident from its exchange current density of 10^{-3} A.cm^{-2} for hydrogen electro-oxidation at ambient temperature. Stonehart and Ross [1] described the mechanism of hydrogen electro-oxidation on Pt in acid electrolytes to proceed by rate-determining dissociative electrosorption of molecular hydrogen (Reactions 1 and 2)

$$H_2 + 2Pt = 2Pt\text{-}H_{ads} \quad (1)$$

$$2Pt\text{-}H_{ads} = 2\ Pt + 2H^+ + 2e^- \quad (2)$$

1.5 Sources of hydrogen

Hydrogen is the most abundant element on earth and only occurs in nature in compound form. Energy is therefore required to produce hydrogen before hydrogen itself can become available for use in energy generation processes. Hydrogen is currently the only practical fuel for use in present generation fuel cells. Pure hydrogen is attractive as a fuel because of its high theoretical energy density, its innocuous combustion product (water), and its unlimited availability as long as a suitable source of energy is available to decompose water via electrolysis. However, with current technology it is generally known that electrolysis is an uneconomical process of producing hydrogen. External processing of hydrocarbon compounds to yield a hydrogen-rich gas mixture seems to be a more viable method of producing large scale quantities of hydrogen in the foreseeable future.

1.5.1 Production of hydrogen via reforming

Some of the most common methods for producing H_2 from hydrocarbons are steam reforming, partial oxidation, and autothermal reforming. Irrespective of which method is selected, the primary hydrogen generating process consists of some combination of the direct reaction between the hydrocarbon compound and steam (3), partial oxidation (POX) (4), the water-gas shift reaction (WGS) (5), and, in the case of methanol, a decomposition reaction (6) [2, 3, 4, 5, 6, 7]. These reactions are shown below.

$$C_mH_n + mH_2O \leftrightarrow mCO + [m + (0.5)n]H_2 \quad (3)$$

$$C_mH_n + (0.5)mO_2 \leftrightarrow mCO + (0.5)nH_2 \quad (4)$$

$$CO + H_2O \leftrightarrow CO_2 + H_2 \quad (5)$$

$$CH_3OH \leftrightarrow CO + 2H_2 \quad (6)$$

One of the most promising hydrocarbon fuels is methanol. The advantages of using methanol as fuel for fuel cell power systems is that it can be converted into a hydrogen-rich stream at temperatures as low as 200°C, much lower than the temperatures required for other liquid or gaseous hydrocarbons [8]. Methanol also has a high energy density and, from an automotive perspective, is much safer to be carried on-board a vehicle than pure hydrogen. In addition, the fact that the current distribution infrastructure for gasoline can be economically converted to one for methanol makes it an attractive source of hydrogen delivery to fuel cell powered vehicles. The methanol can then be reformed on-board the vehicle to produce hydrogen-rich fuel.

The reforming processes typically yield reformates with gas compositions of 40 – 70 per cent H_2, 15 – 25 per cent CO_2, 1 – 2 per cent CO, and small amounts of inert gases such as nitrogen and water vapour. The presence CO in the reformate significantly retards Reaction 1, due to the strong bond formed between CO and the Pt electrocatalyst sites in the anode layer. Even at ppm levels of CO, the CO coverage is above 0.98 [9].

Gottesfeld and Paffort [10] reported in 1988 that CO concentrations as low as 10 ppm in diluted hydrogen streams significantly decreases the performance of the PEM fuel cell. They ascribed this effect to CO preferentially adsorbing onto the active sites of the Pt electrocatalyst at the anode, thereby preventing the dissociative adsorption of hydrogen and its subsequent ionisation. In order to maximise the conversion of H_2 and minimise the CO content, the reforming step is followed by other conversion steps, which require additional, complicated, and expensive reactors, as discussed in detail by Costamagna and Srinivasan [11]. This configuration makes it almost impractical for use on-board a motor vehicle.

It is mainly due to these constraints that the USDoE in 2004 announced a shift in focus from on-board reforming of hydrocarbons to on-board storage of pressurized hydrogen. One of the proposed strategies to establish a hydrogen distribution network is to transport natural gas to localised fueling stations equipped with reforming technologies to produce hydrogen onsite, followed by hydrogen enrichment using various purifications techniques. These purification techniques in itself are expensive and will add an additional cost to producing ultra-pure hydrogen (99.999 per cent). A fuel cell system capable of operating on less pure hydrogen will therefore allow for less complicated hydrogen production techniques and will subsequently offer a cost incentive to the end user.

1.6 Tolerance of CO in fuel cell systems

High surface area PtRu electrocatalysts dispersed on carbon (PtRu/C) have shown enhanced CO tolerance [12, 13, 14, 15, 16]. Although less susceptible to CO poisoning, it has been shown that PtRu anodes are more likely to be poisoned by sulphur containing gases such as H_2S and SO_2 than Pt anodes [17]. In addition, Oetjen *et al.* [15] reported a loss of 270 mV at 1 $A.cm^{-2}$ and 85°C for a PtRu/C electrode operating in CO concentrations of 100 ppm, which is still higher than that desirable for applications in a real system. Similar results were obtained by Ralph *et al.* [16] who reported that even

with an optimised $Pt_{0.5}Ru_{0.5}$ catalyst, the presence of 10 ppm CO significantly decreased the fuel cell's performance. Comparative data is given in Table 2 below:

Table 2: Progressive poisoning from 10, 40 and 100 ppm CO on pure Pt and $Pt_{0.5}Ru_{0.5}$ alloy anodes. Data obtained from [16].

CO (ppm in H_2)	mV at 0.5 $A.cm^{-2}$ over Pt	mV at 0.5 $A.cm^{-2}$ over PtRu
0	0.680	0.657
10	0.483	0.614
40	0.291	0.569
100	0.204	0.511

Even though the $Pt_{0.5}Ru_{0.5}$ anode showed increased CO tolerance at 0.5 $A.cm^{-2}$, the cell potential still decreased by 6.5 per cent in the presence of 10 ppm CO, and 22.2 per cent in the presence of 100 ppm CO.

Another promising mixed metal anode is PtMo/C [18, 19]. Mukerjee *et al.* [20, 21] have shown a threefold increase in CO tolerance in commercial PtMo/C (E-TEK) in the presence of a mixture of H_2 and 100 ppm CO, with a loss of 100 mV at 1 $A.cm^{-2}$.

Although these materials show increased CO tolerance, a certain degree of performance loss still exists. In addition, mixed metal anodes are more expensive than Pt/C anodes. Ideally, a system tolerant of CO concentrations in excess of 100 ppm, without a significant increase in the cost of the system and without any performance loss, is required for this technology to become industrially viable.

1.7 Removal of CO from H_2-rich gas streams

Hydrogen enrichment/purification can typically be achieved by pressure swing adsorption (PSA), or by passing the gas through diffuser membranes made from palladium-silver alloys. Although PSA is effective, a portion of the purified hydrogen stream must be

used as a sweep gas to regenerate the absorbent, which decreases the amount of fuel available for the fuel cell. Furthermore, large quantities of absorbent are needed and heat must be applied to the adsorbent to liberate CO during regeneration [22]. Diffuser membranes produce ultra-pure H_2. However, the flux through the membranes is usually too slow [23] and its expensive nature makes commercial application impractical.

It is also feasible to remove final traces of CO by methanation [24], as shown in Equation 7. However, a drawback of this method is that three moles of H_2 is consumed to convert one mole of CO to CH_4, thereby limiting its applications to H_2 purification from H_2 containing very small amounts of CO. In addition, conventional Ni methanation catalysts typically require temperatures higher than 230°C [23]. Yet another drawback of this method is the fact that the use of pyrophoric Ni as methanation catalyst in mobile applications is considered a potential health hazard.

$$CO + 3H_2 \rightarrow CH_4 + H_2O \qquad (7)$$

Other methods for removing CO from hydrogen include water-gas shift (WGS) (8), or preferential/selective oxidation (PROX / SELOX) (9). Low temperature WGS can be achieved over the temperature range 250 – 300°C using precious metal based systems.

$$\text{WGS:} \quad H_2O + CO \rightarrow H_2 + CO_2 \qquad \Delta H^o = -41.2 \text{ kJ.mol}^{-1} \qquad (8)$$

$$\text{PROX:} \quad CO + 0.5O_2 \rightarrow CO_2 \qquad \Delta H^o = -281.4 \text{ kJ.mol}^{-1} \qquad (9)$$

Of these techniques, selective/preferential CO oxidation (PROX) is the easiest and most economical method of CO removal. Au-based preferential oxidation catalysts are particularly promising since they are active for CO oxidation at low temperatures, even as low as -70°C [27]. Although not yet comprehensively investigated, one possible option to remove CO from the hydrogen feed stream to fuel cells systems is to use metal oxide

supported gold catalysts for the selective catalytic oxidation of CO to CO_2. This can be attempted by incorporating the said catalyst as a bi-layer inside the MEA in front of the Pt, PtRu, or PtMo electrocatalyst, and injecting an air bleed stream to facilitate the combustion reaction, or, by having an external Au/MOx containing PROX reactor in the H_2 feed stream prior to the CO contaminated H_2 entering the fuel cell. The latter concept might allow fuel cells to operate on less pure H_2-rich gas, e.g. from H_2 that would be stored in a fuel tank/cylinder but that would have some CO contamination and would essentially be dry. The use of less pure H_2 should allow a cost incentive to the end user since it can be produced at a significantly lower cost. Both the above mentioned concepts were investigated in this study.

Chapter 2

LITERATURE REVIEW: CATALYTIC ACTIVITY OF GOLD

2.1 Gold based catalysts for CO oxidation

Bulk gold is chemically inert and does not readily adsorb hydrogen and oxygen. However, in 1970 Cha and Parravano [26] found that redistribution of an isotopic carbon tracer between CO and CO_2 occurred on Au/MgO and Au/Al_2O_3 catalysts at 200 – 400°C. Haruta and co-workers have done ground-braking work in the science of gold as a heterogenous catalyst. In 1987, Haruta *et al.* [27] showed that small coprecipitated gold particles on Fe_2O_3, Co_3O_4 and NiO were active for the oxidation of CO at temperatures as low as -70°C.

Since Haruta's findings, several researchers [28, 29, 34, 35, 36, 37] have found that catalysts formed by the dispersion of gold nanoparticles on metal oxide supports, such as TiO_2, Fe_2O_3, CeO_2, Al_2O_3, $FeTiO_2$, ZnO, SiO_2, Co_3O_4, MnO_2, Mn_3O_4, MgO, SnO_2, can be very active for the catalytic oxidation of CO to CO_2. Although the necessity of a metal oxide support for the catalytic activity of Au-based catalysts has generally been confirmed, one ongoing debate is about the role of the metal oxide support in the low temperature activity of these catalysts. Some researchers suggest that the primary role of the metal oxide is to facilitate dispersion of the gold particles [38, 39], while others have reported a distinct dependence of CO oxidation kinetics on the support material used [36, 42]. Another area of conflicting opinions is the nature of the active species. Some authors advocate that ionic gold provides the active sites for CO oxidation [40, 41] whereas others claim metallic gold to be the active species [34, 44]. It has also been suggested that both ionic and metallic gold is essential for catalytic activity [45].

Metal oxide supported gold catalysts are unique compared to other CO oxidation catalysts such as those of Pt, Ru, and Rh in the sense that they show very high catalytic

activity at low temperatures. This characteristic makes gold catalysts ideal for use in low temperature applications such as PEM fuel cells, where the operating temperature is limited to approximately 80°C due to the inability of the current state of the art proton exchange membranes to effectively conduct protons at higher temperatures.

The catalytic activity of the supported gold is intrinsically dependent on the gold dispersion, support oxide and the preparation method used. Haruta [28] reported that hemispherical ultra-fine particles with diameters of 2 – 5 nm give the highest turnover frequencies and product yields. The importance of small particles for catalytic activity is stressed, since smooth surfaces of metallic gold do not absorb CO at room temperature [29]. This has been attributed to CO being activated by adsorption on corner sites or perimeter sites formed between the gold particles and the metal oxide support.

2.1.1 Preparation methods

Some of the most generally used preparation methods for metal oxide supported gold catalysts include impregnation, co-precipitation and deposition-precipitation. Although the conventional impregnation procedures yield highly active platinum group metals catalysts, considerably lower activities are obtained for gold catalysts prepared in a similar way [30]. Okumura [31] reported that the lower activities obtained with impregnation are typically due to: 1) a wide distribution of the gold particle sizes, ranging from small clusters to relatively large particles, and 2) chloride, which poisons the catalysis for many reactions, remains on the catalyst surfaces when the metal oxide support, impregnated with chloroauric acid ($HAuCl_4$), is calcined in air at temperatures below 873 K. Okumura *et al.* [32, 33] reported that catalysts prepared by impregnation exhibit improved activity by reduction with H_2, where chloride is effectively removed as HCl.

Co-precipitation and deposition-precipitation [34] have been shown to be the best preparative methods, producing hemispherical particles strongly attached to the oxide

support. Co-precipitation involves the simultaneous precipitation of two hydroxides by the addition of chloroauric acid ($HAuCl_4$) and a metal nitrate to a basic solution. However, it has been reported that co-precipitation may lead to significant concentrations of sodium or chloride being contained in the catalyst, both of which are detrimental to catalytic performance.

In the case of the deposition-precipitation technique, the precursor of the active gold species is slowly precipitated (in the form of a hydroxide) from solution in the presence of the metal oxide support by raising the pH to between 6 and 10 [34]. Zanella *et al.* [35] reported that the gold species deposited during deposition-precipitation, using sodium hydroxide, is not a chloro-hydroxo compound but a species with a structure close to that of gold hydroxide. They proposed that deposition could occur via a grafting reaction of the metal complexes with hydroxyl groups with the support surface, as depicted in Equation 10. It was reported that such a reaction could lead to the formation of a grafted hydroxy-gold species.

$$TiOH + \left[AuCl\left(OH\right)_3\right]^- \rightarrow Ti - \left[O - Au\left(OH\right)_3\right]^- + H^+ + Cl^- \qquad (10)$$

The deposition-precipitation method using sodium hydroxide gives rise to better catalytic activity than impregnation or co-precipitation [35]. A disadvantage of the deposition-preparation method is that all of the gold present in solution is not deposited onto the support. Higher gold loading efficiencies can be obtained by lowering the pH, but this occurs at the expense of increasing the size of the gold particles, which results in a decrease in catalytic activity.

2.1.2 Synthesis conditions

In addition to the preparation method, synthesis conditions during deposition-precipitation, such as pH during precipitation, ageing temperature and time, temperature

of calcination and the pretreatment conditions (air, vacuum, hydrogen, nitrogen) have a significant effect on the properties of gold-based catalysts. Wolf and Schuth [36] reported that the optimum pH value is slightly dependent on the support and lies between pH 8 and 9. Also, it was found that the catalytic activity for CO oxidation decreased with increasing calcination temperature. These influences of pH and calcination temperature were attributed to a change in the gold particle size. On the contrary, Iizuka *et al.* [37] highlighted the importance of higher calcination temperatures for higher catalytic activity. Although gold particles grew larger, they reported that contact with the support contributes to an additional increase in activity at least by one order of magnitude. This emphasizes that catalytic activity is not exclusively dependant on the size of the gold particles, but also on other factors such as the type of support and the nature of the contact between the gold particles and the support. The highest published activities for CO oxidation to date have been obtained by Moreau *et al.* [43], especially when operating under kinetic control.

In general, gold loadings between 0.5 and 2 wt% Au have previously been investigated. In the present study, the necessity of minimising ohmic overpotential losses in the fuel cell dictated the investigation of gold loadings as high as 20 wt% in order to decrease the thickness of the MEA.

2.1.3 Catalyst performance measurement

The catalytic performance of Au-based catalysts for CO oxidation from H_2-rich gas streams can be presented in terms of CO conversion and the selectivity towards CO conversion in H_2-rich gas streams. Ideally, for fuel cell applications, the conversion of CO to CO_2 has to be maximized while preventing copious amounts of hydrogen being oxidized to water. The desired CO oxidation and undesired H_2 oxidation reactions are shown in Equations 11 and 12 respectively.

$$CO + 0.5O_2 \rightarrow CO_2 \quad (11)$$

$$H_2 + 0.5O_2 \rightarrow H_2O \quad (12)$$

CO conversion is defined as the amount of CO that is oxidised to CO_2 as the gas passes through the catalyst bed, as indicated in Equation 13.

$$X_{CO}(\%) = 100 \times \frac{[CO]_{in} - [CO]_{out}}{[CO]_{in}} \quad (13)$$

where X_{CO} is the CO conversion, $[CO]_{in}$ is the concentration of CO in the feed gas, and $[CO]_{out}$ the residual CO concentration in the exit gas stream. Another commonly used method of expressing the activity of these catalysts is in terms of the rate of CO conversion in micromole CO converted by one gram catalyst in one second ($\mu mol\ CO.g_{cat}^{-1}.s^{-1}$). Besides CO conversion, the residual CO concentration in the H_2-gas after passing through the catalyst bed is of importance. Depending on the specific application, the desired residual CO concentration may be as low as 1 ppm.

The selectivity of catalysts for CO oxidation in H_2-rich streams is important since some of the oxygen might be used to oxidise H_2 to H_2O. This is undesirable since the oxidation of H_2 will decrease the fuel efficiency of the fuel cell. In contrast to Pt-group metal catalysts, supported gold catalysts are intrinsically more active for CO oxidation than for H_2 oxidation [44]. The selectivity for CO oxidation can be quantified by using Equation 14.

$$S_{CO}(\%) = 100 \times \frac{0.5([CO]_{in} - [CO]_{out})}{[O_2]_{in} - [O_2]_{out}} \quad (14)$$

where S_{CO} is the selectivity, $[O_2]_{in}$ is the concentration of oxygen in the feed gas, and $[O_2]_{out}$ the residual oxygen concentration in the exit gas stream.

Schumacher *et al*. [46] reported that hydrogen has a significant effect on the kinetics of the CO oxidation reaction by decreasing the reaction rate as a result of the adsorption and reaction of hydrogen. It was found that selectivity was dependent on the relative amounts of CO and H_2, and also temperature. Changes in selectivity were attributed to changes in CO oxidation, while hydrogen oxidation remained relatively constant.

2.1.4 Catalyst stability

Stability is critical for any catalyst to find commercial application in fuel cells. Stable operating performance of 5000 hours is required for automotive applications, and up to 40 000 hours for stationary applications.

Metal oxide supported gold catalysts tend to deactivate with storage and/or time on-line [47, 48, 49, 50, 51]. Deactivation of Au-metal oxide catalysts for the CO oxidation reaction is mostly attributed to the accumulation of carbonate species, which can block access of CO and O_2 to the active sites [47, 48]. The formation of carbonate-species can occur by the adsorption of CO_2 in air (storage) or from CO_2 present in the reactant or product gas mixture (on-line). It has been reported that the addition of H_2O can prevent the deactivation of Au/α-Fe_2O_3 [47] and Au/Al_2O_3 [49] and may enhance the rate of decomposition of carbonate species by reactive conversion to bicarbonate species, which are thermally less stable. Manzoli *et al*. [51] reported that hydrogen reduced the deactivation of Au/ZnO catalysts by inhibiting the formation of transient intermediates and stable carbonates on the support. FTIR studies suggested the reduction of the amount

of stable species at the interface resulted from the lowered basicity of the reactive oxygen at the metal support interface. Hydrogen inhibition of formate and carbonate formation was also observed by Shumacher *et al*. [46] using Au/TiO_2 catalysts.

Another possible reason for the deactivation of Au-based catalysts might be due to particle size growth. This effect is of particular importance when chlorine (Cl^-) species are present on the surface of the catalyst due to its high mobility.

Although the above mentioned are possible explanations for the deactivation phenomena of metal oxide supported gold catalysts, an exact mechanism for deactivation has not yet been fully comprehended.

2.1.5 Catalyst reactor design - monoliths

Conventional gas processing reactors generally consist of a tubular reactor containing particulate catalysts. Although these reactors have found numerous applications, considerable advantages can be gained by the use of reactors in which heat transfer is optimised. Monolith systems, where the catalysts are deposited / coated onto the walls of a multiple-channeled reactor, are promising examples [52, 53, 54, 55]. The amount of catalyst that is wash-coated onto the monolith generally depends on the viscosity of the catalyst slurry and the number of wash-coats. Monoliths are typically fabricated from ceramics, such as cordierite, or metal alloys, such as FeCr-alloy (Fe = 72.8; Cr = 22; Al = 5; Y = 0.1; Zr = 0.1) [23]. The advantages of monolith systems are that they result in minimal pressure drop and are able to endure repeated temperature cycles. The necessity of controlling the temperature in the selective oxidation process makes monolithic catalysts very attractive. Conceptual drawings of a typical cordierite monolith are presented in Appendix I.

2.1.6 Alternative supports – Au/CeO_2

The use of ceria (CeO_2) supported Au catalysts for CO removal from H_2 rich streams have previously been investigated by various authors [56, 57]. Co-precipitation was the most favoured preparation procedure in both studies, and an average gold particle size of 4.5 nm was quoted by Luengnaruemitchai *et al.* [56]. CeO_2 is the oxide of the rare-earth metal cerium (Ce) which may occur in several compositions, due to the capacity of Ce to switch between its two oxidation states of Ce^{3+} and Ce^{4+}. CeO_2 has been shown to promote the activity of the water-gas-shift reaction, in which H_2O and CO react to reversibly form H_2 and CO_2 [58, 59, 60]. Other functions ascribed to CeO_2 include its role in maintaining the dispersion of the catalytic metals [61], and stabilising the surface area of the support [62].

Of relevance to this study was the oxygen storage capacity of CeO_2 which improves the oxidation of CO and hydrocarbons. For CO oxidation, CeO_2 has been found to lower the activation energy, increase the reaction rate and suppress the usual CO inhibition effect [63]. Holmgren *et al*. [64] reported that CeO_2 promotes the activity of Pt in both lean and rich reactant gases for CO oxidation. This property of CeO_2 prompted Luengnaruemitchai *et al*. [56] to investigate Au/CeO_2 catalysts for selective CO oxidation in H_2 rich streams. They reported that the co-precipitated Au/CeO_2 (1 wt% Au) catalysts remained inactive below 90°C, where after a spike in activity was observed. However, the most active Au/CeO_2 catalyst quoted in their study only yielded 98 per cent CO conversion while introducing 2 per cent oxygen (equivalent to 10 per cent air) at 30 000 $ml.g_{cat}^{-1}.h^{-1}$ with the catalyst bed temperature at 100°C. This is significantly less active than the Au/TiO_2 catalysts (0.6% Au/TiO_2) investigated by Moreau and Bond [43], which yielded 100 per cent CO conversion at 66 000 $ml.g_{cat}^{-1}.h^{-1}$ and a catalyst bed temperature of 25°C.

Compared to TiO_2, Al_2O_3, and Fe_2O_3, ceria has not been widely investigated as support for CO oxidation over Au-based catalysts. In the present study, CeO_2 supported gold

catalysts were prepared via deposition-precipitation and the activity and selectivity were compared to that of the Au/TiO_2 catalysts.

Chapter 3

LITERATURE REVIEW: ELECTROCHEMISTRY OF FUEL CELLS

3.1 Electrochemical energy conversion of H_2/O_2 fuel cells

The conversion of the free-energy change of a chemical reaction directly into electrical energy is termed electrochemical energy conversion. Electrochemical energy conversion can be expressed by Equation 15 from which it is evident that the free-energy change of a chemical reaction *(ΔG)* is directly proportional to the negative thermodynamic reversible potential of the cell *(E_r)*.

$$\Delta G = -nFE_r \tag{15}$$

where *n* is the number of moles transferred, and *F* Faraday's constant (96 485 C.mol electrons^{-1}). For H_2 / O_2 fuel cells the electrochemical half cell reactions and the respective electrode potentials are shown in Equations 16 – 18 below:

Anode: $H_2 \rightarrow 2H^+ + 2e^-$ $E^o = 0.00\ V_{SHE}$ (16)

Cathode: $O_2 + 4H^+ + 4e^- \rightarrow 2H_2O$ $E^o = 1.23\ V_{SHE}$ (17)

Overall: $2H_2 + O_2 \rightarrow 2H_2O$ $E_r = 1.23\ V_{SHE}$ (18)

As shown in Equation 18, the thermodynamic reversible potential for the cell reaction is 1.23 V_{SHE}. Ideally, the terminal cell potential is constant and should be equal to the thermodynamic reversible potential at any drawn current density. However, the cell potential decreases with increasing current densities drawn from the cell. This is due to

overpotential losses that occur because of rate limiting steps in the overall reaction rate. Overpotential losses in fuel cells occur due to the slowness of one or more of the intermediate steps of the reactions occurring at either or both of the electrodes, termed activation overpotential losses; the slowness of mass-transport processes, namely mass transport overpotential losses; and ohmic overpotential losses across the electrolyte. The absorption of CO onto the Pt electrocatalyst surface will typically result in a decrease in active sites for hydrogen oxidation and will therefore result in increased activation overpotential losses.

3.2 Cell potential-current relation

Figure 3 represents a schematic illustration of a polarisation diagram. The curves indicated in this figure represent the change in the half cell electrode potentials of the anodic oxidation of hydrogen and the cathodic reduction of oxygen at different current densities. As illustrated in Figure 3, the cell potential is equal to the difference between the two electrode potentials of the half cell reactions at a specific current density. As the current density increases, the difference between the half cell potentials decreases due to overpotential losses, resulting in a lower terminal cell potential. The terminal cell potential, E, therefore differs from the thermodynamic reversible potential, E_r, by an amount equal to the sum of the overpotential losses.

The influence of overpotential losses on the terminal cell potential is shown in Figure 4. Activation overpotential losses (Figure 4, region A) occur at low current densities where the cell potential may be controlled by impurity reactions. At higher current densities the effects of impurities are small because of their low concentrations. At higher current densities, a linear decrease in the cell potential with increasing current density is evident (Figure 4, region B). This decrease in cell potential is due to the resistance of the electrolyte. The resistivity of the electrolyte layer is largely dependant on the type of electrolyte used, either solid or liquid, and the layer thickness. Finally, at high current densities, the rates of the chemical reactions at the electrodes are high and the diffusion of

reactants to, or products away from the electrode, becomes the rate limiting step (Figure 4, region C).

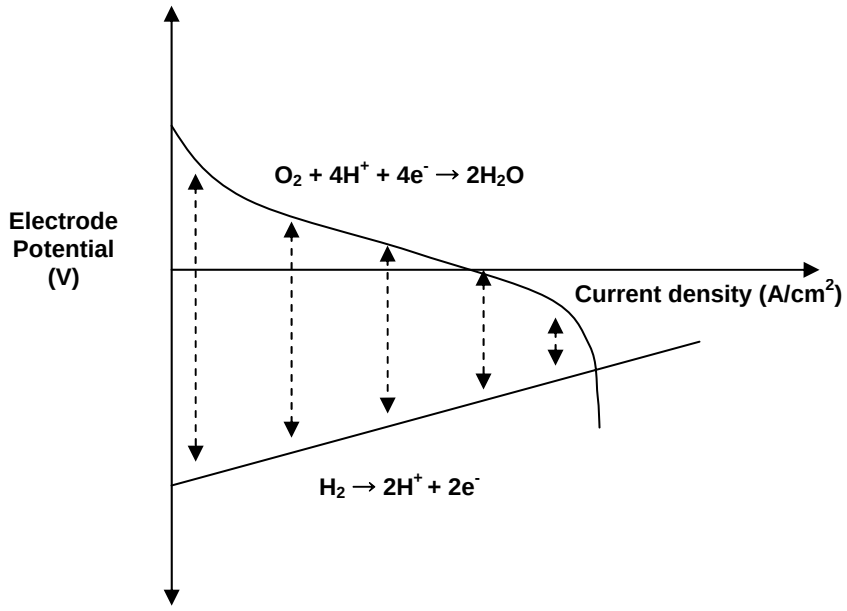

Figure 3: Determination of the cell potential from the anodic and cathodic electrode potentials.

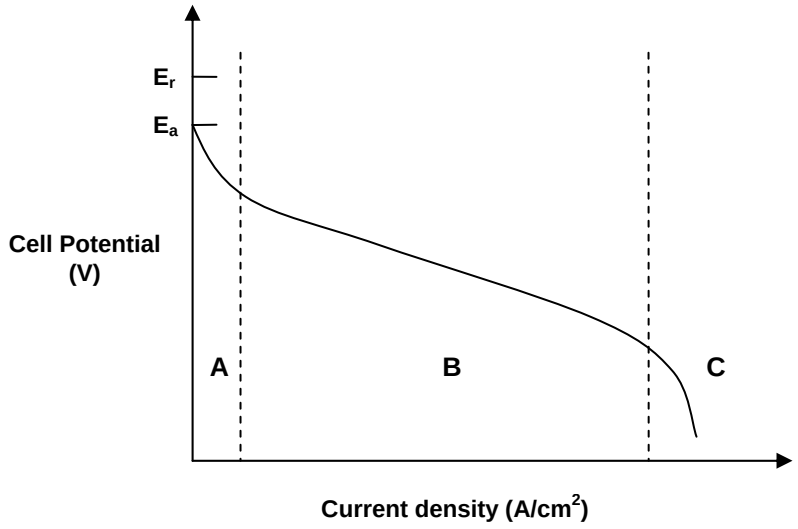

Figure 4: Illustration of the decrease in terminal cell potential with increasing current densities due to: Region A – activation overpotential losses; Region B – ohmic overpotential losses; Region C – mass transfer overpotential losses.

Since the cell potential is equal to the difference between the anodic and cathodic electrode potentials, the expected drawn current from the cell can be calculated by using Equation 19.

$$I = \frac{(V_c - V_a) - \eta_{ohm}}{R_e} \tag{19}$$

where V_c and V_a are the cathodic and anodic half-cell potentials respectively, η_{ohm} the ohmic loss in the cell and R_e the resistance of the external load. The electrode potentials of the anode and cathode are given by Equations 20 and 21 respectively.

$$V_a = V_{r,a} + \eta_{a,act} + \eta_{a,conc} \tag{20}$$

$$V_c = V_{r,c} - \eta_{c,act} - \eta_{c,conc} \tag{21}$$

where $V_{r,a}$ and $V_{r,c}$ are the reversible potentials of the anode and cathode respectively and η_{act} and η_{conc} the overpotential losses due to activation and mass transfer at the electrodes. Since cathodic and anodic processes are associated with negative and positive overpotentials respectively, the cathodic potential diminishes from its reversible potential $(V_{r,c})$ by the overpotential, and the anodic potential enhances from its reversible potential $(V_{r,a})$ by the overpotential. Thus, the adsorption of CO onto the anodic Pt electrocatalyst will result in an increase in activation overpotential losses at the anode, which will cause the anodic potential to increase from its reversible potential. From Equation 19 it is evident that this CO poisoning effect at the anode will thus result in a decrease in the possible drawn current from the fuel cell. In addition, since the overpotential losses increase with increasing current densities, the terminal cell potential, and subsequently the voltage efficiency of the cell, decreases with increasing current density.

Overpotential losses are mainly influenced by the exchange current density *(i_o)*, the internal resistance of the cell *(R_i)* and the limiting current density *(i_L)*. The influence of these parameters on the cell potential is illustrated in Figures 5 to 7. The presence of CO, absorbed onto the Pt electrocatalyst, will result in an increase in the exchange current density of the H_2 / H^+ half cell reaction. From Figure 5 it is evident that the initial activation overpotential losses increase as the exchange current density of the reactions decreases. It is therefore imperative to prevent CO absorption in order to increase the overall efficiency of PEM fuel cells.

The effect of the internal resistance is illustrated in Figure 6. An increase in the slope of the linear region occurs as the cell internal resistance is increased. This is due to higher ohmic overpotential losses when the internal resistance is high. In this illustration, the increase in the cell internal resistance resulted in the potential decreasing to zero before the limiting current is reached.

Figure 7 illustrates the influence of the limiting current density on mass transfer overpotential losses. If significantly reduced, the limiting current will result in lower maximum available power of the fuel cell.

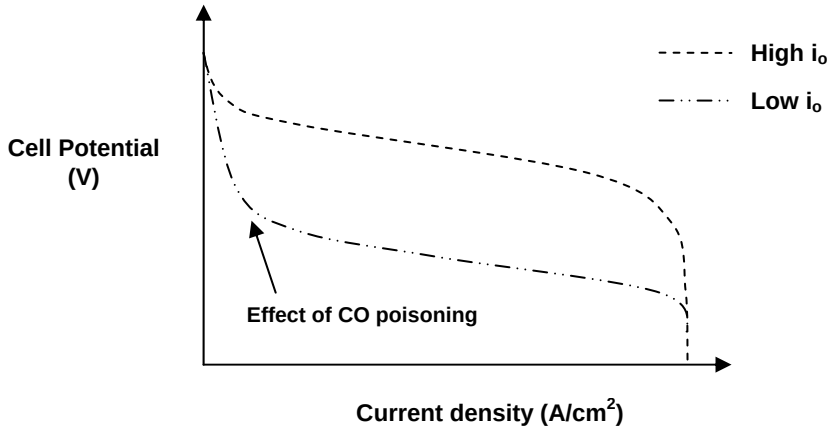

Figure 5: Influence of i_o on the cell potential at different current densities and constant R_i and i_L values. This also serves as an illustration of the effect of CO poisoning.

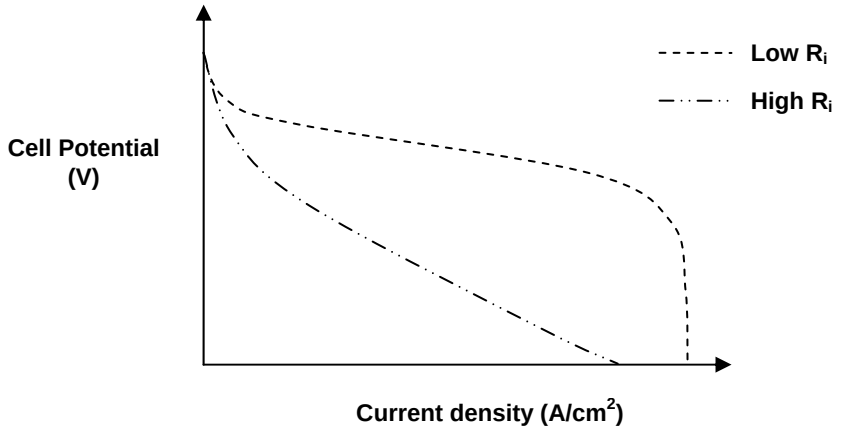

Figure 6: Influence of R_i on the cell potential at different current densities and constant i_o and i_L values.

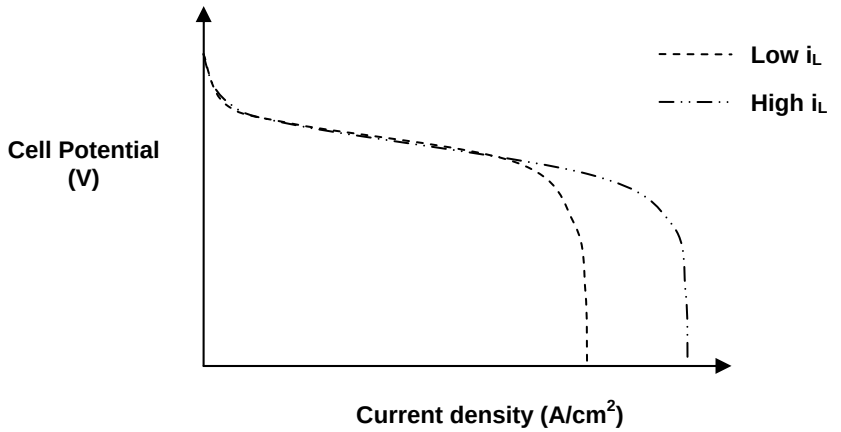

Figure 7: Influence of i_L on the cell potential at different current densities and constant R_i and i_o values.

3.3 Efficiency of fuel cells

For ideally operating fuel cells, the free-energy change of the reaction may be completely converted to electrical energy. The intrinsic maximum efficiency of a fuel cell may be described as:

$$\in_i = \frac{\Delta G}{\Delta H} = 1 - \frac{T\Delta S}{\Delta H} \tag{22}$$

where ΔH is the enthalpy change of the reaction, T the absolute temperature in Kelvin and ΔS the change in entropy. In some cases, ΔG may exceed ΔH, which will result in an intrinsic maximum efficiency of over 100 percent. In general, intrinsic maximum efficiencies for fuel cell reactions under standard conditions are high, typically in excess of 85 percent. This is significantly higher than the intrinsic maximum efficiencies of heat engines, which are nearly always less than 40 percent.

In hydrocarbon-air fuel cells; water, as byproduct of the cell reactions, is in a liquid form when operated below 100°C. Therefore, based on thermodynamics, the entropy change for this reaction is negative, resulting in intrinsic maximum efficiencies of less than 100 per cent (according to Equation 22, considering that ΔH is negative). At temperatures above 100°C water is liberated in vapor form. The entropy changes are thus positive under these conditions, corresponding to intrinsic maximum efficiencies of over 100 per cent.

Although from the preceding paragraph it seems as if 80 percent efficiencies are easily attainable in fuel cells, overpotential losses reduce the practical efficiencies of these fuel cells to values much less than the intrinsic maximum efficiency. However, with the development of suitable electrocatalysts and highly effective proton conducting electrolytes, it might be possible to attain practical efficiencies close to 80 – 90 percent.

In addition to the intrinsic maximum efficiency, voltage efficiency of the fuel cell must also be considered when calculating the overall efficiency of the fuel cell. The voltage efficiency *(ϵ_e)* is expressed as the ratio of the cell potential to the thermodynamic reversible potential as indicated in Equation 23 below:

$$\in_e = \frac{E}{E_r} \tag{23}$$

High voltage efficiencies can be obtained at low current densities. However, as the current density is increased, the voltage efficiency slowly decreases until a limiting value is reached.

The observed current from the cell is typically lower than the theoretical calculated current using Equation 19. The efficiency in terms of the current drawn from the cell is called the faradaic efficiency and is expresses as:

$$\in_f = \frac{I}{I_m} \tag{24}$$

where I is the drawn current from the cell and I_m the theoretically expected current on the basis of the amount of reactants consumed, assuming that the overall reaction in the fuel cell proceeds to completion.

The overall efficiency of the fuel cell can be expressed as the product of the maximum intrinsic efficiency, the voltage efficiency and the faradaic efficiency. One of the main aims in electrochemical energy conversion is to make both ϵ_e and ϵ_f tend to unity.

3.4 Power as a function of current

The power P of an electrochemical reactor is given by:

$$P = IE \tag{25}$$

As previously indicated in Figure 4, E will be high when I is low. On the contrary, when I is high E will be low. Thus, the P-I curve should pass through a maximum as illustrated in Figure 8.

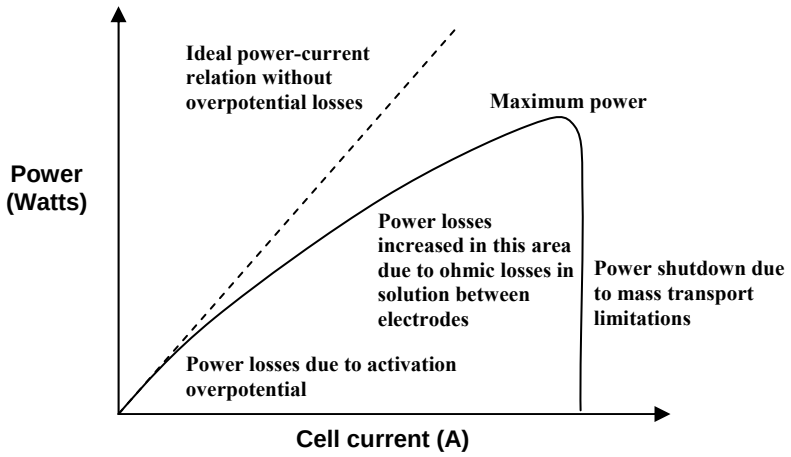

Figure 8: Power vs. current relation, indicating the reasons for power losses at various currents, after Bockris and Srinivasan [65].

The curve passes through the origin since $P = 0$ if $I = 0$. The shape of the P-I curve is dependent on i_o, R_i and i_L. At any particular value of I, the power is significantly increased with increase of i_o. The power is increased by a decrease in R_i. Generally, the maximum power is close to the limiting current, except when the internal resistance is high or when i_o is low. Graphical illustrations of the influence of these parameters on the P-I curve is shown in Figures 9 – 11. The P-I plots are parabolic when the cell voltage tends to zero before the limiting current is reached.

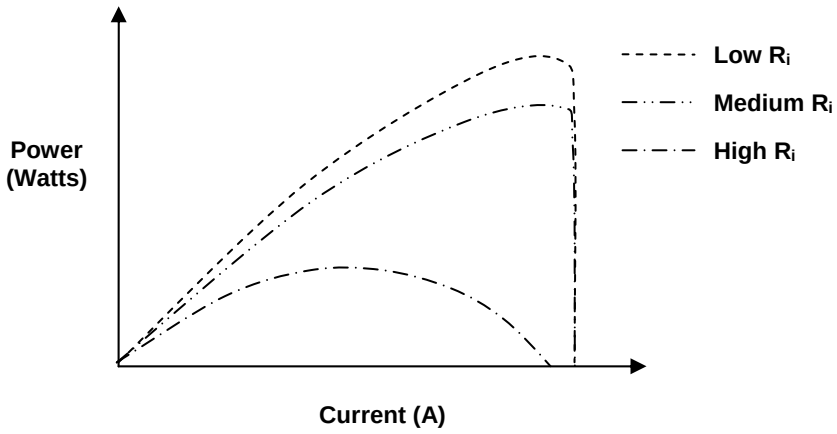

Figure 9: Influence of the internal resistance on the power drawn at specific current values.

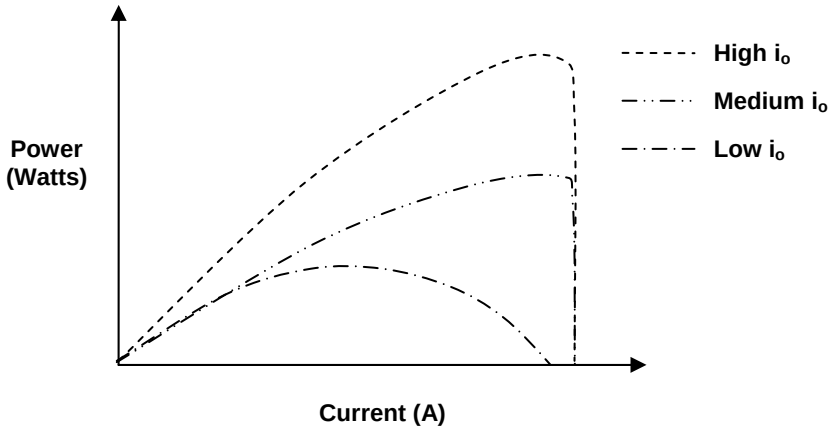

Figure 10: Influence of the exchange current density on the power drawn at specific current values.

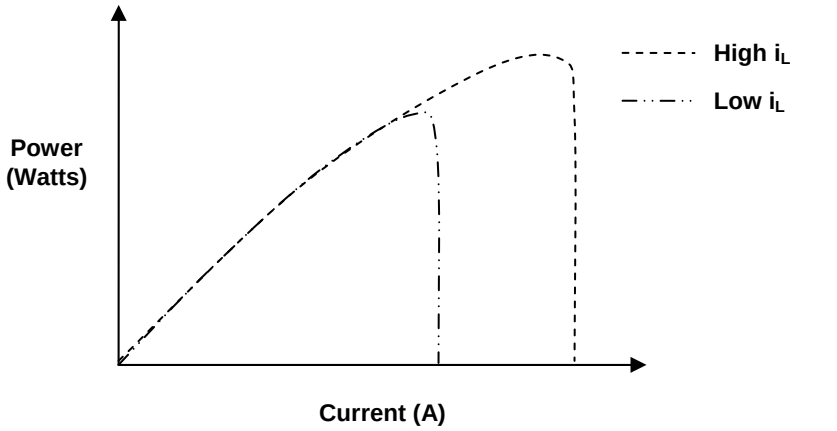

Figure 11: Influence of the limiting current on the power drawn at specific current values.

The utility of a fuel cell is determined by its efficiency at reasonable power outputs and by its maximum power. These in turn depend centrally on the cell potential-current relation of the fuel cell.

Chapter 4

OBJECTIVES OF THIS STUDY

The aim of this work was to determine to what extent metal oxide supported gold catalysts can selectively oxidise CO to CO_2 in hydrogen-rich gas streams in order to prevent CO poisoning of the Pt/C anodes in PEM fuel cells. The efficiency of the Au-based catalysts were investigated in two distinct configurations in the fuel cell system, namely 1) in a bi-layer configuration inside the MEA (as shown in Figure 12), and 2) in an isolated catalyst chamber prior to the fuel cell between the H_2 cylinder and the anode humidifier (as shown in Figure 13).

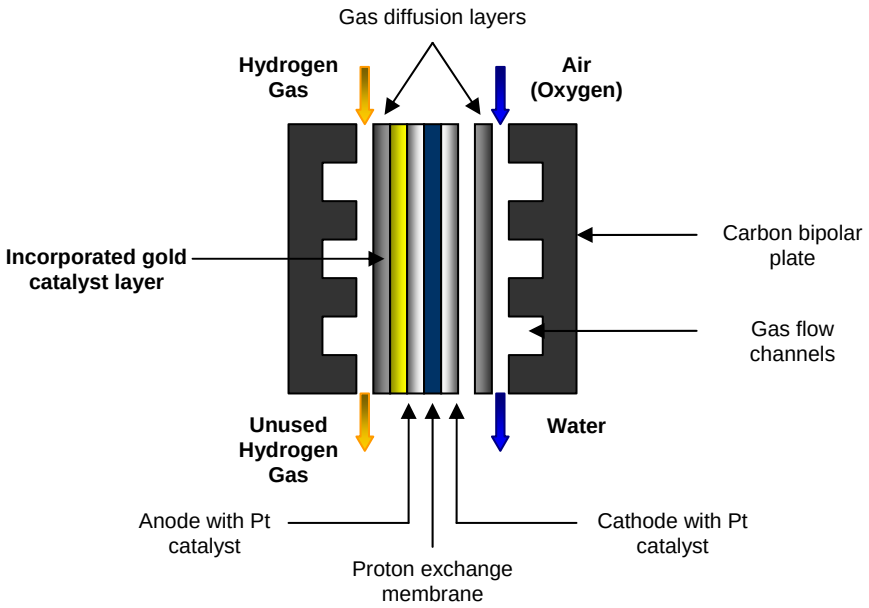

Figure 12: Schematic illustration of the incorporation of a titanium dioxide gold catalyst layer in the MEA of a PEM fuel cell.

The performance of the gold catalysts was firstly characterised in a separate CO oxidation test rig before incorporating the most active catalysts into an actual single cell fuel cell

system. Parameters investigated included the effect of gold loading, space velocity, air/oxygen concentration, CO concentration, temperature, pressure, selectivity in H_2-rich streams, as well as the effect of organic substances used to produce the MEAs.

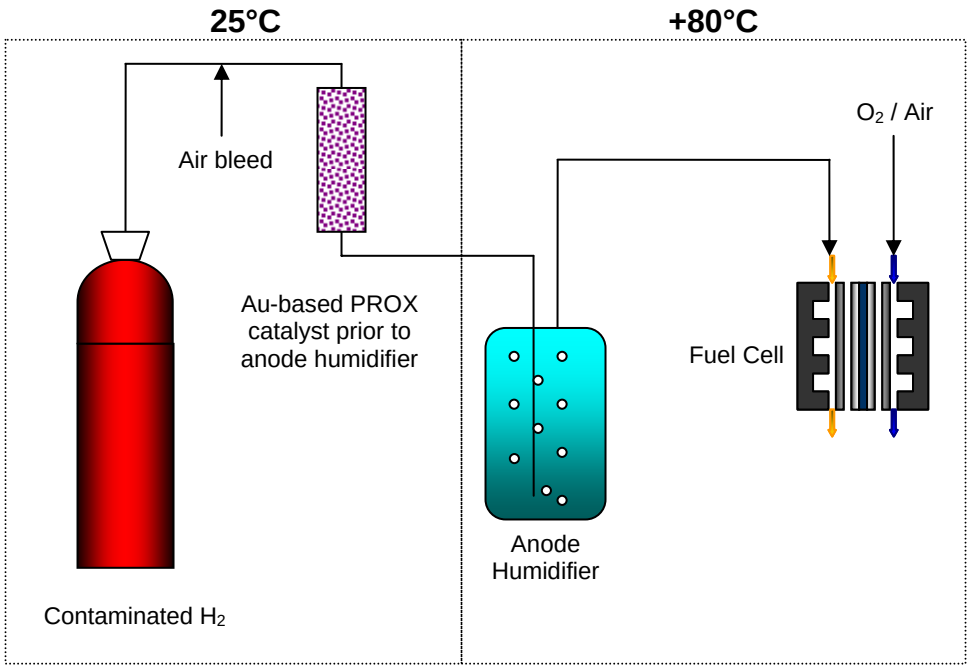

Figure 13: Schematic illustration of the Au-based catalyst chamber in the H_2 feed line between the H_2 containing cylinder and the PEM fuel cell.

Chapter 5

EXPERIMENTAL

5.1 Introduction

The performance of PEM fuel cells are dependent on various factors, such as gas flow rates, humidification, water management, temperature, pressure, conductivity of the proton conducting membrane, Pt-loading, and the overall resistance of the system. The complexity of a fuel cell system makes it relatively difficult to obtain repeatable results, which was essential in the present study in order to determine the influence of the Au/TiO_2 catalysts on the CO tolerance and polarisation behaviour of the PEM fuel cell.

In order to simplify the system, typical fuel cell operating conditions were simulated in a separate CO oxidation test rig, which allowed for accurate and repeatable results. The influence of parameters such as gold loading, oxygen concentration in H_2-rich gas streams, calcination of the Au/TiO_2 catalysts, pressure, temperature, and organic substances, on the catalytic activity of the Au/TiO_2 catalysts, were investigated.

Following these results the most active catalysts were incorporated into a bi-layer configuration inside the MEA, or in a preferential oxidation catalyst chamber in the H_2 feed line to the anode.

5.2 Gold catalysts

5.2.1 Catalyst preparation

The catalysts were prepared by deposition-precipitation of gold from 50 g/l chloroauric acid ($HAuCl_4$) solution onto P25 TiO_2 (i.e. 21 nm TiO_2 particles) at a pH of 7.5 in an

automatic lab reactor (LabMax). Firstly, 120 ml high purity water was heated to 70°C followed by the addition of the necessary amount of $HAuCl_4$. The pH was then adjusted and controlled at 7.5 using 0.1 M Na_2CO_3 and 0.1 M HNO_3, where after 9.4 g P25 TiO_2 was added as support material. The solution was stirred with a glass overhead stirrer at 380 rpm and aged for 60 minutes. The catalyst was washed repeatedly in a five cycle washing process; each consisted of washing with 250 ml high purity water followed by pressure filtering. The catalysts were dried at 120°C for 14 hours, where after the agglomerates were crushed to a fine powder using a mortar and pestle. The gold loading was determined by Inductively Coupled Plasma Emission Spectroscopy (ICPES). All the catalysts were stored in the dark in sealed (N_2-filled) containers for 24 hours before testing.

In order to decrease the mobility of the gold precursors, some of the catalysts received an additional calcination treatment at 300°C for 2 hours. The decreased mobility of the gold precursors typically results in increased stability of the catalysts; this effect also being investigated in the present study.

Au/CeO_2 catalysts (Aldrich Cerium(IV) oxide, 99.999% pure, nanopowder) were prepared by the same deposition-precipitation method used to prepare the Au/TiO_2 catalyst. However, the pH was adjusted and controlled at 8, compared to 7.5 for the Au/TiO_2 catalysts.

5.2.2 Catalyst characterisation

Transmission electron microscopy (TEM) was used to characterise the gold dispersion and particle size distribution of a 3 wt% Au/TiO_2 powder catalyst. The catalyst was crushed between glass slides and dusted onto a holey carbon film supported by a copper grid. The samples were examined in a Tecnai F20 TEM.

5.2.3 Activity measurements and catalyst screening for application in MEA

Standard activity measurements were conducted in a fixed bed u-tube reactor (glass reactor, ID = 4mm) using 28 mg of catalyst without catalyst dilution. The gas mixtures consisted of air and 0.2 per cent CO and were passed through the catalyst bed at 462 $ml.min^{-1}$, yielding an SV of 1000 $\ell.g_{cat}^{-1}.h^{-1}$. These conditions ensured the desired reaction rate. The catalyst temperature was kept constant at 25°C by immersing the u-tube reactor in a temperature controlled water bath. The gas samples were analysed with a Shimadzu GC17A Gas Chromatograph, using both FID and TCD analysis, from where the catalytic activity and CO conversion was calculated using Equation 13. These conditions were kept constant for all tests, unless otherwise stipulated. A schematic representation of the CO oxidation test-rig setup is shown in Appendix II.

The influence of gold loading on CO conversion and catalytic activity was investigated by preparing catalysts containing close to 1.3, 3.5, and 4.7 wt% gold.

In order to characterise the catalytic activity of these catalysts in fuel cell conditions, air was replaced with high purity H_2 (99.999% - Appendix III) and a 2 per cent air bleed stream. The CO concentration was kept at 0.2 per cent CO. The selectivity of the catalysts was characterised by using nitrogen as an inert substitute gas for hydrogen. The difference in CO conversion was used as an indication of the level of selectivity. A similar approach was used to investigate the influence of the air bleed concentration (1, 2, 5, 7.5, and 10 per cent air) on CO conversion and selectivity. Accurate selectivity for CO_2 formation was calculated using Equation 14.

Since there are various opinions on the effect of calcination on the catalytic activity of metal oxide supported gold catalysts, it was decided to investigate the effect of calcination on our catalysts. Some authors [36] state that calcination results in sintering of gold particles and a subsequent decrease in activity, while others [37] claim that calcination is essential for both activity and stability of these catalysts. In this study, the 14 hour drying stage was followed by a 2 hour calcination stage at 300°C.

The influence of pressure was investigated by varying the pressure between 14.5 psi to 43.5 psi in 14.5 psi intervals. Similarly, the temperature was varied from 25°C to 70°C in order to determine its influence on the catalytic activity. The high relative humidity (RH) conditions of PEM fuel cells were also simulated, and its effect investigated on the catalytic activity.

Furthermore, the effect of organic substances such as PTFE, Nafion^{TM}, and propanol was investigated. This was done by rinsing the gold catalysts for 10 minutes in distilled water containing PTFE, Nafion^{TM}, and propanol respectively, where after the catalysts were dried at 120°C for 14 hours, and tested for CO oxidation with the standard activity tests in the CO oxidation test rig.

The influence of the MEA catalyst ink was investigated by mixing various ratios of gold catalyst to Vulcan XC72R in the presence of PTFE containing propanol solution to yield 30 wt% PTFE in the dry sample. This was followed by standard activity measurements in the CO oxidation test rig.

5.2.4 Au/TiO_2 catalysts in simulated fuel cell conditions for application in PROX system

Catalyst activity measurements and screening was followed by simulated gas flow dynamics as would typically be encountered in a fuel cell system. The system was based on a Au-based catalyst chamber incorporated in the H_2 feed line prior to the anode humidifier, as depicted in Figure 13. The simulation was based on a fuel cell system producing 60 kW at peak power. The required H_2 flow rate to deliver 60 kW was calculated using Equation 26.

$$Q = \frac{22.4141 \times mI}{n^{e^-} F} \tag{26}$$

where Q is the volumetric flow rate in $\ell.min^{-1}$, 22.4141 is the volume of one mole of gas ($dm^3.mol^{-1}$), m a stoichiometric constant, I the drawn current in Amps ($C.s^{-1}$), n^{e-} the moles of electrons transferred, and F Faraday's constant (96 485 $C.mol_e^{-1}$). Test work conducted during this investigation was based on a 1000x downscale of the actual fuel cell system. However, test conditions mimicked the actual space velocity as would be encountered in a full scale system.

Three different catalyst systems were investigated, namely 1) Au on P25 TiO_2 nano-powder, 2) Au on P25 TiO_2 granules (+500 -710 μm), and 3) Au on P25 TiO_2 nano-powder wash-coated onto cordierite monoliths. The Au/TiO_2 nanopowder and granulate catalysts were prepared as discussed in Section 5.2.1.

Cordierite ($Mg_2Al_4Si_5O_{18}$) monoliths (length = 7.6 cm; diameter = 1.5 cm; 400 channels / in^2) from Corning were used as the monolith structure to coat with Au/TiO_2 catalyst. The Au/TiO_2 nanopowder catalysts were prepared as in Section 5.2.1 but were not dried at 120°C. In stead, the catalyst was re-slurried with 60 ml high purity water to yield a catalyst slurry containing approximately 13 wt% solids. The solids were kept in suspension by agitating with a magnetic stirrer. The monoliths were dipped into the catalyst slurry and soaked for 2 minutes, where after it was removed and the channels cleaned using slow flowing compressed air. The Au/TiO_2 coated monoliths were dried at 120°C for 14 hours. The amount of catalyst deposited onto the monolith was determined by weighing the monolith before immersing into the catalyst slurry, and again after it was dried for 14 hours

A Pulse Discharge Helium Ionisation Detector (PDHID) was used to measure the residual CO concentration after passing the CO contaminated H_2 through the catalyst bed. These tests were repeated for H_2 containing 10, 50, 100, 2000 ppm CO. The PDHID was certified to accurately detect CO to concentrations of 1.3 ± 0.1 ppm. CO oxidation was facilitated by introducing a 1 or 2 per cent air bleed stream.

The online deactivation characteristics on the Au/TiO_2 catalysts were also investigated by exposing the catalysts to H_2, 2 per cent air, and various CO concentrations over time periods ranging from 24 – 50 hours. For these tests the catalyst bed temperature was not controlled; rather, it was allowed to heat up as would be the case in its intended application in fuel cell systems.

5.3 Incorporation of the Au/TiO_2 catalysts into the MEA of a PEM fuel cell

When incorporating the Au/TiO_2 catalysts into the MEA it is essential to use a fabrication method that will yield repeatable results in order to accurately determine the influence of the newly incorporated Au/TiO_2 catalyst layer. In the present study this was achieved by using a catalyst-ink-casting-method. The performance of the in-housed produced Mintek MEAs was benchmarked against that of a commercial available Electrochem Inc. MEA.

5.3.1 MEA fabrication

The Alfa Aesar Nafion^{TM} membranes (proton exchange membranes), 0.18 mm thick, were first cleaned by boiling in distilled water for 1 hour, followed by heating in 5 per cent hydrogen peroxide for 1 hour at 70 – 80°C to remove organic impurities. It was then boiled in 0.5 M H_2SO_4 for 1 hour. The H_2SO_4 was removed by repeated washing in boiling distilled water. The membranes were stored in distilled water before assembly with the electrodes.

The catalyst ink was prepared using Alfa Aesar 40 wt% Pt Vulcan XC72R, 60 wt% PTFE emulsion for bonded electrodes as binder, 5 wt% Nafion^{TM} solution as ionic conductor, iso-propanol as solvent, and distilled water. These ingredients were added to yield 1 mg $Pt.cm^{-2}$, 30 wt% PTFE and 30 wt% Nafion^{TM} in the dry sample on a 25 cm^2 electro-active area. The solutions containing Vulcan XC72R, PTFE, Nafion^{TM}, iso-propanol and

distilled water were stirred with a magnetic stirrer for 2 hours at 50°C to obtain a homogeneous ink. The homogeneous ink was deposited onto the carbon paper by means of a casting method. The ink was dried at 80°C for 2.5 hours, where after the carbon-paper-ink-assembly was pressed onto the Nafion™ membrane using a hot press at 156 psi and 125°C for 90 seconds. The platinum loading was determined by weighing the carbon paper prior to casting and after drying.

5.3.2 Bi-layer formation

The Au/TiO_2 catalysts were incorporated into the MEA by mixing the catalysts with C-black (75 Au/TiO_2 : 25 C), 60 wt% PTFE emulsion to yield 30 wt% PTFE in the dry sample, and a solution consisting of distilled water and iso-propanol. The ingredients were stirred with a magnetic stirrer for 2 hours at 50°C until a homogeneous ink was obtained. The anodic bi-layer was formed firstly by casting the gold catalyst-carbon-ink onto PTFE impregnated carbon paper and drying at 80°C for 2 hours, where after the Pt-catalyst ink was cast on top of the gold catalyst layer, as discussed in Section 5.3.1. The Pt-catalyst ink was dried at 80°C for 2 hours, where after the bi-layer was calcined at 300°C for 2 hours. The cathode and carbon-paper-ink-assembly were obtained as discussed in Section 5.3.1.

The efficiency of the Au/TiO_2 catalysts in the MEA configuration was firstly classified by assembling the bi-layer in a separate carbon monoxide oxidation test rig in an reactor as shown in Appendix IV. The reactor design allowed for accurate gas flow simulation typically encountered in fuel cells. The reactor in Appendix IV differs from the U-tube reactor in the sense that the bed depth is reduced from approximately 3 mm to 100 μm, thereby replicating fuel cell operating conditions. The samples for this reactor were prepared in exactly the same way as the normal bi-layer anode formation method, but without assembling the carbon paper (containing the bi-layer) with the Nafion™ membrane. The carbon bi-layer containing carbon paper was then fixed inside the reactor leaving an exposed geometric area of 0.785 cm^2.

5.3.3 Polarisation experiments

Single cell test work was performed using an Electrochem Inc. FCT 2000 fuel cell test station and a Scribner Associates Inc. Series 890 load unit (Appendix V). Polarisation experiments were conducted on both the standard 25 cm^2, 20 wt% Pt, 1 mg $Pt.cm^{-2}$ Electrochem Inc. MEAs and the in-house produced 25 cm^2, 40 wt% Pt, 1 ± 0.2 mg $Pt.cm^{-2}$ Mintek MEAs. Hydrogen, 5N, was introduced at a minimum flow rate of 42 $ml.min^{-1}$ and a load based flow rate of 15.35 $ml.min^{-1}.A^{-1}$, and oxygen at a minimum flow rate of 34.86 $ml.min^{-1}$ and a load based flow rate of 12.82 $ml.min^{-1}.A^{-1}$. Humidification of the anodic feed stream was achieved by bubbling the fuel gas through a bubbler, which was set at a temperature 5°C higher than the fuel cell operating temperature. The MEAs were conditioned according to the accepted standardised single cell testing procedure [66]. Initially, fully humidified gases at high flow rates (10 times the stoichiometric amount at 217 $mA.cm^{-2}$) were introduced at ambient pressure and cell temperature of 60°C. The potential was cycled between 0.94 V and 0.6 V for six cycles at 30 minutes per setting, followed by a 6 hour cycle between 0.7 V and 0.5 V for 20 minutes per setting. The cell was then kept in constant current mode at 217 $mA.cm^{-2}$ (5.43A) for 12 hours, followed by 3 consecutive polarisation experiments with 10 minutes waiting periods between each run. The cell was considered to be fully broken in once the deviation from the previous polarisation curve was less that 5 mV at 400 $mA.cm^{-2}$.

For the first performance polarisation diagram, the fuel cell temperature remained at 60°C and the pressure at ambient conditions with fully humidified anodic gases. The current settings, gas flow rates and testing sequence are listed in Table 3. The fuel cell's average voltage was recorded for the last 5 minutes after being kept constant at the desired current set point (refer to Table 3) for 20 minutes.

In the second performance polarisation diagram, the cell temperature was increased to 80°C and the pressure to 25 psi. The current and flow rate settings remained the same as that shown in Table 3. The drawn current and resulting potential were stored on a personal computer through data acquisition software.

Table 3: Standard current and gas flow rate settings for obtaining polarisation data. H_2 flow rates are based on 2.2x stoichiometry and O_2 on 3.67x stoichiometry.

Sequence steps	Current set point ($mA.cm^{-2}$)	H_2 flow rate ($ml.min^{-1}$)	Oxygen flow rate ($ml.min^{-1}$)
0 (< 1 minute)	0	42	34.86
1	108.69	42	34.86
2	217.39	84	69.72
3	434.78	167	139.23
4	652.17	251	208.95
5	869.57	334	278.67
6	1086.96	418	348.18
7	1304.35	501	417.9

5.3.4 CO poisoning tests

Carbon monoxide poisoning was done by introducing 350 ppm CO contaminated H_2 and a 2 per cent air bleed stream to the cell. The cell current was kept at 5.43 A and the resulting potential monitored. The performance of the incorporated 2 mg $Au.cm^{-2}$ Au/TiO_2 bi-layer (protecting a 1mg $Pt.cm^{-2}$ anode) in the MEA was compared to that of the $Pt_{20}Ru_{10}$ anode. The Au/TiO_2 catalyst consisted of 20 wt% Au.

The influence of Au/TiO_2 catalysts was also investigated in the fuel cell system, outside the MEA. The initial setup consisted of a catalyst chamber incorporated between the H_2 gas cylinder and the anode humidifier, containing 1 g of the 20 wt% Au/TiO_2 catalyst, similar to that used in the bi-layer configuration. The results from this work stimulated further in-depth investigation into a Au/TiO_2 PROX system, as discussed in Sections 5.2.4 (*ex situ* test work) and 5.4 (*in situ* test work).

5.4 Incorporation of Au/TiO_2 PROX reactor in actual fuel cell system

The proposed PROX system, Section 5.2.4, was tested in an actual fuel cell test system. The setup consisted of a catalyst chamber containing a Au/TiO_2 wash-coated monolith (length = 7.6 cm, width = 1.5 cm), situated at room temperature between the hydrogen cylinder and the anode humidifier, as depicted in Appendix VI. The CO tolerance obtained with this system was compared to that of a 0.39 mg $Pt.cm^{-2}$ Pt/C anode, a 0.5 mg $Pt.cm^{-2}$ PtRu/C anode, and a 0.52 mg $Pt.cm^{-2}$ PtMo/C anode.

Test work was conducted in a standard Johnson Matthey 49 cm^2 single cell PEM fuel cell system. The MEAs were conditioned at 0.5 $A.cm^{-2}$ overnight. Hydrogen was introduced at 1.5 times the stoichiometric amount and air at 10 times the stoichiometric amount. The cell temperature was controlled at 80°C, while the humidifiers were set at 81.5°C and 82°C for the cathode and anode respectively. The heated lines to the fuel cell were controlled at 95°C.

Once conditioned, and after the potential has stabilised, either 100 or 1000 ppm CO in H_2 was introduced to the anode, together with a 2 per cent air bleed stream. The cell potential was monitored for 1 hour where after the CO was removed. This process was done with and without the catalyst chamber containing the 3 wt% Au/TiO_2 PROX catalyst, and the CO tolerance of the various systems were compared.

In order to compensate for ohmic overpotential losses, the resistance compensated potential was determined by measuring the resistance by means of a current interrupt (CI) method, and subsequently adding the resistance-induced-potential-loss to the measured potential.

Chapter 6

RESULTS AND DISCUSSIONS: Au/TiO_2 BI-LAYER CONFIGURATION

6.1 Catalyst characterisation

The TEM images (Figure 14) show that the sample consists of rounded nanoparticles supported by conglomerated, rounded particles of TiO_2 with occasional crystalline grains. Particle size analysis (Figure 15) shows that the gold nanoparticles are 2-3 nm in diameter. High Angle Annular Dark-Field (HAADF) images (Figure 16) show that the nanoparticles are well-dispersed. Energy Dispersive X-ray (EDX) analysis (Figure 17) confirms the presence of Au and Ti.

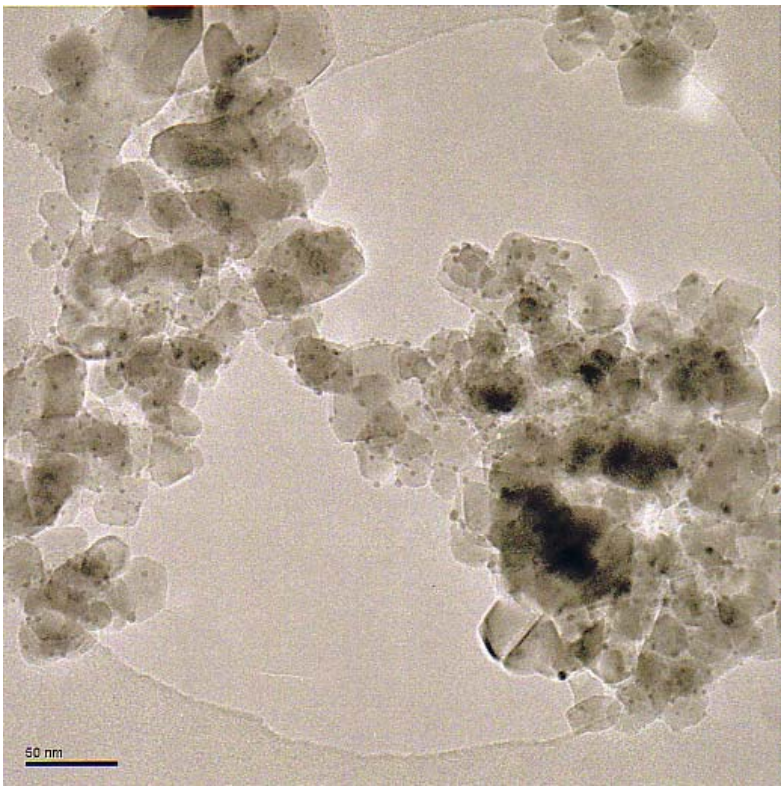

a

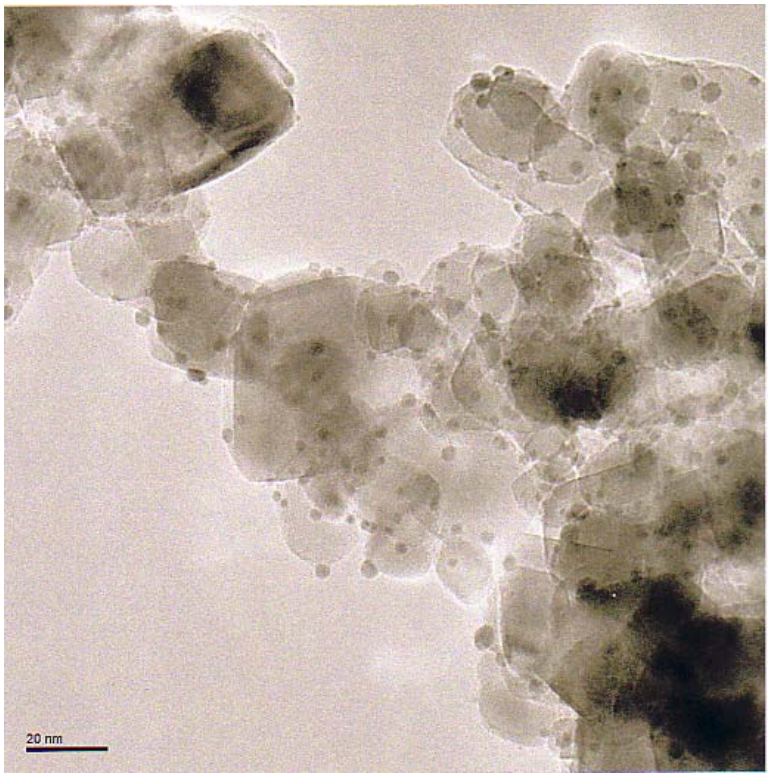

b

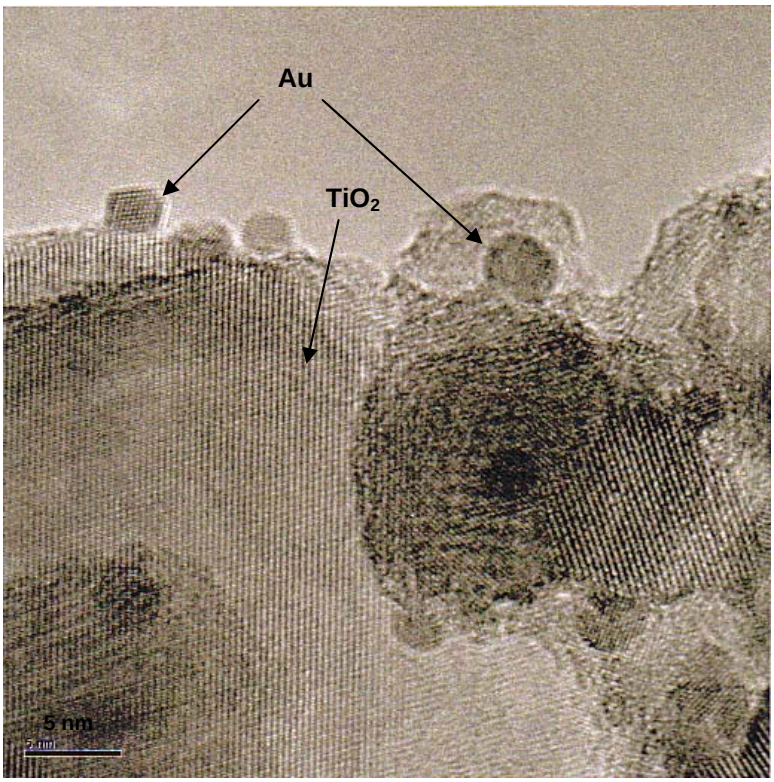

c

Figure 14: TEM images of 3wt% Au dispersed on P25 TiO_2 at different magnifications: a,b,c.

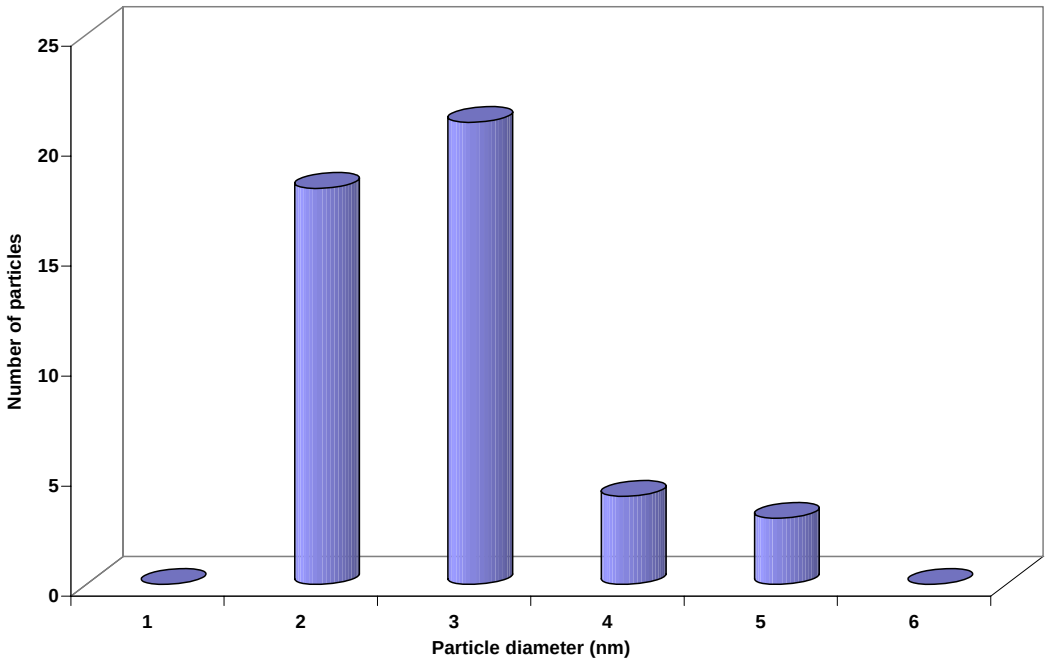

Figure 15: Size distribution of the Au particles on the P25 TiO_2 support (3wt% Au/TiO_2, number of particles considered (N) = 46)

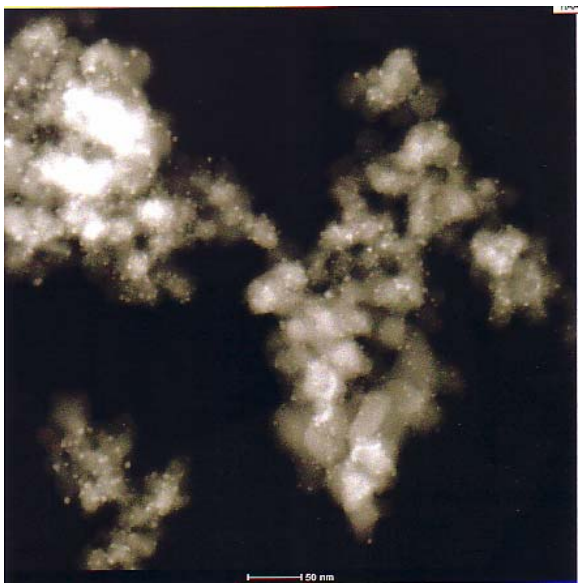

Figure 16: HAADF image of 3wt% Au/TiO_2 catalyst

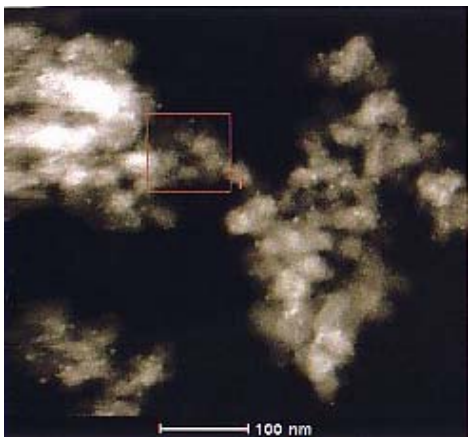

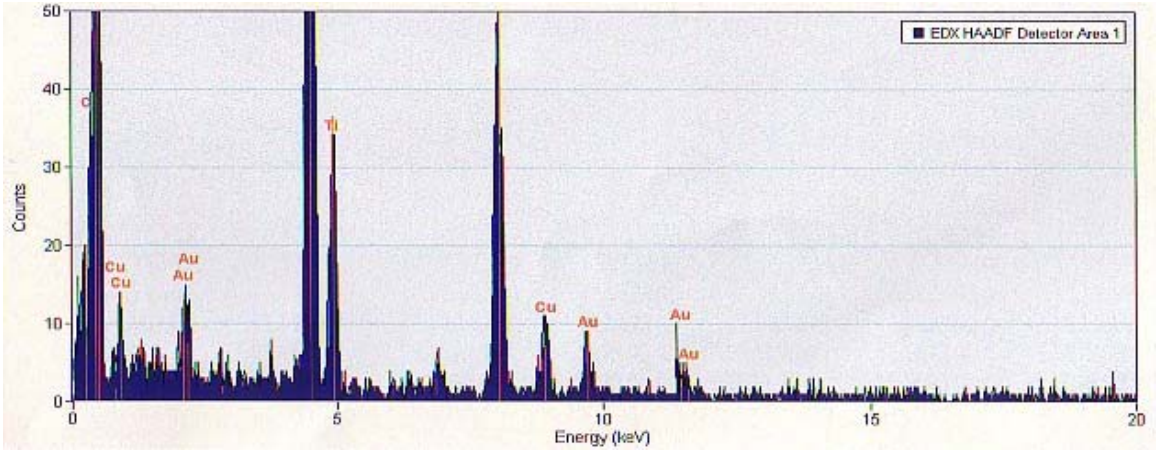

Figure 17: EDX analysis of 3wt% Au/TiO_2 catalyst.

6.2 Au/TiO_2 catalytic activity

6.2.1Influence of gold loading

The necessity of minimising the thickness of the MEA resulted in the investigation of CO oxidation over high gold containing catalysts. The CO conversions obtained over 1.3, 3.5, 4.67 and 11 wt% Au/TiO_2 catalysts are shown in Figure 18. It is evident that catalytic activity increase with gold loading up to 4.67 wt% Au, where after a further increase in the gold loading to 11 wt% caused a decrease in the CO conversion. This

phenomenon can be explained by the size and distribution of the Au particles on the TiO_2 support. The catalytic activity is expected to increase with an increase in gold loading, (since new active sites are formed) up to a point where the gold particles start to agglomerate due to insufficient dispersion. Agglomeration of the nano-gold particles will result in a decrease in the amount of active sites for CO oxidation; hence, lower activities will result.

To confirm this occurrence, the size and dispersion of the gold particles were analysed and are shown in the TEM images in Figures 19 to 22. From these images it is evident that the dispersion and amount of small gold particles was sufficient to yield a highly active catalyst up to a Au loading of 4.67 wt%. However, at 11 wt% Au, insufficient dispersion of the Au particles probably resulted in agglomeration and therefore a decrease in activity.

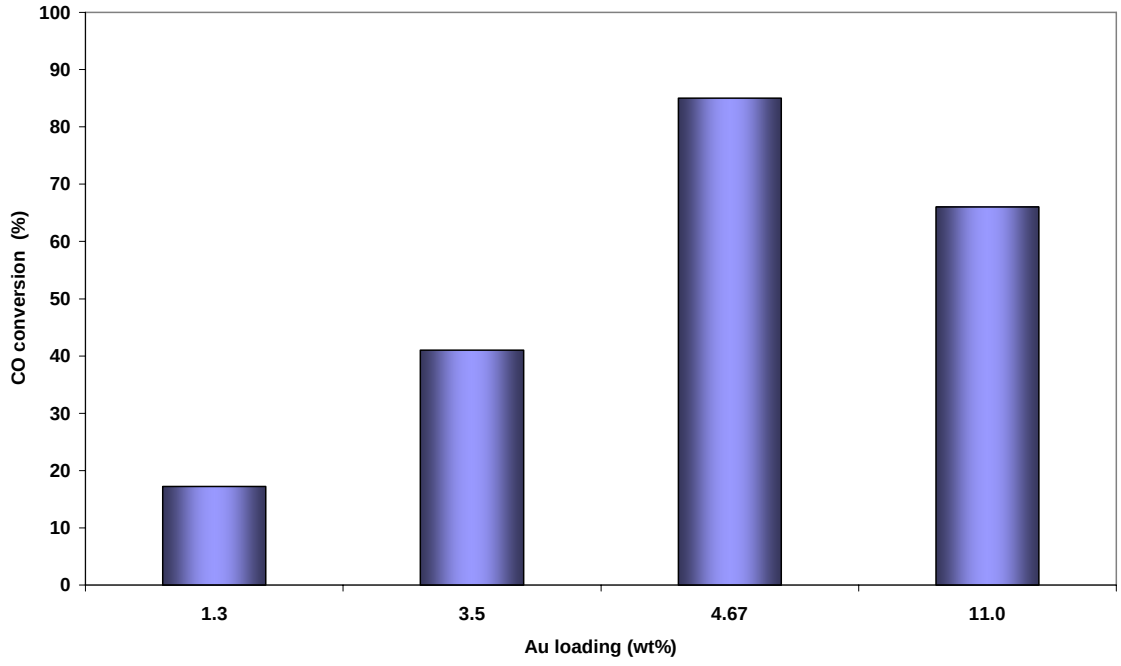

Figure 18: Influence of gold loading on CO conversion (0.2% CO in air at 1000 $l.g_{cat}^{-1}.h^{-1}$, 25°C)

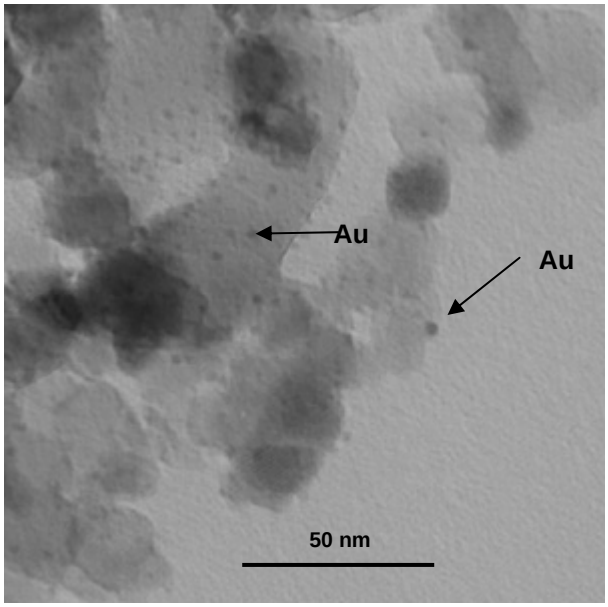

Figure 19: TEM image showing the gold particle size and dispersion of a 1.3 wt% gold catalyst prepared via deposition precipitation onto P25 titania.

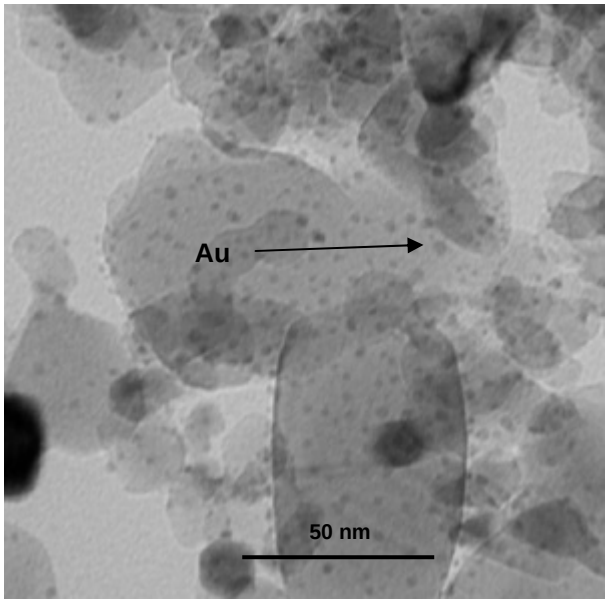

Figure 20: TEM image showing the gold particle size and dispersion of a 3.5 wt% gold catalyst prepared via deposition precipitation onto P25 titania.

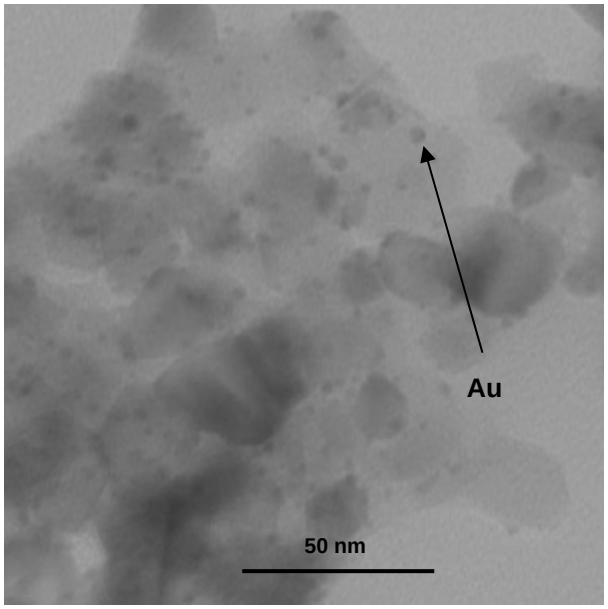

Figure 21: TEM image showing the gold particle size and dispersion of a 4.67 wt% gold catalyst prepared via deposition precipitation onto P25 titania.

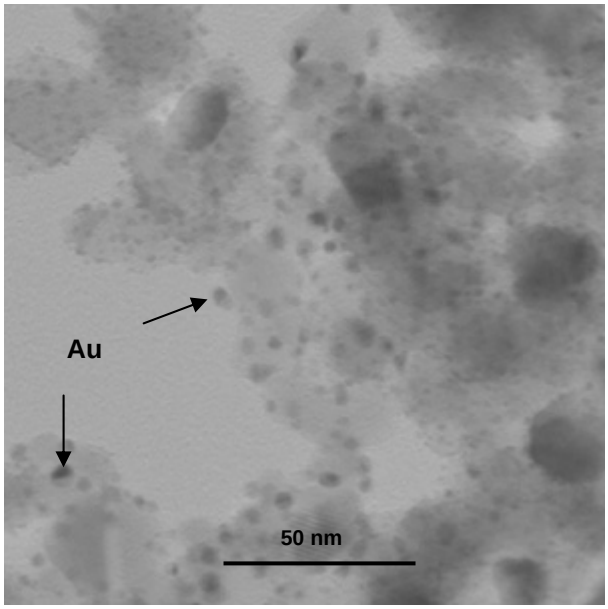

Figure 22: TEM image showing the gold particle size and dispersion of an 11 wt% gold catalyst prepared via deposition precipitation onto P25 titania.

Gottesfeld and Paffort [10] reported that CO concentrations as low as 10 ppm in diluted hydrogen streams significantly decreases the dissociative adsorption of hydrogen on platinum and its subsequent ionisation. Fom Figure 18 it is evident that the gold catalysts were unable to yield 100 per cent CO conversion at the specific test conditions. However, it must be noted that the typical space velocities in the MEAs of PEM fuel cell are estimated to range from about 4.6 – 72.0 $\ell.g_{cat}^{-1}.h^{-1}$ compared to the 1 000 $\ell.g_{cat}^{-1}.h^{-1}$ in the CO test rig. Although not linear, the CO conversion will increase with a decrease in the space velocity. It can therefore be expected that 100 per cent conversion is possible for all three catalysts presented in Figure 18.

6.2.2 Influence of hydrogen as background gas

From Section 6.2.1 it is evident that the preparation method used yielded highly active catalysts at space velocities of 1000 $\ell.g_{cat}^{-1}.h^{-1}$. This was achieved in conditions where excess oxygen, in the form of air, was introduced into the system. In electrocatalytic fuel cells the gas mixture mainly consists of hydrogen as fuel. Air will typically be introduced as a bleed stream in order to combust CO to CO_2. For safety measures, this air bleed stream must be less than 20 to 25 per cent air (4 to 5 per cent oxygen) of the fuel gas. This will limit the amount of oxygen available for the CO oxidation reaction, which might decrease the rate of conversion.

The influence of a decrease in the air concentration to 2 per cent (0.4 per cent oxygen) in hydrogen is shown in Figure 23. The extent to which CO conversion was influenced by the decreased oxygen concentration varied with gold loading of the individual catalysts. Nevertheless, all the results followed the same trend; CO conversion being significantly affected by a decrease in the oxygen concentration. Of significance is the conversions obtained by the 7.6 and 13.2 wt% Au catalysts. Both yielded 100 per cent CO conversion in air. However, with hydrogen as carrier gas the CO conversion over the 13.2 wt% Au catalyst was half that obtained over the 7.6 wt% Au catalyst. This effect might be as a result of a decrease in selectivity of these catalysts at higher gold loadings, resulting in

some of the oxygen being consumed in the hydrogen oxidation reaction. Another possible reason for this occurrence is that agglomeration might have occurred in the 13.2 wt% Au catalyst, which led to a decrease in activity.

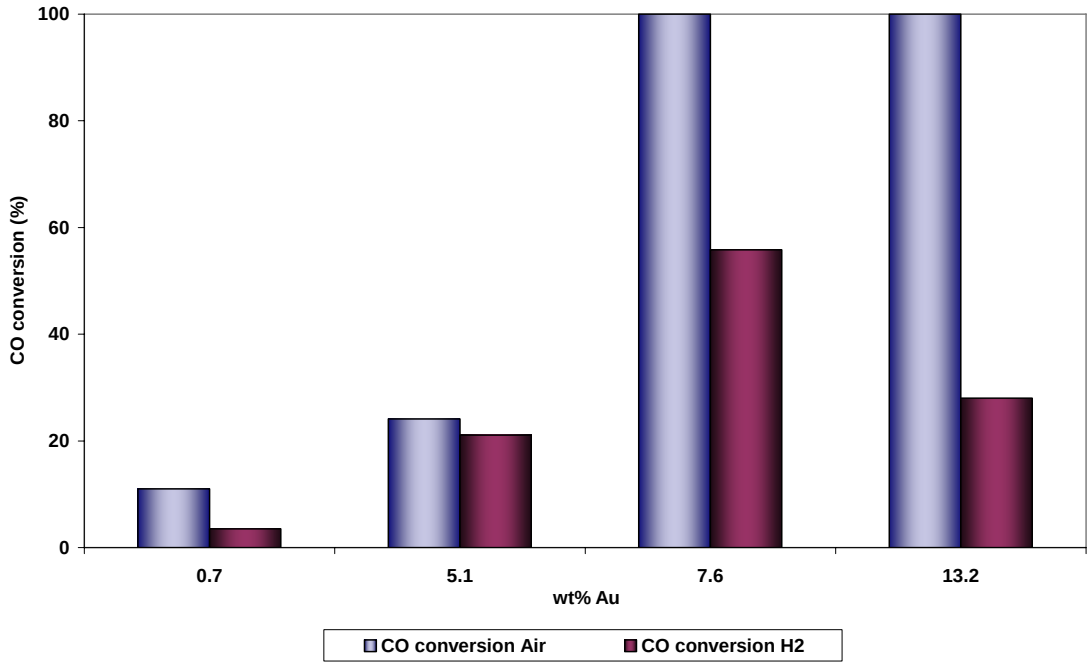

Figure 23: Influence of carrier gas on CO conversion (0.2% CO, 1000 $l.g_{cat}^{-1}.h^{-1}$, 25°C)

The CO conversion tests in hydrogen were repeated at a lower space velocity of 100 $\ell.g_{cat}^{-1}.h^{-1}$, which is more representative of space velocities that will typically be encountered inside the individual single cells of PEM fuel cells. The results are shown in Figure 24. It is evident that 100 per cent CO conversion was obtained at gold loadings as low as 5.1 wt% in H_2 and a 2 per cent air bleed. This is encouraging since lower gold loadings will have a significant impact on the economic viability of these catalysts in fuel cell systems

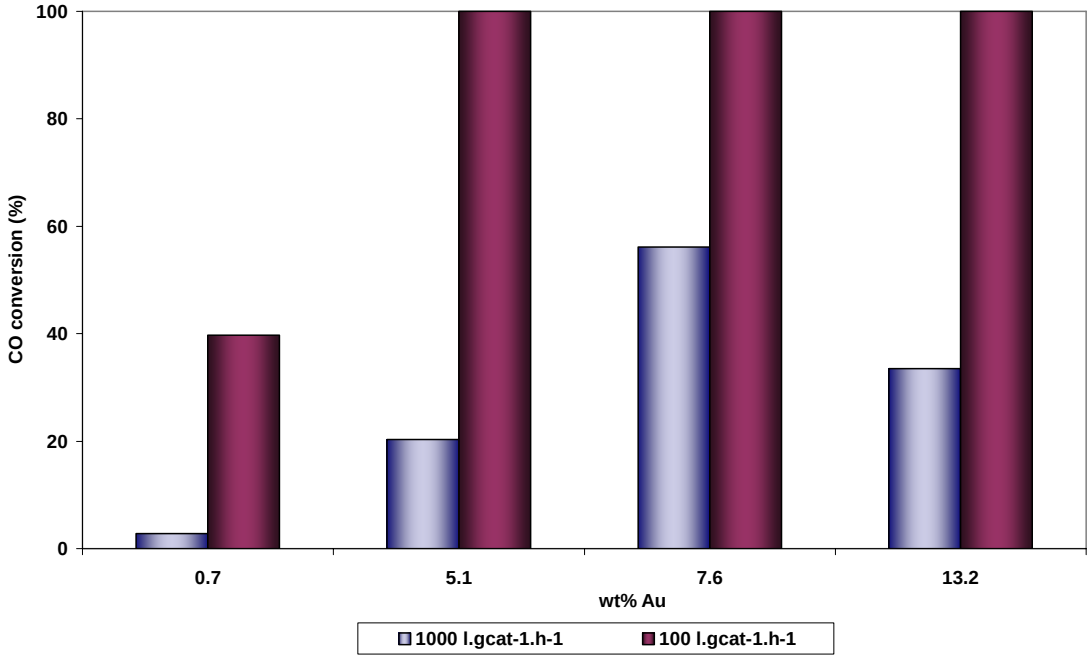

Figure 24: Effect of a 10-fold decrease in space velocity on CO conversion in hydrogen as background gas, 0.2% CO and a 2% air bleed at 25°C

The influence of oxygen concentration on CO conversion was further investigated by injecting 1, 2, 5, 7.5, and 10 per cent air (equivalent to 0.21, 0.42, 1.05, 1.58, and 2.1 per cent oxygen) with hydrogen and 0.2 per cent CO. The results obtained are shown in Figure 25. A significant increase in the rate of CO conversion was observed at higher air concentrations. This effect was even more prominent when nitrogen was used in stead of hydrogen, especially at air concentrations above 7%. Although not quantitative, this might indicate that selectivity is sacrificed when more oxygen is present due to hydrogen oxidation. The oxidation of hydrogen to water is typically undesirable, since it will result in a loss in coulombic efficiency of the fuel cells. Therefore, the ideal is to inject as little as possible air to facilitate sufficient CO oxidation in H_2-rich gas streams.

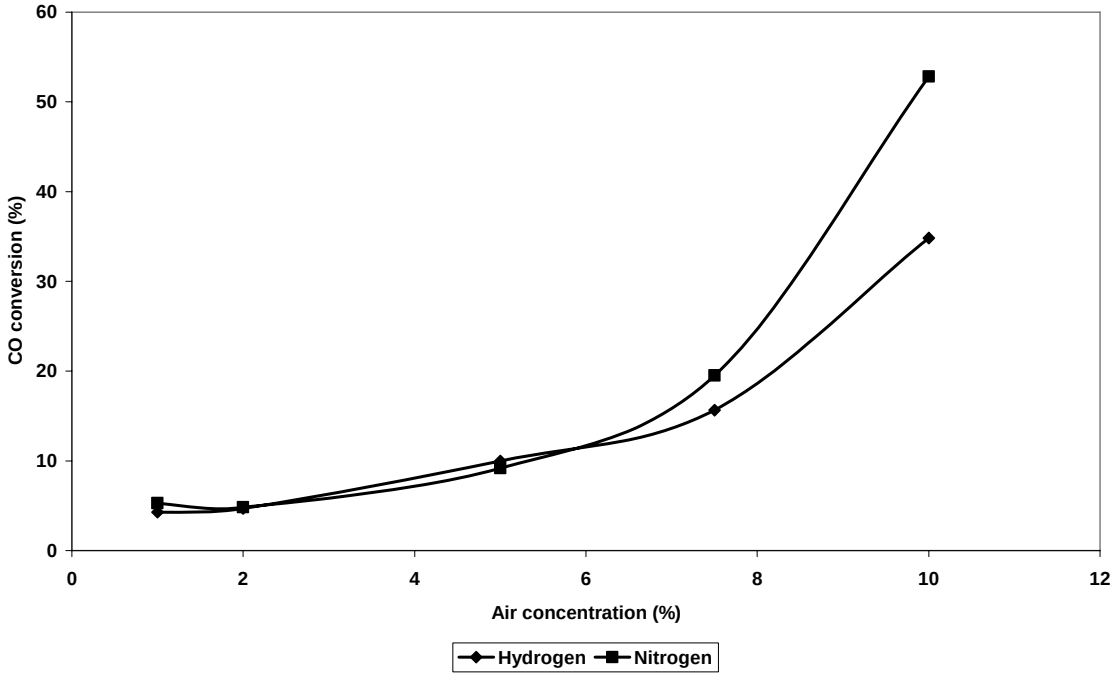

Figure 25: Influence of air concentration on CO conversion and an indication of selectivity over a 5 wt% Au catalyst (0.2% CO, 1000 l.g_{cat}^{-1}.h^{-1}, 25°C).

Although the results in Figure 25 indicate that the Au/TiO_2 catalysts are relatively selective for CO oxidation in hydrogen rich streams at lower oxygen concentrations, it is important to note that these tests were performed at 25°C. Although at slightly different conditions, test work done by Rossignol *et al*. [67] showed a distinct decrease in selectivity when the temperature was increased. They reported that the selectivity decreased from close to 100 per cent at 25°C to less than 80 per cent at 100°C. These results were obtained in a gas mixture containing 2 per cent CO, 2 per cent O_2, and 48 per cent H_2 in helium.

6.2.3 Influence of calcination

Test work done by Roberts *et al.* [68] indicated that calcination has an adverse effect on the reation rate of a 0.5 wt% Au supported on extruded titania granulate catalysts (1 mm in diameter), as indicated in Figure 26. The catalyst was dried overnight at 120°C and divided into three parts; one part left uncalcined, one calcined at 180°C for 2 hours and the other at 400°C for 2 hours. The results obtained from this work clearly illustrated that calcination of Au/TiO_2 catalysts has an undesirable effect on the catalytic activity. This effect might be due to the fact that gold particles sinter at these high calcination temperatures, which results in an increase in the mean particle size.

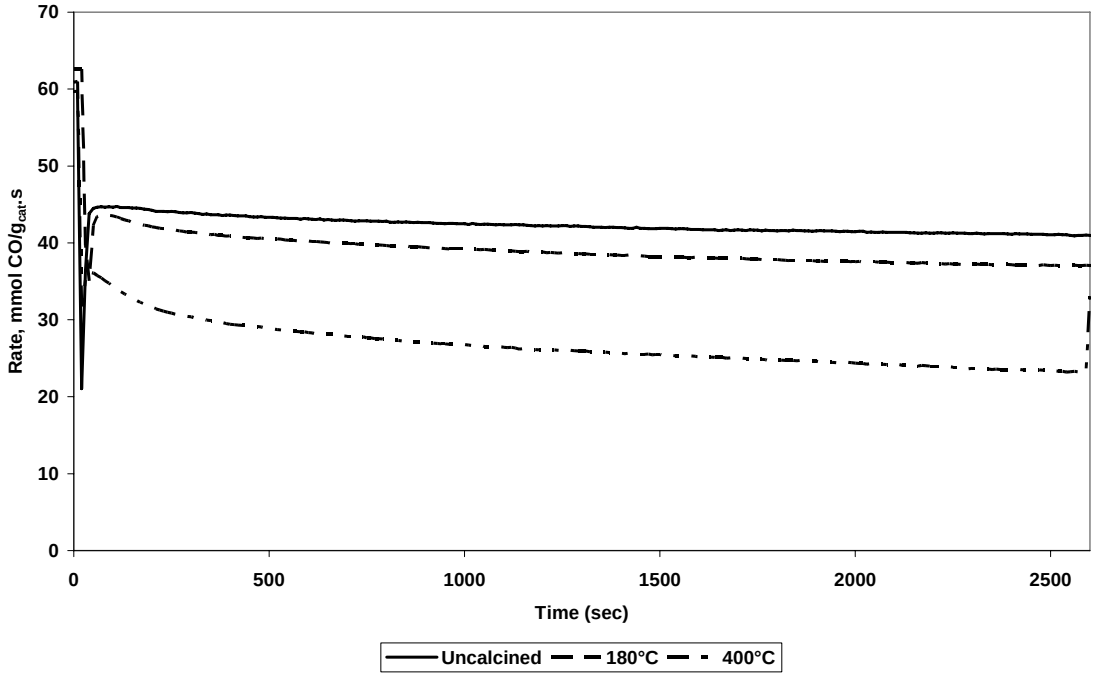

Figure 26: Influence of calcination on the catalytic activity of an extruded titania granule supported gold catalyst (0.5 wt% Au, 1% CO, 600 l.g$_{cat}^{-1}$.h^{-1}, 25°C) [68].

It is important to note that sintering of the gold particles is expected to amplify when the gold particles are concentrated on the surface of the support, implying that it is more likely to occur at high gold loadings [69]. It was therefore expected that the high gold containing catalysts, investigated in the present study, would also show a similar trend. However, the results were in contradiction with those in Figure 26. From Figures 27 and

28 it is evident that the 2 hour calcination treatment at 300°C enhanced the catalytic activity of both the 4.5 and 10.5 wt% Au/TiO_2 catalysts. The same trend was observed for the tests conducted in air and in H_2.

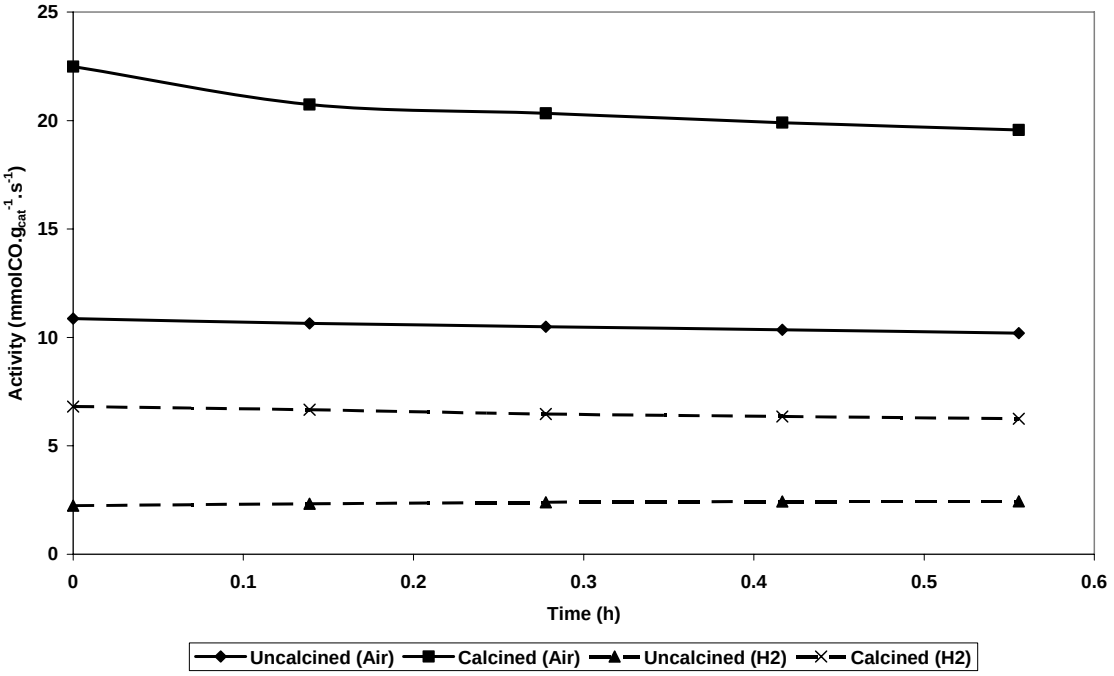

Figure 27: Influence of calcination on the catalytic activity of a P25 titania supported gold catalyst (4.5 wt% Au, 0.2% CO, 1000 l.g$_{cat}^{-1}$.h^{-1}, 25°C)

Only at 16.6 wt% Au (Figure 29) did calcination result in a decrease in activity, in parallel to the findings of Roberts *et al* [68]. Investigation into this phenomenon led to the conclusion that most of the gold load on the outer surface of the 1 mm extruded titania granules, confirmed by the eggshell appearance of granulate metal oxide supported gold catalysts. The effective area available for gold loading is therefore significantly reduced, resulting in high gold loadings in this region. With the P25 nano-titania, the available support area for gold loading is much higher. It is therefore possible that the average gold loading of 0.5 wt% Au on the extruded titania granules may have areas in which the local gold loading is in excess of 16.6 wt%. This might explain why Figures 26 and 29, and Figures 27 and 28 follow similar trends respectively. A schematic illustration of this phenomenon is shown in Figure 30.

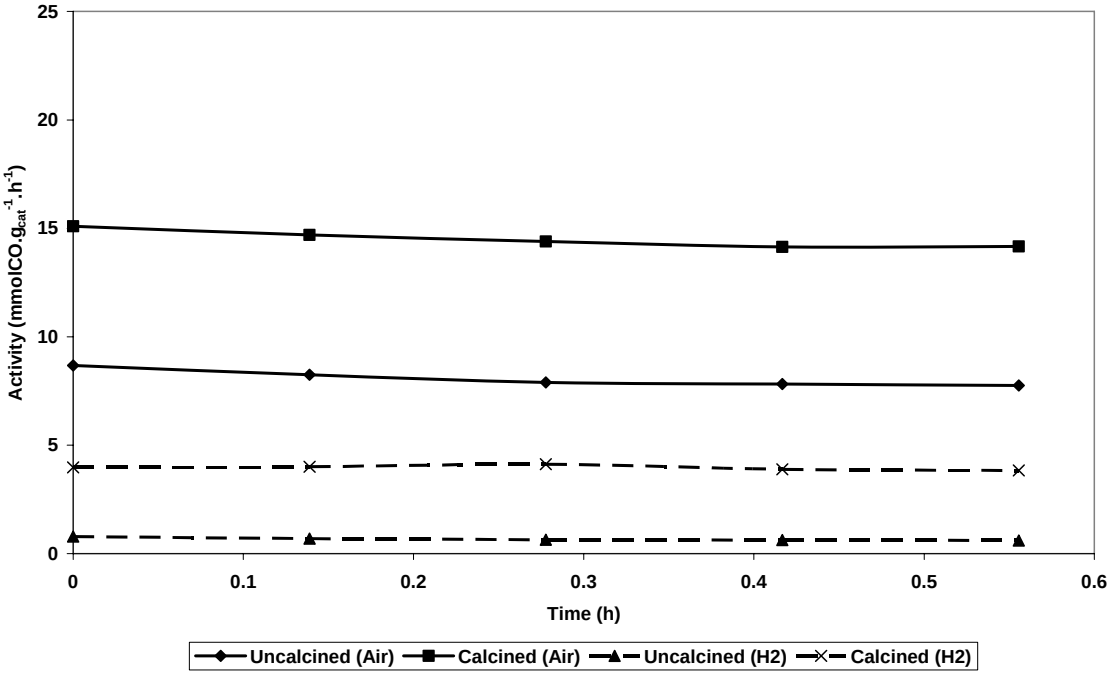

Figure 28: Influence of calcination on the catalytic activity of a P25 titania supported gold catalyst (10 wt% Au, 0.2% CO, 1000 l.g_{cat}^{-1}.h^{-1}, 25°C)

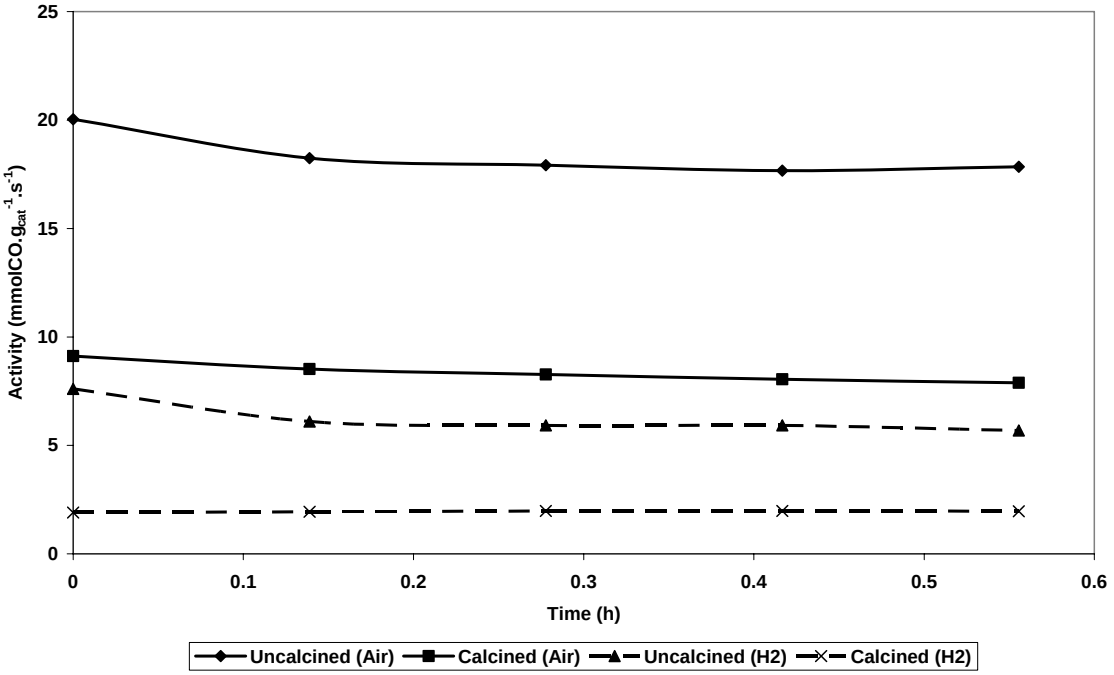

Figure 29: Influence of calcination on the catalytic activity of a P25 titania supported gold catalyst (20 wt% Au, 0.2% CO, 1000 l.g_{cat}^{-1}.h^{-1}, 25°C)

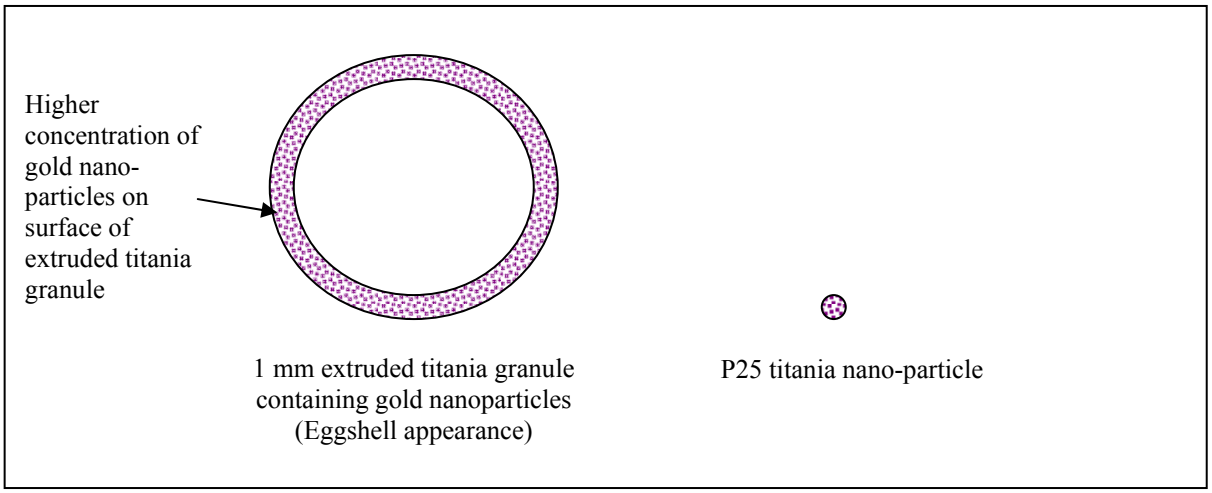

Figure 30: Schematic illustration of the comparison between gold loading on extruded titania granules and P25 titania nano-particles.

6.2.4 Influence of pressure

Although it can be predicted that the CO conversion would increase with and increase in pressure, the extent to which CO conversion is influenced by pressure had to be determined. A typical empirical formula for the rate of CO conversion over gold based catalysts is shown in Equation 27 below:

$$r \propto k\left[P_{total}\right]^{n}.\mathrm{X}_{CO}.\mathrm{X}_{O_2} \tag{27}$$

where r is the rate, k the rate constant, P_{total} the total pressure, X_{CO} the mole fraction of carbon monoxide, X_{O2} the mole fraction of oxygen , and n the reaction order for pressure. Only the influence of pressure on the rate of CO conversion was investigated during this study, since it is generally known that the reaction order for CO concentration is approximately 0.85 and that of oxygen concentration 0.07 [70]. An empirical model was developed for a 5 wt% Au/TiO$_2$ catalyst by changing the pressure (absolute pressure) to 14.5 psi (1 atm), 29 psi (2 atm) and 43.5 psi (3 atm). The logarithm of the pressure and the resulting rate of CO conversion was plotted in order to determine the pressure factor

n, which is defined as the slope of the logarithmic plot. The results are shown in Figure 31 from where it is evident that the reaction order of pressure *(n)* is approximately 0.74 ± 0.09.

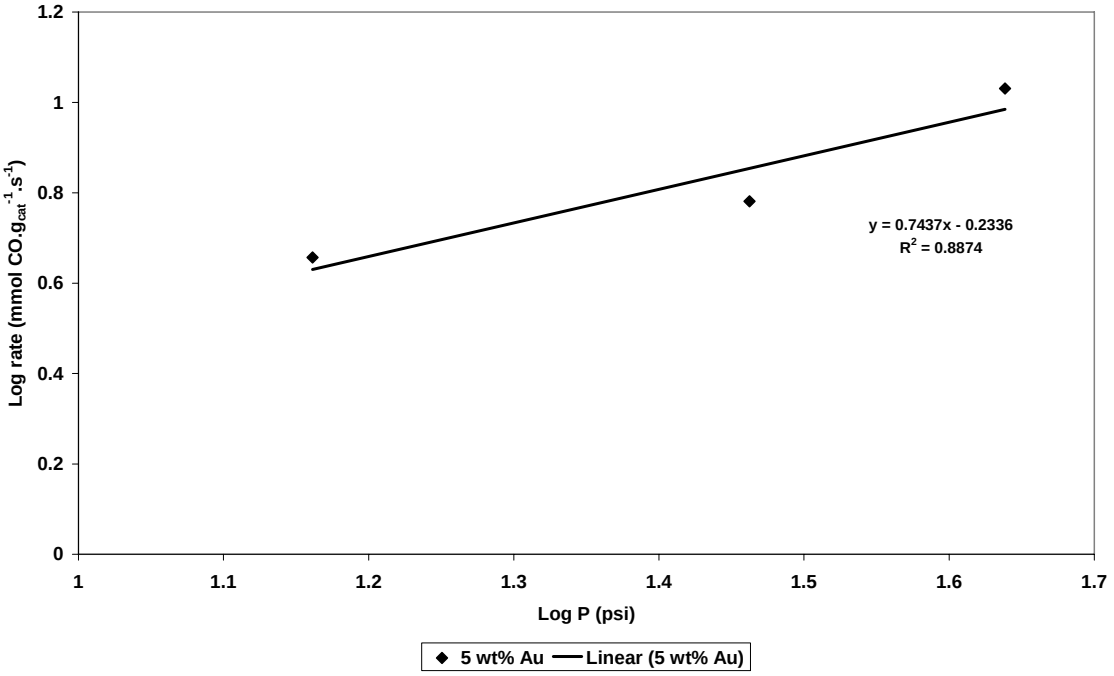

Figure 31: Calculation of the pressure factor, n, for the rate of CO conversion (25ºC).

6.2.5 Influence of temperature

The influence of temperature on the rate of CO conversion was incorporated into the overall rate equation by means of the rate constant *k'* as shown in Equation 28.

$$r \propto k'\left[P_{total}\right]^{n}.\mathrm{X}_{CO}.\mathrm{X}_{O_2} \tag{28}$$

and *k'* is defined by the following Arrhenius equation:

$$k' = Ae^{\frac{-E_A}{RT}} \tag{29}$$

where A is a constant, E_A the activation energy in J.mol^{-1}, R the universal gas constant (8.314 J.mol^{-1}.K^{-1}), and T the absolute temperature in Kelvin. The activation energy was calculated as 24.4 + 0.9 kJ.mol^{-1} from the Arrhenius plot in Figure 32.

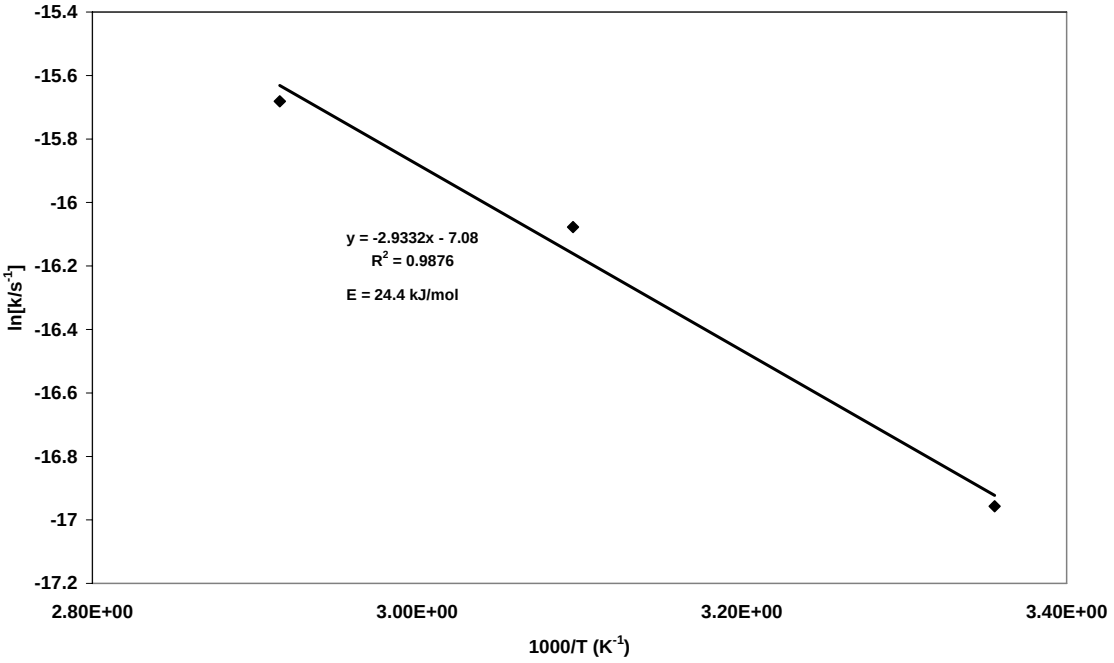

Figure 32: Calculation of the activation energy for the CO oxidation reaction over a 1 wt% Au on P25 titania catalyst from an Arrhenius plot.

The activation energy calculated is approximately double that quoted by Bondzie *et al.* in 1999 [71], but is closer to those widely reported since for Au/TiO_2 catalysts.

6.2.6 Influence of MEA constituents

The technique of producing MEAs involves the addition of chemical additives like propanol, PTFE emulsion, Nafion^{TM}, and carbon black, as discussed in Section 5.3.1. A systematic approach was taken to investigate the influence of each of these constituents on the catalytic activity of the Au/TiO_2 catalysts. At the outset, 0.5g of a 4.5 wt% Au catalyst was suspended in 10 ml distilled water for 10 minutes and vacuum filtered,

where after it was dried at 120°C for 14 hours. The same procedure was used to investigate the influence of a 90:10 propanol to distilled water solution (termed batch solution) containing PTFE emulsion to yield 30 wt% PTFE in the dry sample, and batch solution containing Nafion™ solution to yield 30 wt% Nafion™ in the dry sample. A summary of the results are shown in Figure 33 below:

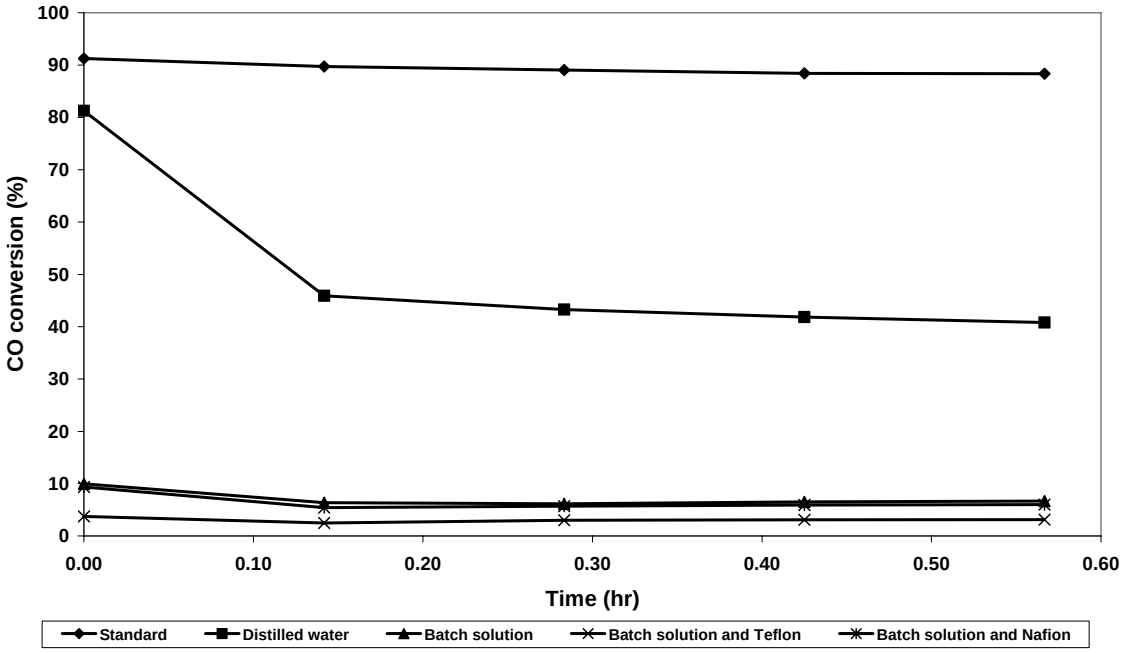

Figure 33: Influence of catalyst ink additives on the catalytic activity of a 4.5 wt% Au/TiO_2 catalyst (1000 $l.g_{cat}^{-1}.h^{-1}$, 0.2% CO, 25°C)

A significant decrease in activity was observed, even when the catalyst was suspended in distilled water. The CO conversion decreased from the initial 90 per cent to less than 10 per cent when propanol and PTFE, or propanol and Nafion™, was added. This "poisoning" effect of the MEA constituents proved to be of major concern. However, the effect of distilled water was difficult to comprehend. An additional calcination step at 300°C for 2.5 hours was conducted in an attempt to reactivate the catalysts. The calcination step resulted in a significant increase in the catalytic activity, as shown in Figure 34. This effect might be ascribed to the fact that a calcination treatment is necessary to render the PTFE in the catalyst layer hydrophobic. Therefore, without the

300°C calcination temperature, water condensation on the catalyst surface is likely during operation in high relative humidity conditions. Water condensation has a deleterious effect on catalystic activity, as discussed in detail in Section 6.2.7.

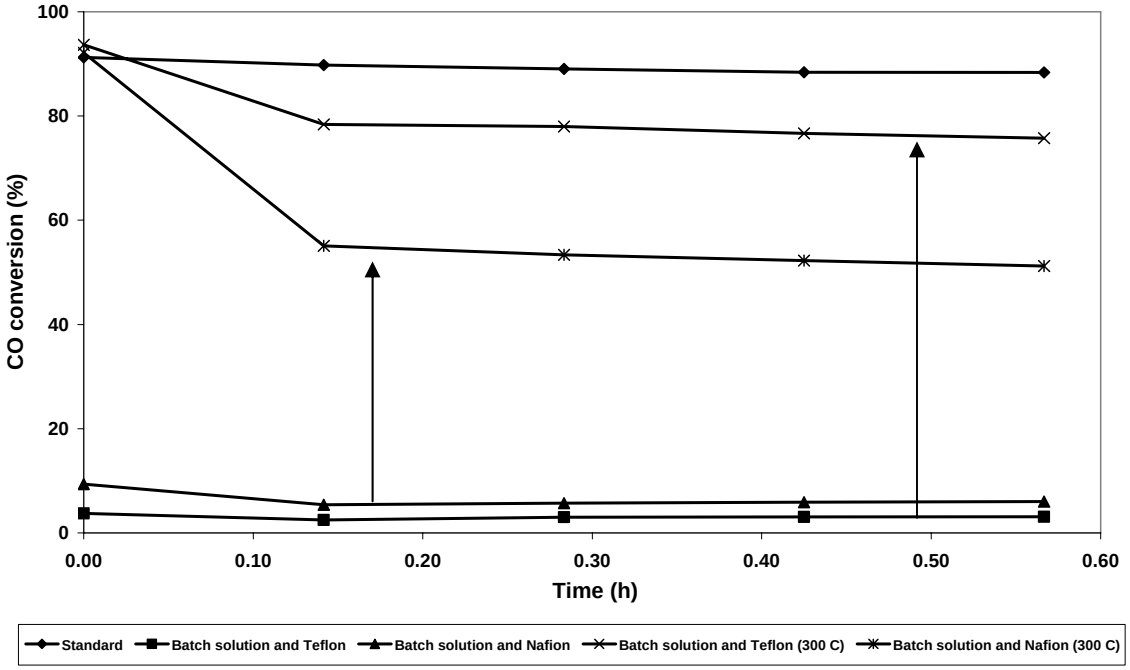

Figure 34: Influence of calcining at 300°C for 2.5 hours on catalytic activity of a 4.5 wt% Au catalyst containing 30 wt% Teflon or Nafion (1000 l.g$_{cat}^{-1}$.h^{-1}, 0.2% CO, 25°C).

From Figure 34 it is evident that the calcination treatment had a greater effect on the PTFE containing catalyst compared to the one containing Nafion^{TM}. PTFE is typically added to the catalyst ink in the form of an emulsion, while Nafion^{TM} is added as a 5 wt% Nafion solution. The polymeric structure of the Nafion^{TM} may therefore coat the catalyst, hence a decrease in activity. However, ionic conduction is not required in the Au/TiO$_2$ layer in the MEA; rather, good inter-particulate adhesion between the carbon black an Au/TiO$_2$ is required. The necessary adhesion was obtained by adding 30 wt% PTFE to the catalyst-carbon black layer.

Additional catalyst-ink simulations were done by mixing Au/TiO$_2$ with carbon-black in a weight ratio 75 Au/TiO$_2$: 25 C. PTFE was used as binder (30 wt% in dry sample) and

the ink was prepared as stipulated in Section 5.3.1, except for the heat treatment, which comprised of 2 hours drying at 120°C and calcining at 300°C for 2.5 hours. The results obtained are shown in Figure 35.

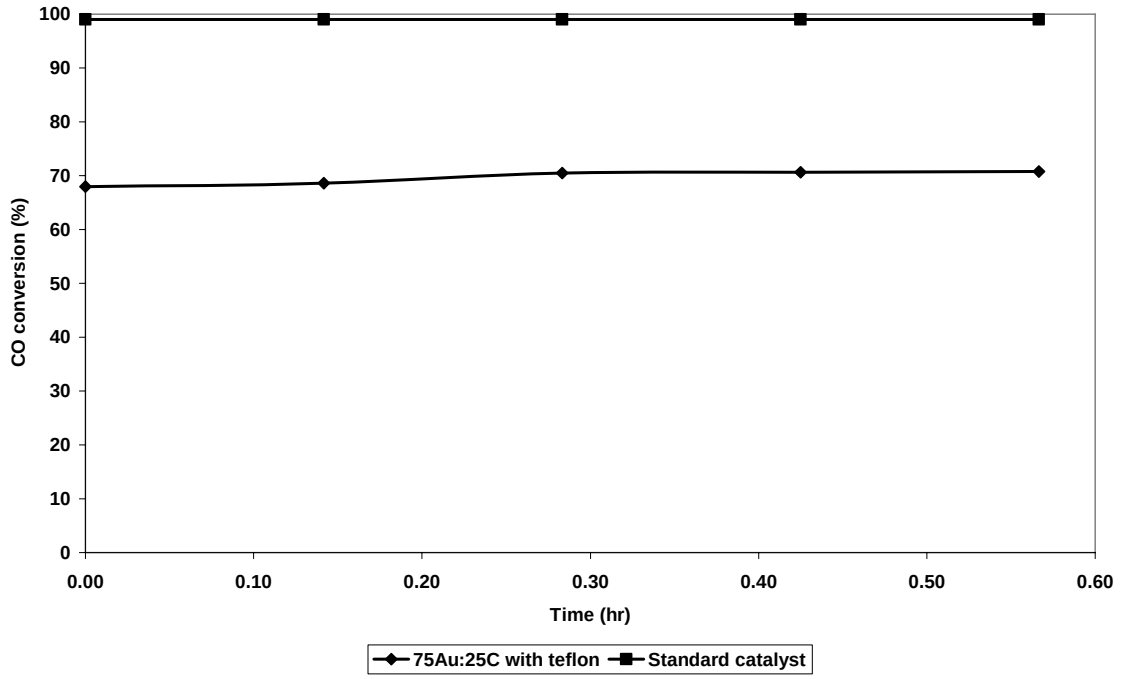

Figure 35: Influence of 25 wt% C-black and 30 wt% Teflon on catalytic activity of a 10 wt% Au/TiO$_2$ catalyst (1000 l.g$_{cat}^{-1}$.h^{-1}, 0.2% CO, 25°C).

Although the CO conversion decreased by approximately 30 per cent when C-black and PTFE was added, the catalyst still remained exceptionally active for the CO oxidation reaction. This result proves that the Au/TiO$_2$ catalyst should be active inside the MEA of a PEM fuel cell for the given MEA preparation procedure, assuming that the operating conditions inside the fuel cell does not affect the catalytic activity of the Au/TiO$_2$ catalyst.

6.2.7 Influence of water formation on catalytic activity

In order to ensure 100 per cent relative humidity in fuel cells, the temperature of the anode and cathode humidifiers are typically set at 5°C higher than the operating temperature of the fuel cell. Therefore, water typically condensates inside the fuel cell, which might have an effect on the activity of the Au/TiO_2 catalysts. This effect was simulated in the CO oxidation test rig by immersing the catalyst containing u-tube reactor, midway through the test run, in a water bath 5°C cooler than the water in the humidification column. Results obtained are shown in Figure 36 below:

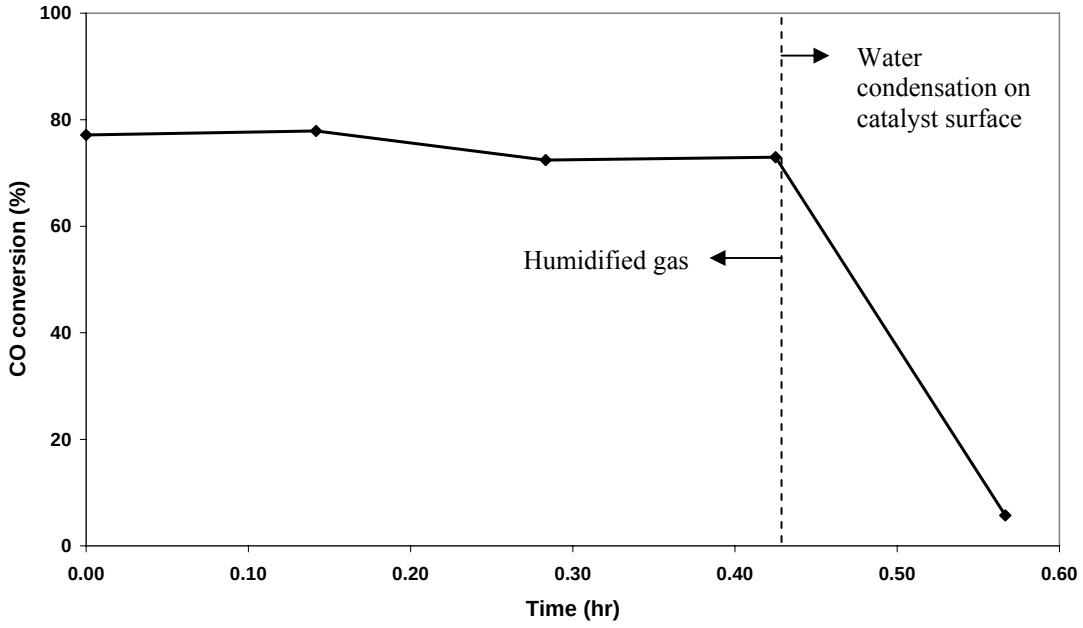

Figure 36: Influence of water formation on the catalyst surface on CO conversion (1000 $l.g_{cat}^{-1}.h^{-1}$, 0.2% CO, 25°C, 5 wt% Au/TiO_2, dried at 120°C for 14 hours)

It is evident that the condensation of water on the catalyst's surface significantly reduces the catalytic activity. For these catalysts to find commercial application in fuel cells, it is imperative that it should be able to operate under 100 per cent relative humidity conditions where liquid water formation is likely. The effect of adding PTFE to the catalyst was investigated in an attempt to increase the 'water resistance' of the Au/TiO_2

catalysts. Apart from the fact that PTFE acts as a binder in the MEA, it also exhibits the property of being hydrophobic, thereby protecting the platinum electrocatalysts from being flooded with water in the fuel cell. Thus, it is possible that the addition of PTFE to the Au/TiO_2 catalysts might prevent the formation of water on the catalyst's surface. The test in Figure 36 was repeated, this time using a 10 wt% Au/TiO_2 catalyst containing 30 wt% PTFE. Results are shown in Figure 37. Although the CO conversion decreased slightly, a significant increase in the water resistance of the catalyst was observed when 30 wt% PTFE was added.

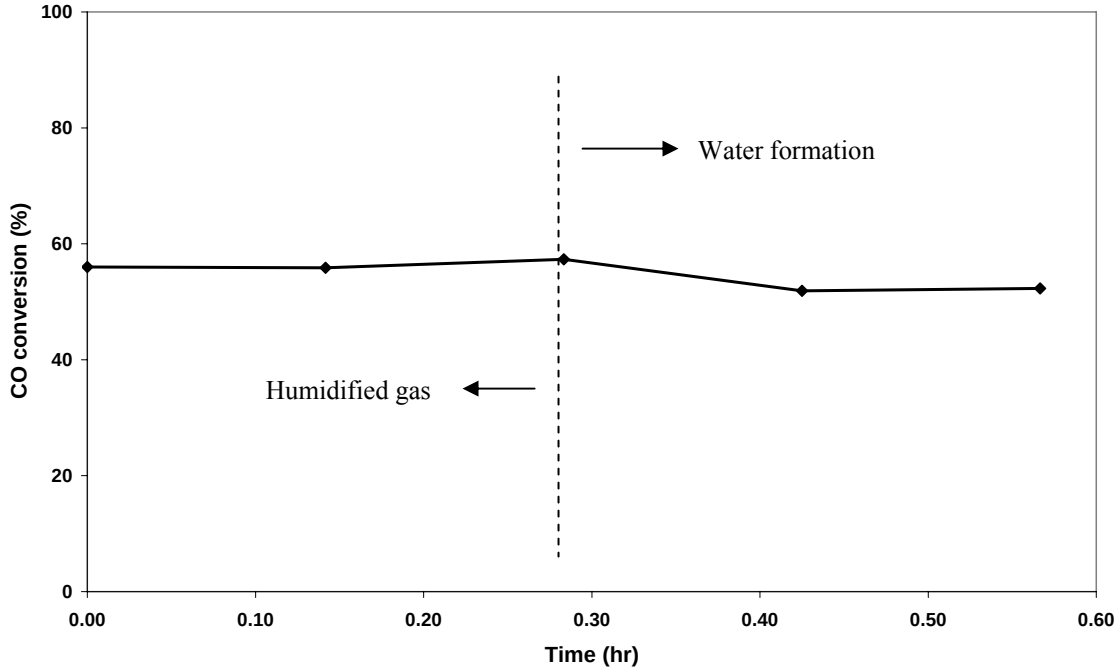

Figure 37: Influence of water formation on the catalyst surface on CO conversion (10 wt% Au, 75:25 Au:C-black, 30 wt% Teflon, dried at 120°C for 14 hours, calcined at 300°C for 2.5 hours, 1000 $l.g_{cat}^{-1}.h^{-1}$, 0.2% CO, 25°C).

6.3 Fuel cell results – bi-layer configuration

6.3.1 MEA fabrication and bi-layer formation

It is imperative to limit the thickness of the MEA in order to minimize ohmic overpotential losses. This can be achieved by using high wt% metal catalysts in order to obtain a certain metal loading within the MEA in terms of mg metal.cm^{-2}. However, the decrease in the layer thickness will result in a decrease in contact time between the gas and the catalyst bed in the bi-layer MEA.

A test regime was followed in order to determine the optimum amount of Au/TiO_2 to be used in the formation of the bi-layer MEAs. The factors considered included the interparticulate adhesion and structural robustness upon hot-pressing, as well as the estimated space velocity that would be encountered over the bi-layer inside the fuel cell. Table 4 shows the possibilities investigated.

Table 4: Calculations highlighting the effect of gold loading on the estimated space velocity over the gold based catalysts in the MEA of a 25 cm^2 single cell PEM fuel cell. Calculations are based on a fuel cell system operating at 500 $mA.cm^{-2}$ and H_2 stoichiometry of 2.2 (as used in standardised single cell testing procedure [66]).

Au loading ($mgAu/cm^2$)	Au on catalyst (wt%)	Catalyst mass (g)	Estimated space velocity * ($l.g_{cat}^{-1}.h^{-1}$)
0.5	5	0.25	46.1
0.5	10	0.125	92.2
1	5	0.5	23.0
1	10	0.25	46.1
2	20	0.25	46.1

**Detailed calculations presented in Appendix VII.*

Test work proved that poor structural robustness was obtained upon hot-pressing when the layer was too thick. This was due to insufficient interparticulate adhesion of the carbon and catalyst particles inside the layer. Improved adhesion was obtained when the

layer thickness was decreased, typically achieved when high gold containing catalysts were used.

The test work campaign indicated that the best MEAs, in terms of structural robustness, were obtained when aimed for 0.5 mg $Au.cm^{-2}$ using a 10 wt% Au catalyst, which resulted in 0.125 g of gold catalyst being used in the bi-layer. With this configuration, space velocities of up to 92.2 $l.g_{cat}^{-1}.h^{-1}$ will be obtained over the Au/TiO_2/C bi-layer inside the MEA.

6.3.2 Polarisation results

The polarisation behavior of a standard 25 cm^2 Electrochem Inc. MEA (1 mg $Pt.cm^{-2}$, 20 wt% Pt-Vulcan XC72R) was determined and used as benchmark (Figure 38). Also shown in Figure 38 is the polarisation behaviour of the in-house produced Mintek SM4 MEA, which comprised of 1 mg $Pt.cm^{-2}$ at both the anode and cathode using 40 wt% Pt-Vulcan XC72R, as well as a 0.5 mg $Au.cm^{-2}$ (using 10 wt% Au/TiO_2) catalyst layer at the anode in a bi-layer assembly, as previously described in Figure 12. From Figure 38 it is evident that the in-house produced Mintek SM4 MEA shows inferior performance compared to the Electrochem Inc. MEA. Lower performance can be observed in all three the areas where overpotential losses occur. The main cause of decreased performance of the Mintek MEAs was as a result of ohmic overpotential losses. This is due to the fact that an additional, semi-conductive layer is introduced into the MEA, which increases the resistance. The effects of ohmic overpotential losses were substantiated when the bi-layer thickness was increased to yield a gold loading of 2 mg $Au.cm^{-2}$ using a 16 wt% Au/TiO_2 catalyst, also shown in Figure 38.

Although the aim of this study was not to produce MEAs with superior performance over commercially available products, the increased resistance is of concern. Nevertheless, the initial aim of incorporating a Au/MOx bi-layer into the MEA was to illustrate the viability for CO tolerance, and not necessarily electrochemical performance.

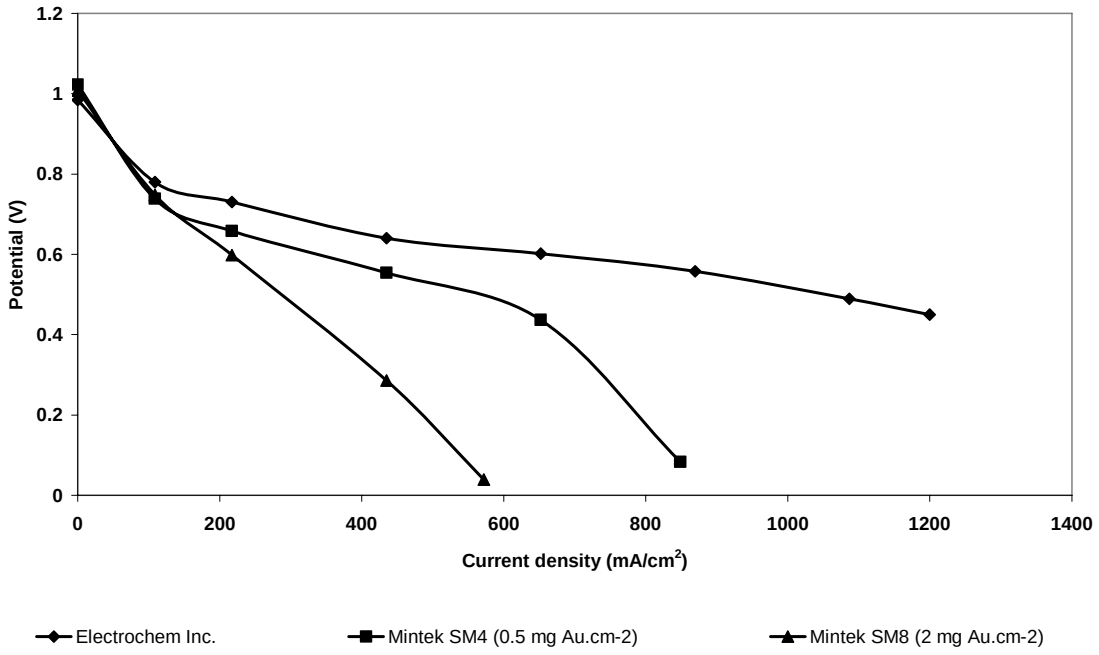

Figure 38: Comparison between the polarisation performance of a standard Electrochem Inc. MEA and an in-house produced Mintek MEAs. (Fuel flow rate: 42 ml.min^{-1} + 15.35 ml.min^{-1}.A^{-1}; Oxidiser flow rate: 34.86 ml.min^{-1} + 12.82 ml.min^{-1}.A^{-1}; 80°C, 25 psi).

6.3.3 Influence of Au/TiO_2 on CO tolerance

Test work in the external CO oxidation test rig proved that the 10 wt% Au/TiO_2 catalysts, used in the Mintek SM4 MEA, yielded 55 per cent CO conversion from gas mixtures containing 2 per cent air, 2000 ppm CO in H_2 at 1000 $\ell.g_{cat}^{-1}.h^{-1}$, 25°C and atmospheric pressure. The influence of this catalyst inside the Mintek SM4 MEA was investigated in the PEM fuel cell. Also, the CO tolerance of the Mintek SM4 MEA was compared to that of the Mintek SM3 MEA; an MEA similar to the Mintek SM4 MEA except that it did not contain a Au/TiO_2/C bi-layer. The current was kept constant at 5.43 A (217 mA.cm^{-2}) until the potential stabilised, where after 350 ppm CO and a 2 per cent air bleed stream was introduced with the H_2 fuel. The initial results (Figure 39) did not look promising. No effect was seen with the introduction of a Au/TiO_2 bi-layer inside the MEA. Both the Mintek SM3 and SM4 MEAs deactivated due to CO poisoning.

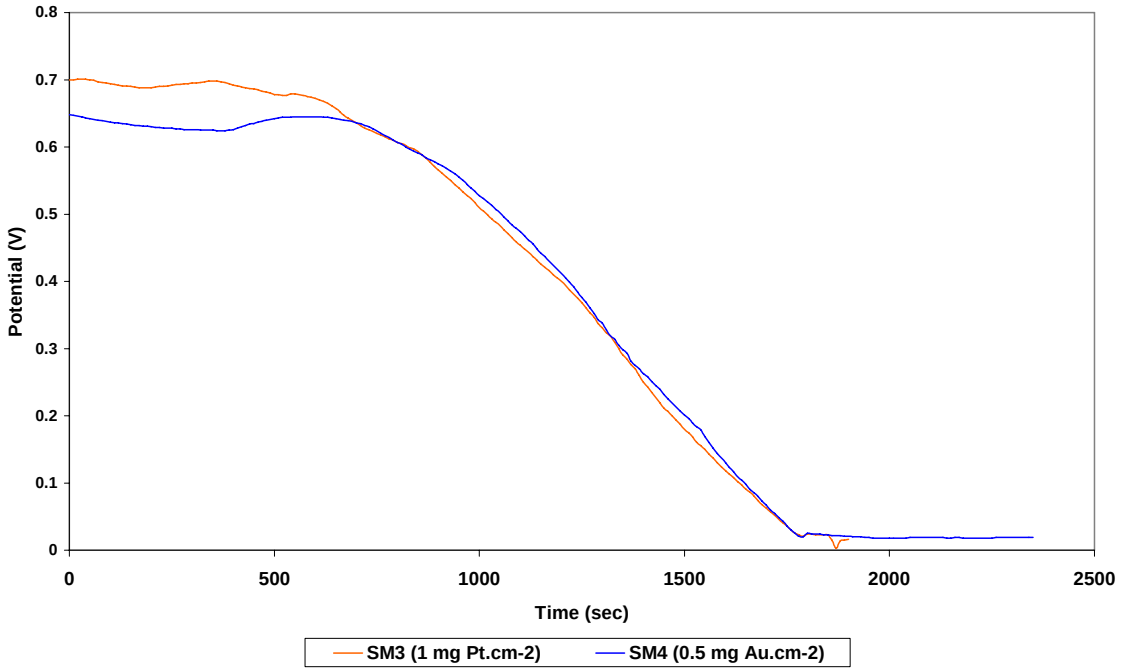

Figure 39: Poisoning effect of 350 ppm CO on the Mintek SM3 and SM4 MEAs (217 mA.cm^{-2}, fuel flow rate: 42 ml.min^{-1} + 15.35 ml.min^{-1}.A^{-1}; oxidiser flow rate: 34.86 ml.min^{-1} + 12.82 ml.min^{-1}.A^{-1}; 80°C, 25 psi). Air was introduced into the H_2 fuel as a 2% bleed stream.

Although the Au/TiO_2 proved to be active for the oxidation of CO to CO_2 in a separate CO oxidation test rig, the same results could not be obtained inside the fuel cell. In order to advance the simulation of the fuel cell gas flow dynamics through the catalyst layer, a 'flat bed' reactor, similar to that discussed in Section 5.3.2 and Appendix IV, was used in the CO oxidation test rig. This setup allowed the gas to pass through the actual bi-layer assembly, as used in the fuel cell. No CO conversion was obtained with the bi-layer containing 0.5 mg Au.cm^{-2} (10 wt% Au/TiO_2) as was used inside the MEA in Figures 38 and 39. Compared to the 55 per cent CO conversion obtained with the same catalyst in the u-tube reactor, this might indicate that the contact time over the thin Au catalyst layer inside the MEA is insufficient to yield significant conversion.

In order to increase the gas contact time over the catalyst layer, 0.25 g of a 20 wt% Au/TiO_2 catalyst (yielding 2 mg Au.cm^{-2}) was incorporated into the bi-layer with 75 Au_{cat} : 25 carbon, thereby doubling the thickness of the Au catalyst layer. This

catalyst yielded 85 per cent CO conversion in the normal u-tube reactor at a space velocity of 1000 $\ell.g_{cat}^{-1}.h^{-1}$, and 30 per cent CO conversion in the 'flat bed' reactor configuration. The space velocity over the gold layer in the 'flat bed' reactor was calculated to be 764 $\ell.g_{cat}^{-1}.h^{-1}$. Even though an improvement was seen with the use of a 20 wt% Au on TiO_2 catalyst (2 mg $Au.cm^{-2}$), it was evident that mass transfer limitations were still of concern inside the MEA.

Nevertheless, a bi-layer MEA was produced using the 20 wt% Au/TiO_2 catalyst to yield a gold loading of 2 mg $Au.cm^{-2}$, protecting the anodic 1 mg $Pt.cm^{-2}$ Pt electrocatalyst. Results obtained were compared to that in Figure 39, as well as results obtained from an in-house produced $Pt_{20}Ru_{10}$ (1 mg $Pt.cm^{-2}$) anode MEA, and an in-house produced 2 mg $Au.cm^{-2}$ (using 20 wt% Au catalyst) $Pt_{20}Ru_{10}$ (1 mg $Pt.cm^{-2}$) bi-layer MEA. These results are shown in Figure 40.

From Figure 40 it is evident that a slight increase in the CO tolerance was obtained with the 2 mg $Au.cm^{-2}$ Au/TiO_2 bi-layer MEA. However, the CO tolerance of this MEA was inferior to that of the $Pt_{20}Ru_{10}$ MEA configuration. Interesting was the 2 mg $Au.cm^{-2}$ Au/TiO_2 bi-layer configuration with a $Pt_{20}Ru_{10}$ electrocatalyst. The CO tolerance of this MEA proved to be lower than that of the normal $Pt_{20}Ru_{10}$ MEA. In addition, the incorporation of the Au/TiO_2 layer resulted in oscillatory behaviour. Although not conclusive, this oscillatory behaviour might be induced by an electrochemical interaction between the Au/TiO_2 and the $Pt_{20}Ru_{10}C$ layers.

From the above mentioned results it is evident that no significant CO tolerance was obtained with the incorporation of a Au/TiO_2/C bi-layer into the MEA, even when the contact time was significantly increased by increasing the layer thickness. A possible explanation for the lack of activity inside the MEA might be that water formation inside the fuel cell results in mass transfer limitations of the CO contaminated H_2 gas to the active areas of the Au/TiO_2 catalyst. In addition, Haruta [72] reported that the localised acidic conditions in the PEM fuel cell, resulting from the formation of H^+ ions at the anode, might have an adverse effect on the activity of Au/TiO_2 catalysts.

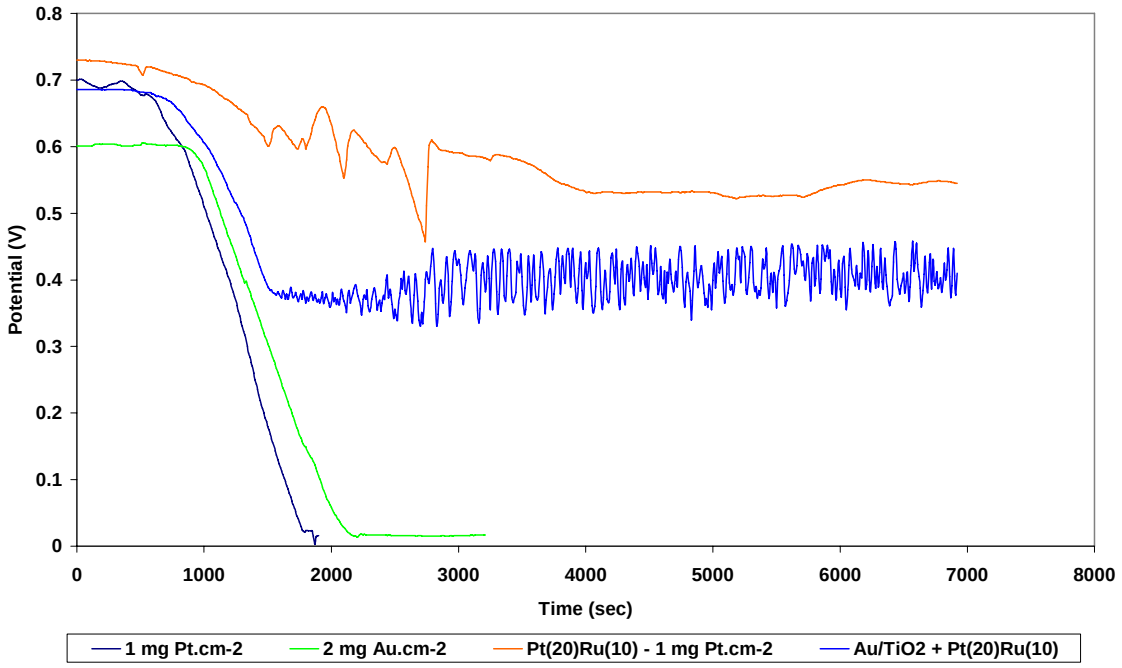

Figure 40: Poisoning effect of 350 ppm CO on the in-house produced Mintek MEAs (217 mA.cm^{-2}, fuel flow rate: 42 ml.min^{-1} + 15.35 ml.min^{-1}.A^{-1}; oxidiser flow rate: 34.86 ml.min^{-1} + 12.82 ml.min^{-1}.A^{-1}; 80°C, 25 psi). Air was introduced into the H_2 fuel as a 2% bleed stream.

6.4 Fuel cell results – catalyst chamber configuration

The decrease in efficiency of the Au/TiO$_2$ catalysts inside the MEA, compared to that in the CO oxidation test rig, resulted in an investigation in which the Au/TiO$_2$ catalysts were removed from the MEA configuration and incorporated in a PROX catalyst chamber, just prior to the fuel cell, as discussed in Section 5.2.4. This configuration ruled out the possible poisoning effects of MEA constituents and the acidic conditions at the anode, as well as preventing the formation of water on the catalyst surface. In addition, with this configuration no polarisation performance, in terms of ohmic overpotential losses, was sacrificed in order to incorporate an additional layer into the MEA. The results obtained with the catalyst chamber arrangement are shown in Figure 41. A significant increase in the CO tolerance was observed. The catalyst chamber arrangement resulted in CO tolerance superior to that of the $Pt_{20}Ru_{10}$ anode.

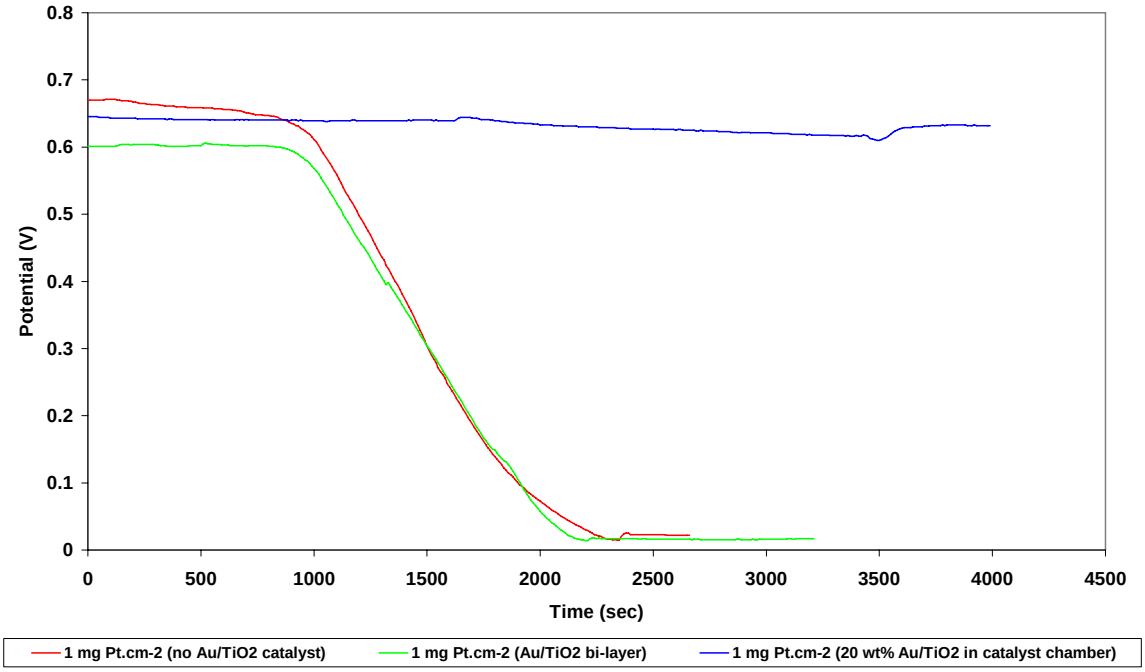

Figure 41: Influence of a 20 wt% Au on TiO_2 catalyst on the CO tolerance of a 1 mg $Pt.cm^{-2}$ MEA. (Fuel flow rate: 42 $ml.min^{-1}$ + 15.35 $ml.min^{-1}.A^{-1}$; Oxidiser flow rate: 34.86 $ml.min^{-1}$ + 12.82 $ml.min^{-1}.A^{-1}$; 350 ppm CO, 80°C, 25 psi). Air was introduced into the H_2 fuel as a 2% bleed stream.

Although a slight decrease in potential was observed after 2000 seconds it must be noted that these results do not represent an optimised system. Based on these preliminary results it was decided to further investigate and optimise the PROX catalyst chamber configuration for fuel cell applications. The challenges that remained at this stage included: simulating an actual fuel cell system and removing CO to less than 1 ppm from CO containing H_2 gas streams at representative space velocities while introducing the minimum amount of oxygen. These parameters had to be investigated with the aim of developing an economically viable system that will meet both technical and economical requirements of a commercially viable fuel cell system.

Chapter 7

RESULTS AND DISCUSSIONS: Au/TiO_2 PREFERENTIAL OXIDATION (PROX) SYSTEM

7.1 Introduction

The work discussed thus far in this document was mainly focused on cleaning CO from simulated reformate hydrogen, such as that produced from the reforming of methanol. However, the practical and economical problems associated with the onboard reforming of methanol to produce H_2-rich gas have resulted in a generic shift towards the onboard storage of pressurized ultra-pure H_2. Although this method simplifies the overall fuel cell system by removing the onboard fuel processing units, other problems have to be solved for this system to become commercially viable. One of the most prominent challenges is the trade-off between the purity and cost of hydrogen. Currently, commercially available 99.99% pure H_2 (JIS K 0512 Grade 3) contains 10 ppm CO [17], which is sufficient to significantly reduce the performance of a PEM fuel cell, even when operating with PtRu/C anodes [16]. A further increase in purity will result in an additional increase in the cost of the H_2 to the end user. Gold based catalysts can play a significant role in removing low concentrations of residual CO from already-purified-H_2. Therefore, in the following Chapters, the focus was on removing small amounts of CO from impure H_2-rich gas, e.g. from H_2 that would be stored in a fuel tank/cylinder onboard the vehicle but that would have some CO contamination and would essentially be dry.

7.1.1 Selection of CO oxidation system

The diverse results obtained between the activity of the Au/TiO_2 catalysts in the CO oxidation test rig (Section 6.2) and in the bi-layer MEA configuration (Section 6.3) have led to the investigation of using these catalysts outside the fuel cell in a preferential oxidation configuration – a configuration similar to that in the CO oxidation test rig.

Three different systems were investigated, namely 1) Au on P25 TiO_2 nano-powder, 2) Au on P25 TiO_2 granules (+500 -710 µm), and 3) Au on P25 TiO_2 nano-powder wash-coated onto cordierite monoliths.

7.2 Comparison of Au/TiO_2 powder, granulate, and monolith systems

Figures 42 and 43 show the CO conversions obtained with the three different systems in H_2-rich gas mixtures containing either 2000 or 50 ppm CO and a 2 per cent air bleed stream. Both Figures indicate that the highest conversion is obtained over the powder catalyst, followed by the granulate catalyst and finally the powder catalyst dispersed over cordierite monoliths. Note that the space velocity was constant for all these tests at 850 000 $ml.g_{cat}^{-1}.h^{-1}$. For the 2000 ppm CO tests, the 5 wt% Au/TiO_2 powder catalyst was able to remove CO to less than 10 ppm, as is evident from Figure 42. The 5 wt% Au/TiO_2 granules and catalyst coated monoliths were unable to remove CO to the desired levels of less than 10 ppm.

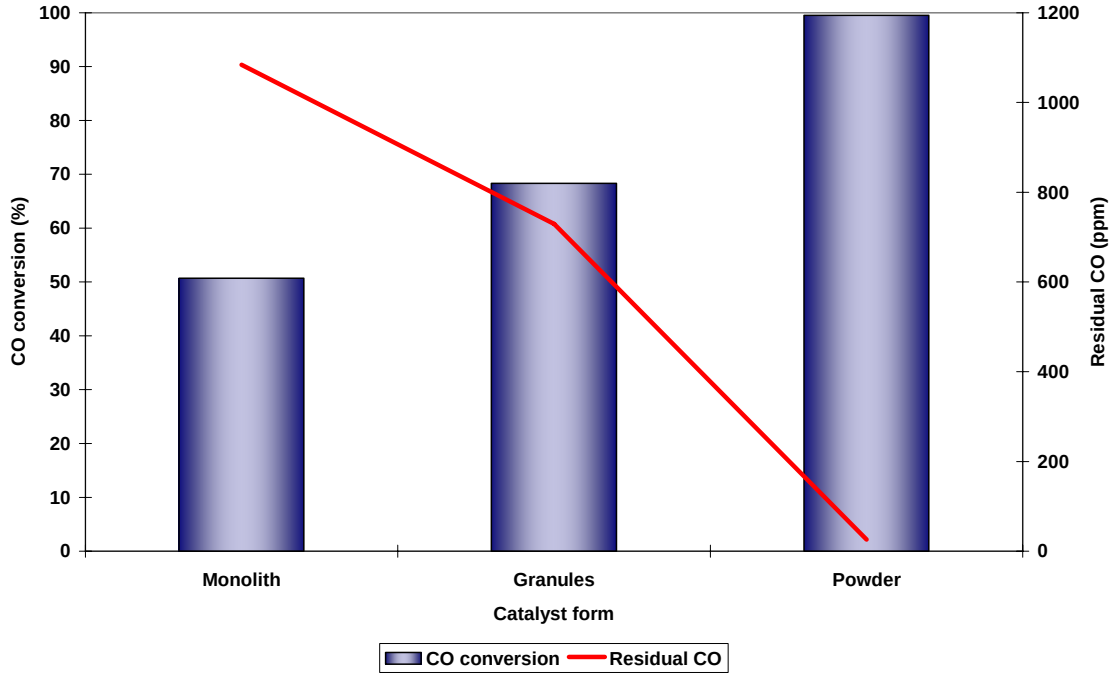

Figure 42: Comparison between CO conversion over a 5wt% Au on TiO_2 coated monolith, 5wt% Au on TiO_2 granules, and 5wt% Au on TiO_2 nano-powder (0.2% CO, 2% air, balance H_2, SV 850 000 $ml.g_{cat}^{-1}.h^{-1}$, dry, 25°C)

For H_2 gas containing 50 ppm CO, all three systems were able to remove CO to less than 10 ppm, as shown in Figure 43. The 3 wt% Au/TiO_2 powder catalyst completely removed CO to concentrations below the detection limit of the PDHID of 1.3 ppm CO. For the 3 wt% Au/TiO_2 granules the residual CO concentration was approximately 5 ppm, and 6 ppm for the 3 wt% Au/TiO_2 coated monoliths.

The higher CO conversions obtained over the powder catalyst bed might be due to an increase in the pressure drop over the packed bed of catalyst powder compared to the granules and monoliths. It is also likely that the difference in CO conversion is due to a temperature effect, where the compact powder bed operates at a higher temperature than the granules and monoliths due to a higher thermal capacitance.

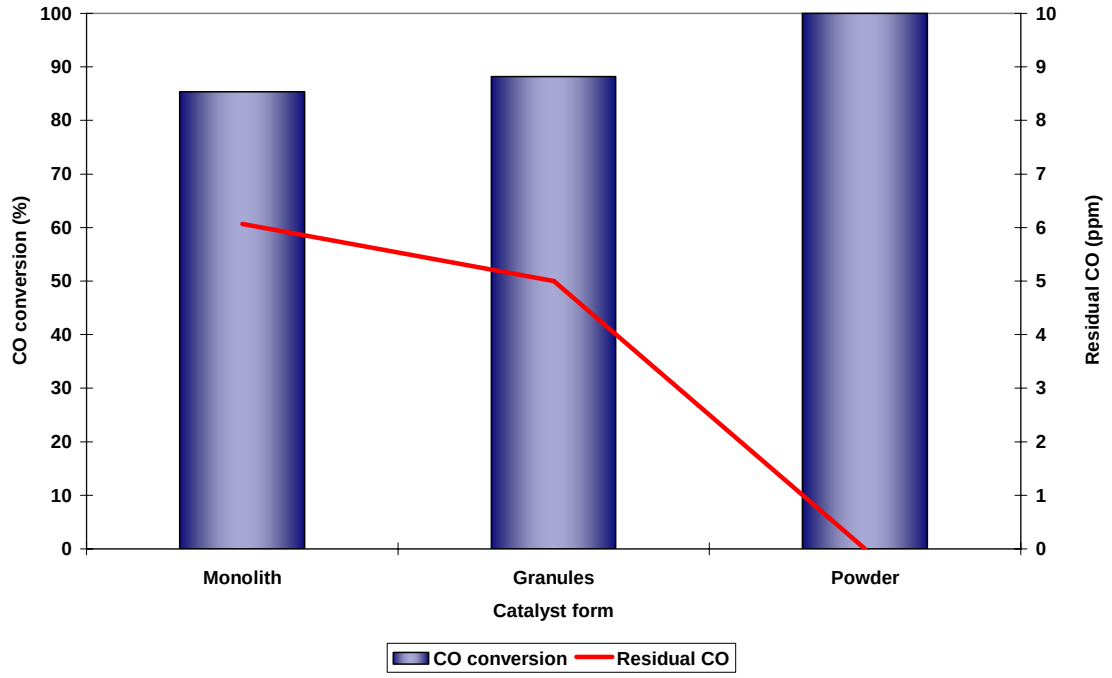

Figure 43: Comparison between CO conversion over a 3 wt% Au on TiO_2 coated monolith, 3wt% Au on TiO_2 granules, and 3wt% Au on TiO_2 powder (50 ppm CO, 2% air, balance H_2, SV 850 000 ml.g_{cat}^{-1}.h^{-1}, dry, 25°C)

Although a higher CO conversion is obtained across the powder catalyst, it is essential to determine the pressure drop over this packed bed of catalyst in order to establish whether it would be practical to scale-up for actual automotive flow conditions. The pressure

drop over a packed bed of catalysts can be calculated using the following Ergun Equation:

$$\Delta p = \frac{f_p L \rho V_s^{\,2}}{D_p}\left(\frac{1-\varepsilon}{\varepsilon^3}\right) \tag{30}$$

where Δp is the pressure drop (Pa), f_p the friction factor, L the length of the bed (cm), ρ the density of the gas (g.cm^{-3}), V_s the superficial velocity (cm.s^{-1}), D_p the equivalent spherical diameter of the particle (cm), and ε the void fraction of the bed.

Table 5 presents the calculated pressure drop over the three different catalyst systems at a volumetric gas flow rate of 1500 ml.min^{-1} and space velocity of 850 000 ml.g_{cat}^{-1}.h^{-1}. The calculation details are shown in Appendix VIII. The void fraction of the catalyst bed, which is defined as 1 minus the ratio between the bulk density *(ρ_b)* and the material/particle density *(ρ_p)*, was calculated as 0.79 for the granules and 0.81 for the powder catalyst. These calculations were based on bulk densities of 0.87 g.cm^{-3} and 0.79 g.cm^{-3} for the granules and powder respectively, and a material density of 4.2 g.cm^{-3} for Titanium(IV) oxide. Although the P25 TiO_2 nanopowder particles are approximately 21 nm in diameter, agglomeration of the particles occur during preparation of the catalysts. The average size of agglomerated powder particles after catalyst preparation and crushing with a mortar and pestle was approximated as 75 um for calculation purposes. For the catalyst coated monoliths, the bulk density was estimated by determining the amount of catalyst coated onto the monolith and calculating the volume of the monolith. Thus, for a 1.6 cm diameter, 7.4 cm long monolith, coated with 0.2 g of Au/TiO_2 catalyst, the estimated bulk density is 0.013 g.cm^{-3}.

Table 5: Calculated pressure drop, in kPa, over the different catalyst packed-bed systems using the Ergun Equation (1500 ml.min^{-1}, SV = 850 000 ml.g_{cat}^{-1}.h^{-1}). Detailed calculations are presented in Appendix VIII. *(* L = d = 0.4 cm)*

Powder*	Granules*	Monolith
0.224 kPa	0.022 kPa	0.0015 kPa

From Table 5 it is evident that pressure drop over all three the systems investigated is relatively low and should be scalable for automotive fuel cell systems.

7.3 Influence of Au concentration on CO conversion over Au/TiO_2 coated monoliths

The influence of gold loading on the activity of the Au/TiO_2 coated monoliths is shown in Figure 44. The increase in CO conversion with an increase in the gold loading is similar to the results previously reported in Section 6.2.1. The 5wt% Au/TiO_2 coated monolith was able to remove CO to a level below the detection limit of the PDHID of 1.3 ppm CO, even in the presence of a reduced air bleed stream of 1 per cent. The 1 and 3 wt% Au/TiO_2 coated monoliths respectively yielded CO conversions of 4.0 and 76.3 per cent in 1 per cent air, and 6.8 and 85.3 per cent in 2 per cent air, also shown in Figure 44. It is evident that there was not a significant increase in CO conversion when the air concentration was doubled to 2 per cent. This signifies that a 1 per cent air bleed (0.21 per cent O_2) is sufficient to facilitate the CO oxidation reaction over these catalysts for low CO concentrations. Any further increase in the air concentration is likely to result in a decrease in the selectivity of the catalyst, and hence a decrease in the fuel efficiency of the fuel cell system.

The 1 and 3 wt% Au/TiO_2 coated monoliths were not able to remove 100 per cent of the CO, as is evident from Figure 44. In an attempt to increase activity, these catalyst coated monoliths were calcined at 300°C for 2.5 hours. The results are shown in Figure 45. It is evident that calcination resulted in a 3-fold increase in CO conversion obtained with the 1 wt% Au/TiO_2 coated monolith; where as no significant change in activity was observed for the 3 wt% Au/TiO_2 coated monolith. However, even with a calcination treatment, these catalysts were unable to completely remove CO at the specified conditions.

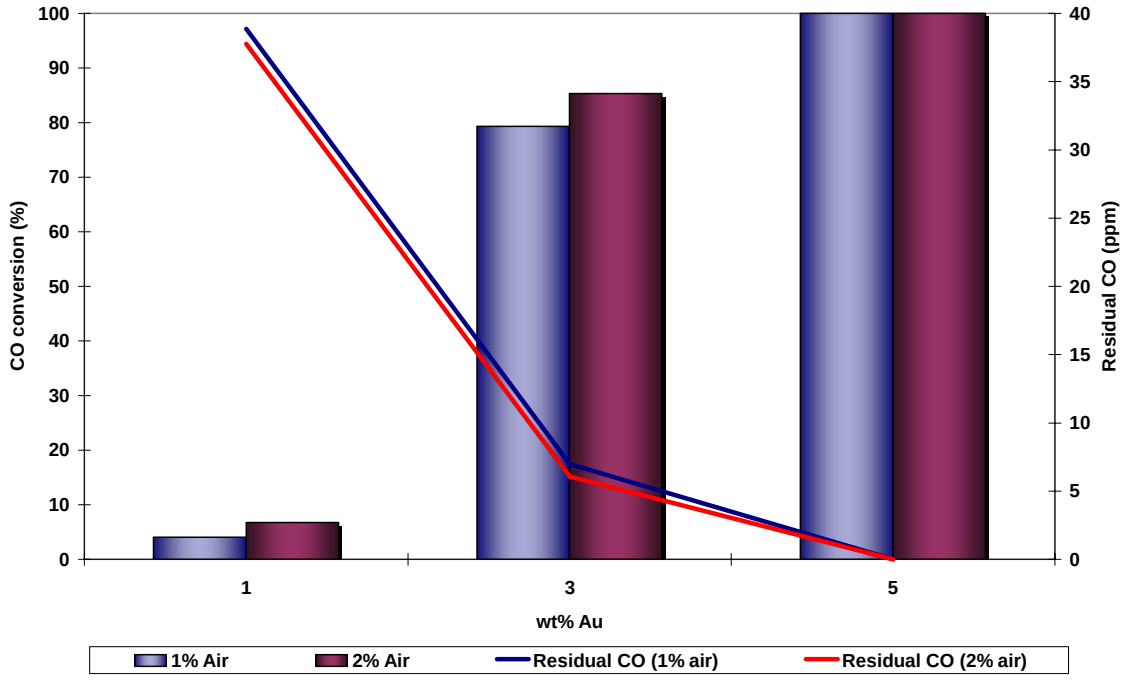

Figure 44: CO removal from dry hydrogen gas containing 50 ppm CO over Au/TiO_2 catalysts on cordierite monoliths at 850 000 ml.g_{cat}^{-1}.h^{-1}, and 25°C.

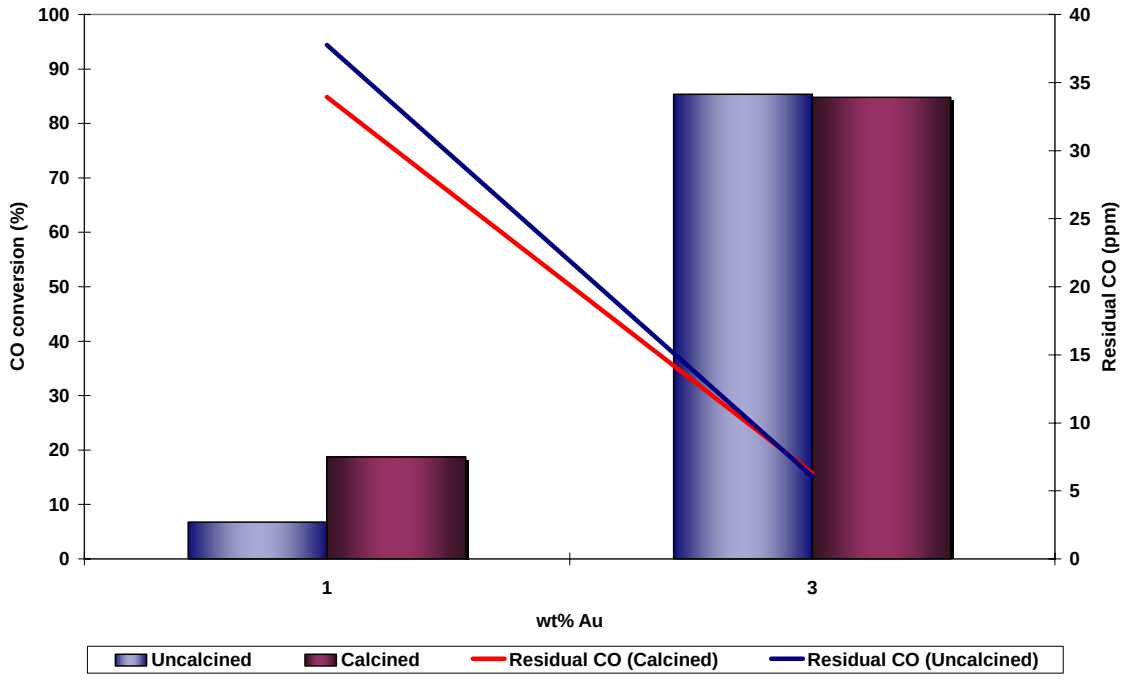

Figure 45: Effect of calcination on catalytic activity of Au/TiO_2 catalysts on cordierite monoliths (850 000 ml.g_{cat}^{-1}.h^{-1}, 50 ppm CO, 2% air, balance H_2)

The 5 wt% Au/TiO$_2$ coated monolith yielded 100 per cent CO conversion as shown previously in Figure 44. In order to obtain a better understanding of the actual activity of this catalyst the space velocity was doubled to 1 700 l.g$_{cat}^{-1}$.h^{-1}. The results obtained are shown in Figure 46 below:

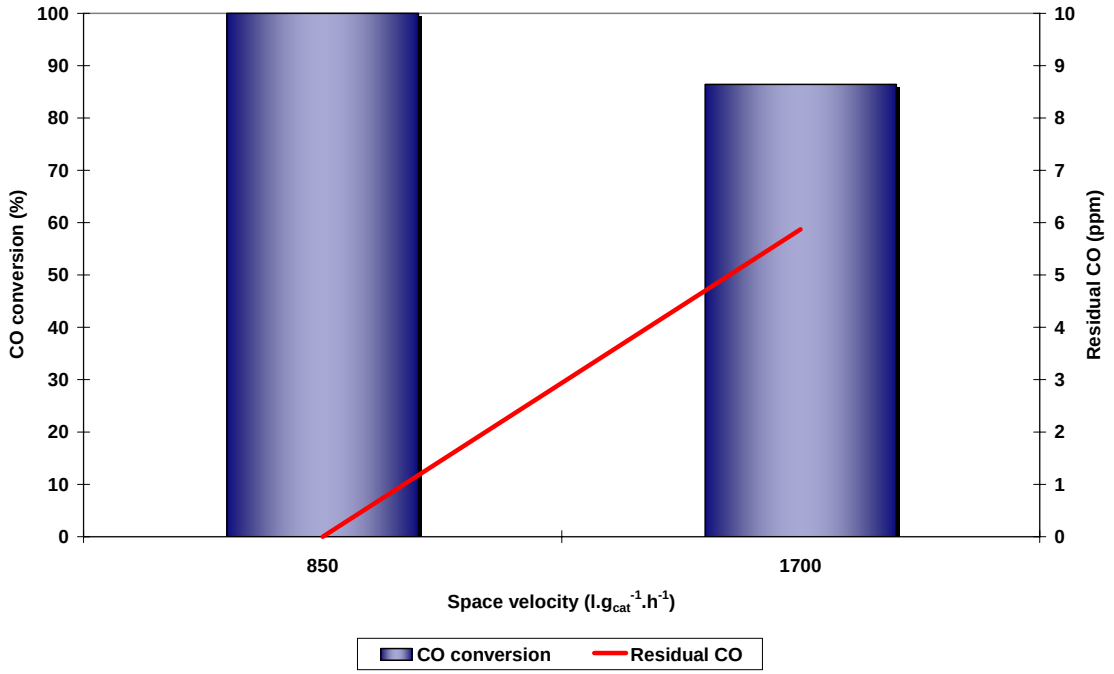

Figure 46: Influence of space velocity on CO conversion over a 5 wt% Au/TiO$_2$ catalyst on cordierite monolith (50 ppm CO, 2% air, balance H$_2$)

Even at this high space velocity the catalyst was able to achieve 86 percent CO conversion. These results look very promising in terms of technical performance. However, in order for this system to find an application in fuel cell systems it has to meet both technical and economical requirements. Thus, there will be a trade-off between the economics (amount and cost of the catalyst / gold loading) and the technical performance that can be obtained with these Au-based catalysts.

7.4 Influence of CO_2 on conversion of Au/TiO_2

The presence of CO in H_2-rich gas streams inevitably implies that CO_2 will also be present – typically at significantly higher concentrations. In order to investigate the effect of CO_2 on the activity of the Au/TiO_2 catalysts, 0.1, 0.2 and 0.5 per cent CO_2 was co-introduced with 80 ppm CO in H_2 and a 2 per cent air bleed stream. The temperature was controlled at 25°C. Results are shown in Figure 47.

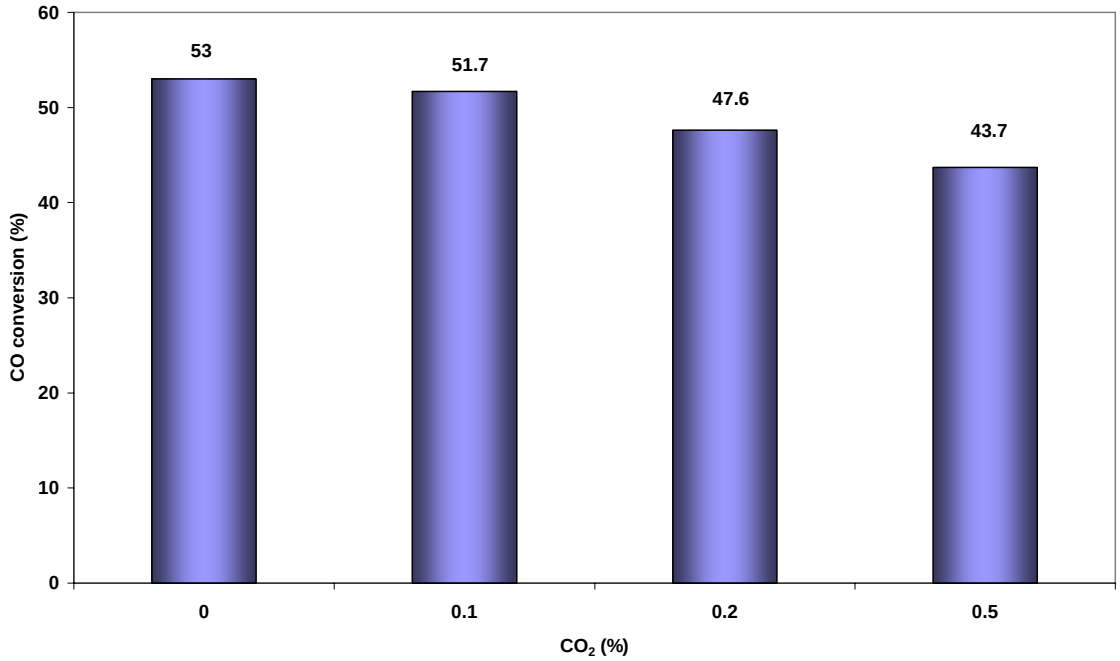

Figure 47: Influence of CO_2 on CO conversion (5 wt% Au/TiO_2 granulate catalyst, 25°C, 80 ppm CO in H_2, 2% air bleed stream, SV = 2 000 000 ml.g_{cat}^{-1}.h^{-1})

A decrease in CO conversion was observed for all the tests conducted in the presence of CO_2. However, the presence of CO_2 did not have a deleterious effect on catalytic activity, as is evident from Figure 47 and Table 6. For typical reformer systems, the ratio of CO_2:CO in the reformate is generally in the order of 20:1. If this ratio can be assumed to remain constant during further hydrogen purification steps, then the test in 0.2 per cent CO_2 is most representative of the composition expected from actual purification/ enrichment processes. From Table 6 it is evident that approximately 10 per cent of the CO conversion activity is lost at these conditions, which is relatively insignificant.

Table 6: The effect of CO_2 on CO conversion obtained over a 5 wt% Au/TiO_2 granulate catalyst (25°C, 80 ppm CO in H_2, 2% air bleed stream, SV = 2 000 000 ml.g_{cat}^{-1}.h^{-1})

%CO_2	CO conversion (%)	% decrease in CO conversion
0	53.0	0
0.1	51.7	2.5
0.2	47.6	10.2
0.5	43.7	17.5

Even though these results indicate that CO_2 has only a limited effect on catalytic activity of Au/TiO_2 (for CO oxidation at the conditions specified) it is important to determine its long-run effect on catalyst stability. This subject is elaborated on in Section 7.5.1.

7.5 Online deactivation of Au/TiO_2 granulates and Au/TiO_2 coated monoliths

Preparation and pretreatment conditions have a significant effect on the activity and stability of Au/TiO_2 catalysts [73, 74, 75]. For catalysts to find commercial application in fuel cell systems it has to operate at the necessary level of activity for at least 5000 h for automotive applications, and up to 40 000 h for stationary applications. In the following sections, possible deactivation mechanisms, such as carbonate formation, hydration of the catalyst's surface, and thermal degradation of the catalyst, are discussed.

7.5.1 Influence of Carbonate species on deactivation

The accumulation of carbonate species (CO_3^{2-}) on the active sites of gold-based catalysts has previously been identified as one of the main causes of online deactivation [47, 48]. In order to rationalize this claim, different concentrations of CO were introduced to the catalyst bed in the presence of hydrogen and a 2 per cent air bleed stream. Depending on CO conversion, this resulted in different amounts of CO_2 being formed, which, in the presence of water, can react to form carbonate species according to Equation 31.

$$H_2O + CO_2 \rightarrow 2H^+ + CO_3^{2-} \quad (31)$$

The online deactivation of 3wt% Au/TiO_2 granulate catalysts in the presence of 10, 50, 100 and 2000 ppm CO is shown in Figure 48. Significant deactivation was observed over a 20 hour test period. Online deactivation was more pronounced at lower CO concentrations, as if evident from Figure 49. This effect was in contrast to the reasoning that the formation of carbonate species (which is dependent on the amount of CO_2 formed) on the catalyst surface is the main reason for online deactivation.

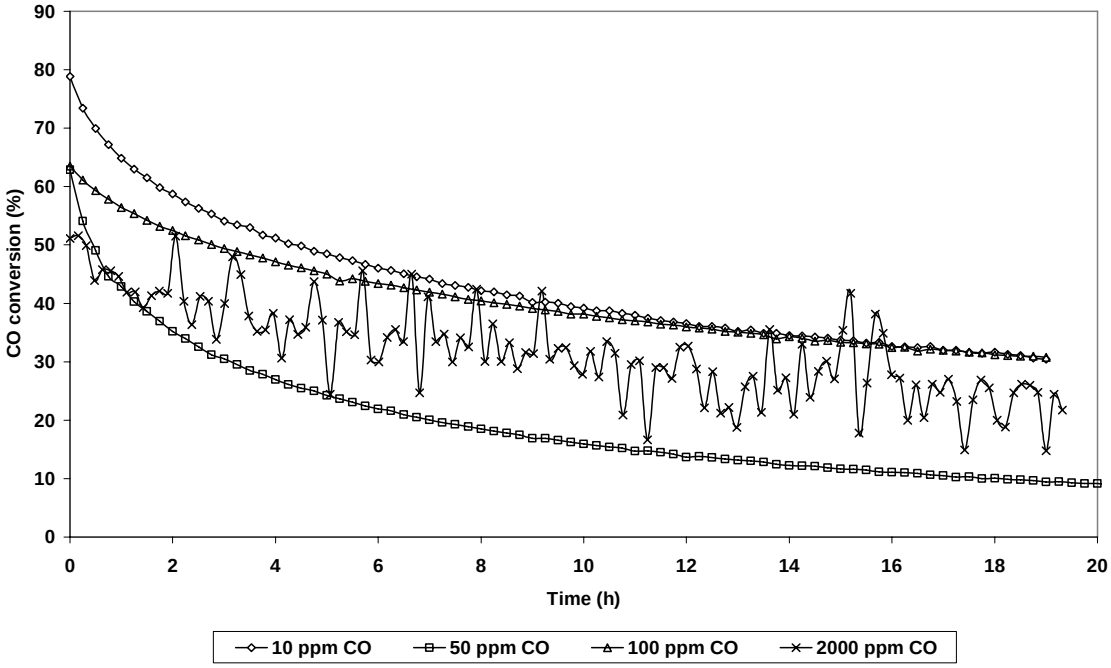

Figure 48: Influence of CO concentration on deactivation of a 3 wt% Au/TiO$_2$ granulate (+500 µm -710 µm) catalyst (2% air, balance H$_2$, SV = 1 700 000 ml.cat^{-1}.h^{-1})

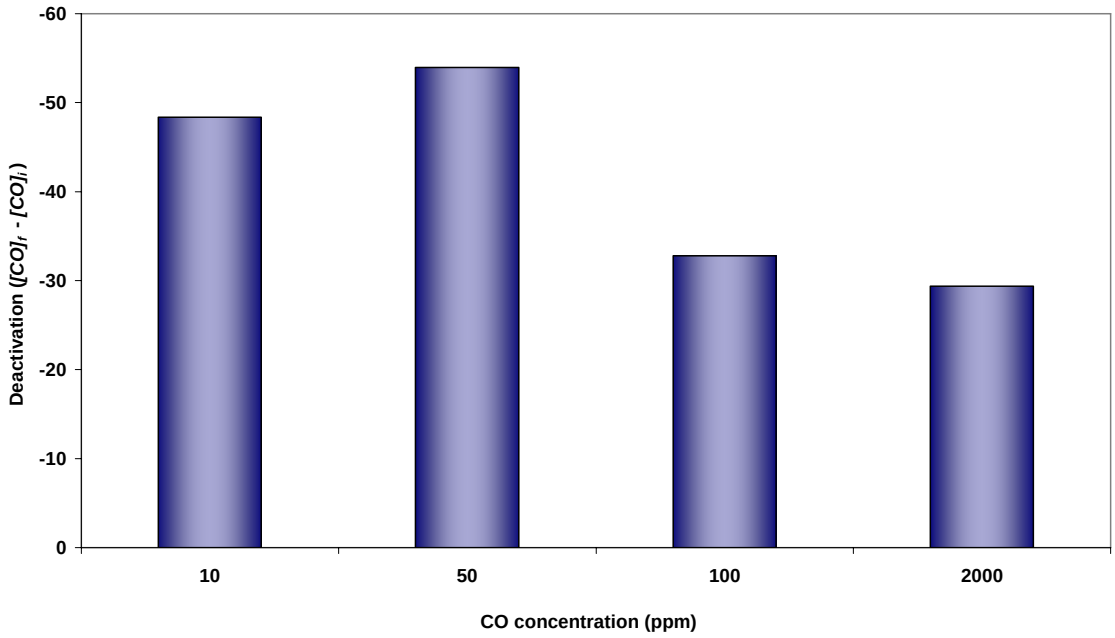

Figure 49: Influence of CO concentration in the H$_2$ feed gas on the deactivation of a 3 wt% Au/TiO$_2$ granulate catalyst (granule size +500 µm -710 µm, gas composition: 2% air, balance H$_2$, SV = 1 700 000 ml.g$_{cat}^{-1}$.h^{-1})

Even though Figure 49 confirms that there was a decrease in the overall rate of deactivation with CO concentration, it is evident from Figure 48 that deactivation occurred at different rates during the 20 hour test, especially at low CO concentrations (10, 50, and 100 ppm CO). At these CO concentrations, the initial rates (t < 8 hours) of deactivation were significantly higher than those towards the end of the test (t > 8 hours). The deactivation test with the 2000 ppm CO proved to be approximately linear throughout the 20 hour test period. To quantify the difference in the rates of deactivation during different stages of the tests, the initial rate of deactivation was compared to the final rate of deactivation for all four CO concentrations investigated. Results are shown in Figure 50. It is evident that the initial deactivation rates followed the same trend as that of the overall deactivation rates in Figure 48. However, the final rates of deactivation were approximately the same for all four tests, as shown in Figure 50 (and the slope of the curves towards the end of the tests in Figure 48).

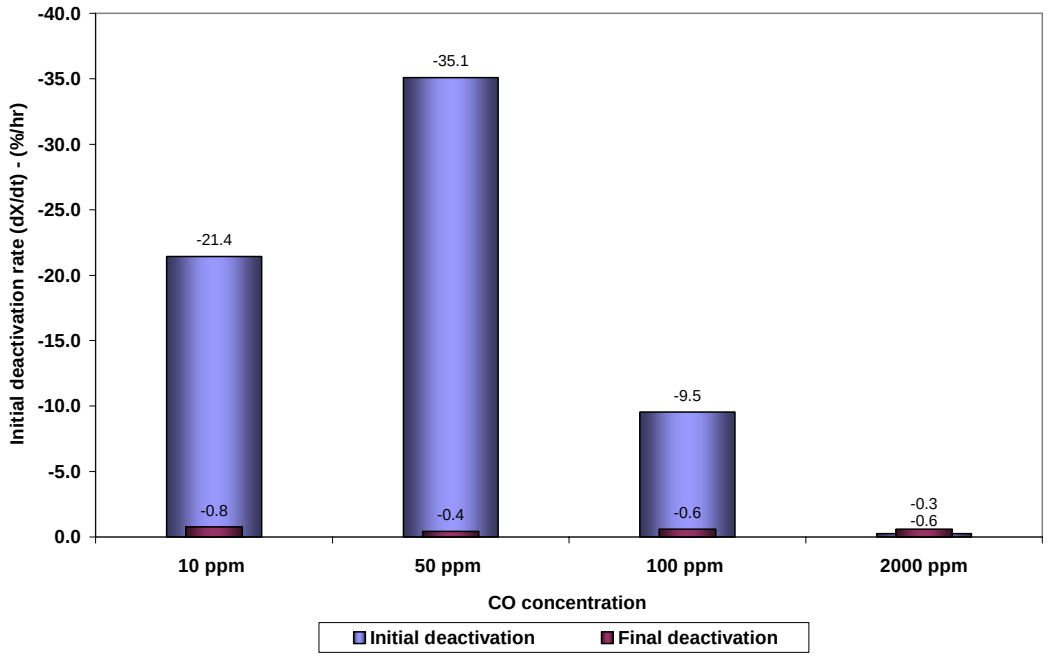

Figure 50: Influence of CO concentration on the initial and final rate of deactivation of a 3 wt% Au/TiO_2 granulate catalyst (granule size +500 µm -710 µm, gas composition: 2% air, balance H_2, SV = 1 700 000 ml.g_{cat}^{-1}.h^{-1})

The differences in the rates of deactivation might indicate that on-line deactivation of Au-based catalysts in PROX systems is more complicated than just the build-up of carbonate species on the catalyst surface. Other possibilities can include anyone, or a combination, of the following:

- carbonate species accumulating on the catalyst surface and blocking active sites,
- surface water build-up with time due to the fact that the Au/TiO_2 catalysts are not 100 per cent selective for CO oxidation, and therefore oxidize H_2 to H_2O, which may poison Au/TiO_2 catalysts by hydrating the surface and preventing oxygen adsorption [76] (even though some authors report that water increases the rate [77]), or it might impose mass transfer limitations of the reactant gases to and from the reaction interface,
- gold particle size growth with time on-line,
- trace amounts of metal-carbonyl species in CO containing gas cylinders that adsorb onto the catalyst surface and blocking active sites; this effect was eliminated by incorporating a zeolite molecular sieve in the CO feed-line to the catalyst.

Even though the initial investigation indicated that the formation of carbonate species might only partially be responsible for online deactivation, it was important to determine the fraction of deactivation attributable to the formation of carbonates at the active sites of the gold based catalyst. In an attempt to quantify this effect, 80 ppm CO and 2 per cent air in H_2 was introduced to 0.015 g of a 3 wt% Au/TiO_2 powder catalyst at 1125 ml.min^{-1}. A carbon mass balance was performed by monitoring the CO and CO_2 concentrations using a PDHID. The CO concentration in the CO contaminated H_2 gas cylinder was confirmed using the PDHID while bypassing the catalyst reactor. This CO concentration was used as the $[CO]_{in}$ value (see Equation 13) from where the CO conversion was calculated. Typically, the difference between the concentration of CO in the feed gas and the exit gas should yield the concentration of CO_2 formed, as shown in Equation 32.

$$[CO]_{in} - [CO]_{out} = [CO_2]_{formed} \quad (32)$$

Based on this principle, the theoretical amount of CO_2 that should be formed, given a specific CO conversion, was compared to the CO_2 concentration detected by the PDHID. The difference between these two values was used as an estimate of the amount of CO_2 that was unaccounted for, i.e., CO_2 that either adsorbed or desorbed from the catalyst surface. The results obtained are shown in Figure 51. For the missing/additional CO_2 measurement, presented on the secondary Y-axis, a positive value implies that a quantity of CO_2 is missing (i.e. PDHID analysis shows less CO_2 than what theoretically should have formed). A negative value implies that additional CO_2 was formed (i.e. PDHID analysis shows more CO_2 than what theoretically should have formed). From the former it can be assumed that the missing CO_2 was adsorbed on the catalyst surface, probably at the Au-TiO_2 interface where it was formed, while the latter may represent desorption of CO_3^{2-} species from the catalyst's surface as CO_2 (this process is possible through the enhanced decomposition of carbonate species to thermally less stable bicarbonate species in the presence of H_2O, as discussed in Section 2.1.4). The desorbed CO_2 might be from a different source than from the CO_2 adsorbed during the CO conversion reaction. For example, during catalyst preparation (Section 5.2.1) Na_2CO_3 is used to adjust the pH, during which CO_3^{2-} species is readily formed on the catalyst's surface, which is not entirely removed during the washing process. Therefore, it might be possible that these CO_3^{2-} species desorb during online operation in the presence of H_2.

Taking the above arguments into account, there might be a continuous adsorption of CO_2 at the active sites (however decreasing with time as active sites become saturated with CO_3^{2-}, and until equilibrium adsorption is established). There might also be a continuous desorption of CO_3^{-2} from the catalyst's surface (not necessarily from the active sites). Thus, in region A of Figure 51, there is a net adsorption of CO_2, whereas a net desorption of CO_3^{2-} as CO_2 occurs in region B. This can possibly explain why there is a continuous decrease in catalytic activity with time, even though analysis indicates that CO_2 is released from the surface during the later stages of the test (region B).

Although the afore mentioned explanations are not irrefutable, a significant correlation exists between the rate of deactivation and the amount of CO_2 that is adsorbed onto the

catalyst – presumably as carbonates. Significant deactivation was observed within the first 3 hours of operation, which corresponds to the time period in which CO_2 seemingly adsorbed on the active sites of the catalyst and when the rate of deactivation was the highest. After 8 hours, the rate of deactivation decreased significantly and appeared to be linear.

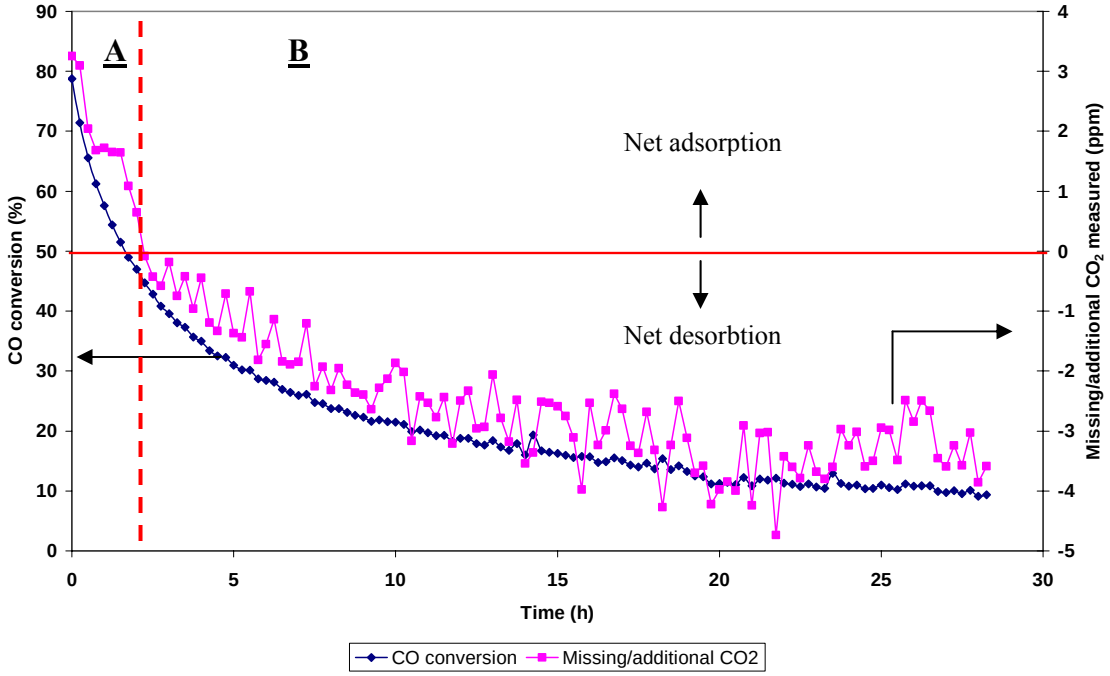

Figure 51: Correlation between catalyst online deactivation and unaccounted CO_2 (80 ppm CO, 2% air, balance H_2, 4 500 000 ml.g_{cat}^{-1}.h^{-1}, 3 wt% Au/TiO_2).

Following these results, it seemed applicable to control the amount of CO_2 introduced into the system and to conduct a pre and post test surface analysis on the Au/TiO_2 samples in order to determine the degree of carbonate accumulation on the catalyst's surface during operation. As in Section 7.4, CO_2 was introduced into the system at a CO_2:CO ratio of approximately 20:1. The test was conducted at 25°C over a 23 hour period. The influence of CO_2 on the rate of deactivation is shown in Figure 52, and the FTIR pre and post test surface analysis in Figures 53 and 54. As is evident from Figure 52, the presence of 2000 ppm CO_2 in the reaction gas mixture caused the initial CO conversion to decrease by approximately 8 per cent, which is consistent with the result in Section 7.4. However, the overall rate of deactivation was lower for the CO_2 containing

test. Also, the results from the CO_2 and non-CO_2 containing tests seemed to converge after approximately 13 hours and remained the same for the remainder of the test. This result might suggest that there is an equilibrium CO_2 and CO_3^{2-} adsorption limit, which is reached within the first few hours of operation (13 hours in this case), where after the rate of deactivation is as a result of another deactivation mechanism(s).

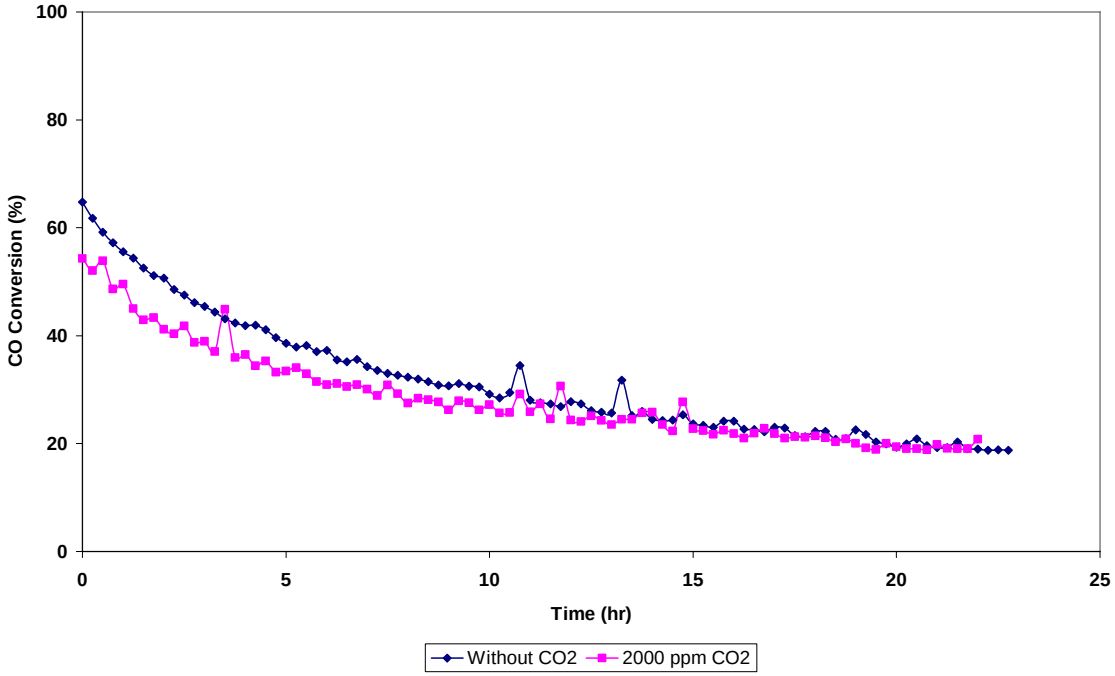

Figure 52: Influence of 2000 ppm CO_2 on deactivation of a 5wt% Au/TiO_2 granulate catalyst (80 ppm CO, balance H_2, 2% air bleed, SV = 2 000 000 ml.g_{cat}^{-1}.h^{-1}, 25°C).

Figure 53a shows the FTIR spectra of Au/TiO_2 before and after the 23 hour CO oxidation tests. An intense broad band at 3600-3000cm^{-1} in the OH-stretching region typifies this spectrum. In the 1800-1100 cm^{-1} region, an intense band at 1612 cm^{-1} can be observed which is due to δ(HOH) [78, 79]. The medium- to low-intensity bands at 1410 and 1196 cm^{-1} may be assigned to either monodentate or uncoordinated carbonate species [80], or to bicarbonate species [81] adsorbed on the support, although carboxylate species also have absorption bands in the same region [78]. In Figure 53b, the three spectrums were aligned to overlap in the 2800-2000 cm^{-1} region, the region most representative of the base-line spectra. This was done in order to accurately compare the difference between the spectrums, and the possible change in surface characteristics.

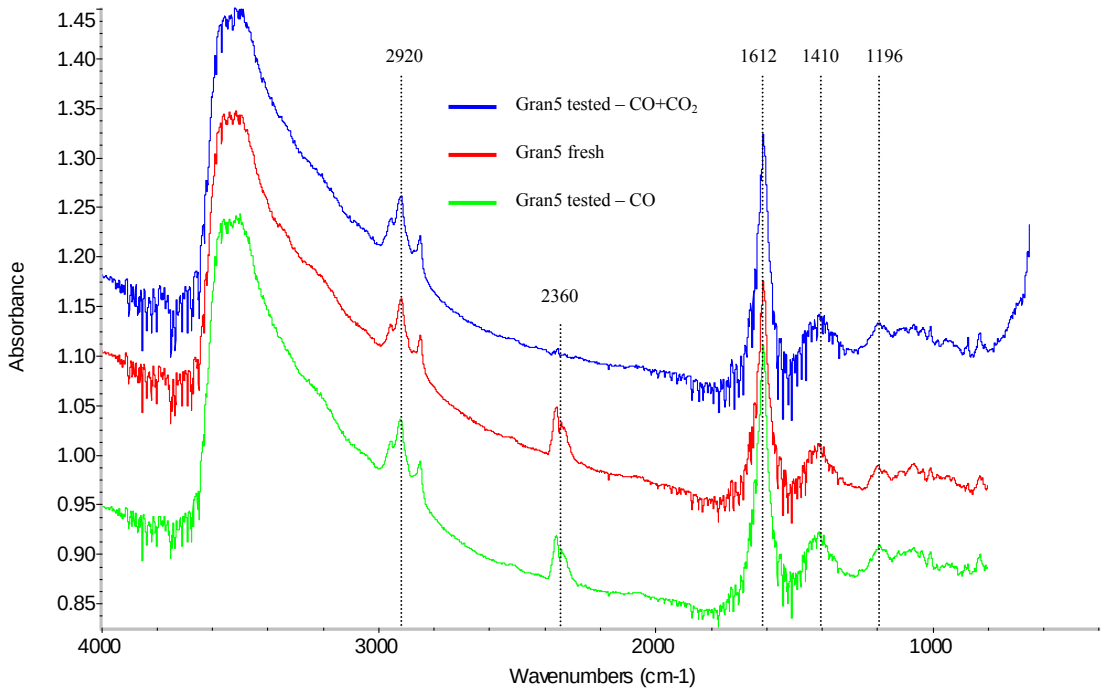

a

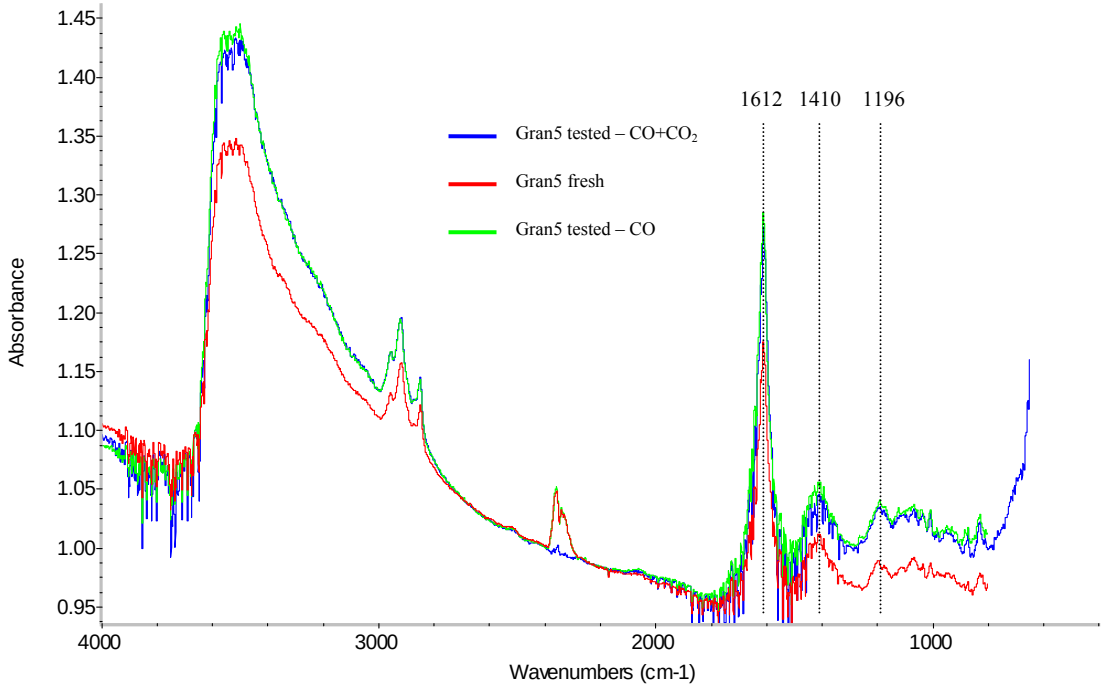

b

Figure 53: FTIR spectra recorded before and after CO oxidation over Au/TiO$_2$ (5 wt% Au/TiO$_2$, CO oxidation tests: 80 ppm CO in H$_2$, 2% air, with or without 0.2% CO$_2$, SV = 2 000 000 ml.g$_{cat}^{-1}$.h^{-1}, 25°C, 23 hours online operation). Figure a) spaced view, b) aligned view.

From Figure 53a it is evident that both the Au/TiO_2 catalysts tested in 80 ppm CO, with and without CO_2, yielded similar spectrums, while they were distinct compared to the spectra of the untested catalyst. The results clearly show a marked accumulation of H_2O and a marginal increase in the amount of adsorbed CO_3^{2-} species during online CO oxidation. Note that the baseline in the 1500-800 cm^{-1} region was lower for the fresh catalyst than for those tested, which might be due to the fact that the tested samples were removed from the CO oxidation rig and placed in the IR-analyser. Even though this change-over only took a few minutes, it is possible that it might have affected the baseline characteristics. Comparison of the spectrums in this region on the same base-line is shown in Figure 54, from where it is evident that only a small amount of carbonates adsorbed during the CO oxidation tests.

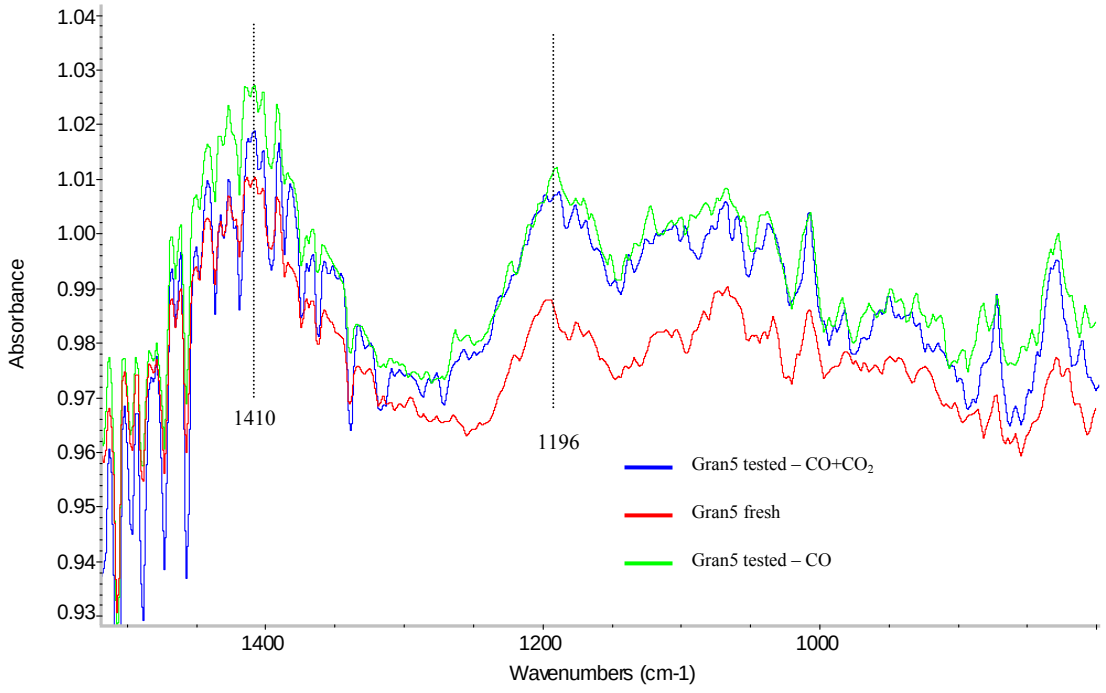

Figure 54: FTIR spectra recorded (1525 – 800 cm^{-1}) before and after CO oxidation over Au/TiO_2 (5 wt% Au/TiO_2, CO oxidation tests: 80 ppm CO in H_2, 2% air, with or without 0.2% CO_2, SV = 2 000 000 ml.g_{cat}^{-1}.h^{-1}, 25°C, 23 hours online operation).

These results indicated that hydration of the catalyst's surface might have a greater effect on deactivation than the build up of carbonate species. In an attempt to eliminate the hydration effect, the catalyst bed was heated to 60°C in a temperature controlled water bath, while the inlet gas temperature remained constant at 25°C. The effect of this change in operating conditions is shown in Figure 55. It is evident that the increase in temperature had a limited effect on deactivation. The rate of deactivation seemed to have slowed for the heated catalyst toward the end of the 20 hour deactivation test. Nevertheless, deactivation was still pronounced. In an attempt to dry the catalyst, N_2 was introduced to the heated catalyst bed (60°C) at 960 ml.min^{-1} for 24 hours. However, from Figure 55 it is evident that this had no distinct effect on deactivation.

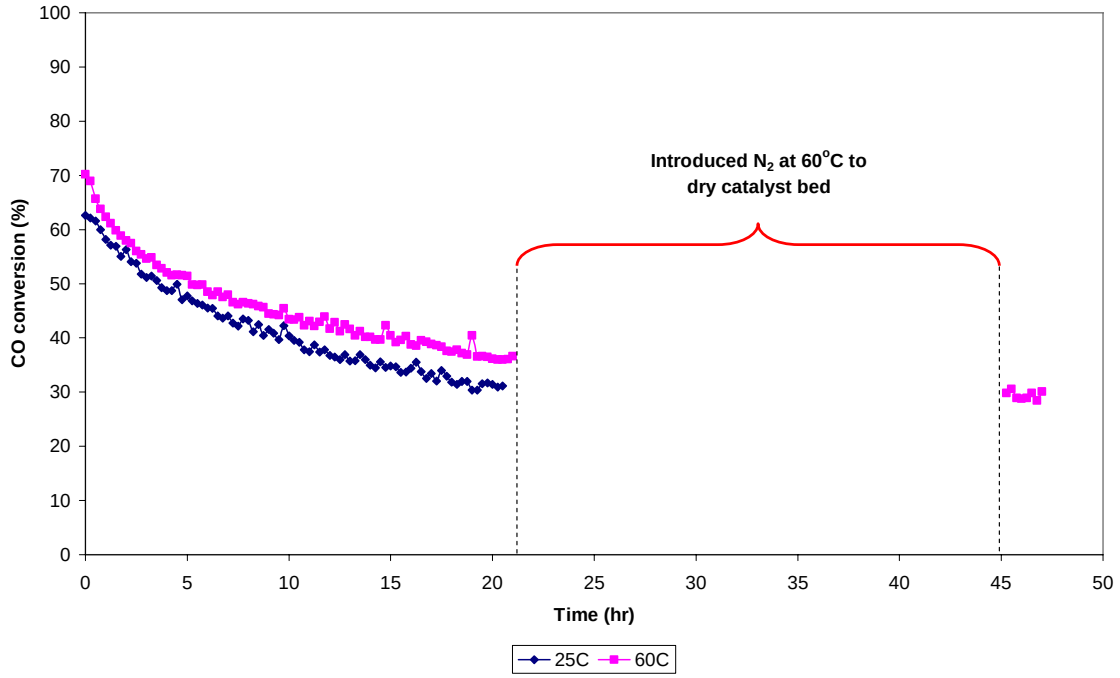

Figure 55: Influence of catalyst bed temperature and drying on the deactivation of a 5wt% Au/TiO$_2$ granulate catalyst (50 ppm CO in H$_2$, 2% air, 2000 ppm CO$_2$, SV = 2 000 000 ml.g$_{cat}^{-1}$.h^{-1}).

It is evident that the perceived deactivation effect due to the accumulation of water on the catalyst's surface was not the dominating deactivation mechanism.

The question that remained at this stage of the investigation was whether deactivation of the Au/TiO_2 catalysts is due to an intrinsic transformation in the catalytic properties of Au/TiO_2. An example of such a transformation is the change in the oxidation state of the gold species, i.e. Au^{x+} or Au^0. Various researchers have different opinions about what they believe the active form of gold is [34, 40, 41, 44]. Bond and Thompson [45] proposed an interesting mechanism, suggesting that it is not exclusively ionic or metallic gold that cause gold-based catalyst to be active, but that the presence of both may be necessary. Visco and co-workers [82] have also observed a decrease in activity during online operation and have ascribed this effect to the reduction of Au^{x+} ions by carbon monoxide to Au^0, although an initial increase in activity has been observed before reaching a stable high level [83], confirmed by work reported later in Section 7.5.2. The deactivation mechanism due to the reduction of ionic gold to metallic gold by carbon monoxide in air is of concern since, for the application in this study, the gas mixture will consists mainly of a reducing gas, namely hydrogen. If the mechanism proposed by Bond and Thompson is accurate, and if the deactivation effect proposed by Visco *et al*. is correct, then it might be possible that the apparent deactivation seen in the present investigation is due to an intrinsic, maybe irreversible, transformation in the catalytic / chemical properties of Au/TiO_2. To investigate this possibility, a 5 wt% Au/TiO_2 catalyst was exposed to a gas mixture similar to that in Figure 55 (50 ppm CO, 2000 ppm CO_2, balance H_2 and a 2 per cent air bleed) and the initial CO conversion was measured, where after the CO, CO_2, and air was removed and 5N pure H_2 was introduced for 12 hours (thereby eliminating the possibility of deactivation due to the accumulation of carbonates or due to surface hydration). After 12 hours in pure H_2 the initial gas mixture was re-introduced and the CO conversion measured. As is evident from Figure 56, significant deactivation occurred, much more severe than that presented in Figure 55. This clearly indicates that, for this system, the accumulation of carbonates and water has minor effects on deactivation. The results in Figure 56 might therefore indicate that the proposed "balance" between ionic and metallic gold [45] is distorted during online operation in a reducing atmosphere. What supports this hypothesis even more is the fact that deactivation is more pronounced in the absence of oxygen, possibly due to faster reduction of the Au^{x+} to Au^0, as shown in Figure 57.

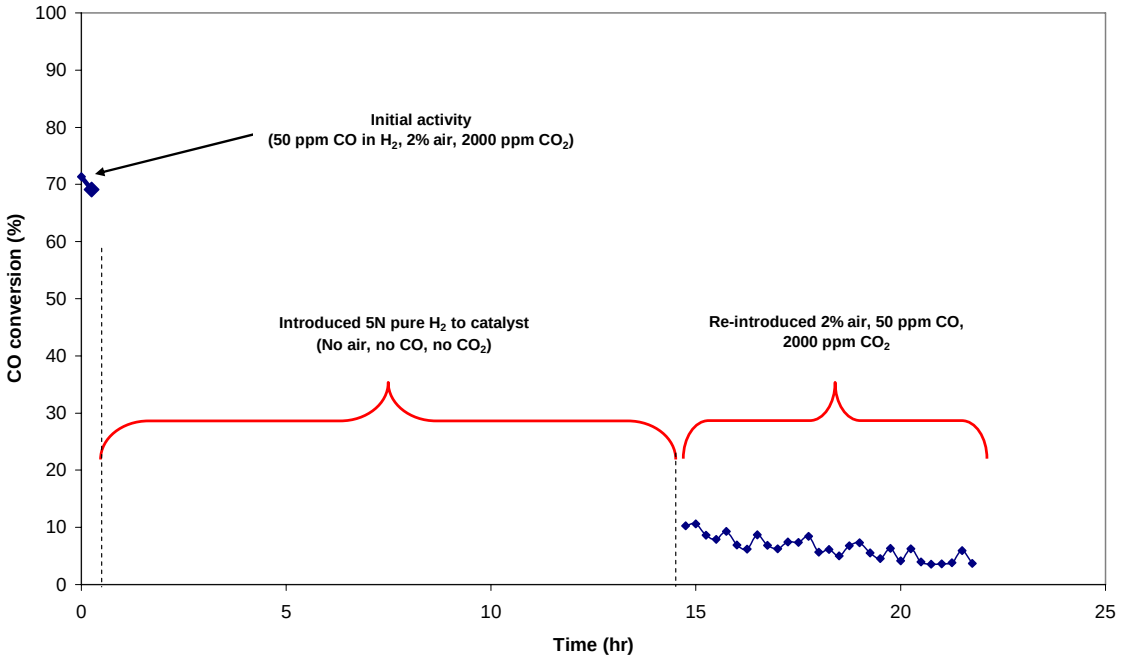

Figure 56: Influence of 12 hour 5N H_2 treatment on catalytic activity of a 5 wt% Au/TiO_2 granulate catalyst (CO conversion from gas mixture containing 50 ppm CO in H_2, 2% air, 2000 ppm CO_2, SV = 2 000 000 $ml.g_{cat}^{-1}.h^{-1}$, 25°C).

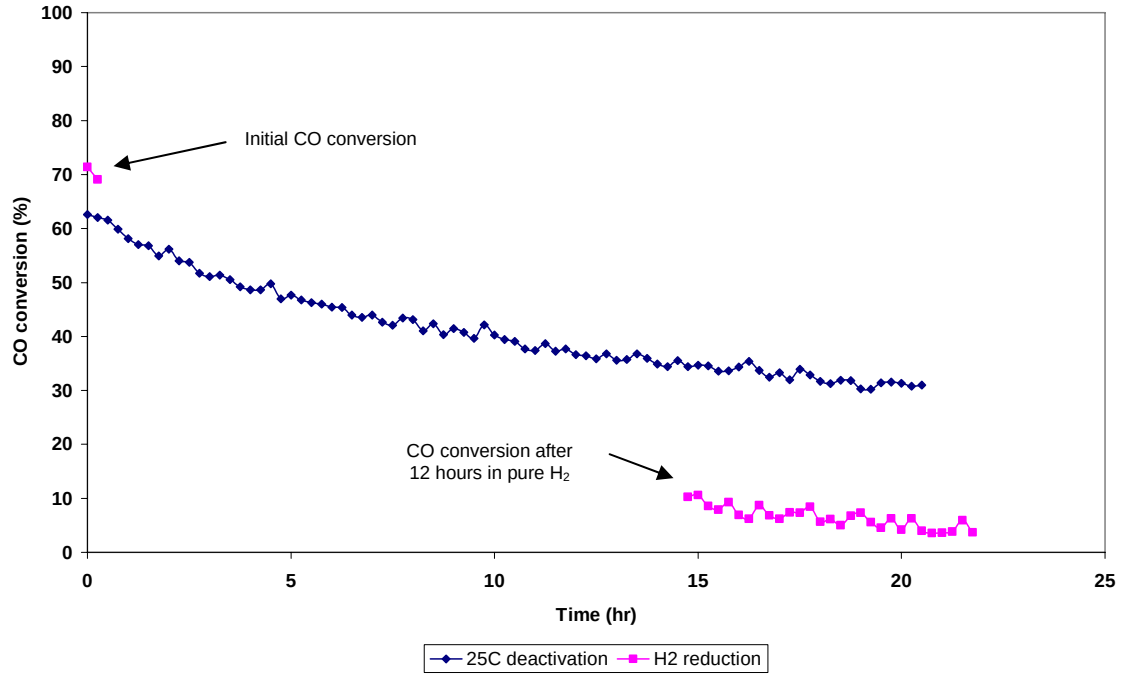

Figure 57: Difference in the rate of deactivation of a 5 wt% Au/TiO_2 catalyst in the presence and absence of oxygen (50 ppm CO, 2000 ppm CO_2, balance H_2, 2% air bleed, SV=2 000 000 $ml.g_{cat}^{-1}.h^{-1}$, 25°C).

If the hypothesis discussed above is valid, then reactivation of the catalyst might be possible in an oxidizing atmosphere by withdrawing electrons from perimeter site gold atoms, thereby re-establishing the proposed "balance" between Au^0 and Au^{x+}. This was investigated by systematically introducing air, oxygen, and ozone (Ozone Industries Ltd. AirMaid 3290, 100 mg O_3/hr) to the catalyst after deactivation ("over-reduction") in pure H_2. The results are shown in Figure 58, from where it is evident that the H_2 deactivation effect observed in Figure 56 has been confirmed. A 3 hour treatment in 45 $ml.min^{-1}$ air (period 21 – 23 hours in Figure 58) had a very small effect on reactivation. However, on-line deactivation continued when the test gas mixture was reintroduced (period 23 – 25 hours in Figure 58). Significant reactivation was observed following a 18 hour treatment in 45 $ml.min^{-1}$ pure oxygen. The CO conversion increased from 18 per cent to over 43 per cent. In addition, the online stability appeared to have increased following the 18 hour O_2 treatment (period 42 – 45 hours on Figure 58). The activity was further increased to 50 per cent after a 2 hour treatment in 45 $ml.min^{-1}$ O_3. These results support the hypothesis that both Au^0 and Au^{x+} are essential for CO oxidation.

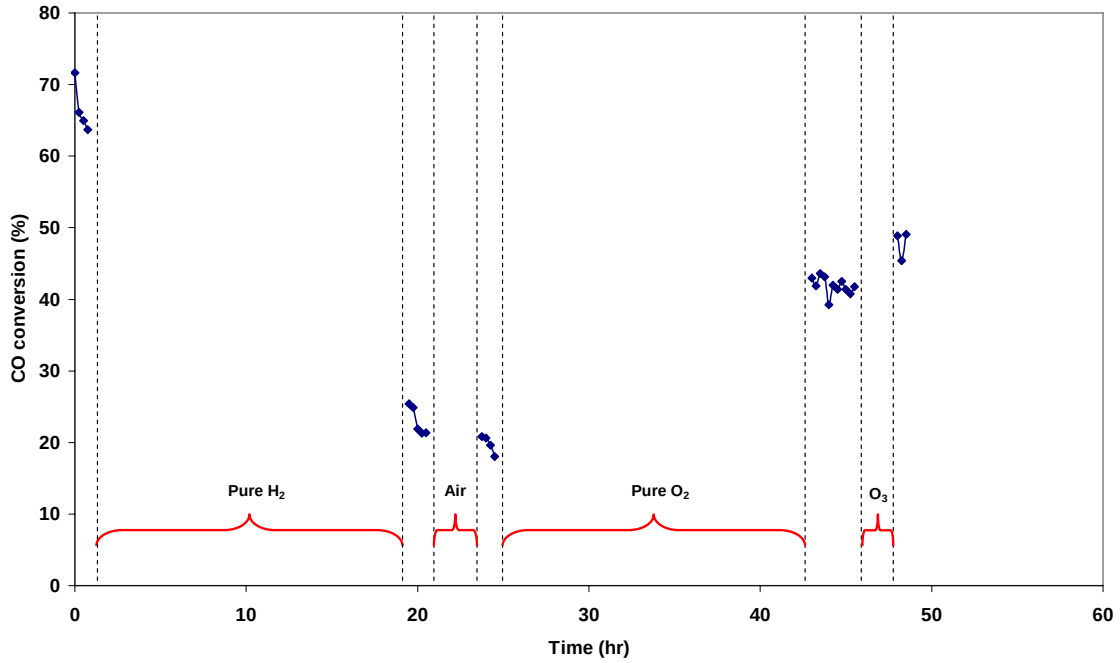

Figure 58: Influence of reducing/oxidizing atmosphere on the catalytic activity of a 5 wt% Au/TiO_2 granulate catalyst (50 ppm CO, 2000 ppm CO_2, balance H_2, 2% air bleed, SV = 2 000 000 $ml.g_{cat}^{-1}.h^{-1}$, 25°C).

7.5.2 Deactivation due to gold particle size growth during online operation

The importance of small gold particles for catalytic activity has been discussed in Section 2.1. Gold particles can typically increase in size due to sintering and/or agglomeration, although the former is only expected to occur at elevated temperatures. Even though a strong argument for the mechanism of deactivation was presented in Section 7.5.1, it was important at this stage of the investigation to determine whether a change in the particle size was a significant component of the overall deactivation effect. In order to elucidate this possibility, the catalyst used in Figure 56 was investigated under a TEM prior to and after testing. The results are shown in Figures 59 A and B. The results indicated that, in contrast to expectations, the particles decreased in size during testing. A possible explanation is that the majority of the gold particles in the fresh sample were still in an oxide-, hydroxide-, oxy-hydroxy-, or chloro-complex state, which is typical of unreduced Au-based catalysts prepared via deposition-precipitation. Some of these gold complexes were possibly reduced to Au^0 during online operation in H_2 during which oxides and hydroxides were removed as water; and, in the case of chloro species, as HCl.

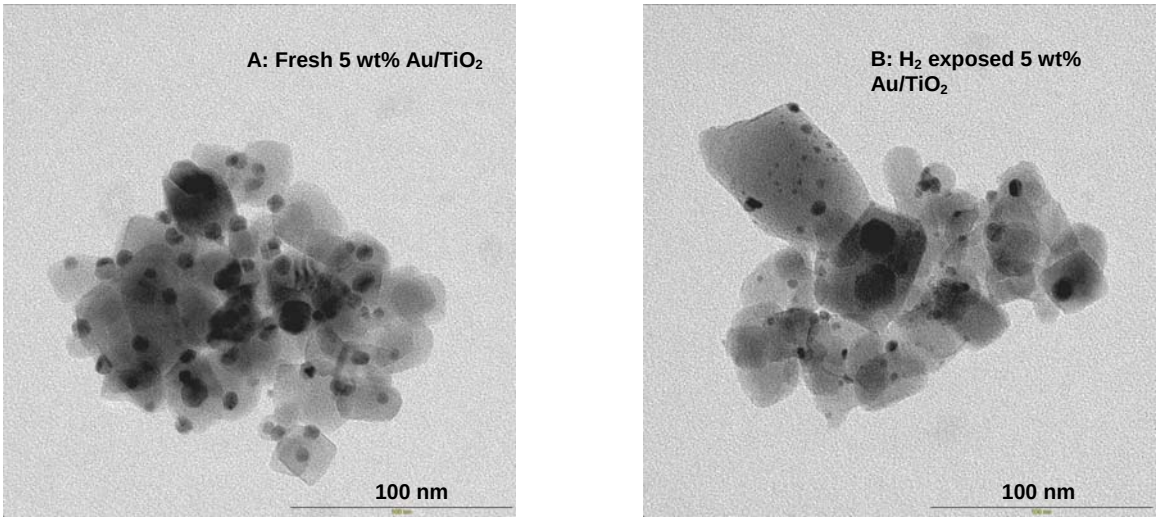

Figure 59: TEM images of: A) fresh 5 wt% Au/TiO_2 granulate catalyst, and B) the same 5 wt% Au/TiO_2 catalyst exposed to 1000 ml.min^{-1} 5N pure H_2 for 12 hours at 25°C.

Although no intrinsic increase in the gold particle size was observed during online operation, the results presented are insufficient to conclude that particle size growth did, or did not, contribute to online deactivation.

7.5.3 Influence of catalyst bed temperature on activation

Of interest was the online stability results obtained over a 3 wt% Au/TiO_2 coated monolith operating in 2000 ppm CO, 2% air, balance H_2. In contrast to the granulate catalyst, CO conversion over the monolith increased with time online, as shown in Figure 60. The reason for the difference in the online characteristics of the Au/TiO_2 granules and the Au/TiO_2 coated monoliths was not well understood at this stage. One possible explanation for this effect might be that the online activation of powder catalysts, granulate catalysts, and monoliths are distinct due to a difference in the online heating characteristics of the different catalyst systems. In order to investigate this temperature effect on the activation characteristics, a 3 wt% Au/TiO_2 powder catalyst was placed in a packed bed U-tube reactor and compared with the monolith in Figure 60. The results are shown in Figure 61 (Note the difference between the scale of the x-axis for Figures 60 and 61).

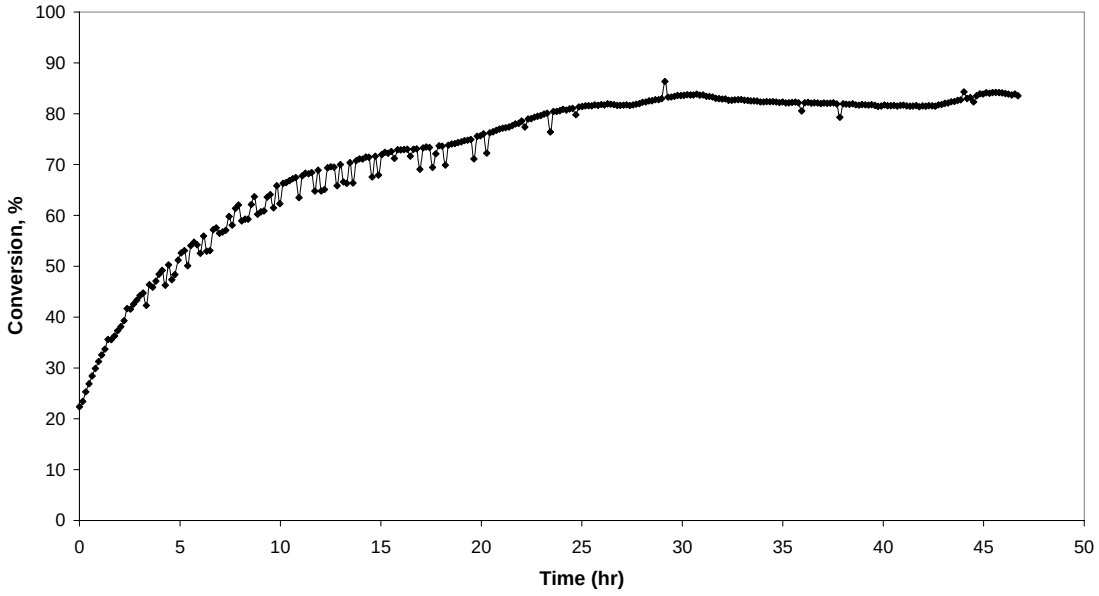

Figure 60: Influence of online operation on catalytic activity of a 3wt% Au/TiO_2 coated monolith (2% air bleed, 2000 ppm CO, balance H_2, SV = 850 000 ml.g_{cat}^{-1}.h^{-1}, 25°C)

It is evident that Figures 60 and 61 follows the same activation trend. However, in the case for the packed bed Au/TiO_2 catalyst powder, the catalyst's activity peaked after approximately 25 seconds compared to 30 hours for the monoliths system. The activation test with the powder catalyst was repeated while monitoring the catalyst bed temperature, as shown in Figure 62. It is evident that the bed heats up to 53°C within the first 50 seconds of operation, while the monolith temperature stays approximately constant at room temperature during operation. This is because the heat loss from a packed bed of powder catalyst is significantly lower than for catalysts dispersed on monoliths. The conclusion is that both the catalyst systems undergo an initial activation period, possibly due to an initial reduction of Au^{x+} to Au^0 until an optimum balance is reached; the rate of which is temperature dependent. Operating at higher temperatures results in rapid activation for powder catalysts, while the lower operating temperature of the monoliths result in significantly slower activation.

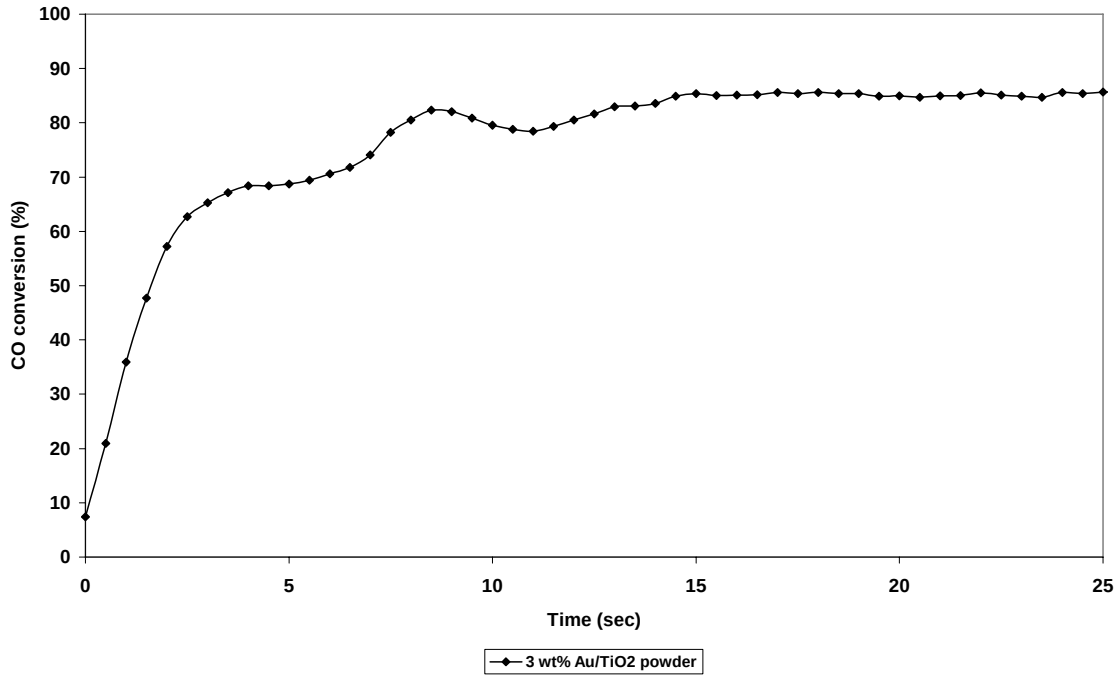

Figure 61: Online activation of a 3 wt% Au/TiO_2 nano-powder catalyst (2% air bleed, 2000 ppm CO, balance H_2, SV = 2 500 000 ml.g_{cat}^{-1}.h^{-1}, analysis via infra-red (IR) analyser).

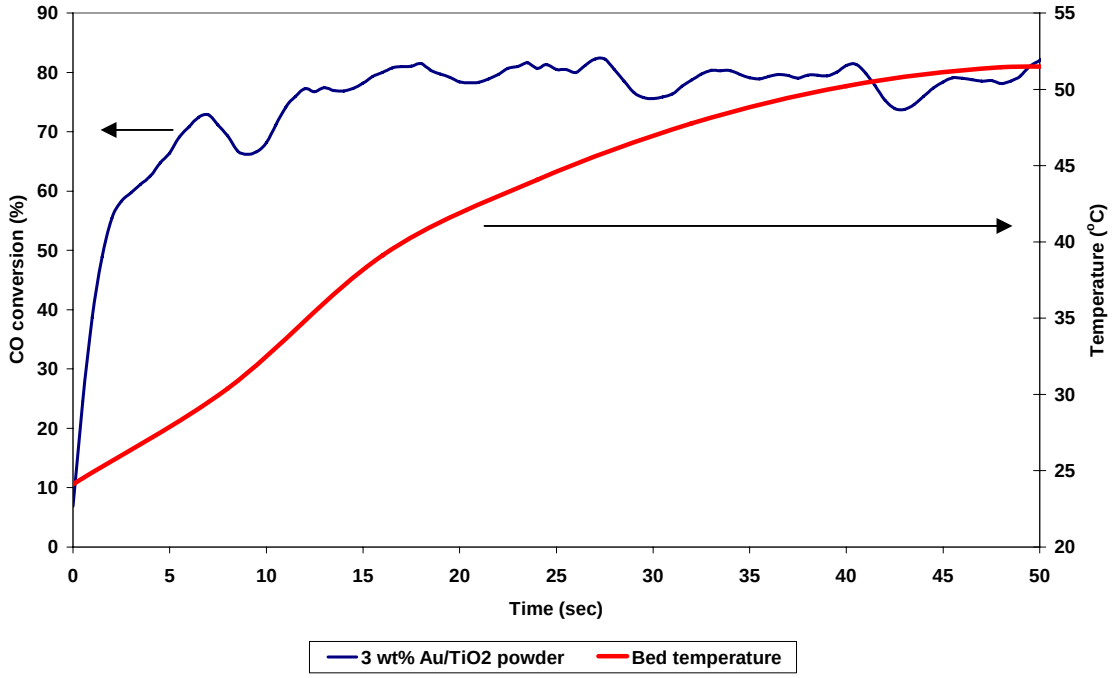

Figure 62: Temperature effect during online activation of a 3 wt% Au/TiO$_2$ nano-powder catalyst (2% air bleed, 2000 ppm CO, balance H$_2$, SV = 2 500 000 ml.g$_{cat}^{-1}$.h^{-1}, analysis via infrared analyser).

7.6 Electrochemical investigation

The results in Sections 7.2 and 7.3 clearly indicated that the Au/TiO$_2$ catalysts were able to remove significant amounts of CO from H$_2$-rich gas streams with a 1 or 2 per cent air bleed stream. Following these results, the influence of the Au/TiO$_2$ catalysts on the CO tolerance of an actual single cell fuel cell system (Johnson Matthey Technology Center, JMTC) was investigated, and the results compared with the known CO tolerance technologies mentioned in Section 1.6. These CO tolerant technologies were used as benchmarks for the performance of the proposed Au/TiO$_2$ PROX system. In sections 7.6.1, 7.6.2, and 7.6.3 the respective CO tolerances of the Johnson Matthey Pt/C, PtRu/C, and PtMo/C anodes in 1000 and 100 ppm CO are reported. The influence of a 3 wt% Au/TiO$_2$ coated monolith PROX system on the CO tolerance of these anodes is also reported.

7.6.1 Pt/C

The influence of 1000 ppm CO with and without the Au/TiO_2 PROX system on the performance of a 0.39 mg Pt.cm^{-2} Pt/C anode is shown in Figure 63. As expected, the Pt/C anode did not show any tolerance against CO poisoning, even with the introduction of a 2 per cent air bleed stream. In contrast, no performance loss was observed over a 1 hour test period with the Au/TiO_2 PROX system prior to the fuel cell. To exclude the possible influence of varying ohmic overpotential losses of the fuel cell, Figure 63b (Appendix IX) shows the resistance compensated potential over the same 1 hour test period.

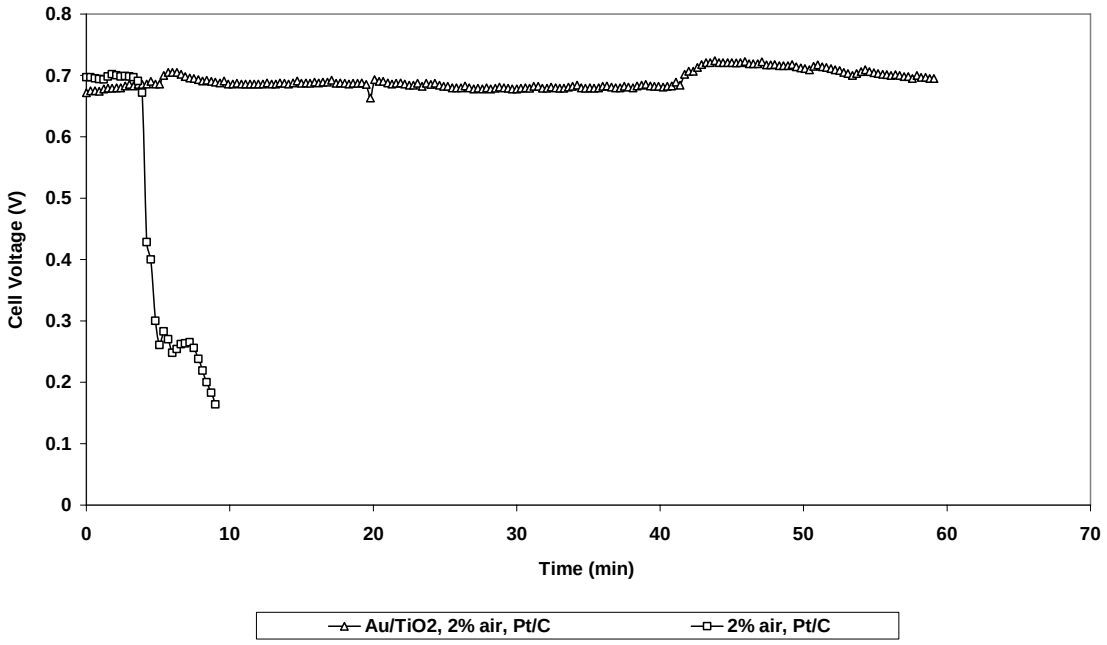

Figure 63: CO tolerance of a 0.39g Pt.cm^{-2} Pt/C anode with and without a 3wt% Au/TiO_2 coated monolith PROX reactor (1000 ppm CO, 0.5 A.cm^{-2}, 1.5x stoichiometric H_2 flow rate, SV over Au/TiO_2 catalyst 250 000 ml.g_{cat}^{-1}.h^{-1}, catalyst chamber at 25°C, cell temperature at 80°C, 0.84 mgPt.cm^{-2} Pt/C cathode).

Figure 64 shows the influence of 100 ppm CO on the performance of the Pt/C anodes. The cell potential decreased due to poisoning in the absence of the PROX system and an

air bleed stream. However, of interest is the fact that significant CO tolerance was obtained when a 2 per cent air bleed was introduced in the absence of the PROX system. This result is inconsistent to previously published results [16]. Also, when compared to the performance of PtRu/C in similar conditions (section 7.6.2) this result seems anomalous. The presence of the Au/TiO$_2$ PROX system yielded superior results, as is evident from Figure 64.

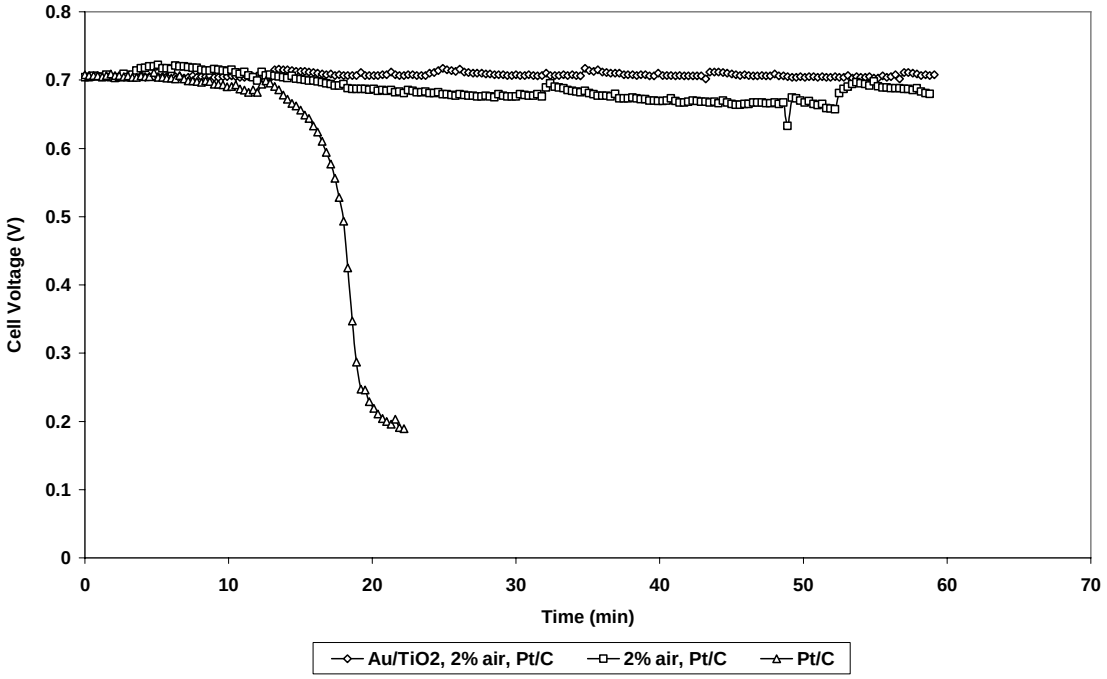

Figure 64: CO tolerance of a 0.39 mg Pt.cm^{-2} Pt/C anode with and without a 3wt% Au/TiO$_2$ coated monolith PROX reactor (100 ppm CO, 0.5 A.cm^{-2}, 1.5x stoichiometric H$_2$ flow rate, SV over Au/TiO$_2$ catalyst 330 000 ml.g$_{cat}^{-1}$.h^{-1}, catalyst chamber at 25°C, cell temperature 80°C, 0.84 mg Pt.cm^{-2} Pt/C cathode).

7.6.2 PtRu/C

It is typically expected that PtRu/C anodes will yield better CO tolerance than Pt/C anodes. Again the influence of 1000 and 100 ppm CO on the electrochemical performance of the fuel cell with and without the Au/TiO$_2$ PROX system was

investigated. The results are shown in Figures 65 and 66 (the resistance compensated potential versus time graphs are presented in Appendix IX).

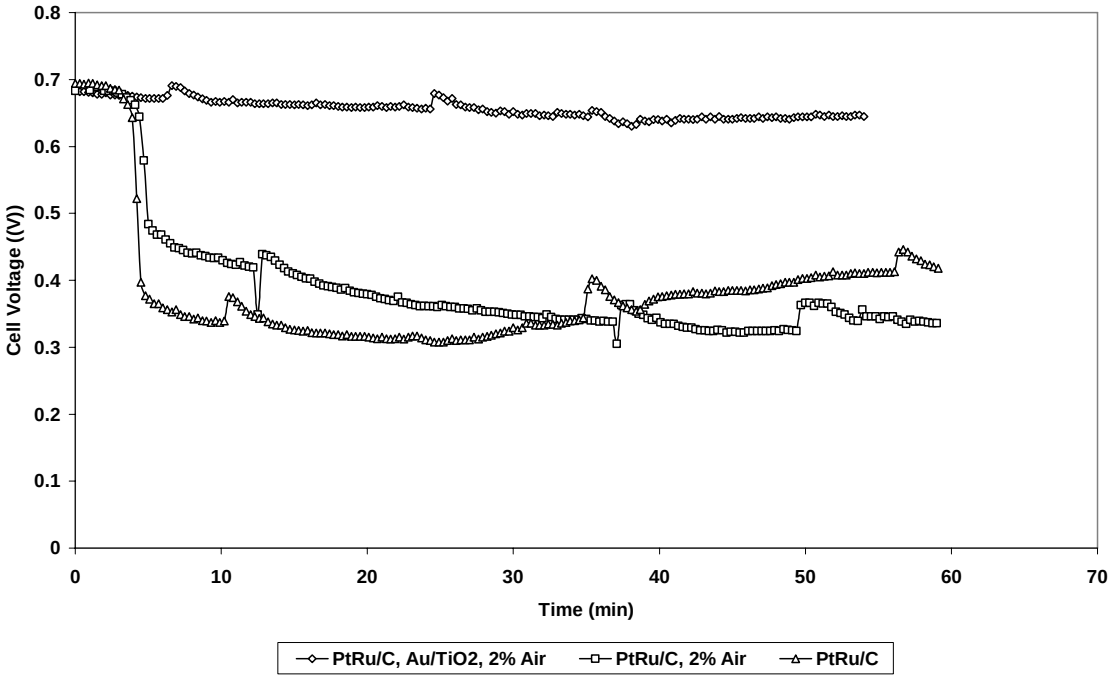

Figure 65: CO tolerance of a 0.5 mg Pt.cm^{-2} PtRu/C anode with and without a 3wt% Au/TiO$_2$ coated monolith PROX reactor (1000 ppm CO, 0.5 A.cm^{-2}, 1.5x stoichiometric H$_2$ flow rate, SV over Au/TiO$_2$ catalyst 250 000 ml.g$_{cat}^{-1}$.h^{-1}, catalyst chamber at 25°C, cell temperature 80°C, 0.84 mg Pt.cm^{-2} Pt/C cathode).

The 0.5 mg Pt.cm^{-2} PtRu/C anode yielded significant CO tolerance compared to the Pt/C anode in the presence of 1000 ppm CO with and without an air bleed stream. Nevertheless, 1000 ppm CO resulted in a performance loss of 46 percent (356 mV) at 0.5 A.cm^{-2}. No significant effect was observed with the introduction of a 2 per cent air bleed stream. As in section 7.6.1 the presence of the Au/TiO$_2$ PROX system prevented any performance loss of the fuel cell.

Similar CO poisoning effects were observed on the PtRu/C anode when 100 ppm CO was introduced to the fuel cell. In this instance, approximately 9 per cent (67 mV) of the fuel cell's performance was lost due to CO poisoning. From Figure 66 it is evident that the Au/TiO$_2$ PROX system yielded superior results in these conditions.

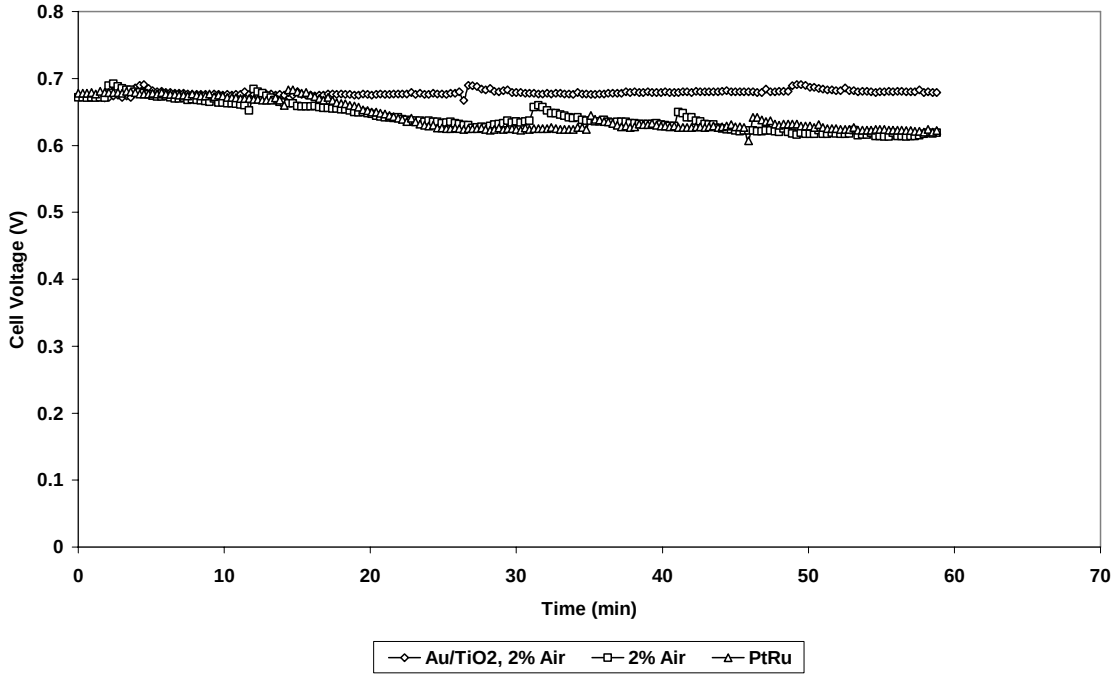

Figure 66: CO tolerance of a 0.5 mg Pt.cm^{-2} PtRu/C anode with and without a 3wt% Au/TiO_2 coated monolith PROX reactor (100 ppm CO, 0.5 A.cm^{-2}, 1.5x stoichiometric H_2 flow rate, SV over Au/TiO_2 catalyst 330 000 ml.g_{cat}^{-1}.h^{-1}, catalyst chamber at 25°C, cell temperature 80°C, 0.84 mg Pt.cm^{-2} Pt/C cathode).

7.6.3 PtMo/C

The results obtained for a 0.52 mg Pt.cm^{-2} PtMo/C anode is shown in Figures 67 and 68. Even though PtMo/C offers improved CO tolerance compared to Pt/C and PtRu/C at higher CO concentrations, approximately 20 per cent (153 mV) of the fuel cell's performance was still lost in the presence of 1000 ppm CO, and 9.2 per cent (70 mV) in 100 ppm CO at 0.5 A.cm^{-2} with or without an air bleed stream. The decrease in performance due to CO poisoning is significant and might influence the applicability of these catalysts in commercial fuel cell systems operating on contaminated H_2 gas streams. As in sections 7.6.1 and 7.6.2, the incorporation of a Au/TiO_2 PROX system was the superior method for CO removal / tolerance, as is evident from Figures 67 and 68 (the resistance compensated potential versus time graphs are presented in Appendix IX).

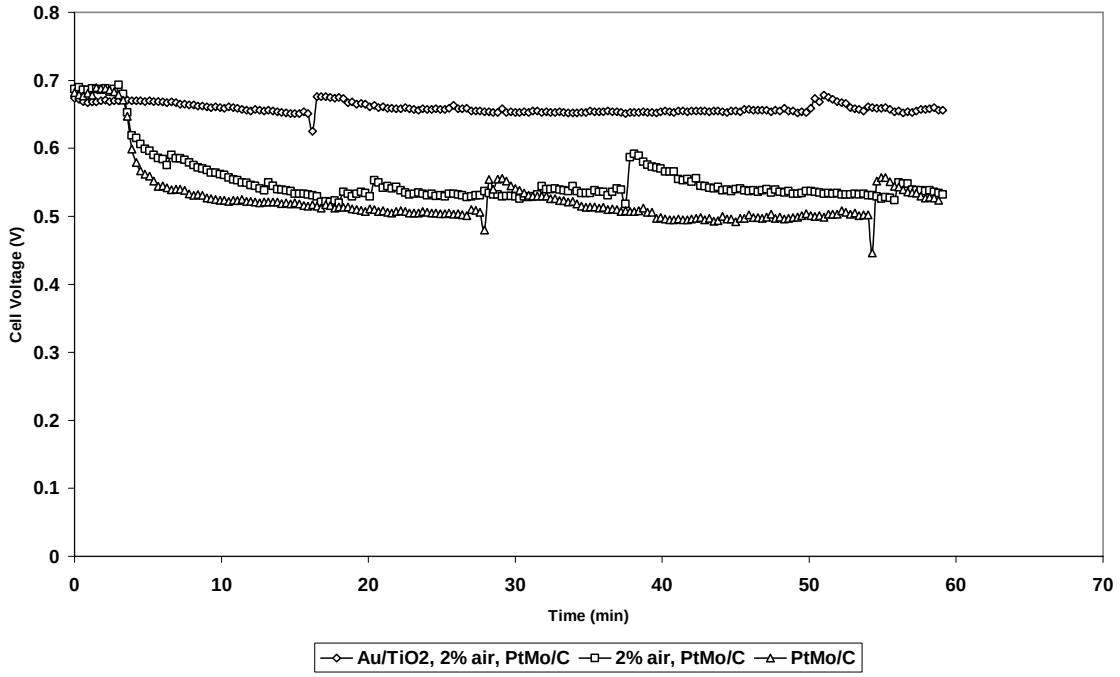

Figure 67: CO tolerance of a 0.52 mg Pt.cm^{-2} PtMo/C anode with and without a 3wt% Au/TiO$_2$ coated monolith PROX reactor (1000 ppm CO, 0.5 A.cm^{-2}, 1.5x stoichiometric H$_2$ flow rate, SV over Au/TiO$_2$ catalyst 250 000 ml.g$_{cat}^{-1}$.h^{-1}, catalyst chamber at 25°C, cell temperature 80°C, 0.84 mg Pt.cm^{-2} cathode).

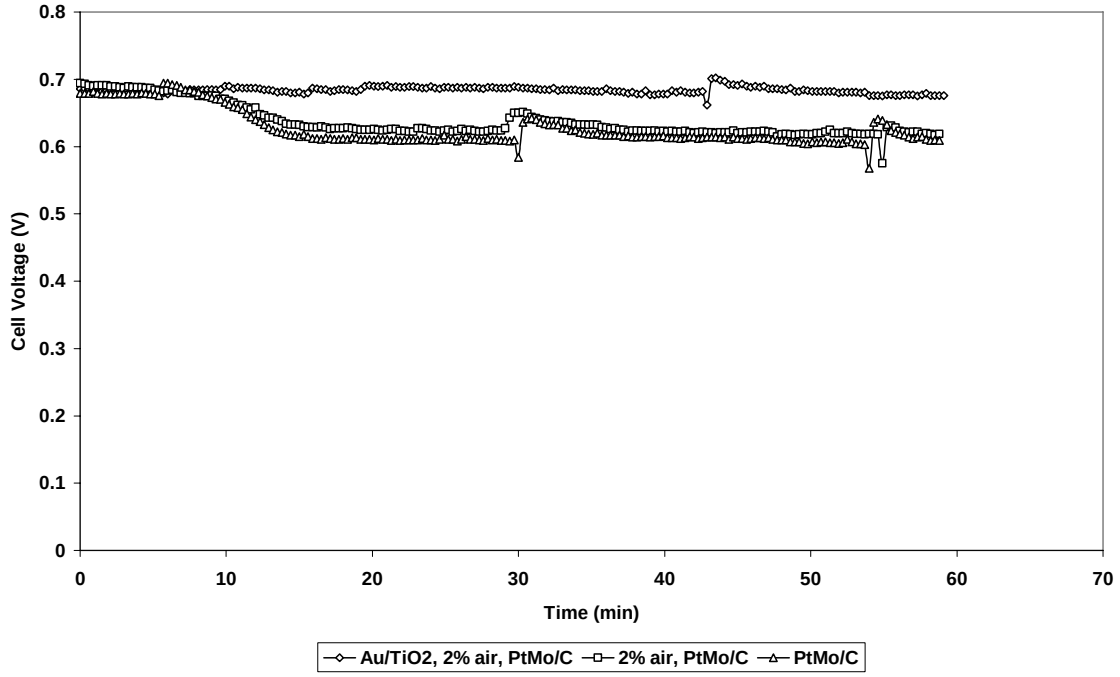

Figure 68: CO tolerance of a 0.52 mg Pt.cm^{-2} PtMo/C anode with and without a 3wt% Au/TiO$_2$ coated monolith PROX reactor (100 ppm CO, 0.5 A.cm^{-2}, 1.5x stoichiometric H$_2$ flow rate, SV over Au/TiO$_2$ catalyst 330 000 ml.g$_{cat}^{-1}$.h^{-1}, catalyst chamber at 25°C, cell temperature 80°C, 0.84 mg Pt.cm^{-2} cathode).

A summary of the results are shown in Figures 69 and 70. The presence of the Au/TiO_2 PROX system in front of the Pt/C anode, the least CO tolerant anode, yielded superior results.

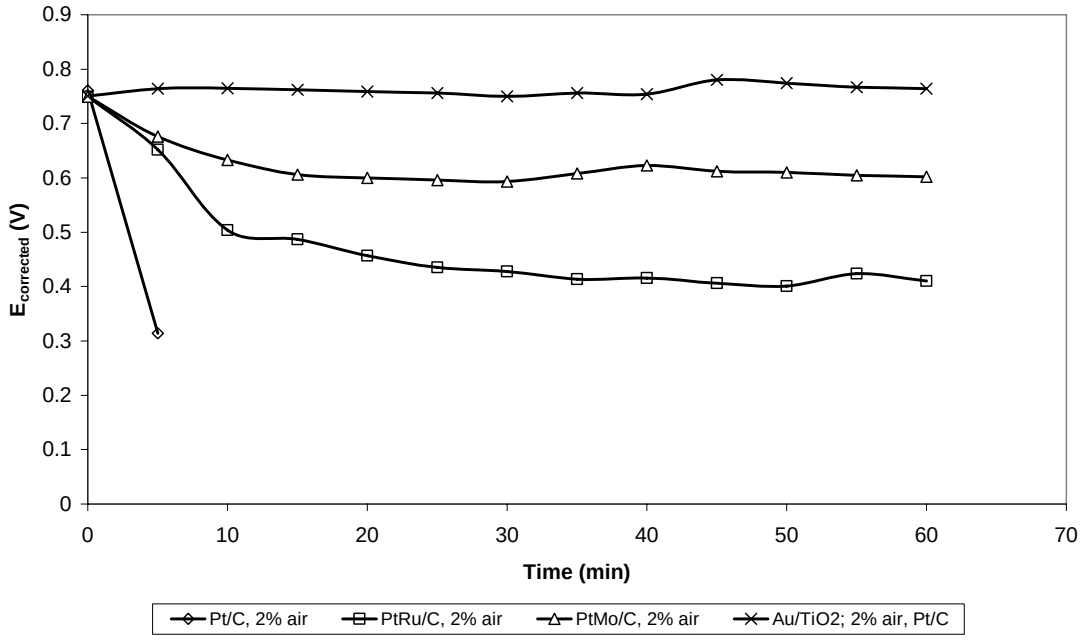

Figure 69: Summary of CO tolerance results (1000 ppm CO, 0.5 A.cm^{-2}, 1.5x stoichiometric H_2 flow rate, SV over 3 wt% Au/TiO_2 catalyst = 250 000 ml.g_{cat}^{-1}.h^{-1}, catalyst chamber 25°C, fuel cell 80°C)

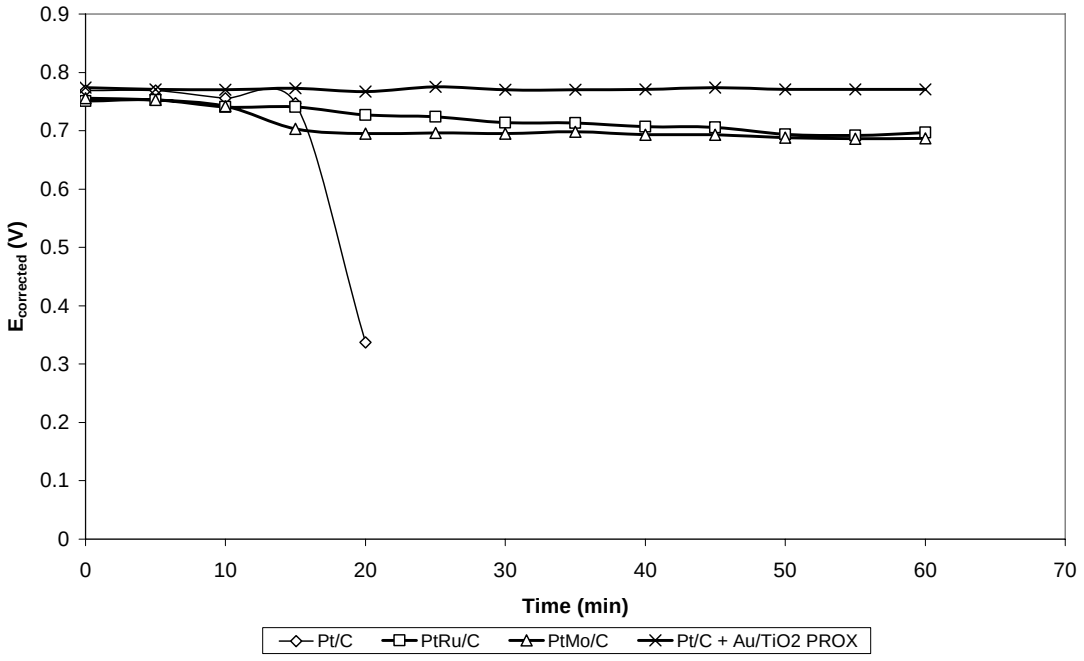

Figure 70: Summary of CO tolerance results (100 ppm CO, 0.5 A.cm^{-2}, 1.5x stoichiometric H_2 flow rate, SV over 3 wt% Au/TiO_2 catalyst = 330 000 ml.g_{cat}^{-1}.h^{-1}, catalyst chamber 25°C, fuel cell 80°C)

From the results discussed in sections 7.6.1, 7.6.2, and 7.6.3 it is evident that the Au/TiO_2 PROX system can act as a 'guard bed' in front of any fuel cell anode (Pt/C, PtRu/C, and PtMo/C) when CO is present (10 ppm – 1000+ ppm CO) in the H_2 fuel stream. For all the anodes investigated, the presence of the Au/TiO_2 PROX system eliminated the CO poisoning effect. These results are significant, since H_2 purity and the cost of H_2 to the end user are two of the main challenges for fuel cells to commercialize. The proposed Au/TiO_2 PROX system might therefore play an integral role in the pursuit towards large scale fuel cell commercialisation [84].

7.6.4 Influence of Au/TiO_2 PROX system on fuel efficiency

For fuel cells to become the preferred method of power generation for automobiles it has to have distinct advantages compared to the ICE powered vehicles. One of these advantages includes fuel efficiency. It is generally known that Au-based catalysts have limited selectivity towards CO oxidation in H_2-rich gas streams [44, 85, 86]. It is therefore important in this study to develop a system that will increase the fuel cell's performance in CO contaminated H_2 without significantly influencing important end-user requirements, like fuel efficiency.

The Au/TiO_2 catalyst investigated in this study proved to be very active for CO oxidation in H_2-rich gas streams. However, an excess amount of oxygen is typically introduced to facilitate CO oxidation, which might have an adverse effect on fuel efficiency by oxidizing H_2 to H_2O. To quantify this effect, 1.02 times the stoichiometric amount of H_2 (without air and CO) was fed to the fuel cell at 0.7 $A.cm^{-2}$ and time was allowed for the cell potential to stabilise. This was followed by introducing the Au/TiO_2 PROX system (3 wt% Au/TiO_2 coated cordierite monolith, 2 per cent air bleed, H_2 space velocity of 250 000 $ml.g_{cat}^{-1}.h^{-1}$). The cell potential was monitored and the results are presented in Figure 71. As shown in Figure 71, the cell potential stabilised at approximately 630 mV in the presence of 1.02 times the stoichiometric amount of H_2. After 13 minutes the

Au/TiO_2 PROX system was introduced together with a 2 per cent air bleed stream, which resulted in a 9 mV decrease in cell potential, equivalent to a 1.43 per cent decrease in the fuel cell's performance at 0.7 $A.cm^{-2}$.

The 1.43 per cent decrease in performance is very small (compared to the performance loss with PtRu/C and PtMo/C) and should be dependent on the amount of O_2 introduced into the system. It has been shown (Figure 44) that for low CO concentrations, an air bleed stream of 1 per cent (0.21 per cent O_2) is sufficient to facilitate complete removal of CO. In addition, the presence of CO in the H_2 feed will consume a fraction of the O_2 that was available for H_2 oxidation in Figure 71. Therefore, even better results than that presented in Figure 71 are expected if the concentration of O_2 is reduced and if CO is present in the H_2 feed gas. Table 7 shows the effect of air bleed streams on the fuel cell's performance when 1.02 times the stoichiometric amount of H_2 is introduced to the cell at 0.7 $A.cm^{-2}$. A decrease of 1.47 per cent in performance was observed with the introduction of a 1 per cent air bleed stream (in the absence of the Au/TiO_2 catalyst). This effect was worsened when the air bleed was doubled to 2 per cent, resulting in the cell potential decreasing to below the system limit of 0.3 V. This effect was not seen when the Au/TiO_2 catalyst was present in the system, as is evident from Figure 69 and Table 7. It might be that without the Au/TiO_2 catalyst the majority of the O_2 is used to oxidise H_2 to H_2O at the anode inside the fuel cell, resulting in a flooding effect. Because H_2 is introduced close to its stoichiometric limit, this flooding effect leads to fuel starvation and a subsequent decrease in cell potential. With the Au/TiO_2 PROX catalyst present in the system prior to the humidifiers, significant amounts of O_2 are used to oxidize H_2 before it enters the humidifiers, and therefore, before it enters the fuel cell. This limits the amount of water formed at the anode, and decreases the flooding effect. Although the oxidation of H_2 to H_2O is an undesirable effect, the results obtained indicate that a system operating with an air bleed stream should perform better if a Au/TiO_2 PROX catalyst is present prior to the humidifiers, thereby preventing water formation, and thus flooding, at the anode.

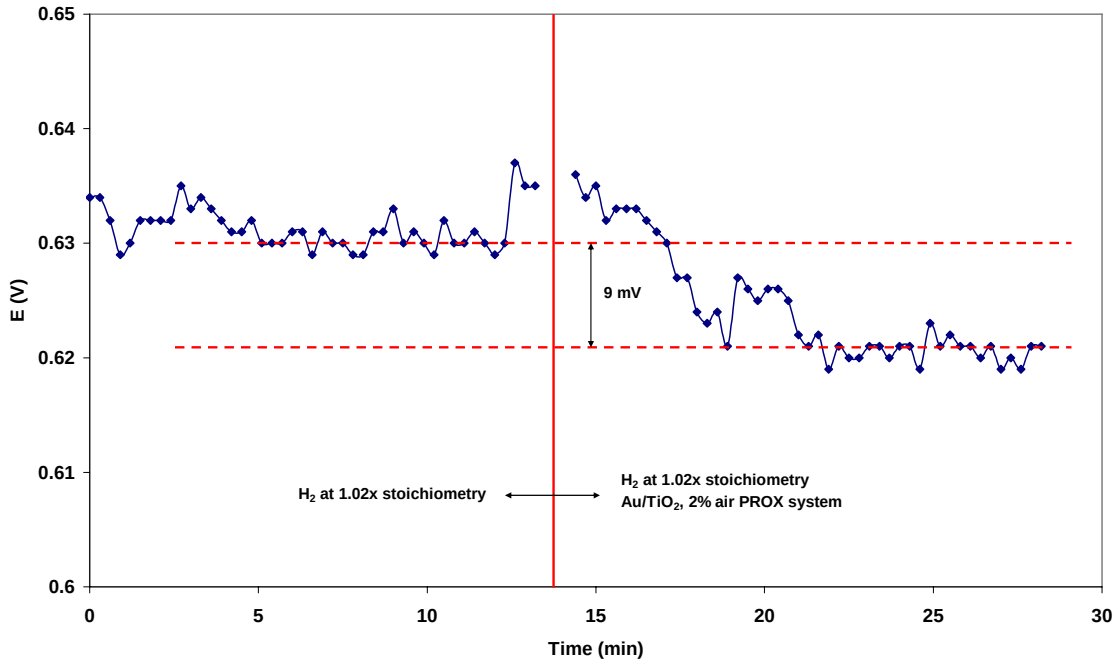

Figure 71: The comparative performance of a fuel cell operating at 0.7 A.cm^{-2} and H_2 stoichiometry of 1.02 (290 000 ml.g$_{cat}^{-1}$.h^{-1}) and a 2% air bleed stream in the absence and presence of the 3 wt% Au/TiO_2 PROX system (anode: 0.39 mg Pt.cm^{-2}, cathode: 0.84 mg Pt.cm^{-2}, fuel cell at 80°C, Au/TiO_2 PROX system at room temperature, 25 psi.)

Table 7: Influence of PROX system on the electrochemical performance of the fuel cell.

	E_i (V)	E_f (V)	% Performance loss
1% Air	0.611	0.602	1.47
2% Air	0.638	Tripped	-
1% Air + PROX	0.634	0.620	2.21
2% Air + PROX	0.630	0.621	1.43

7.7 Alternative support – Au/CeO_2

As with TiO_2, CeO_2 has been identified as a promising support for Au-based catalysts. Comparative results are shown in Figure 72 for 1, 3, and 5 wt% Au on TiO_2 and CeO_2 respectively. The results indicate that Au/TiO_2 is generally more active than Au/CeO_2, except for the 3 wt% Au catalysts. These results are encouraging since our preparation method for Au/TiO_2 is optimised, and that for Au/CeO_2 not, suggesting that the activity of the Au/CeO_2 catalysts should perform even better when preparation thereof can be optimised. Although no thorough investigation was conducted on the Au particle size and particle distribution etc. during this study, it is suggested that a more complete investigation on Au/CeO_2 be conducted for the applications specific to this study.

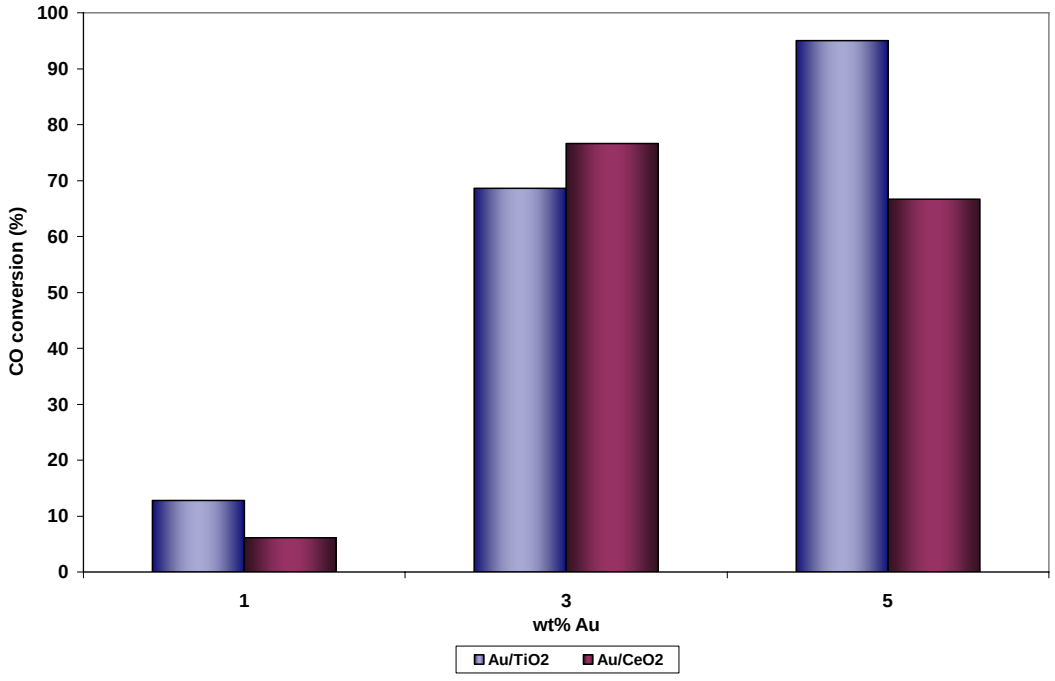

Figure 72: Comparison between the catalytic activity of Au/TiO_2 and Au/CeO_2 powders (0.2% CO, 2% air, balance H_2, 850 000 ml.g_{cat}^{-1}.h^{-1}, dry)

Chapter 8

ECONOMICS AND COMMERCIAL VIABILITY OF SYSTEM

8.1 Economic feasibility analysis of Au/TiO_2 PROX system

Apart from CO tolerance, a number of economic and socio-economic challenges exist in order for fuel cell powered vehicles to become the preferred means of automotive transport. One of these challenges is to produce an affordable product/system to the end user/general public. What makes this avowal even more challenging is the fact that such a product/system should be able to compete with the performance, durability, safety, and reliability of the current internal combustion engine technologies. The 2010 cost target for an economically competitive system, as stipulated by the USDoE [87], is $45/kW. Since the present study is focused on developing an economically viable Au-based catalyst that will comply with the technical requirements of preventing CO poisoning of the fuel cell, it is imperative to not only consider the technical performance of each catalyst, but also the cost efficiency relative to the target cost as stipulated by the USDoE.

Tables 8 and 9 presents the amount of gold, and total cost of gold, for different amounts of catalysts and a variety of gold loadings in the fuel cell system, respectively. *(Note: The calculations in Tables 8 – 10 and 11 – 12, as well as Figures 73 – 76, were based on the following conditions and assumptions: Assume 60 kW system operating at peak output at 0.65 V (drawing 92 308 A). Hydrogen flow to fuel cell at 1.02 stoichiometry, thus 656 $l.min^{-1}$ - calculation of this flow rate is shown in Appendix X).* From Tables 8 and 9 it is evident that the cost of gold that will be used in a fuel cell system justifiably depends on the gold loading and the amount of catalyst needed to remove CO to sufficiently low levels. Higher gold loadings will add to the cost of the system, but in turn, would yield more active catalysts (Sections 6.2.1 and 7.3), and subsequently less catalyst. Thus, there exists a trade-off between gold loading and catalytic activity. In the present study, complete removal of CO has been achieved with a 3 wt% Au/TiO_2 catalyst

at 850 000 $ml.g_{cat}^{-1}.h^{-1}$. From Tables 8 and 9 it is evident that with the current performance, approximately 1.4 g gold will be needed in a 60 kW fuel cell, constituting approximately $22.65 assuming a gold price of $500/oz.

Table 8: A presentation of the mass of gold needed at different amounts of catalysts with different gold loadings, yielding different space velocities. Calculations are based on the following conditions and assumptions:

Mass of catalyst (g)	Space velocity ($l.g_{cat}^{-1}.h^{-1}$)	Mass of gold in fuel cell system (g), for different gold loadings (wt%)					
		1wt%	2wt%	3wt%	5wt%	10wt%	20wt%
20	1989	0.2	0.4	0.6	1.0	2.0	4.0
46.8	850*	0.5	0.9	1.4	2.3	4.7	9.4
50	795	0.5	1.0	1.5	2.5	5.0	10.0
100	398	1.0	2.0	3.0	5.0	10.0	20.0
150	265	1.5	3.0	4.5	7.5	15.0	30.0
200	199	2.0	4.0	6.0	10.0	20.0	40.0
300	133	3.0	6.0	9.0	15.0	30.0	60.0
400	99	4.0	8.0	12.0	20.0	40.0	80.0

**Current operating conditions in CO oxidation test rig*

Table 9: A presentation of the cost associated with different amounts of catalysts with different gold loadings, yielding different space velocities. Assume gold price of $500/oz.

Mass of catalyst (g)	Space velocity ($l.g_{cat}^{-1}.h^{-1}$)	Cost of gold in fuel cell system, in US$, for different gold loadings (wt%)					
		1wt%	2wt%	3wt%	5wt%	10wt%	20wt%
20	1989	3.23	6.45	9.68	16.13	32.26	64.52
46.8	850*	7.55	15.10	22.65	37.74	75.48	150.97
50	795	8.06	16.13	24.19	40.32	80.65	161.29
100	398	16.13	32.26	48.39	80.65	161.29	322.58
150	265	24.19	48.39	72.58	120.97	241.94	483.87
200	199	32.26	64.52	96.77	161.29	322.58	645.16
300	133	48.39	96.77	145.16	241.94	483.87	967.74
400	99	64.52	129.03	193.55	322.58	645.16	1,290.32

**Current operating conditions in CO oxidation test rig*

In Table 10 the economic viability is presented in terms of the percentage cost of gold relative to the USDoE cost target of $45/kW.

Table 10: A presentation of the percentage cost of Au relative to the USDoE cost target of $45/kW for different amounts of catalysts with different gold loadings, yielding different space velocities. Assume gold price of $500/oz.

Mass of catalyst (g)	Space velocity ($l.g_{cat}^{-1}.h^{-1}$)	% cost of Au relative to $45/kW target, for different gold loadings (wt%)					
		1wt%	2wt%	3wt%	5wt%	10wt%	20wt%
20	1989	0.12	0.24	0.36	0.60	1.19	2.39
46.8	850*	0.28	0.56	0.84	1.40	2.80	5.59
50	795	0.30	0.60	0.90	1.49	2.99	5.97
100	398	0.60	1.19	1.79	2.99	5.97	11.95
150	265	0.90	1.79	2.69	4.48	8.96	17.92
200	199	1.19	2.39	3.58	5.97	11.95	23.89
300	133	1.79	3.58	5.38	8.96	17.92	35.84
400	99	2.39	4.78	7.17	11.95	23.89	47.79

**Current operating conditions in CO oxidation test rig*

The green blocks in Table 10 present systems in which the total cost of gold will be less than 1 per cent of the $45/kW cost target. These systems should be economically feasible for fuel cell systems, provided that the catalysts are able to remove CO to less than 1 ppm. Since no precise cut-off cost is specified for the CO removal section the costs between 1 and 2 per cent of the target cost are marked in orange, implying that it might be economically feasible for certain systems, or in specific conditions. Costs above 2 per cent of the target are considered to be uneconomical and are marked in red. Note that the standards mentioned above comply with the strategy of the present study.

The information presented in Tables 9 and 10 is justifiably sensitive to changes in the gold price. A sensitivity analysis was conducted taking into account the influence of the gold price (400 – 1000 $/oz) and the gold loading on the metal oxide support (1 – 10 wt% Au) in a PROX system operating at 850 000 $ml.g_{cat}^{-1}.h^{-1}$ (for the simulated 60 kW system operating at peak power, this represents 46.8 g of catalyst). The results are shown in

Figures 73 and 74. From Figure 73, and for the scenarios mentioned above, it is evident that the cost of gold in a 60 kW system can vary from \$6.04 using a 1 wt% Au catalyst at a gold price of \$400/oz, to \$151 using a 10 wt% Au catalyst at a gold price of \$1000/oz. In Section 7.2 it was shown that complete removal of CO is possible over a 3 wt% Au/TiO_2 catalyst operating at 850 000 $ml.g_{cat}^{-1}.h^{-1}$. In this case, the cost of gold can vary from \$18.1 (at a gold price of \$400/oz), to \$45.3 (at a gold price of \$1000/oz), as is evident from Figure 73. This represents 0.67 per cent and 1.68 per cent of the USDoE \$45/kW target for the \$400/oz and \$1000/oz scenarios respectively, as shown in Figure 74. Comparing this information with that in Table 10, it is evident that this system should still be economically viable (less than 2 per cent – green blocks in Table 10) even at a gold price of \$1000/oz. Only at \$1200/oz will the cost of gold be higher than 2 per cent of the USDoE target of \$45/kW (for a 3 wt% Au/TiO_2 PROX system operating at a SV of 850 000 $ml.g_{cat}^{-1}.h^{-1}$). The details on the calculations in this section are presented in Tables XI A – XI H in Appendix XI.

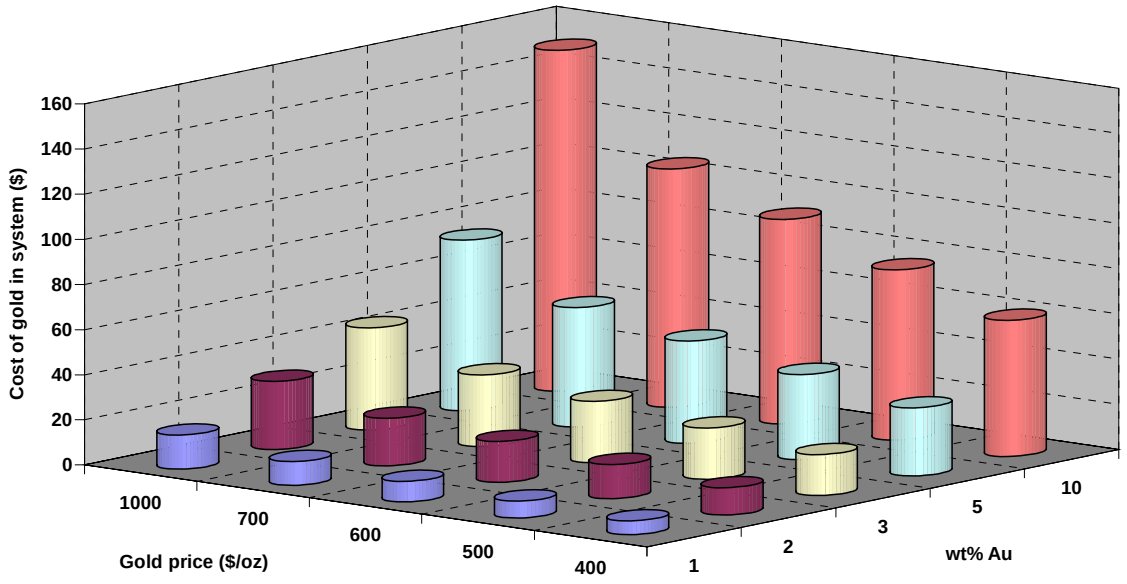

Figure 73: Sensitivity analysis of the influence of the gold price and the wt% gold on the cost of gold in a 60 kW fuel cell system operating at peak power and at a potential of 0.65 V (drawing 92 308 A). Calculations based on a SV of 850 000 $ml.g_{cat}^{-1}.h^{-1}$ over the Au/TiO_2 PROX system.

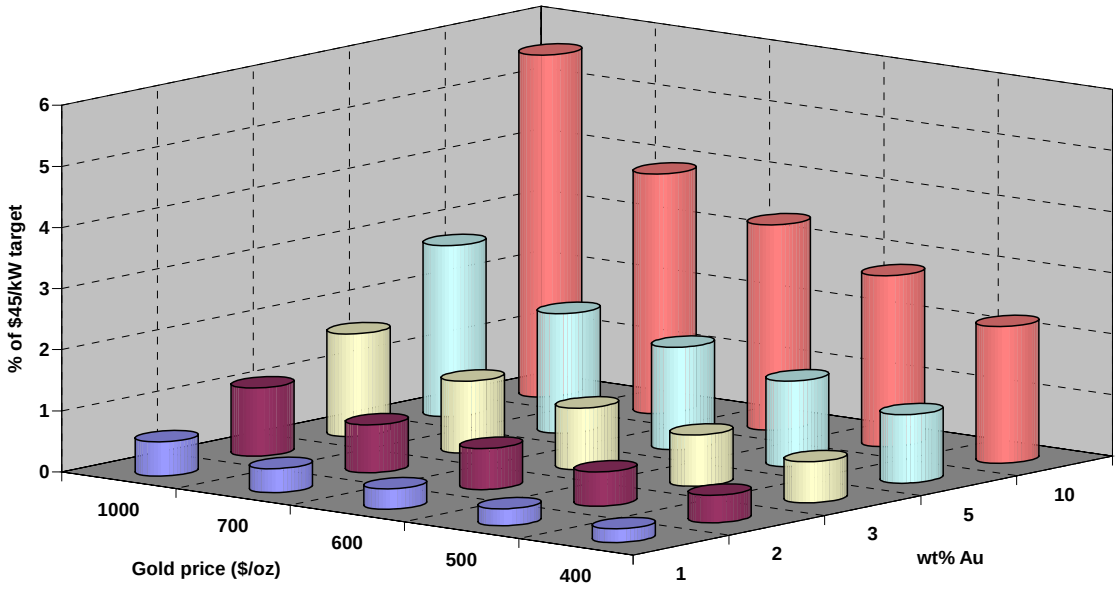

Figure 74: Sensitivity analysis of the influence of the gold price and the wt% gold on percentage cost of gold relative to the USDoE target cost of $45/kW. Calculations based on a 60 kW fuel cell system operating at peak power and at a potential of 0.65 V (drawing 92 308 A). Gas flow calculations based on a SV of 850 000 ml.g_{cat}^{-1}.h^{-1} over the Au/TiO_2 PROX system.

8.2 Projected gold usage

In order to establish if the current annual gold production is sufficient to satisfy new demand, it is important to estimate the annual amount of gold that will be consumed should the proposed technology commercialize. Table 11 presents statistics of vehicle production for 1990 and 2000. This data was obtained from the Office of Transportation Technologies (OTT) Bureau of Transportation Statistics (US) and Auto Industry.

Table 11: Indication of new vehicle production in 1990 and 2000.

	1990	2000
Vehicle Production	50 048 000	58 441 000

Vehicle production increased by 16.76 per cent from 1990 to 2000. If it can be assumed that the percentage increase was linear over this period, the average year on year (YOY) growth in vehicle production was 1.68 per cent. If the same YOY growth rate can be assumed, the projected vehicle production for 2020 is approximately 78.1 million new vehicles.

The amount of gold that will be used in a fuel cell powered vehicle will largely depend on the gold loading and the amount of catalyst used. The influence of these variables on the amount of gold that will be used in a 60 kW fuel cell powered vehicle was presented in Table 8. Figures 75 and 76 were constructed by using this information and assuming different levels of market penetration of fuel cell powered vehicles. In Figure 75, the estimated annual gold usage is presented in terms of the estimated market penetration and the gold loading (assuming a Au-based catalyst PROX system operating at 850 000 $ml.g_{cat}^{-1}.h^{-1}$). From this simulation it is evident that annual gold usage can vary from 0.37 to 54.8 tons depending on gold loading and market penetration. For the current optimum system (3 wt% Au/TiO_2 operating at 850 000 $ml.g_{cat}^{-1}.h^{-1}$) the annual gold usage is estimated at 1.1 – 16.4 tons, depending on the level of market penetration (1 – 15 per cent). Comparing this estimated usage to the 2005 global gold production of 2519 tons [88], it is evident that the gold supply should be sufficient to satisfy the envisaged demand.

The estimated gold revenue based on market penetration and gold price is shown in Figure 76. This simulation is based on a 3 wt% Au-based catalyst PROX system operating at 850 000 $ml.g_{cat}^{-1}.h^{-1}$. From this simulation it is evident that the estimated gold revenue varies between \$14.14 million to \$1,060.84 million (depending on the gold price and market penetration), should the current optimum system commercialize.

The Tables and calculations for the graphs in Section 8.2 are presented in Appendix XII.

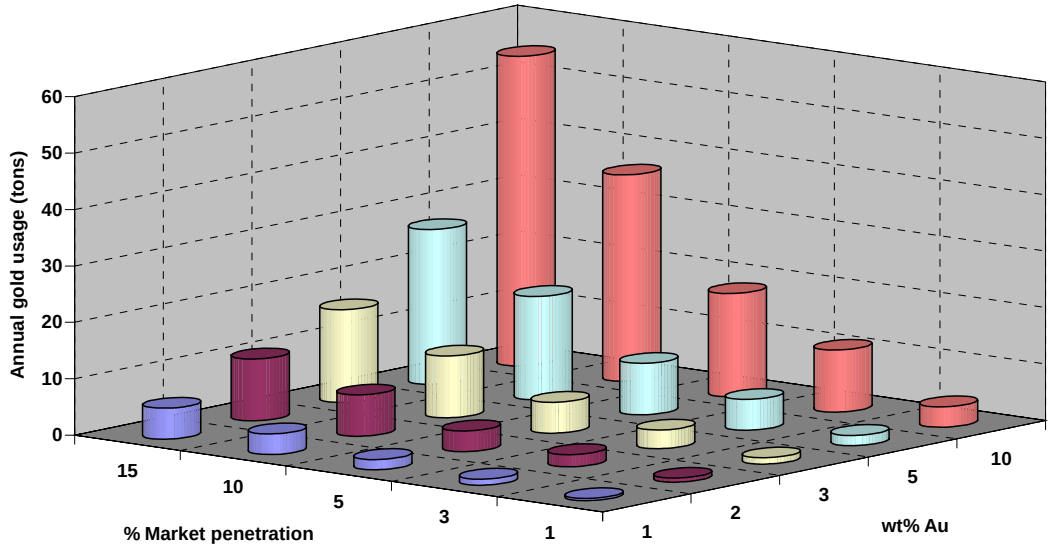

Figure 75: Estimated annual gold usage based on different levels of market penetration (by 2020) and different gold loadings for a Au-based catalyst PROX system operating at 850 000 ml.g_{cat}^{-1}.h^{-1} (Assume 60 kW fuel cell systems, and annual vehicle production in 2020 = 78.1 million).

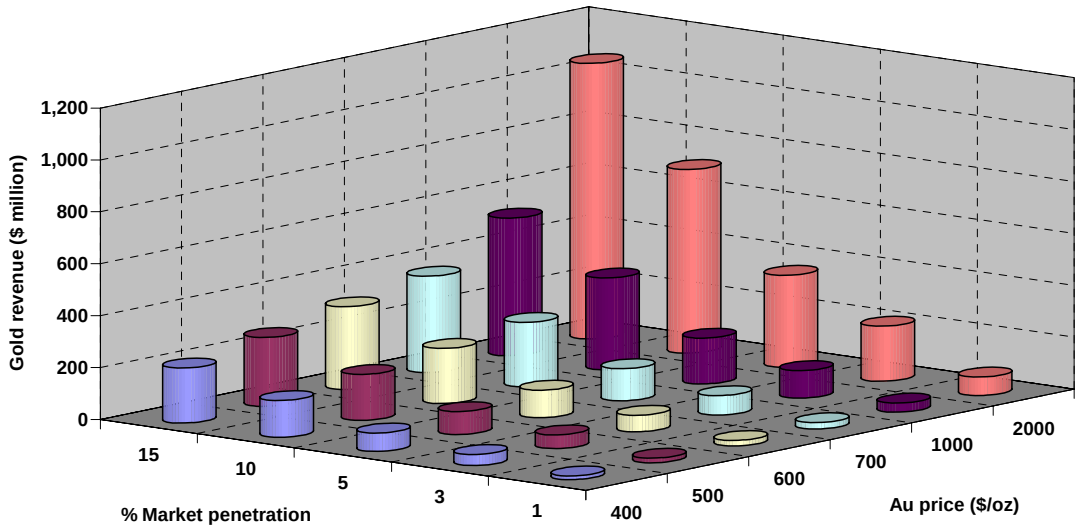

Figure 76: Estimated annual gold revenue based on projected market penetration by 2020 and different gold prices for a 3 wt% Au-based PROX system operating at 850 000 ml.g_{cat}^{-1}.h^{-1} (Assume 60 kW fuel cell systems, and annual vehicle production in 2020 = 78.1 million).

8.3 Other practical aspects

In addition to the economical viability of the system, certain practical requirements need to be addressed during the design and selection of a Au-based catalyst reactor for CO removal, such as the mass and volume of the system. For the Au/TiO_2 nanopowder and +500 μm -710 μm granules, the volumes were calculated by measuring the bulk density of each form of the support material and specifying the weight. The bulk density was determined as 0.87 $g.cm^{-3}$ for the +500 μm -710 μm TiO_2 granules, and 0.79 $g.cm^{-3}$ for the TiO_2 nanopowder. The volume of the monolith reactor was calculated by determining the amount of Au/TiO_2 catalyst coated onto a 1.6 cm diameter, 7.4 cm length monolith containing 400 channels per square inch. The mass ratio of Au/TiO_2 : monolith was used to extrapolate the volume of the monolith needed to carry a specified amount of catalyst. The estimated volumes of the systems are shown in Table 12. Note that the volume of a monolith reactor can vary significantly depending on the amount of catalyst that is coated onto the monolith (which is dependent on the wt% solids in the slurry and the number of wash-coats), and the channel density of the monolith ($channels.inch^{-2}$).

From Table 12 it is evident that the granules and powder will consume significantly less space than the monolith system. However, both the afore mentioned forms of supports will result in higher pressure drops over the catalyst beds, which can have a significant effect at flow rates of 656 $\ell.min^{-1}$. To quantify the pressure drop, the calculations and procedures in Section 7.2 and Appendix VIII was repeated. The reactor design for these calculations was a cylinder with volumes quoted in Table 12, assuming a diameter : height ratio of 1:2. The calculated pressure drops for the powder, granules, and monolith catalysts for a 60 kW fuel cell system is shown in Table 13.

Table 12: An estimation of the volume required by the catalyst reactor for three different systems and different amounts of catalysts.

Mass of catalyst (g)	Space velocity ($l.g_{cat}^{-1}.h^{-1}$)	Total volume of catalyst reactor (ℓ)		
		Granules**	Powder**	Monolith***
20	1989	0.023	0.025	1.5
46.8	850*	0.054	0.059	3.6
50	795	0.058	0.063	3.9
100	398	0.115	0.127	7.7
150	265	0.172	0.190	11.5
200	199	0.230	0.253	15.4
300	133	0.345	0.380	23.1
400	99	0.460	0.506	30.8

** Current operating conditions in CO oxidation test rig*
*** Volume calculations based on the bulk density of the support without any gold*
**** Dependent on the amount of catalyst coated onto monolith and the channel density*

Table 13: Calculation of the pressure drop over the 3 different catalyst systems for a 60 kW fuel cell system operating at peak output at 0.65 V (drawing 92 308 A). Particle sizes used for the calculations were 500 um for the granules and 75 um for the powder catalyst. The simulated reactor had a length : diameter ratio of 2:1.

Mass of catalyst (g)	Space velocity ($l.g_{cat}^{-1}.h^{-1}$)	Pressure drop over catalyst bed (kPa)		
		Granules	Powder	Monolith
20	1989	32.0	179.7	0.025
46.8	850*	13.8	81.5	0.011
50	795	12.9	76.9	0.010
100	398	6.6	41.7	0.005
150	265	4.5	29.8	0.004
200	199	3.4	23.7	0.003
300	133	2.3	17.4	0.002
400	99	1.8	14.1	0.001

** Current operating conditions in CO oxidation test rig*

From Table 12 it is evident that the powders and granules will yield significantly more compact systems than the monoliths. For a system operating at 850 000 $ml.g_{cat}^{-1}.h^{-1}$, 0.54

and 0.59 ℓ is typically required for the granulate and powder catalyst systems respectively, while 3.6 ℓ is required for the catalyst coated monolith system. However, the more compact the system, the higher the pressure drop across the catalyst bed, as is shown in Table 13. For the same operating conditions, the pressure drops over a packed bed of granulate and powder catalysts are 13.8 and 81.5 kPa respectively, compared to 0.011 kPa over the monolith system.

8.4 Fuel cells: Technical targets

In addition to cost, size, and weight, other technical targets that need to be achieved in order for fuel cells to find commercial applications include: power density, specific power, transient response, cold start-up time, durability with cycling, and survivability. A summary on the current status and future targets [87] are shown in Appendix XIII.

Chapter 9

CONCLUSIONS

The notion of electrochemical energy generation through fuel cells is a promising concept that might revolutionize the global energy industry. However, significant technical and economical challenges still exist that have to be surmounted in order for fuel cells to become the preferred means of energy generation. Two of the main challenges remaining are the purity and cost of hydrogen; in particular, the technical and economical challenges of reducing the CO content to sub-ppm levels. The poisoning effect of CO on the Pt catalysts in fuel cells has prompted an investigation into CO removal from hydrogen-rich gas streams using gold based catalysts. Two distinct approaches were investigated, namely 1) increasing the CO tolerance of the anode by incorporating a $Au/TiO_2/C$ bi-layer into the MEA, and 2) enriching hydrogen by the preferential oxidation of CO contaminants from partially purified hydrogen, i.e. purified hydrogen that still contains traces of CO contamination (10 – 2000 ppm CO) and that would essentially be dry.

9.1 Bi-layer system

Encouraging results were obtained when typical fuel cell operating conditions were simulated in an isolated CO oxidation test rig. Initial catalyst screening in air indicated that the catalytic activity increased with an increase in gold loading up to 4.67 wt% Au, where after a further increase in the gold loading to 11 wt% resulted in a slight decrease in activity due to agglomeration of poorly dispersed particles. A decrease in CO conversion was observed when air was replaced with hydrogen as background gas (while injecting an 1.8 per cent air bleed stream) at a SV of 1000 $\ell.g_{cat}^{-1}.h^{-1}$. However, 100 per cent CO conversion was obtained over the 5.1, 7.6, and 13.2 wt% Au/TiO_2 catalysts when the space velocity was decreased to 100 $\ell.g_{cat}^{-1}.h^{-1}$; a space velocity more representative of the specific application. The rate of CO conversion increased with an increase in the oxygen concentration, however, thereby sacrificing selectivity.

Calcination at 300°C for 2.5 hours resulted in an increase in the activity of catalysts containing 4.5 and 10.5 wt% Au, and a decreased in activity for a catalyst containing 16.6 wt% Au. This effect might be due to the sintering of poorly dispersed gold particles at higher gold loadings.

An empirical model was developed for the influence of pressure, which indicated that the reaction order of pressure is approximately 0.74 ± 0.09. The catalytic activity increased with temperature. The activation energy of a 1 wt% Au catalyst for the CO oxidation reaction was calculated as 24.4 ± 0.9 $kJ.mol^{-1}$.

Both the influence of MEA constituents and water formation initially proved to be of concern. However, a heat treatment at 300°C almost entirely eliminated the influence of the MEA constituents, while the addition of PTFE increased the resistance of the catalysts to water formation.

Satisfactory polarisation performance was obtained from the first in-house produced gold containing bi-layer MEA. However, the incorporation of the 0.5 mg $Au.cm^{-2}$ Au/TiO_2 bi-layer did not show any significant CO tolerance in a simulated reformate (350 ppm CO, 2 per cent air bleed stream, balance H_2). Fuel cell gas flow dynamics were simulated in a 'flat-bed' reactor in the CO oxidation rig, which also indicated that this catalyst was inactive for CO conversion in the MEA configuration. An increase in gold loading to 2 mg $Au.cm^{-2}$ using a 20 wt% Au/TiO_2 catalyst yielded 30 per cent CO conversion in the same 'flat bed' reactor, and 85 per cent conversion in the u-tube fixed bed reactor. However, even with this active catalyst, a four times increase in the gold concentration in the MEA bi-layer did not result in a significant increase in CO tolerance of the PEM fuel cell. The performance of a $Pt_{20}Ru_{10}$ anode proved to have superior performance concerning CO tolerance.

9.2 Isolated catalyst chamber / PROX system

Even though the Au/TiO_2 proved to have little effect on the CO tolerance inside the MEA, a significant increase in the CO tolerance was obtained when the same 20 wt% Au on TiO_2 catalyst was incorporated in a separate catalyst chamber just prior to the fuel cell as a preferential oxidation (PROX) catalyst. This configuration resulted in stable performance over 4000 seconds, even in the presence of 350 ppm CO.

Further investigation in a separate CO oxidation test rig revealed that complete removal of CO (<1.3 ppm CO) was obtained with a 3 wt% Au/TiO_2 (powder) PROX system operating at room temperature and un-humidified gas streams at a SV of 850 $\ell.g_{cat}^{-1}.h^{-1}$. However, the activity proved to be significantly higher for packed bed configurations than for monolith systems.

The application of the least active catalyst form (monolith system) was investigated in an actual Johnson Matthey single cell PEM fuel cell test system. The 3 wt% Au/TiO_2 (monolith) PROX system proved to be superior compared to other state of the art PtRu/C and PtMo/C CO tolerant anodes. No potential loss was observed at 0.5 $A.cm^{-2}$ when 100 and/or 1000 ppm CO in H_2 was introduced to a 0.39 mg $Pt.cm^{-2}$ Pt/C anode in the presence of the Au/TiO_2 PROX system. On the contrary, the potential loss for the 0.5 mg $Pt.cm^{-2}$ PtRu/C and 0.52 mg $Pt.cm^{-2}$ PtMo/C was 356 mV and 153 mV (46 per cent and 20 per cent) respectively in the presence of 1000 ppm CO, and 54 mV and 69 mV (7.2 per cent and 9.1 per cent) in the presence of 100 ppm CO in H_2. The proposed Au/TiO_2 PROX system is distinct from conventional PROX systems in the sense that it does not exclusively focus on CO removal from reformate streams. Rather, it has been developed to completely remove CO over a wide range, ppm to percentage levels, from impure H_2-rich gas, e.g. from H_2 that would be stored in a fuel tank/cylinder but that would have some CO contamination and would essentially be dry.

A financial evaluation indicated that complete removal of CO (as high as 2000 ppm CO) can be achieved at a cost of gold of 0.84 per cent of the USDoE target of $45/kW (or $22.65 of gold per 60 kW vehicle - assuming a gold price of $500/oz).

Online deactivation of the Au/TiO_2 catalysts proved to be of concern. Significant online deactivation was observed for the powder and granulate catalysts over a 24 hour test period. It was concluded that deactivation was due to a combination of factors; including the accumulation of carbonate species, surface hydration, and possibly due to a process in which the catalyst is over-reduced, i.e. an extinction of Au^{x+} species; this process being reversible in an oxidizing atmosphere. In contrast to the powder and granulate catalysts, the Au/TiO_2 coated monoliths showed a slow activation period over 35 hours, where after it stabilised up to 50 hours. This effect was attributed to the different heat transfer effects in packed bed systems compared to monolith systems, where higher bed temperatures results in activation taking place within a few seconds in packed beds, whereas monoliths activate over a few hours in the same operating conditions.

Nonetheless, Au/TiO_2 proved to be very active for the selective catalytic oxidation of CO to CO_2 at room temperature. The work presented in this document suggests that Au/TiO_2 catalysts can play a significant role in the realization of large scale commercialisation of fuel cell systems for automotive, residential, and portable applications, provided that the problem of online deactivation can be surmounted. Test work has shown that Au/TiO_2, in the suggested configuration, is superior to other CO tolerance technologies. In addition, the incorporation of the proposed Au/TiO_2 PROX systems into automotive fuel cell systems should allow fuel cells to operate effectively on less pure H_2, thereby presenting a cost incentive to the end user.

Chapter 10

REFERENCES

1. Stonehart, P., Ross, P.N., *Catalysis Review Science and Engineering*, vol. 12, pp. 1, 1975.

2. Trimm, D.L., and Ilsen Onsan, Z., *Catalysis Review Science and Engineering*, vol. 43, no. 31, 2001.

3. Twigg, M., Catalyst Handbook, 2nd edition, London, pp. 330, 1996.

4. Golunski, S., *Platinum Metal Review,* vol. 42(1), pp. 2, 1998.

5. Carpenter, I., Edwards, N., Ellis, S., Frost, J., Golunski, S., Van Keulen, N., Petch, M., Pignon, J., and Reinkingh, J., 'On-board Hydrogen Generation for PEMFC in Automotive Applications', *SAE technical paper series*, 1999-01-13 420, (1999).

6. CAPRI final report, European Commission, JOE3-CT95-0039.

7. Song, C., Fuel processing for low-temperature and high-temperature fuel cells. Challenges, and opportunities for sustainable development in the 21st century, *Catalysis Today*, vol. 77, pp. 17, 2002.

8. Vielstich, W., Lamm, A., Gasteiger, H.A., Handbook of Fuel Cells – Fundamentals Technology and Applications, Vol. 3, 2004.

9. Ralph, T.R., Hards, G.A., Thompsett, D., Gascoyne, J.M., Fuel Cell Seminar Extended Abstracts, San Diego, CA, pp. 199, 1994.

10. Gottesfeld, S., Pafford, J., *Electrochemical Society,* vol. 135, pp. 2651, 1988.

11. Costamagna, P., Srinivasan, S., Quantum jumps in the PEMFC science and technology from the 1960s to the year 2000, Part II, *Journal of power sources*, vol. 102, pp. 253, 2001.

12. Gottesfeld, S., Zawodzinski, T.A., *Adv. Electrochemical Science and Engineering*, vol 5, pp. 219, 1997.

13. Wilson, M.S., Derouin, C.R., Valerio, J.A., and Gottesfeld, S., Proc. 28th Intersociety Energy Conversion Engineering Conference, Atlanta, Georgia, 1993, vol. 1, pp. 1203.

14. Iwase, M., and Kawatsu, S., in "First International Symposium on Proton Conducting Membrane Fuel Cells I", eds. A.R. Landgrebe, S. Gottesfeld and G. Halpert, *The Electrochemical Society*, Pennington, NJ, 1995, PV 95-23, pp. 12.

15. Oetjen, H.F., Schmidt, V.M., Stimming, U., and Trila, F., *Electrochemical Society,* vol. 143(12), pp.3838, 1996

16. Ralph, T.R., and Hogarth, M.P., Catalysis for Low Temperature Fuel Cells Part II, *Platinum Metals Review*, vol. 46(3), pp. 117, 2002

17. Watanabe, S., Influence of Impurities in Hydrogen on Fuel Cell Performance, *Hydrogen Codes and Standards Coordinating Committee Fuel Purity Specifications Workshop*, 26 April 2004.

18. Grgur, B.N., Zhuang, G., Markovic, N.M., Ross, P.N., *Journal of Physical Chemistry*, vol. 101, pp. 3910, 1997.

19. Grgur, B.N., Zhuang, G., Markovic, N.M., Ross, P.N., *Journal of Physical Chemistry*, vol. 102, pp. 2494, 1998.

20. Mukerjee, S., Lee, S.J., Ticianelli, E.A., McBreen, J., Grgur, B.N., Markovic, N.M., Ross, P.N., Giallombardo, J.R., De Castro, E.S., *Electrochemical Solid State Letters*, vol. 2, pp. 12, 1999.

21. Mukerjee, S., Urian, R.C., *Electrochemica Acta*, vol. 47, pp. 3219, 2002.

22. Roark, S.E., White, J.H., Selective removal of carbon monoxide, *United States Patent 6,787,118*, September 7, 2004.

23. Trimm, D.L., Minimisation of carbon monoxide in a hydrogen stream for fuel cell application, *Applied Catalysis A: General*, vol. 296, pp. 1, 2005.

24. Farrauto, R.J., *Applied Catalysis B: Environ.*, vol. 56, pp. 5, 2005.

25. Korotkikh, O., Farrauto, R., *Catalysis Today*, vol. 36, pp. 249, 2000.

26. Cha, D.Y., Rarravano, G., Surface reactivity of Supported Gold I. Oxygen Transfer Between CO and CO_2, *Journal of Catalysis*, vol. 18, pp. 200, 1970.

27. Haruta, M., Kobayashi, T., Sano, H., Yamada, N., Novel Gold Catalysts for the Oxidation of Carbon Monoxide at a Temperature far Below 0°C, *Chemistry letters*, pp. 405, 1987.

28. Haruta, M., *Catalyst Today*, vol. 36, pp. 153, 1997

29. Boccuzzi, F., Chiorino, A., Manzoli, M., Lu, P., Akita, T., Ichikawa, S., Haruta, M., *Journal of Catalysis*, vol. 202, pp. 256, 2001.

30. Bond, G.C., Thompson, D.T., *Catalysis Review – Science and Engineering*, vol. 41, pp. 319, 1999.

31. Okumura, M., Report of the research achievements of interdisciplinary basic research section (April 1994 – March 1999) "The Abilities and Potential of Gold as a Catalyst", *Report of the Osaka National Research Institute (ONRI)*, No. 393, pp. 6, August 1999.

32. Okumura, M., Tsubota, S., Iwamoto, M., Haruta, M., Chemical Vapor Deposition of Gold Nanoparticles on MCM-41 and Their Catalytic Activities for the Low-temperature Oxidation of CO and of H_2, *Chemistry Letters*, vol. 4, pp. 315, 1998.

33. Okumura, M., Nakamura, S., Tsubota, S., Nakamura, T., Azuma, M., Haruta, M., *Catalysis Letters*, vol. 51, pp. 53, 1998.

34. Haruta, M., Tsubota, S., Kobayashi, T., Kageyama, H., Genet, M.J., Delmon, B., *Journal of Catalysis*, vol. 144, pp. 175, 1993.

35. Zanella, R., Delannoy, L., Louis, C., Mechanism of deposition of gold precursors onto TiO_2 during the preparation by cation adsorption and deposition-precipitation with NaOH and urea, *Applied Catalysis A: General*, vol. 291, pp. 62, 2005.

36. Wolf, A., Schuth, F., *Journal of applied catalysis,* vol. 226, pp. 1, 2002.

37. Iizuka, Y., Tode, T., Takao, T., Yatsu, K., Takeuchi, T., Tsubota, S., *Journal of Catalysis*, vol. 187, pp. 50, 1999.

38. Lopez, N., Janssens, T.V.W., Clausen, B.S., Xu, Y., Mavrikakis, M., Bligaard, T., Norskov, J.K., *Journal of Catalysis*, vol. 223, pp. 232, 2004.

39. Okumura, M., Tsubota, S., Haruta, M., *Journal of Molecular Catalysis A*, vol. 199, pp. 73, 2003.

40. Minico, S., Scire, S., Crisafulli, C., Visco, A.M., Galvagno, S., *Catalysis Letters*, vol. 47, pp. 273, 1997.

41. Chang, C.K., Chen, Y.J., Yeh, C., *Applied Catalysis A*, vol. 174, pp. 13, 1998.

42. Schubert, M.M., Hackenberg, S., van Veen, A.C., Muhler, M., Plzak, V., Behm, R.J., *Journal of Catalysis*, vol. 197, pp. 113, 2001.

43. Moreau, F., Bond, G.C., Taylor, A.O., *Journal of Catalysis*, vol. 231, pp. 105, 2005.

44. Haruta, M., Yamada, N., Kobayashi, T., Iijima, S., *Journal of Catalysis*, vol. 115, pp. 301, 1989.

45. Bond, G.C., Thompson, D.T., Gold-Catalysed Oxidation of Carbon Monoxide, *Gold Bulletin*, vol. 33, pp. 41, 2000.

46. Shumacher, B., Denkwitz, Y., Plzak, V., Kinne, M., Behm, R.J., *Journal of Catalysis*, vol. 224, pp. 449, 2004.

47. Schubert, M.M., Venugopal, A., Kahlich, J.J., Plzak, V., Behm, R.J., *Journal of Catalysis*, vol. 222, pp. 32, 2004.

48. Schubert, M., Plzak, V., Garche, J., Behm, R.J., *Catalysis Letters*, vol. 76, pp. 143, 2001.

49. Costello, C.K., Yang, H.Y., Wang, Y., Lin, J.N., Marks, L.D., King, M.C., King, H.H., *Applied Catalysis*, vol. 243, pp. 15, 2003.

50. Konova, P., Naydenov, A., Tabakova, T., Mehandjiev, D., *Catalysis Communications*, vol. 5, pp. 537, 2004.

51. Manzoli, M., Chiorino, A., Boccuzi, F., *Applied Catalysis B Environ*, vol. 52, pp. 259, 2004.

52. Liu, X., Ruettinger, W., Xu, X., Farrauto, R., *Applied Catalysis B: Environ.*, vol. 56, pp. 69, 2005.

53. Giroux, T., Hwang, S., Liu, Y., Ruettinger, W., Shore, L., *Applied Catalysis B: Environ.*, vol. 55, pp. 185, 2005.

54. Ismagilor, Z.R., Pushkcarev, V.V., Podyacheva, O., Koryabkeina, N.A., Veringa, H., *Chemical Engineering Journal*, vol. 82, pp. 355, 2001.

55. Robbins, F.A., Zhu, H., Jackson, G.S., *Catalysis Today*, vol. 83, pp. 141, 2003.

56. Luengnaruemitchai, A., Osuwan, S., Gulari, E., Selective catalytic oxidation of CO in the presence of H_2 over gold catalyst, *International Journal of Hydrogen Energy*, vol. 29, pp. 429, 2004.

57. Panzera, G., Modafferi, V., Candamano, S., Donato, A., Frusteri, F., Antonucci, P.L., CO selective oxidation on ceria-supported Au catalysts for fuel cell application, *Journal of Power Sources*, vol. 135, pp. 177, 2004.

58. Barbier, Jr, J., Duprez, D., Steam effects in 3-way catalysis, *Applied Catalysis B*: *Environ*, vol. 4(2-3), pp. 105, 1994.

59. Bunluesin, T., Gorte, R.J., Graham, G.W., Studies of the water-gas-shift reaction on ceria-supported Pt, Pd, and Rh: implications for oxygen-storage properties, *Applied Catalysis B: Environ*, vol. 15, pp. 107, 1998.

60. Whittington, B.I., Jiang, C.J., Trimm, D.L., Vehicle exhaust catalysis: I, The relative importance of catalytic oxidation, steam reforming and water-gas-shift reactions, *Catalysis Today*, vol. 26, pp. 41, 1995.

61. Diwell, A.F., Rajaram, R.R., Shaw, H.A., Truex, T.J., Role of ceria in three-way catalysts, *Stud Surf Sci Catal*, vol. 71, pp. 139, 1991.

62. Ozawa, O., Kimura, M., Effect of cerium addition on the thermal stability of gamma alumina support, *Journal of Material Science Letters*, vol. 9(3) , pp. 291, 1990.

63. Shalabi, M.A., Harji, B.H., Kenney, C.N., Kinetic modeling of CO oxidation on Pt/CeO_2 in a gradientless reactor, *J Chem Technol Biotechnol*, vol. 65, pp. 317, 1996.

64. Holmgren, A., Andersson, B., Duprez, D., Interaction of CO with Pt/ceria catalysts, *Applied Catalysis B: Environ*, vol. 22(2), pp. 215, 1999.

65. Bockris, J. O'M. and Srinivasan, S., Fuel Cells: Their electrochemistry, McGraw-Hill Book Company, 1969.

66. Lane, D., Teather, E., Rockward, T.Q., Uribe, F.A., McNeil, D., Bailey, R., Pien, M., Establishing a Standardized Single Cell Testing Procedure through Industry Participation, Consensus, and Experimentation, *2004 Fuel Cell Seminar*, 1 – 5 November 2004, San Antonio, Texas.

67. Rossignol, C., Arrii, S., Morfin, F., Piccolo, Laurent., Caps, V., Rousset, J., Selective oxidation of CO over model-based catalysts in the presence of H_2, *Journal of Catalysis*, vol. 230, pp. 476, 2005.

68. Roberts, S., Influence of calcination on the catalytic activity of a Au/TiO_2 catalyst, MINTEK in-house report, 2003.

69. Zanella, R., Louis, C., Influence of the conditions of thermal treatments and of storage on the size of the gold particles in Au/TiO_2 samples, *Catalysis Today*, vol. 107, pp. 768, 2005.

70. Konova, P., Naydenov, Cv. Vencov., Mehandjiev, D., Andreeva, D., Tabakova, T., Activity and deactivation of Au/TiO_2 catalyst in CO oxidation, *Journal of Molecular Catalysis A*, vol. 213, pp. 235, 2004.

71. Bondzie, V.A., Parker, S.C., and Champbell, C.T., The kinetics of CO oxidation by adsorbed oxygen on well-defined gold particles on $TiO_2(110)$, *Catalysis Letters*, vol. 63, pp. 143, 1999.

72. Haruta, M., Gold as Novel Catalyst in the 21st Century: Preparation, Working Mechanism, and Application, *Gold Bulletin*, vol. 37, 2004.

73. Cunningham, D., Tsubota, S., Kamijo, N., Haruta, M., *Res. Chem. Intermed,* vol. 19 pp. 1, 1993.

74. Lin, S., Bollinger, M.A., Vannice, M.A., *Catalysis Letters*, vol.17, pp. 245, 1993.

75. Tsubota, S., Haruta, M., Kobayashi, T., Ueda, A., Nakahara, Y., *Stud. Surf. Sci. Catal.*, vol. 63, pp. 695, 1991.

76. Bollinger, M.A., Vannice, M.A., *Applied Catalysis B: Environ.*, vol. 8, pp. 417, 1996.

77. 'The Abilities and Potential of Gold as a Catalyst', Report of the National Research Institute, Osaka, Japan, 1999.

78. Debeila, M.A., Wells, R.P.K., Anderson, J.A., *Journal of Catalysis*, vol. 239, pp. 162, 2006.

79. Bocuzzi, F., Chiorino, A., Manzoli, M., Andreeva, D., Tabakova, T., *Journal of Catalysis*, vol. 188, pp. 176, 1999.

80. Bollinger, M.A., Vannice, M.A., *Applied Catalysis B: Environ.*, vol. 8, pp. 417, 1996.

81. Boccuzzi, F., Chiorino, A., Tsubota, S., Haruta, M., *Journal of Physical Chemistry*, vol. 100, pp. 3625, 1996.

82. Visco, A.M., Neri, F., Neri, G., Donato, A., Milone, C., Galvagno, S., *Phys. Chem. Chem. Phys.*, vol. 1, pp. 2869, 1999.

83. Finch, R.M., Hodge, N.A., Hutchings, G.J., Meagher, A., Pankhurst, Q.A., Siddiqui, M.R.H., Wagner, F.E., Whyman, R., *Phys. Chem. Chem. Phys.*, vol. 1, pp. 485, 1999.

84. Steyn, J., Pattrick, G., Van der Lingen, E., Scurrell, M.S., Hildebrandt, D., South African Preliminary Patent No. 2006/01120, 8 February 2006.

85. Griesel, R.J.H., Nieuwenhuys, B.E., Selective Oxidation of CO over Supported Au Catalysts, *Journal of Catalysis*, vol. 199, pp. 48, 2001.

86. Mariño, F., Descorme, C., Duprez, D., Noble metal catalysts for the preferential oxidation of carbon monoxide in the presence of hydrogen (PROX), *Applied Catalysis B: Environ.*, vol. 54, pp. 59, 2004.

87. U.S. Department of Energy – Energy Efficiency and Renewable Energy, *Multi-Year Research, Development, and Demonstration Plan: Fuel cells,* INTERNET. http://www.eere.energy.gov/hydrogenandfuelcells/mypp/pdfs/fuel_cells.pdf. Cited 27 March 2006.

88. Gold Survey 2006, GMFS Limited, April 2006.

APPENDIXES

APPENDIX I

Conceptual drawings of a typical monolith reactor

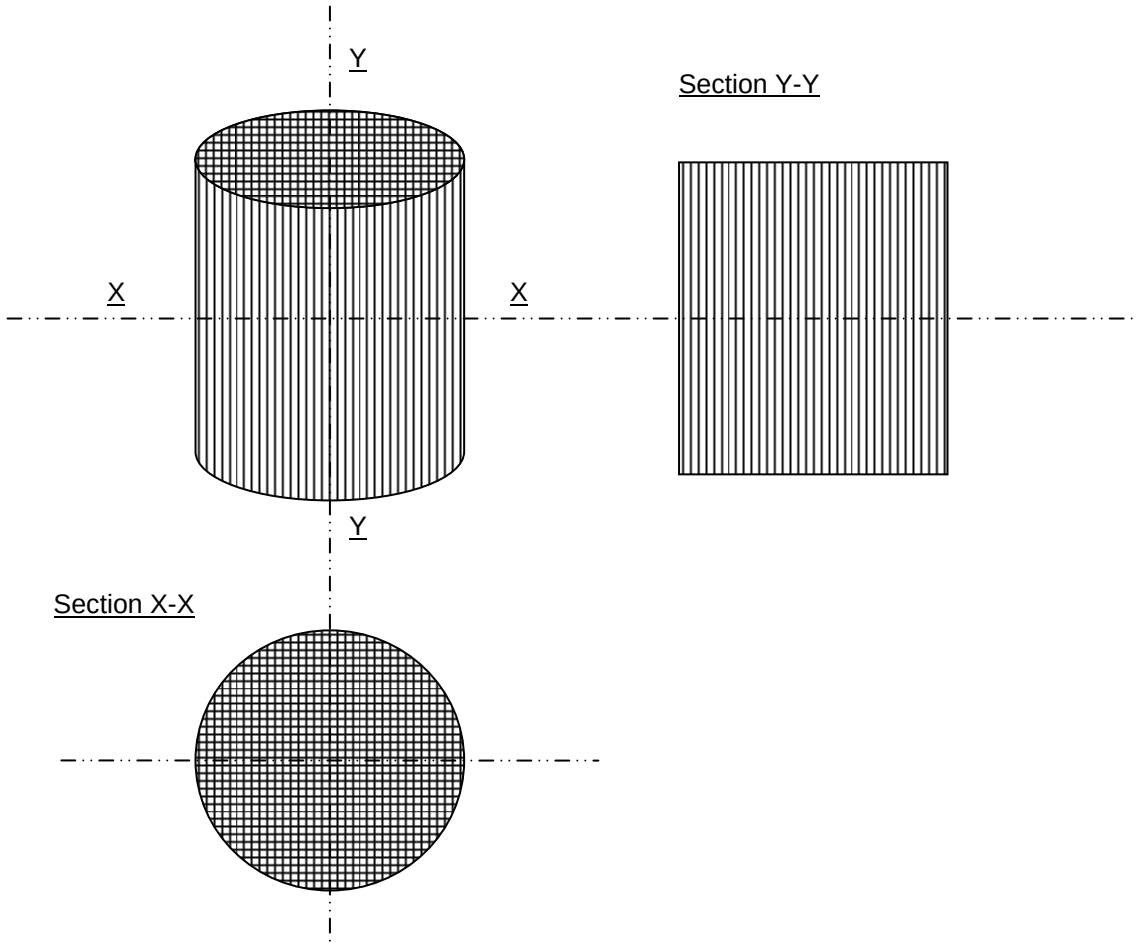

APPENDIX II

Diagrammatic representation of the CO oxidation test rig

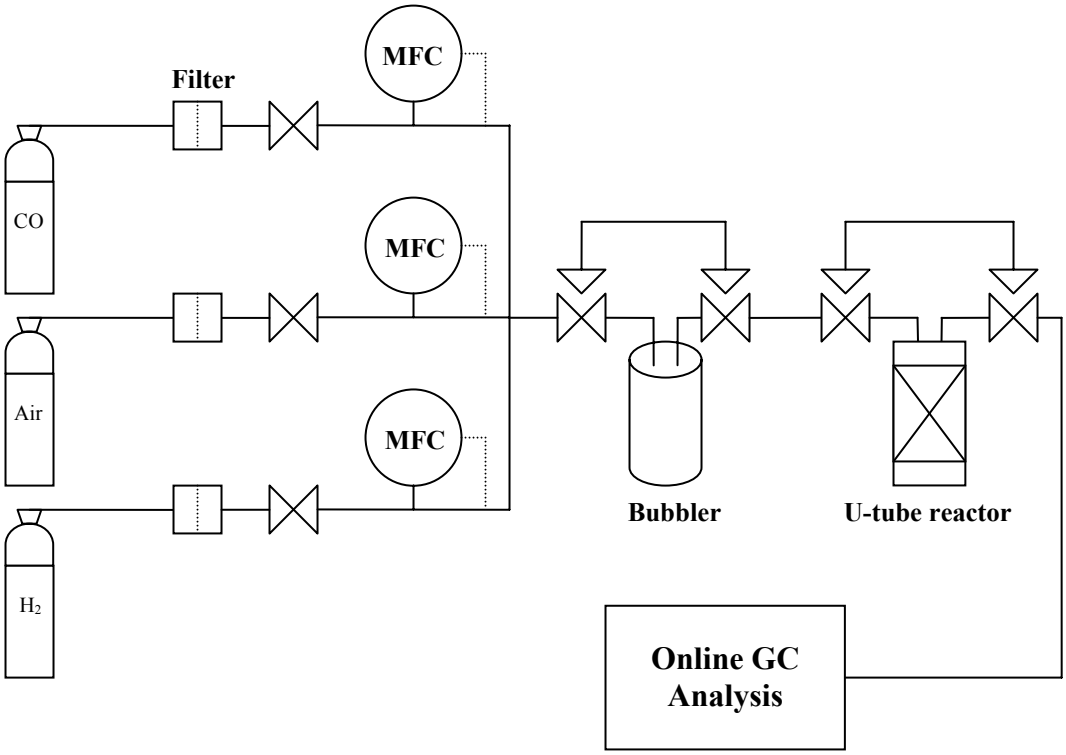

APPENDIX III

Hydrogen Specifications

Gases: Special

Hydrogen (H_2), Compressed

HYDROGEN, PROCESS (N4.8)

SPECIFICATION

Gas	Purity
Minimum purity	99,998% (N4.8)

Maximum impurities	
Oxygen	5 ppm
Moisture	5 ppm

Typical impurities	
Nitrogen	10 ppm
Total impurities not to exceed	20 ppm

NOTE

Item number	Cylinder size	Contents kg	Charging pressure kPa at 20°C	Valve outlet connection
340/133	ZZ	0,74	20 000	5/8" BSPF left hand female
341/015	MCP	11,1	20 000	

HYDROGEN INSTRUMENT GRADE (N5.0)

SPECIFICATION

Gas	Purity
Minimum purity	99,999% (N5.0)

Maximum impurities	
Oxygen	2 ppm
Moisture	2 ppm
Nitrogen	2 ppm
Carbon dioxide	0,5 ppm
Carbon monoxide	0,5 ppm
THC as CH_4	0,5 ppm
Total impurities not to exceed	10 ppm

NOTE

Item number	Cylinder size	Contents kg	Charging pressure kPa at 20°C	Valve outlet connection
340/130	ZZ	0,74	20 000	5/8" BSPF left hand female

APPENDIX IV

Detailed drawing of the 'flat bed' reactor

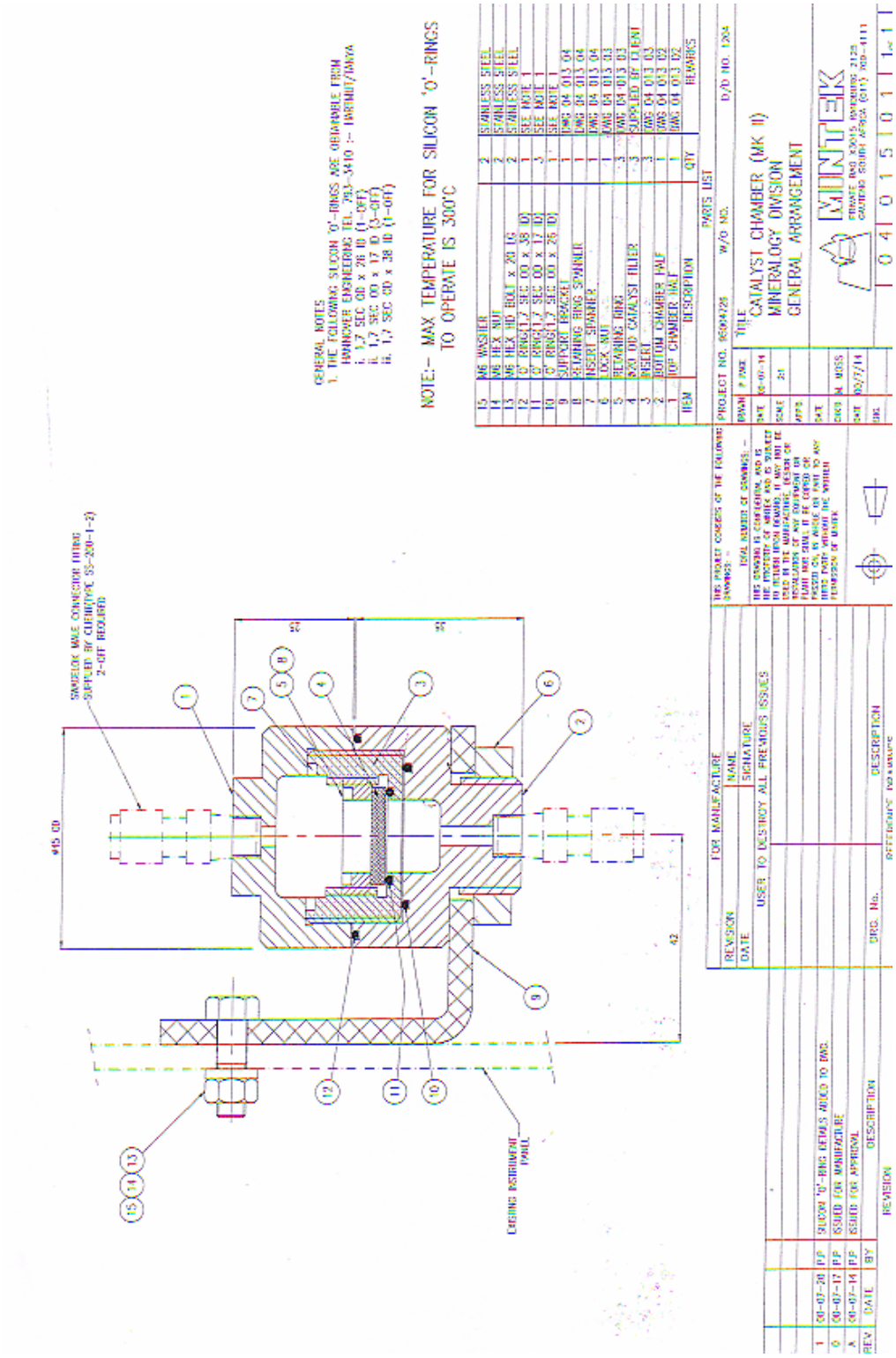

APPENDIX V

Diagrammatic representation of fuel cell test station

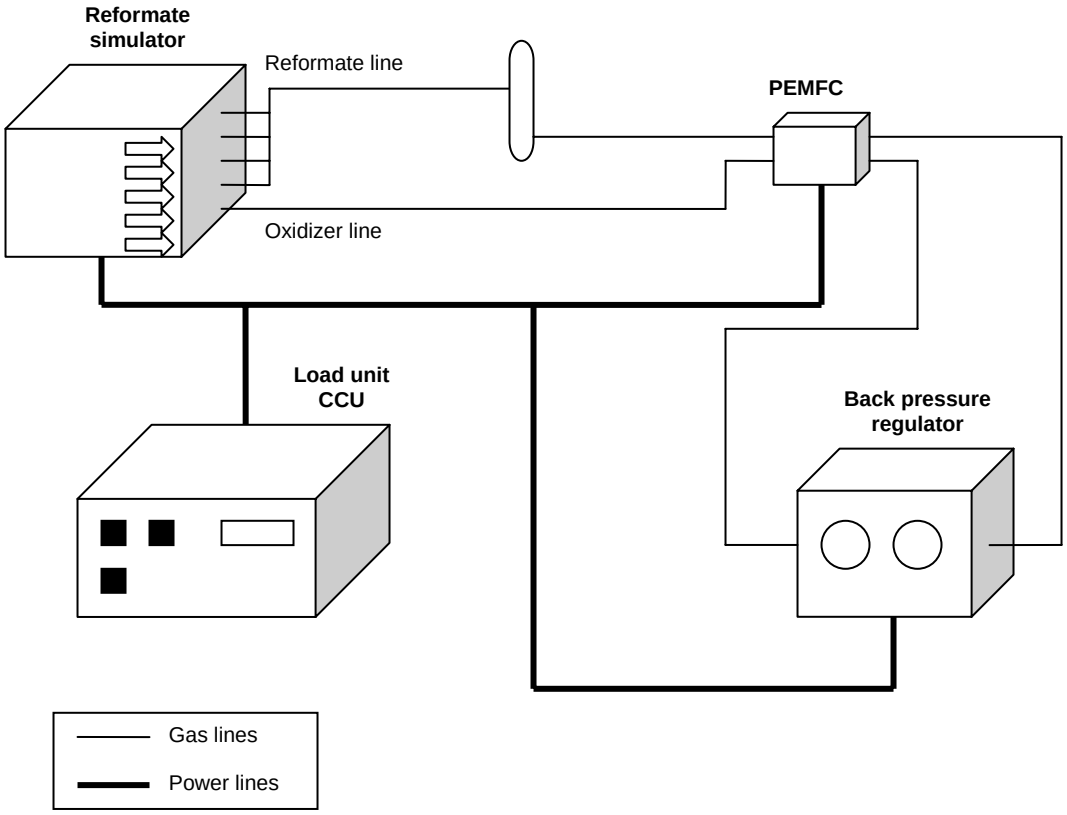

APPENDIX VI

Au/TiO_2 PROX configuration in Johnson Matthey fuel cell system

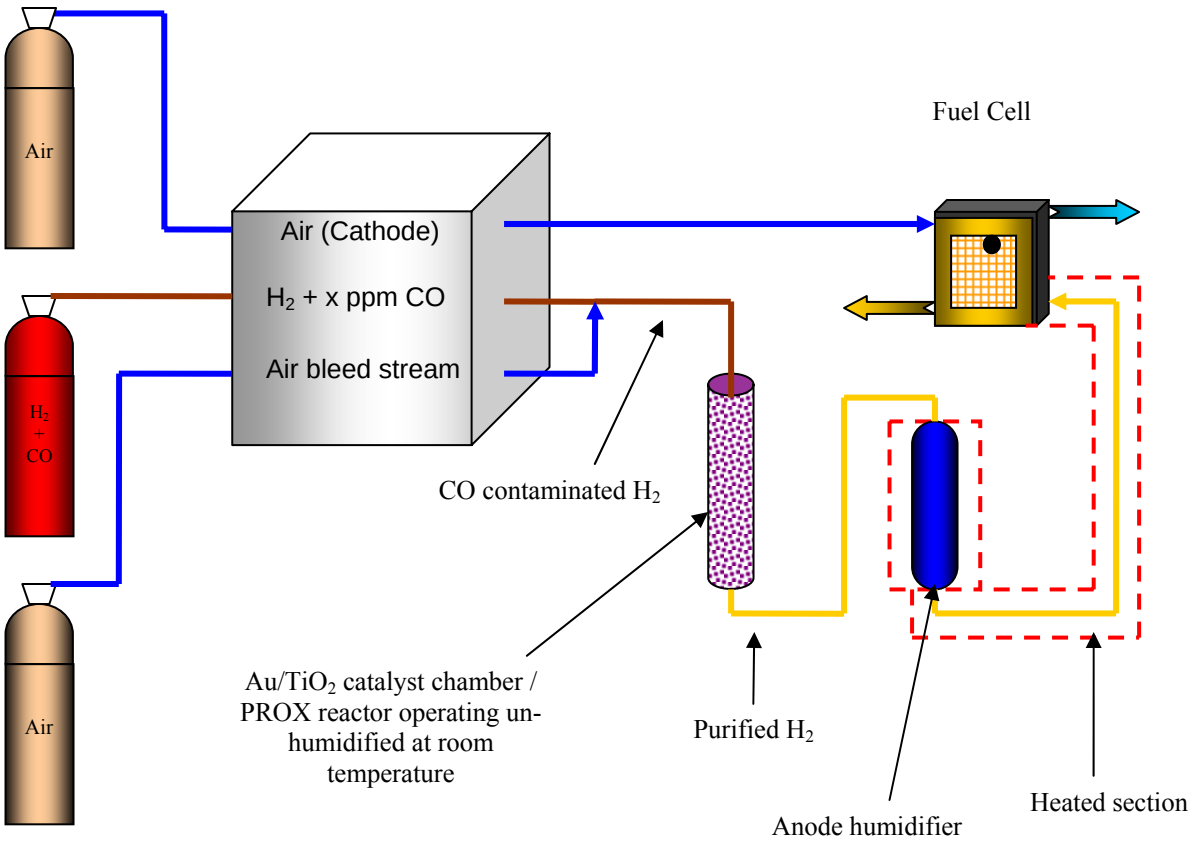

Note: Drawing not to scale

APPENDIX VII

Calculation of H_2 flow rate and space velocity over single cell Au/TiO_2 bi-layer

Parameter	Unit	Value
Operating current density	$A.cm^{-2}$	0.5
Single cell MEA area	cm^2	25
Current drawn from single cell	A	12.5

At the anode, hydrogen gets oxidized according to Reaction 16:

$$H_2 \rightarrow 2H^+ + 2e^- \qquad E^o = 0.00\ V_{SHE} \qquad (16)$$

The volumetric flow rate of H_2 to deliver the desired optimum power can be calculated using Equation 26.

$$Q = \frac{22.4141 \times mI}{nF} \qquad (26)$$

According to Reaction 16, the moles of electrons transferred *(n)* are equal to 2. For this calculation, the H_2 stoichiometry *(m)* is specified as 2.2, as per the standardised single cell test procedure, thus:

$$Q = \frac{22.4141 \times 2.2 \times 12.5 \times 60}{2 \times 96{,}485}$$

$$\therefore Q = 191.7\ m\ell.min^{-1}$$

Catalyst mass (m_c) (g)	H_2 flow rate (Q) ($ml.min^{-1}$)	$MHSV = \frac{Q \times 60}{m_c}$
0.25	191.7	46080
0.125	191.7	92160
0.5	191.7	23040
0.25	191.7	46080
0.25	191.7	46080

APPENDIX VIII

Calculation of the pressure drop over packed beds of powder catalyst, granulate catalyst and catalyst coated monoliths.

The mathematical definition of the pressure drop over a packed-bed is given below:

$$\Delta p = \frac{f_p L \rho V_s^{\,2}}{D_p}\left(\frac{1-\varepsilon}{\varepsilon^3}\right) \tag{30}$$

where,

$$V_s = \frac{Q}{A} \tag{30.1}$$

$$D_p = 6\frac{V_p}{A_p} \tag{30.2}$$

$$f_p = \frac{150}{\mathrm{Re}_p} + 1.75 \tag{30.3}$$

$$\mathrm{Re}_p = \frac{D_p V_s \rho}{(1-\varepsilon)\mu} \tag{30.4}$$

$$\varepsilon = 1 - \frac{\rho_b}{\rho_p} \tag{30.5}$$

Symbol	Definition	Units	Value		
			powder	granules	monolith
L	Length of the bed	cm	0.4	0.4	-
ρ	Density of the gas	$g.cm^{-3}$	8.18E-05	8.18E-05	8.18E-05
V_s	Superficial velocity	$cm.s^{-1}$	199	199	-
D_p	Equivalent spherical diameter of particle	μm	75	500	-
ε	Void fraction of the bed	-	0.81	0.79	-
Q	Volumetric flow rate	$cm^3.min^{-1}$	1500	1500	-
A	Cross-sectional area of the bed (L=2d)	cm^2	0.126	0.126	-
V_p	Volume of the particle	cm^3	2.21E-07	6.54E-05	-
A_p	Surface area of the particle	cm^2	0.00018	0.00785	-
f_p	Friction factor	-	3.74	2.04	-
Re_p	Reynolds number	-	75.34	514.99	-
μ	Dynamic viscosity of the gas (H_2)	Pa.s	8.4E-06	8.4E-06	8.4E-06
ρ_b	Bulk density of support	$g.cm^{-3}$	0.79	0.87	-
ρ_p	Particle density of support material	$g.cm^{-3}$	4.2	4.2	-

APPENDIX IX

Resistance compensated voltage vs. time curves illustrating CO poisoning and effect of Au/TiO_2 PROX system on CO tolerance

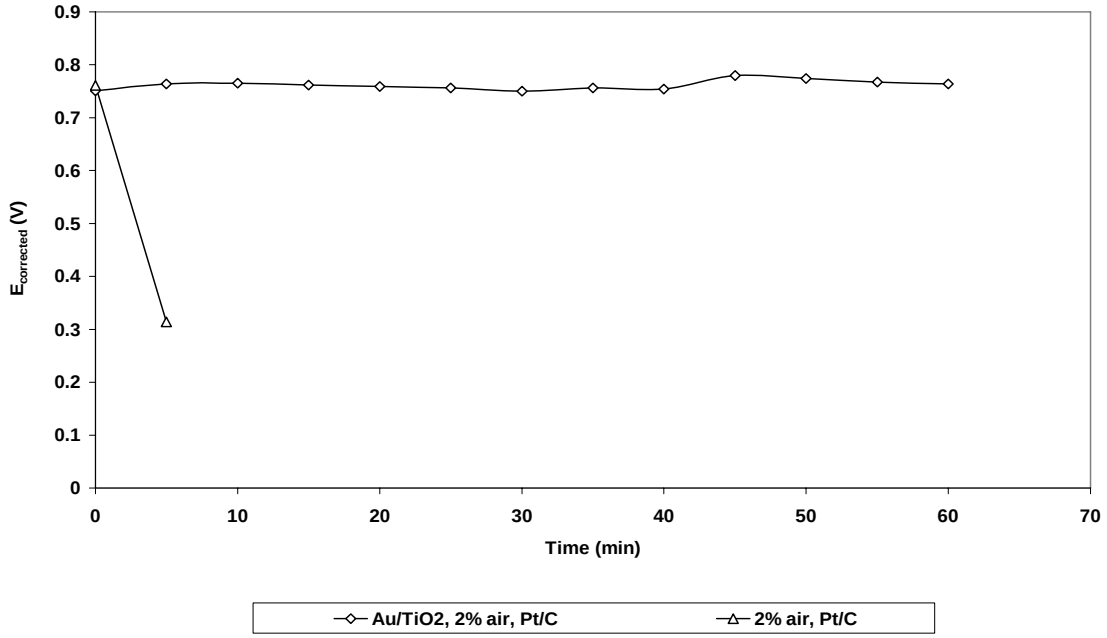

Figure 63b: Resistance compensated potential vs. time graph for 1000 ppm CO over Pt/C. Similar conditions than Figure 63.

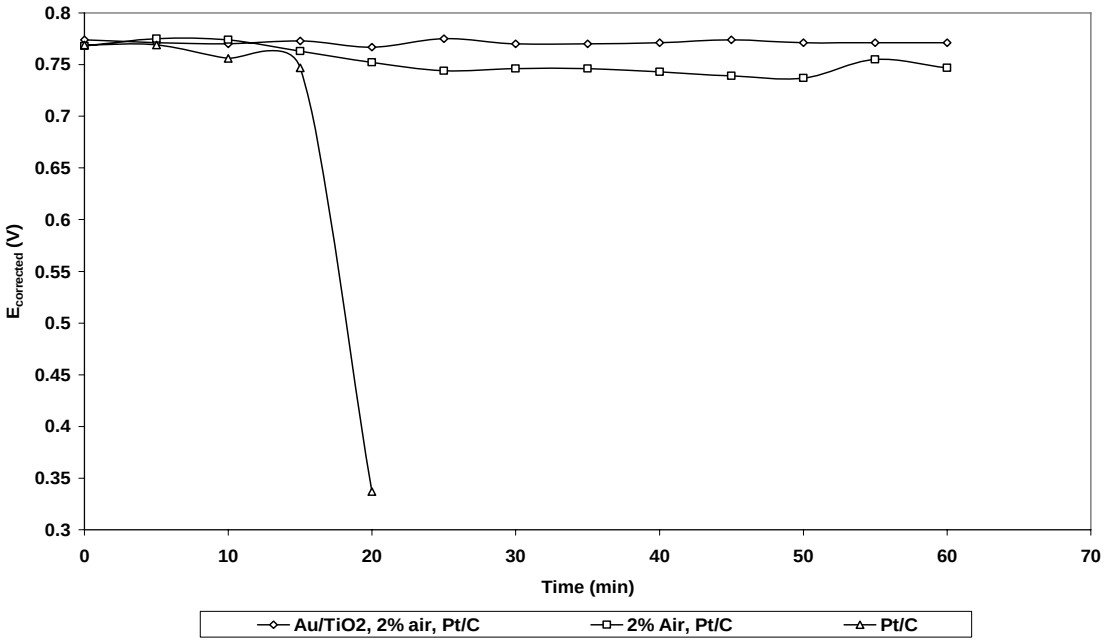

Figure 64b: Resistance compensated potential vs. time graph for 100 ppm CO over Pt/C. Similar conditions than Figure 64.

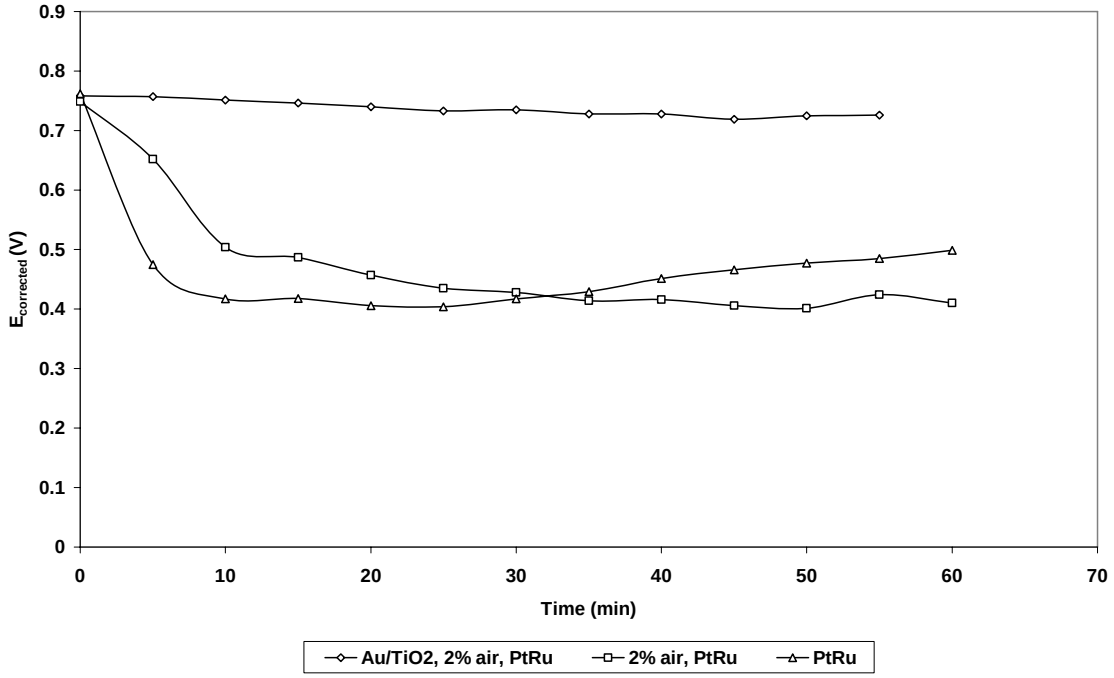

Figure 65b: Resistance compensated potential vs. time graph for 1000 ppm CO over PtRu/C. Similar conditions than Figure 65.

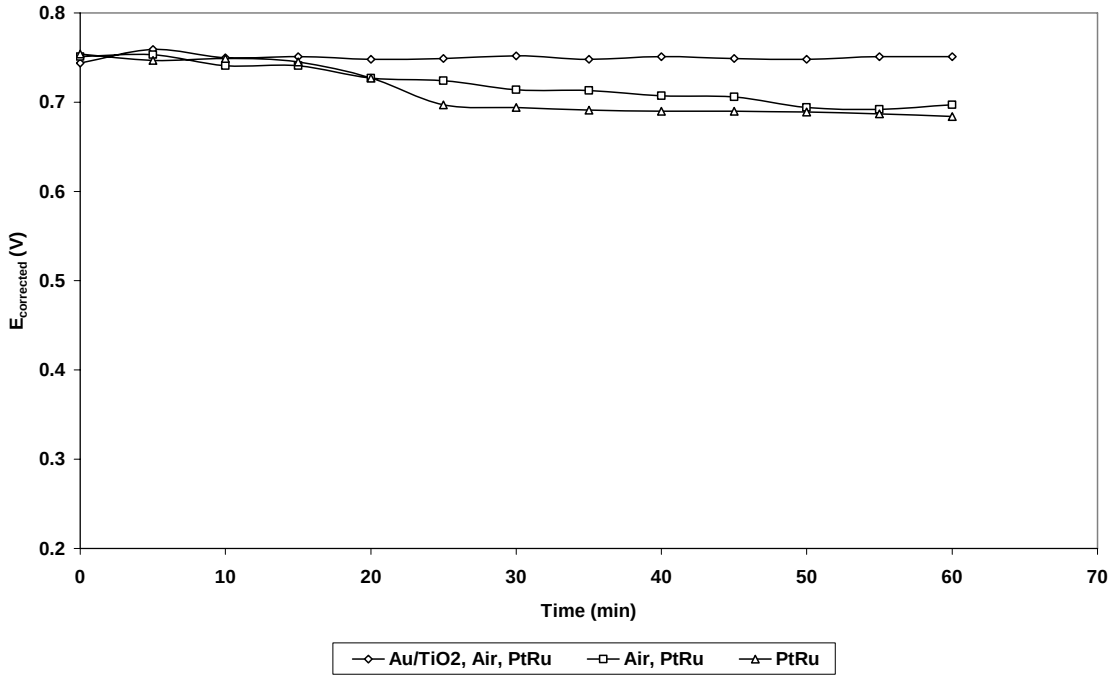

Figure 66b: Resistance compensated potential vs. time graph for 100 ppm CO over PtRu/C. Similar conditions than Figure 66.

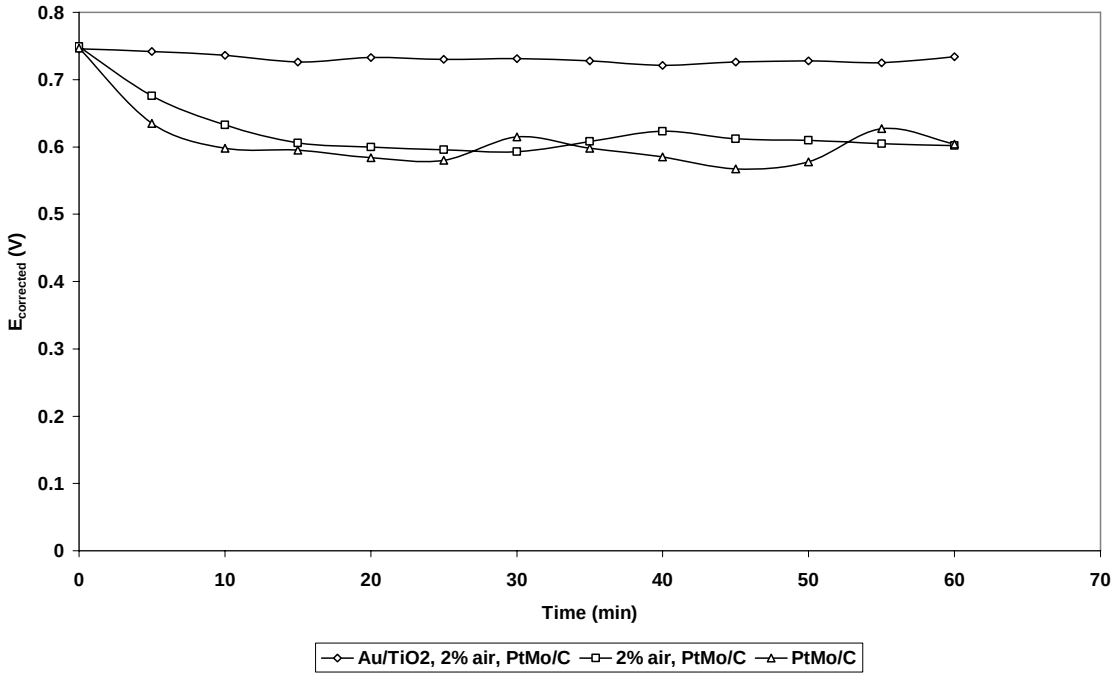

Figure 67b: Resistance compensated potential vs. time graph for 1000 ppm CO over PtMo/C. Similar conditions than Figure 67.

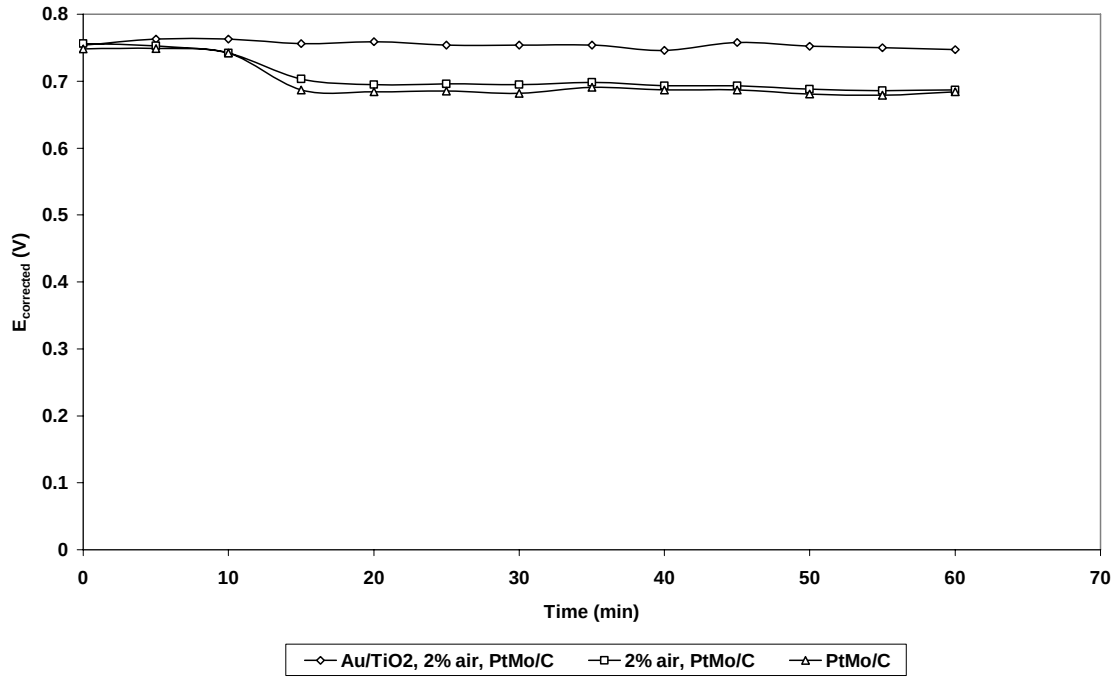

Figure 68b: Resistance compensated potential vs. time graph for 1000 ppm CO over PtMo/C. Similar conditions than Figure 68.

APPENDIX X

Calculation of H_2 flow rate to a 60 kW fuel cell system operating at optimum power

Parameter	Unit	Value
Optimum power output *(P)*	kW	60
Operating potential of fuel cell stack *(E)*	V	0.65
H_2 stoichiometry *(m)*	-	1.02

Current *(I)* drawn at optimum power:

$$P = IE \tag{25}$$

$$\therefore 60{,}000 = 0.65I$$

$$\therefore I = \underline{92{,}307.7A}$$

At the anode, hydrogen gets oxidized according to Reaction 16:

$$H_2 \rightarrow 2H^+ + 2e^- \qquad E^o = 0.00\ V_{SHE} \tag{16}$$

The volumetric flow rate of H_2 to deliver the desired optimum power can be calculated using Equation 26.

$$Q = \frac{22.4141 \times mI}{nF} \tag{26}$$

According to Reaction 16, the moles of electrons transferred *(n)* are equal to 2. The H_2 stoichiometry *(m)* is specified as 1.02, thus:

$$Q = \frac{22.4141 \times 1.02 \times 92{,}307.7 \times 60}{2 \times 96{,}485}$$

$$\therefore Q = 656.2\ \ell.\text{min}^{-1}$$

APPENDIX XI

Sensitivity analysis for the projected cost of gold in fuel cell systems to changes in the gold price

Table XI A: A presentation of the cost associated with different amounts of catalysts with different gold loadings, yielding different space velocities. Calculations are based on the following conditions and assumptions: Assume 60 kW system operating at peak output at 0.65 V (drawing 92 308 A). Hydrogen flow to fuel cell at 1.02 stoichiometry, thus 656 l.min^{-1} (calculation of this flow rate is shown in Appendix IX). Assume gold price of $400/oz.

Mass of catalyst (g)	Space velocity ($l.g_{cat}^{-1}.h^{-1}$)	Cost of gold in fuel cell system, in US$, for different gold loadings (wt%)					
		1wt%	2wt%	3wt%	5wt%	10wt%	20wt%
20	1989	2.58	5.16	7.74	12.90	25.81	51.61
46.8	850*	6.04	12.08	18.12	30.19	60.39	120.77
50	795	6.45	12.90	19.35	32.26	64.52	129.03
100	398	12.90	25.81	38.71	64.52	129.03	258.06
150	265	19.35	38.71	58.06	96.77	193.55	387.10
200	199	25.81	51.61	77.42	129.03	258.06	516.13
300	133	38.71	77.42	116.13	193.55	387.10	774.19
400	99	51.61	103.23	154.84	258.06	516.13	1,032.26

**Current operating conditions in CO oxidation test rig*

Table XI B: A presentation of the percentage cost of Au relative to the USDoE cost target of $45/kW for different amounts of catalysts with different gold loadings, yielding different space velocities. Calculations are based on the following conditions and assumptions: Assume 60 kW system operating at peak output at 0.65 V (drawing 92 308 A). Hydrogen flow to fuel cell at 1.02 stoichiometry, thus 656 l.min^{-1} (calculation of this flow rate is shown in Appendix IX). Assume gold price of $400/oz.

Mass of catalyst (g)	Space velocity ($l.g_{cat}^{-1}.h^{-1}$)	% cost of Au relative to $45/kW target, for different gold loadings (wt%)					
		1wt%	2wt%	3wt%	5wt%	10wt%	20wt%
20	1989	0.10	0.19	0.29	0.48	0.96	1.91
46.8	850*	0.22	0.45	0.67	1.12	2.24	4.47
50	795	0.24	0.48	0.72	1.19	2.39	4.78
100	398	0.48	0.96	1.43	2.39	4.78	9.56
150	265	0.72	1.43	2.15	3.58	7.17	14.34
200	199	0.96	1.91	2.87	4.78	9.56	19.12
300	133	1.43	2.87	4.30	7.17	14.34	28.67
400	99	1.91	3.82	5.73	9.56	19.12	38.23

**Current operating conditions in CO oxidation test rig*

Table XI C: A presentation of the cost associated with different amounts of catalysts with different gold loadings, yielding different space velocities. Calculations are based on the following conditions and assumptions: Assume 60 kW system operating at peak output at 0.65 V (drawing 92 308 A). Hydrogen flow to fuel cell at 1.02 stoichiometry, thus 656 l.min^{-1} (calculation of this flow rate is shown in Appendix IX). Assume gold price of $600/oz.

Mass of catalyst (g)	Space velocity ($l.g_{cat}^{-1}.h^{-1}$)	Cost of gold in fuel cell system, in US$, for different gold loadings (wt%)					
		1wt%	2wt%	3wt%	5wt%	10wt%	20wt%
20	1989	3.87	7.74	11.61	19.35	38.71	77.42
46.8	850*	9.06	18.12	27.17	45.29	90.58	181.16
50	795	9.68	19.35	29.03	48.39	96.77	193.55
100	398	19.35	38.71	58.06	96.77	193.55	387.10
150	265	29.03	58.06	87.10	145.16	290.32	580.65
200	199	38.71	77.42	116.13	193.55	387.10	774.19
300	133	58.06	116.13	174.19	290.32	580.65	1,161.29
400	99	77.42	154.84	232.26	387.10	774.19	1,548.39

**Current operating conditions in CO oxidation test rig*

Table XI D: A presentation of the percentage cost of Au relative to the USDoE cost target of $45/kW for different amounts of catalysts with different gold loadings, yielding different space velocities. Calculations are based on the following conditions and assumptions: Assume 60 kW system operating at peak output at 0.65 V (drawing 92 308 A). Hydrogen flow to fuel cell at 1.02 stoichiometry, thus 656 l.min^{-1} (calculation of this flow rate is shown in Appendix IX). Assume gold price of $600/oz.

Mass of catalyst (g)	Space velocity ($l.g_{cat}^{-1}.h^{-1}$)	% cost of Au relative to $45/kW target, for different gold loadings (wt%)					
		1wt%	2wt%	3wt%	5wt%	10wt%	20wt%
20	1989	0.14	0.29	0.43	0.72	1.43	2.87
46.8	850*	0.34	0.67	1.01	1.68	3.35	6.71
50	795	0.36	0.72	1.08	1.79	3.58	7.17
100	398	0.72	1.43	2.15	3.58	7.17	14.34
150	265	1.08	2.15	3.23	5.38	10.75	21.51
200	199	1.43	2.87	4.30	7.17	14.34	28.67
300	133	2.15	4.30	6.45	10.75	21.51	43.01
400	99	2.87	5.73	8.60	14.34	28.67	57.35

**Current operating conditions in CO oxidation test rig*

Table XI E: A presentation of the cost associated with different amounts of catalysts with different gold loadings, yielding different space velocities. Calculations are based on the following conditions and assumptions: Assume 60 kW system operating at peak output at 0.65 V (drawing 92 308 A). Hydrogen flow to fuel cell at 1.02 stoichiometry, thus 656 l.min^{-1} (calculation of this flow rate is shown in Appendix IX). Assume gold price of $700/oz.

Mass of catalyst (g)	Space velocity ($l.g_{cat}^{-1}.h^{-1}$)	Cost of gold in fuel cell system, in US$, for different gold loadings (wt%)					
		1wt%	2wt%	3wt%	5wt%	10wt%	20wt%
20	1989	4.52	9.03	13.55	22.58	45.16	90.32
46.8	850*	10.57	21.14	31.70	52.84	105.68	211.35
50	795	11.29	22.58	33.87	56.45	112.90	225.81
100	398	22.58	45.16	67.74	112.90	225.81	451.61
150	265	33.87	67.74	101.61	169.35	338.71	677.42
200	199	45.16	90.32	135.48	225.81	451.61	903.23
300	133	67.74	135.48	203.23	338.71	677.42	1,354.84
400	99	90.32	180.65	270.97	451.61	903.23	1,806.45

**Current operating conditions in CO oxidation test rig*

Table XI F: A presentation of the percentage cost of Au relative to the USDoE cost target of $45/kW for different amounts of catalysts with different gold loadings, yielding different space velocities. Calculations are based on the following conditions and assumptions: Assume 60 kW system operating at peak output at 0.65 V (drawing 92 308 A). Hydrogen flow to fuel cell at 1.02 stoichiometry, thus 656 l.min^{-1} (calculation of this flow rate is shown in Appendix IX). Assume gold price of $700/oz.

Mass of catalyst (g)	Space velocity ($l.g_{cat}^{-1}.h^{-1}$)	% cost of Au relative to $45/kW target, for different gold loadings (wt%)					
		1wt%	2wt%	3wt%	5wt%	10wt%	20wt%
20	1989	0.17	0.33	0.50	0.84	1.67	3.35
46.8	850*	0.39	0.78	1.17	1.96	3.91	7.83
50	795	0.42	0.84	1.25	2.09	4.18	8.36
100	398	0.84	1.67	2.51	4.18	8.36	16.73
150	265	1.25	2.51	3.76	6.27	12.54	25.09
200	199	1.67	3.35	5.02	8.36	16.73	33.45
300	133	2.51	5.02	7.53	12.54	25.09	50.18
400	99	3.35	6.69	10.04	16.73	33.45	66.91

**Current operating conditions in CO oxidation test rig*

Table XI G: A presentation of the cost associated with different amounts of catalysts with different gold loadings, yielding different space velocities. Calculations are based on the following conditions and assumptions: Assume 60 kW system operating at peak output at 0.65 V (drawing 92 308 A). Hydrogen flow to fuel cell at 1.02 stoichiometry, thus 656 l.min^{-1} (calculation of this flow rate is shown in Appendix IX). Assume gold price of $1000/oz.

Mass of catalyst (g)	Space velocity ($l.g_{cat}^{-1}.h^{-1}$)	Cost of gold in fuel cell system, in US$, for different gold loadings (wt%)					
		1wt%	2wt%	3wt%	5wt%	10wt%	20wt%
20	1989	6.45	12.90	19.35	32.26	64.52	129.03
46.8	850*	15.10	30.19	45.29	75.48	150.97	301.94
50	795	16.13	32.26	48.39	80.65	161.29	322.58
100	398	32.26	64.52	96.77	161.29	322.58	645.16
150	265	48.39	96.77	145.16	241.94	483.87	967.74
200	199	64.52	129.03	193.55	322.58	645.16	1,290.32
300	133	96.77	193.55	290.32	483.87	967.74	1,935.48
400	99	129.03	258.06	387.10	645.16	1,290.32	2,580.65

**Current operating conditions in CO oxidation test rig*

Table XI H: A presentation of the percentage cost of Au relative to the USDoE cost target of $45/kW for different amounts of catalysts with different gold loadings, yielding different space velocities. Calculations are based on the following conditions and assumptions: Assume 60 kW system operating at peak output at 0.65 V (drawing 92 308 A). Hydrogen flow to fuel cell at 1.02 stoichiometry, thus 656 l.min^{-1} (calculation of this flow rate is shown in Appendix IX). Assume gold price of $1000/oz.

Mass of catalyst (g)	Space velocity ($l.g_{cat}^{-1}.h^{-1}$)	% cost of Au relative to $45/kW target, for different gold loadings (wt%)					
		1wt%	2wt%	3wt%	5wt%	10wt%	20wt%
20	1989	0.24	0.48	0.72	1.19	2.39	4.78
46.8	850*	0.56	1.12	1.68	2.80	5.59	11.18
50	795	0.60	1.19	1.79	2.99	5.97	11.95
100	398	1.19	2.39	3.58	5.97	11.95	23.89
150	265	1.79	3.58	5.38	8.96	17.92	35.84
200	199	2.39	4.78	7.17	11.95	23.89	47.79
300	133	3.58	7.17	10.75	17.92	35.84	71.68
400	99	4.78	9.56	14.34	23.89	47.79	95.58

**Current operating conditions in CO oxidation test rig*

APPENDIX XII

Projected gold usage: Tables and calculations

Projected gold usage:

$$Au(tons) = \frac{m_{Au}.N_{nv}.\left(\frac{M_{pen}}{100}\right)}{1\times10^{6}} \quad (33)$$

where *Au(tons)* is the projected mass of gold that will be consumed in tons, m_{Au} the projected mass of gold in one fuel cell powered vehicle (g), N_{nv} the projected number on new vehicles produced, and M_{pen} the percentage market penetration. Based on Equation 33, the following can be presented.

Table XII A: Estimated gold usage based on different levels of market penetration and different catalyst gold loadings for a PROX system operating at 850 000 ml.g_{cat}^{-1}.h^{-1} (Assume 60 kW fuel cell systems, and annual vehicle production in 2020 = 78.1 million).

% Market penetration	Projected gold usage, in tons, for different Au loadings (wt%)					
	1 wt%	2 wt%	3 wt%	5 wt%	10 wt%	20 wt%
15	5.48	10.96	16.44	27.41	54.81	109.62
10	3.65	7.31	10.96	18.27	36.54	73.08
5	1.83	3.65	5.48	9.14	18.27	36.54
3	1.10	2.19	3.29	5.48	10.96	21.92
1	0.37	0.73	1.10	1.83	3.65	7.31

Table XII B: Estimated gold revenue based on different levels of market penetration and different gold prices for a 3 wt% Au-based PROX system operating at 850 000 ml.g_{cat}^{-1}.h^{-1} (Assume 60 kW fuel cell systems, and annual vehicle production in 2020 = 78.1 million).

% Market penetration	Projected gold revenue, in $, at different gold prices ($/oz)					
	$400/oz	$500/oz	$600/oz	$700/oz	$1000/oz	$2000/oz
15	212.17	265.21	318.25	371.29	530.42	1,060.84
10	141.45	176.81	212.17	247.53	353.61	707.23
5	70.72	88.40	106.08	123.76	176.81	353.61
3	42.43	53.04	63.65	74.26	106.08	212.17
1	14.14	17.68	21.22	24.75	35.36	70.72

APPENDIX XIII

Technical Targets

Technical targets: 80-kW_e (net) integrated transportation fuel cell power system operating on direct hydrogen[a] [87]					
Characteristic	**Units**	**2004 Status**	**2005**	**2010**	**2015**
Energy efficiency[b] at 25% of rated power	%	59	60	60	60
Energy efficiency at rated power	%	50	50	50	50
Power density	W/L	450	500	650	650
Specific power	W/kg	420	500	650	650
Cost[c]	$/$kW_e$	120[d]	125	45	30
Transient response (time from 10% to 90% of rated power)	sec	1.5	2	1	1
Cold start-up time to 90% of rated power					
at -20°C ambient temp	sec	120	60	30	30
at +20°C ambient temp	sec	60	30	15	15
Durability with cycling	Hours	~1000[e]	2000	5000[f]	5000[f]
Survivability[g]	°C	-20	-30	-40	-40

[a] Targets exclude hydrogen storage.

[b] Ratio of DC output energy to the lower heating value of the input fuel (hydrogen). Peak efficiency occurs at about 25% rated power.

[c] Based on 2002$ and cost projected to high-volume (500,000 stacks per year).

[d] Based on 2004 TIAX Study and will be periodically updated.

[e] Steady-state durability is 9,000 hours.

[f] Includes typical drive cycle.

[g] Performance targets must be achieved at the end of 8-hour cold-soak at temperature.

APPENDIX XIV

List of Publications

Steyn, J., Pattrick, G., Scurrell, M.S., Hildebrandt, D., Van der Lingen, E., An unconventional Au/TiO_2 PROX system for complete removal of CO from non-reformate hydrogen, Oral presentation to be presented at Fuel Cells Science & Technology 2006: Scientific Advances in Fuel Cell Systems, September 13 – 14, 2006, Turin, Italy.

Steyn, J., Pattrick, G., Scurrell, M.S., Hildebrandt, D., Van der Lingen, E., Comparative performances of an unconventional Au/TiO_2 PROX system and state of the art bi-alloy CO tolerant anodes, Oral presentation to be presented at the International Conference on the Science, Technology and Industrial Applications of Gold, September 3 – 6, 2006, Limerick, Ireland.

Steyn, J., Thompson, D.T., Pattrick, G., Efficient Gold Catalyst System for Hydrogen Purification, Forum Participation at Hannover Fair 2006, April 24 – 28, 2006, Hannover, Germany.

Steyn, J., Pattrick, G., Scurrell, M.S., Roberts, S.R., Van der Lingen, E., TiO_2 supported Au Catalysts for Selective Catalytic Oxidation of CO to CO_2 in Fuel Cell Operating Conditions, Proceedings of 3rd European Fuel Cell Forum, July 4 – 8, 2005, Lucerne, Switzerland.

Steyn, J., Pattrick, G., Scurrell, M.S., Online deactivation of Au/TiO_2 catalysts for CO oxidation in hydrogen-rich gas streams, Submitted to Catalysis Communications, May 2006.

Steyn, J., Pattrick, G., Van der Lingen, E., Thompson, D.T., New Au-based catalyst system for the purification of stored impure hydrogen for fuel cell applications, Submitted to Gold Bulletin, May 2006.

Steyn, J., Pattrick, P., Scurrell, M.S., Hildebrandt, D., Van der Lingen, E., Increasing the CO tolerance of proton exchange membrane fuel cell systems using gold-based catalysts, Submitted to Electrochemical Communications, May 2006.